

Università degli Studi di Siena



Facoltà di Scienze Matematiche Fisiche e Naturali

Tesi di Dottorato in Fisica Sperimentale  
PhD Thesis in Experimental Physics

XIX Ciclo

**Measurement of the branching fraction  
ratio  $\frac{BR(B^+ \rightarrow \bar{D}^0 K^+ \rightarrow [K^+ \pi^-] K^+)}{BR(B^+ \rightarrow \bar{D}^0 \pi^+ \rightarrow [K^+ \pi^-] \pi^+)}$  with the CDF II  
detector**

Candidato

**Paola Squillacioti**

Relatore

**Dott. Maria Agnese Ciocci**

Tutor

**Prof. Giovanni Punzi**



*a Riccardo*





# Acknowledgments

I would like to thanks many people that helped me in these three years of PhD.

First of all I would like to thanks my supervisor, Maria Agnese Ciocci, to introduce me in the high energy physics, for being so patient with me at the beginning when I did not know anything about particle physics and CDF. Thanks also for being patient with my telegraphic writing.

Then I would like to thanks Giovanni Punzi, my tutor. He was my guide for the developing of the Particle IDentification tool and for the  $B^+ \rightarrow \overline{D}^0 K^+$  analysis. He gave me always the right suggestion and he was always present during the crucial moment, like the presentations for the Collaboration approvation of the PID tool and of the analysis . Thanks also for the nights passed to write the CDF internal notes and to discuss the remain things to be included in the presentations.

I would like to thanks Mauro Donegá, Stefano Giagu and Diego Tonelli for the help in the work relative to the dE/dx, and Stephanie Menzemer for helping with the Time Of Flight. Thanks to Saverio Da Ronco and Kim Giolo for the help in the MC sample generation and thanks to Michael Joseph Morello that assisted me in the developing of the Unbinned Maximum Likelihood Fit.

I would like to thanks Simone Donati, Paola Giannetti and Mauro Dell'Orso for the corrections and the suggestions in the writing of this thesis.

I would like to thanks my physics teacher at the high school, Riccardo Bagnolesi, prematurely disappeared, that most of all has driven me towards the physics.

Thank you Pierluigi to have always believed in us, also when all seemed to go in the worse way.

Finally I would like to thank my parents, always present in the difficult and critical moments, my friends Ele, Giulia, Martina, Donatella and the *Comitato*.



# Contents

<b>Acknowledgments</b>	<b>v</b>
<b>Introduction</b>	<b>1</b>
<b>1 Theoretical review</b>	<b>3</b>
1.1 CP violation in the Standard Model. . . . .	3
1.2 The unitarity triangle . . . . .	5
1.3 CP violation in B decays . . . . .	7
1.3.1 CP violation in decay . . . . .	9
1.3.2 CP violation in Mixing . . . . .	9
1.3.3 CP Violation in the interference between decays with and without mixing . . . . .	10
1.4 Motivation for Measuring $\gamma$ . . . . .	11
1.5 Methods for the measurement of the angle $\gamma$ . . . . .	11
1.5.1 The Gronau-London-Wyler method . . . . .	13
1.5.2 The Atwood-Dunietz-Soni method . . . . .	16
1.5.3 The Giri-Grossmann-Soffer-Zupan method . . . . .	17
<b>2 The Tevatron collider and the CDF-II Detector</b>	<b>19</b>
2.1 $p\bar{p}$ acceleration and collisions . . . . .	20
2.2 The CDF II Detector . . . . .	22
2.3 Standard Definitions in CDF . . . . .	23
2.4 The CDF II Tracking System . . . . .	26
2.4.1 The Silicon Detectors . . . . .	27
2.4.2 The Central Outer Tracker . . . . .	30
2.4.3 Pattern Recognition Algorithms . . . . .	32
2.5 The Time Of Flight Detector . . . . .	33
2.6 The Calorimeters . . . . .	36
2.7 The Muon detector . . . . .	37
2.8 The Trigger . . . . .	37
2.8.1 Level 1 trigger . . . . .	39
2.8.2 Level 2 trigger . . . . .	41
2.8.3 Level 3 trigger . . . . .	43
2.8.4 Organization of a Trigger Table . . . . .	44

2.8.5	The Two Track Trigger Path (TTT)	44
2.8.6	The Two Track Trigger selection	44
2.9	Standard data processing	46
2.10	Luminosity Measurement	46
<b>3</b>	<b>Combined Particle Identification</b>	<b>49</b>
3.1	Data sample used for PID studies	51
3.2	Method to combine PID: ingredients and recipes	53
3.3	Parameterization of Particle IDentification distributions	57
3.3.1	dE/dx parameterization	60
3.3.2	TOF parameterization	77
3.4	Systematics treatment	82
3.5	Combined PID performance	84
3.5.1	Single track	85
3.5.2	Separation compute	88
3.5.3	Test of the combined Likelihood for track pairs: $\phi \rightarrow K^+ K^-$ decay	89
3.6	Combined PID applications	93
<b>4</b>	<b>Measurement of <math>\frac{BR(B^+ \rightarrow \bar{D}^0 K^+)}{BR(B^+ \rightarrow \bar{D}^0 \pi^+)}</math></b>	<b>97</b>
4.1	Data sample	97
4.2	Monte Carlo Simulation	101
4.3	Likelihood anatomy	103
4.4	Kinematics vs trigger	107
4.5	Mass probability density function	109
4.5.1	Signal pdf	109
4.5.2	Background pdf	109
4.6	Kinematical parameterization	111
4.6.1	Signal pdf	113
4.6.2	Physical background pdf	118
4.6.3	Combinatorial background pdf	119
4.7	PID parameterization	121
4.8	Fit implementation and test on toy MC	122
4.9	Fit results	123
4.9.1	Efficiency corrections	124
4.9.2	Fit projection	125
4.10	Systematics	131
4.10.1	Mass resolution tails	131
4.10.2	Input mass	131
4.10.3	dE/dx induced systematics	132
4.10.4	Combinatorial background systematics	132
4.10.5	$\bar{D}^{*0} \pi^+$ mass model	133
4.10.6	Check of $\bar{D}^{*0} \pi^+$ mass model	135
4.10.7	Monte Carlo statistics and XFT efficiency	139
4.10.8	Total systematic uncertainties	139

4.11 Final result . . . . .	139
4.12 Fit of $B^+ \rightarrow D_{CP+}^0 \pi^+$ with $D_{CP+}^0 \rightarrow K^- K^+, \pi^- \pi^+$ . . . . .	139
4.12.1 Uncertainties achievable on $A_{CP+}, R_{CP+}$ . . . . .	146
<b>Conclusions</b>	<b>147</b>
<b>References</b>	<b>149</b>



# Introduction

Understanding CP violation in the *bottom* quark sector is one of the central problem in high energy physics.

In the Standard Model (SM), CP violation in weak processes arises from a single complex phase in the mixing matrix for quarks, the Cabibbo-Kobayashi-Maskawa (CKM) matrix. A quantitative knowledge of the values of CKM matrix elements is important both in itself, and for the purpose of detecting possible phenomena beyond the SM by comparing determinations of the same quantities from different observable physical processes. Intense experimental efforts are underway in the *b* quark sector (B-physics) to determine these parameters. An often-adopted convention for discussing CP violation in the context of the SM is to relate the possible CP-violating observables to the angles ( $\alpha$ ,  $\beta$  and  $\gamma$ ) of a triangle formed by an equation stating the unitarity of the CKM matrix (“Unitarity Triangle”).

The  $\gamma$  angle is the most difficult to determine, due to the smallness of the branching ratios involved in the processes sensitive to this parameter, and to the frequent presence of amplitudes beyond the tree level and other theoretical uncertainties that complicate the interpretation of the data.

A central role in this field is played by  $B \rightarrow DK$  decays, where only tree-level diagram enter, and theoretical uncertainties are small. Several of these modes are currently being actively studied in dedicated  $B$  experiments at  $e^+e^-$  “B-factories”.

Similar measurements have also been planned some time ago at a  $p\bar{p}$  collider by the CDF experiment[1], where in addition to the nonstrange  $B$  modes, the  $B_s \rightarrow D_s K$  mode is also available. The success of this programs depends on the capability of the experiment to keep alive the B-physics triggers based on online detection of secondary decay vertexes (SVT trigger, Section 2.8) up to high luminosities [2]. The recent trigger upgrades [3] [4] increase the probability of a successful program at CDF.

Several methods have been proposed for the  $\gamma$  angle measurement by using the  $B \rightarrow DK$  decay modes, and they are described in Chapter 1 of this thesis.

The subject of this thesis is the measurement of the ratio<sup>1</sup>  $R = \frac{BR(B^+ \rightarrow \bar{D}^0 K^+ \rightarrow [K^+ \pi^-] K^+)}{BR(B^+ \rightarrow \bar{D}^0 \pi^+ \rightarrow [K^+ \pi^-] \pi^+)}$  with the CDF II detector at Fermilab, using an integrated luminosity of  $360 \text{ pb}^{-1}$ .

This represents the first, mandatory step, of a program of  $DK$  measurements aimed at the  $\gamma$  angle, starting with the GLW (Gronau-London-Wyler) method (Section 1.5.1). To perform this measurement I implemented an unbinned maximum likelihood fit

---

<sup>1</sup>Throughout this thesis, references to a specific charge state imply the charge-conjugate as well, unless otherwise specified

(Chapter 4), which combines the small kinematics differences between distinct decay modes and the Particle IDentification information (Chapter 3) to distinguish between different final states.

This fit technique, when applied to larger samples of data, is well-suited also for other analyses allowing extraction of the  $\gamma$  angle: the ADS (Atwood-Dunietz-Soni) method, described in Section 1.5.2, that uses the  $B^+ \rightarrow \bar{D}^0 K^+$  decay where  $D^0 \rightarrow K^+ \pi^-$ , and the time-dependent analysis of  $B_s \rightarrow D_s^- K^+ \rightarrow [\phi \pi^-] K^+$  (Section 1.5).

As discussed in Section 1.5.1, the CDF experiment will move from the GLW method to the other more efficient methods, after a complete test of the “analysis machinery” on more abundant decay modes is performed.

The Particle IDentification (PID) is also a crucial ingredient of my analysis. In fact, it is necessary to discriminate the  $B^+ \rightarrow \bar{D}^0 K^+$  from the much larger background of  $B^+ \rightarrow \bar{D}^0 \pi^+$ , falling in the nearby mass region.

As described in Chapter 3, I developed a tool that combines the information of two PID methods: the Time Of Flight measurement (TOF) (Section 2.5) and the  $dE/dx$  (specific ionization in the drift chamber) measurement. I studied the PID distributions for many different particles and different momentum ranges for the whole data set of  $1 \text{ fb}^{-1}$ , and parameterized them and their systematic uncertainties in a way that allows to use them easily in a maximum Likelihood fit.

The corresponding code has been adopted by the CDF II collaboration and it is widely used in several analysis. Important examples are the flavor tagging in  $B_s$  mixing [5] and the  $B_{(s)}^0 \rightarrow h^+ h'^-$  analysis [6] [7].

In the analysis that is described in this thesis, only the  $dE/dx$  information is used, since the momentum range is currently restricted by a cut on the transverse momentum of the track from B ( $p_t > 2 \text{ GeV}/c$ ) (Section 4.4), and the contribution of the TOF to K- $\pi$  separation at these transverse momenta is small in comparison to  $dE/dx$ .

To complete the GLW analysis, it is necessary to also measure

$$A_{CP\pm} = \frac{BR(B^- \rightarrow D_{CP\pm}^0 K^-) - BR(B^+ \rightarrow D_{CP\pm}^0 K^+)}{BR(B^- \rightarrow D_{CP\pm}^0 K^-) + BR(B^+ \rightarrow D_{CP\pm}^0 K^+)}$$

and

$$R_{CP\pm} = \frac{BR(B^- \rightarrow D_{CP\pm}^0 K^-) + BR(B^+ \rightarrow D_{CP\pm}^0 K^+)}{BR(B^- \rightarrow D^0 K^-) + BR(B^+ \rightarrow \bar{D}^0 K^+)}$$

. They can be performed by applying the same methods described here to the decays  $B^+ \rightarrow D_{CP\pm}^0 \pi^+$  with  $D_{CP+}^0 \rightarrow [K^+ K^-, \pi^+ \pi^-]$  (even state) and  $D_{CP-}^0 \rightarrow [K_s^0 \pi^0, K_s^0 \omega, K_s^0 \Phi]$  (odd state). From my results obtained using the  $D_{CP+}^0$  modes on  $360 \text{ pb}^{-1}$  (Section 4.12), the sample of  $360 \text{ pb}^{-1}$  is too small to provide significant measurements of  $A_{CP+}$  and  $R_{CP+}$ . Is possible, however, to estimate the  $A_{CP+}$  and  $R_{CP+}$  resolutions expected on  $1 \text{ fb}^{-1}$  of data. I found  $\sigma = 0.12$  for  $A_{CP+}$  and  $\sigma = 0.28$  for  $R_{CP+}$ . These are comparable to the resolutions currently achieved by BaBar and Belle experiments.

The analysis with the larger statistic is already in progress with the methods described in this thesis, as is the extension to the pion transverse momentum range below  $2 \text{ GeV}/c$ .



# Chapter 1

## Theoretical review

### 1.1 CP violation in the Standard Model.

In the Standard Model (SM) [8] the fundamental constituent of matter are quarks and leptons. The interactions between particles are described by the exchange of gauge bosons: the photons for the electromagnetic interaction; the bosons  $W^\pm$  and  $Z^0$  for the weak interaction and finally the gluons, which are neutral but carry the color (strong charge), for the strong interaction.

Experimentally [9], there are three generations of these particles and the weak interaction couples with their left-handed version. The left-handed quarks are arranged in  $SU(2)_L$  doublets:

$$\begin{pmatrix} u \\ d' \end{pmatrix}_L \begin{pmatrix} c \\ s' \end{pmatrix}_L \begin{pmatrix} t \\ b' \end{pmatrix}_L$$

where the primes refer to the fact that the weak eigenstates of the down type quarks are not necessarily equal to the mass eigenstates, denoted (d,s,b), but are a linear superimposition of them. The matrix that transforms the mass eigenstates into the weak ones is the Cabibbo-Kobayashi-Maskawa (CKM) matrix denoted  $V_{CKM}$  which must be unitary ( $V_{CKM}^\dagger V_{CKM} = I$ ) [10]:

$$\begin{pmatrix} d' \\ s' \\ b' \end{pmatrix}_L = \begin{pmatrix} V_{ud} & V_{us} & V_{ub} \\ V_{cd} & V_{cs} & V_{cb} \\ V_{td} & V_{ts} & V_{tb} \end{pmatrix} \begin{pmatrix} d \\ s \\ b \end{pmatrix}_L \quad (1.1)$$

In the SM, CP violation effects in weak processes may originate from the charged-current interactions of quarks arising from a single irremovable complex phase in the mixing matrix for quarks: this is called the Cabibbo-Kobayashi-Maskawa (CKM) mechanism [11].

The condition of unitarity imposed on the CKM matrix, combined with the requirement that any phase must be non-trivial (i.e. cannot be set to zero with a redefinition of the field), means that the CKM matrix can be completely determined by four quantities, three real angles and one remaining non trivial-phase. The form of the CKM

matrix is shown in equation (1.2) where it is presented in the “standard parameterization” [12].

$$V_{CKM} = \begin{pmatrix} c_{12}c_{13} & s_{12}c_{13} & s_{13}e^{-i\delta} \\ -s_{12}c_{23} - c_{12}s_{23}s_{13}e^{i\delta} & c_{12}c_{23} - s_{12}s_{23}s_{13}e^{i\delta} & s_{23}c_{13} \\ s_{12}s_{23} - c_{12}c_{23}s_{13}e^{i\delta} & -c_{12}s_{23} - s_{12}c_{23}s_{13}e^{i\delta} & c_{23}c_{13} \end{pmatrix} \quad (1.2)$$

where  $c_{ij} = \cos \theta_{ij}$  and  $s_{ij} = \sin \theta_{ij}$ .  $\theta_{12}$ ,  $\theta_{23}$  and  $\theta_{13}$  are three real angles and  $\delta$  is the no-trivial phase, which is the only possible source of CP violation in the SM [10][11].

Experimental information on  $V_{CKM}$  is obtained from the following processes [13]:

- Nuclear  $\beta$  decays and measurement of neutron lifetime  $\Rightarrow |V_{ud}| = 0.97377 \pm 0.00027$ ;
- Semileptonic kaon decays:  $K \rightarrow \pi l \nu \Rightarrow |V_{us}| = 0.2257 \pm 0.0021$ ;
- Semileptonic charm decays ( $D \rightarrow K l \nu$  and  $D \rightarrow \pi l \nu$ ) and neutrino and antineutrino interactions  $\Rightarrow |V_{cd}| = 0.230 \pm 0.011$ ;
- Semileptonic D or leptonic  $D_s$  decays ( $D_s^+ \rightarrow l^+ \nu$ ,  $D \rightarrow K l \nu$  and  $D \rightarrow \pi l \nu$ ) using evaluated hadronic form factors  $\Rightarrow |V_{cs}| = 0.957 \pm 0.017 \pm 0.093$ ;
- Exclusive and inclusive semileptonic decays of B mesons to charm ( $b \rightarrow c l \nu$ )  $\Rightarrow |V_{cb}| = (4.16 \pm 0.6) \times 10^{-3}$
- Exclusive and inclusive  $b \rightarrow u l \nu$  decays  $\Rightarrow |V_{ub}| = (4.31 \pm 0.30) \times 10^{-3}$ ;
- Top decays ( $\bar{t} \rightarrow \bar{b} l \bar{\nu}$ ) for the direct determination of  $V_{tb} \Rightarrow V_{tb} > 0.78$  at 95% C.L.;
- $B - \bar{B}$  oscillations  $\Rightarrow |V_{td}/V_{ts}| = 0.208_{-0.006}^{+0.008}$ .

We observe a resulting hierarchy of the strengths of the charged current quark-level processes: transitions within the same generation are governed by CKM matrix elements of  $O(1)$ , transitions between the first and the second generation are suppressed by CKM factors of  $O(10^{-1})$ , transitions between second and third generation are suppressed by  $O(10^{-2})$ , and the transition between the first and the third generation are even suppressed by CKM factors of  $O(10^{-3})$ .

There are several parameterizations and approximations of the CKM matrix. A useful parameterization that points out the hierarchy between the matrix elements is the “Wolfenstein parameterization” [14]. This parameterization uses four real parameters to write the matrix elements,  $\lambda$ ,  $A$ ,  $\rho$  and  $\eta$ :

$$V_{CKM} = \begin{pmatrix} 1 - \frac{\lambda^2}{2} & \lambda & A\lambda^3(\rho - i\eta) \\ -\lambda & 1 - \frac{\lambda^2}{2} & A\lambda^2 \\ A\lambda^3(1 - \rho - i\eta) & -A\lambda^2 & 1 \end{pmatrix} + O(\lambda^4) \quad (1.3)$$

This parameterization is obtained by expanding in powers of the element  $\lambda = V_{us}$ <sup>1</sup> and making the definitions  $V_{cb} = A\lambda^2$  and  $V_{ub} = A\lambda^3(\rho - i\eta)$ , where  $A$ ,  $\rho$  and  $\eta$  are all  $O(1)$ .

The quantities  $\lambda$  and  $A$  (see equation (1.4)) are well determined experimentally [13], measurements are dominated from the semileptonic decays of kaons and B-mesons respectively, but  $\rho$  and  $\eta$  are not and hence their measurement it is one of the goals of particle physics<sup>2</sup>.

$$\begin{aligned}\lambda &= 0.2272 \pm 0.0010 \\ A &= 0.818^{+0.007}_{-0.017} \\ \bar{\rho} &= 0.221^{+0.064}_{-0.028} \\ \bar{\eta} &= 0.340^{+0.017}_{-0.045}\end{aligned}\tag{1.4}$$

## 1.2 The unitarity triangle

The unitarity of the CKM matrix is described by:

$$V_{CKM}V_{CKM}^+ = V_{CKM}^+V_{CKM} = I\tag{1.5}$$

where  $I$  is the identity matrix. Equation (1.5) leads to a set of twelve equations, consisting of six normalization and six orthogonality relations. Let us now have a closer look at the orthogonality equations:

$$\underbrace{V_{ud}V_{us}^*}_{O(\lambda)} + \underbrace{V_{cd}V_{cs}^*}_{O(\lambda)} + \underbrace{V_{td}V_{ts}^*}_{O(\lambda^5)} = 0\tag{1.6}$$

$$\underbrace{V_{us}V_{ub}^*}_{O(\lambda^4)} + \underbrace{V_{cs}V_{cb}^*}_{O(\lambda^2)} + \underbrace{V_{ts}V_{tb}^*}_{O(\lambda^2)} = 0\tag{1.7}$$

$$\underbrace{V_{ud}V_{ub}^*}_{(\rho+i\eta)A\lambda^3} + \underbrace{V_{cd}V_{cb}^*}_{-A\lambda^3} + \underbrace{V_{td}V_{tb}^*}_{(1-\rho-i\eta)A\lambda^3} = 0\tag{1.8}$$

$$\underbrace{V_{ud}^*V_{cd}}_{O(\lambda)} + \underbrace{V_{us}^*V_{cs}}_{O(\lambda)} + \underbrace{V_{ub}^*V_{cb}}_{O(\lambda^5)} = 0\tag{1.9}$$

$$\underbrace{V_{cd}^*V_{td}}_{O(\lambda^4)} + \underbrace{V_{cs}^*V_{ts}}_{O(\lambda^2)} + \underbrace{V_{cb}^*V_{tb}}_{O(\lambda^2)} = 0\tag{1.10}$$

$$\underbrace{V_{ud}^*V_{td}}_{(1-\rho-i\eta)A\lambda^3} + \underbrace{V_{us}^*V_{cs}}_{-A\lambda^3} + \underbrace{V_{ub}^*V_{cb}}_{(\rho+i\eta)A\lambda^3} = 0\tag{1.11}$$

where we have also indicated the structures that arise if we apply the “Wolfenstein parameterization”. Each equation can be represented as a triangle in the complex plane

<sup>1</sup> $\lambda$  is the sine of the Cabibbo angle:  $\lambda = \sin \theta_C = 0.2265 \pm 0.0020$  [15]

<sup>2</sup> $\bar{\rho}$  and  $\bar{\eta}$ , within the 3% are equal to  $\rho$  and  $\eta$ , and are obtained extending the “Wolfenstein parameterization” to  $O(\lambda^5)$

[16], but the only two non squashed triangles are those corresponding to equations (1.8) and (1.11). In fact, all the addendum sides are of similar magnitude  $O(\lambda^3)$ . However the corresponding orthogonality relations agree with each other at the  $\lambda^3$  level, yielding

$$[(\rho + i\eta) + (-1) + (1 - \rho - i\eta)]A\lambda^3 = 0. \quad (1.12)$$

Consequently, equations (1.8) and (1.11) describe the same triangle, which is usually referred to as the unitarity triangle of the CKM matrix. The first one of these triangles (equation (1.8)) rescaled by  $\frac{1}{|V_{cd}V_{cb}^*|}$  is shown in Fig. 1.1 and takes the name of Normalized Unitarity Triangle.

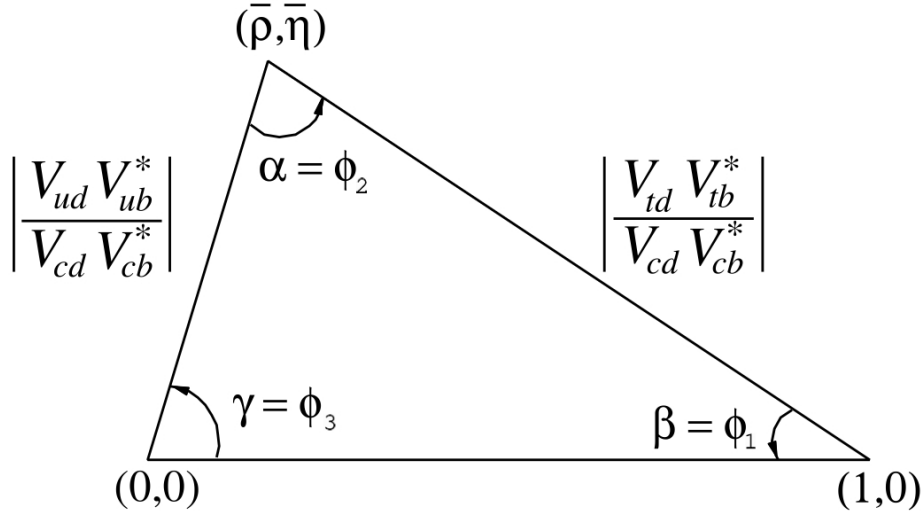


Figure 1.1: Graphic representation of the Normalized Unitarity Triangle in the complex  $(\bar{\rho}, \bar{\eta})$  plane.

The apex has coordinates  $\bar{\rho}$  and  $\bar{\eta}$ , which are related to the original  $\rho$  and  $\eta$  in the Wolfenstein parameterization through equations (1.13), which are calculated from an extension of this parameterization to  $O(\lambda^5)$ . Since  $\lambda = 0.22$ ,  $\bar{\rho} = \rho$  and  $\bar{\eta} = \eta$  within 3%.

$$\bar{\rho} \equiv \rho \left(1 - \frac{1}{2}\lambda^2\right), \quad \bar{\eta} \equiv \eta \left(1 - \frac{1}{2}\lambda^2\right) \quad (1.13)$$

The special relevance of the Unitarity Triangle is due to the fact that, in the sector of B-physics, there are several B meson decays which are expected to have rates and CP-violating effects that can be measured at B factories and at the collider experiments, and from which we can gain information on the sides and on the angles of the unitarity triangle. It is important that these measurements are made through as many independent modes as possible in order to attempt to over-constrain the triangle and to probe for contribution for physics beyond the SM. New physics contributions could, for example, cause disagreement between measurements in different processes of what, in the SM, should be the same angle.

Information on the lengths of the sides comes from [15]:

- the values of  $|V_{ub}|$  and  $|V_{cb}|$ , measured in inclusive or exclusive semileptonic  $B \rightarrow X_{u,c} l \nu_l$  decays ( $l = e, \mu$ ), which constrain the radius  $R_b$  of the circle centered in  $(0,0)$  that passes through  $(\bar{\rho}, \bar{\eta})$ :

$$R_b = \left(1 - \frac{\lambda^2}{2}\right) \frac{1}{\lambda} \frac{|V_{ub}|}{|V_{cb}|}. \quad (1.14)$$

- the values of  $\Delta m_d$  and  $\Delta m_s$ , respectively the mass differences between the mass eigenstates of the neutral  $B_d$  and  $B_s$ , measured in the  $B^0 - \bar{B}^0$  and  $B_s - \bar{B}_s$  oscillations [13]. These mass differences constrain the radius of the circle centered in  $(1,0)$   $R_t = \frac{1}{V_{cd}} \cdot \frac{V_{td}}{V_{ts}}$ . In fact  $\frac{\Delta m_s}{\Delta m_d} = \xi^2 \cdot \frac{m_{B_s}}{m_{B_d}} \cdot \frac{|V_{ts}|^2}{|V_{td}|^2}$ , where  $\xi = 1.210_{-0.035}^{+0.047}$  [17]. The recent measurement of  $\Delta m_s$  at CDF II [5] has been very important to provide a more stringent constraint on  $R_t$ . An additional constraint is the measured value of the indirect CP violation parameter  $\epsilon_K$  of the neutral kaon system.

Information on the angles  $\alpha$ ,  $\beta$  and  $\gamma$  can be obtained from the measurement of CP-violating B meson decays. In Section 1.5 we will describe the methods to measure the  $\gamma$  angle using  $B \rightarrow D^0 K$  decay modes.

In Fig. 1.2 one can see the constraints in the  $(\bar{\rho}, \bar{\eta})$  plane, from the current measurement of  $|V_{ub}/V_{cb}|$ ,  $\Delta m_d$ ,  $\Delta m_s$ ,  $\epsilon_K$ , and the angles  $\alpha$ ,  $\beta$  and  $\gamma$ , together with the  $3\sigma$  allowed region for the apex of the Unitarity Triangle obtained from a combined fit to these constraints [15].

### 1.3 CP violation in B decays

There are three discrete symmetries in the Standard Model in addition to the continuous Lorentz and gauge transformation. Parity (P) and Time-reversal (T) are space-time transformations that respectively cause  $\vec{x} \rightarrow -\vec{x}$  and  $t \rightarrow -t$ . Both of these operators have the effect of reversing the momentum vector leaving the spin unchanged. Charge Conjugation does not affect space-time quantities but instead changes particles into anti-particles by changing the internal quantum numbers of the particle. In a quantum field theory constructed under very general assumptions, any Hamiltonian operator (H) which is invariant under Lorentz transformation will be invariant under the combined operation CPT [18].

Since CPT is conserved, CP violation also implies T violation. T transforms the  $e^{-iEt}$  to  $e^{iEt}$  and transforms the Hamiltonian H into its complex conjugate  $H^*$ . If  $H \neq H^*$  then T and hence CP are violated. This is the reason for which the presence in  $V_{CKM}$  of complex elements is the potential source of CP violation.

Moreover, the fact that the matrix  $V_{CKM}$  is not real appears in the elements that connect the first quark generation to the third one, the transitions  $t \rightarrow d$  and  $b \rightarrow u$ . Since a bound state containing a quark top does not exist, it is evident that bound states containing a quark bottom, B mesons and  $\Lambda_b$  baryons, become very important.

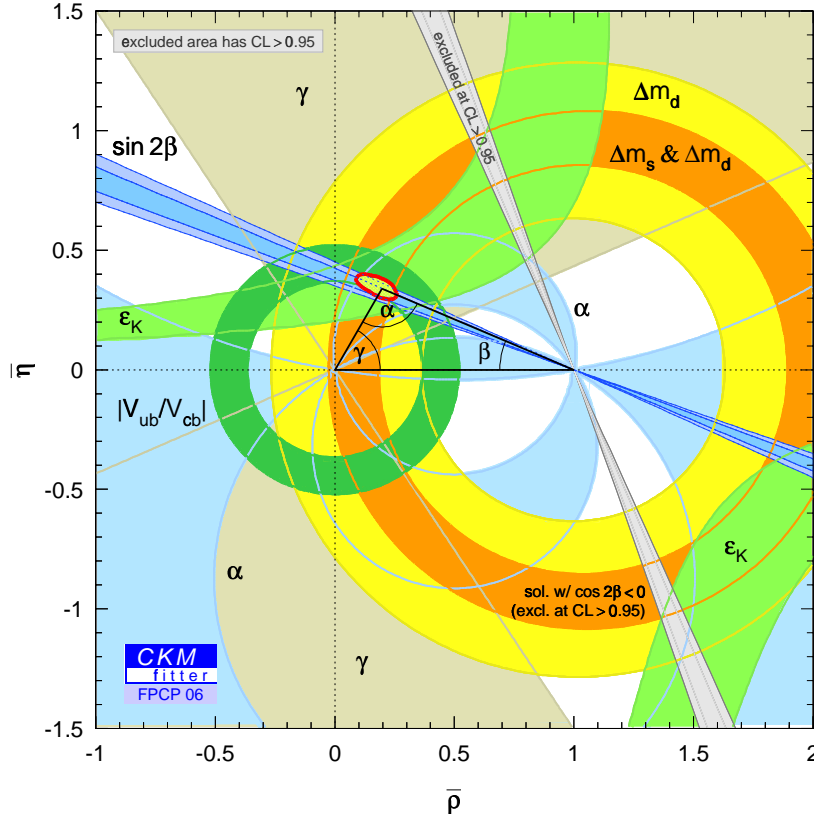


Figure 1.2: Constraints (at 68% and 95% C.L.) on the position of the apex of the Unitarity Triangle in the  $(\bar{\rho}, \bar{\eta})$  plane from the measured value of  $|V_{cb}|$ ,  $|V_{ub}|$ ,  $\Delta m_d$ ,  $\Delta m_s$ ,  $\epsilon_K$ ,  $\sin 2\beta$ . The combined  $3\sigma$  allowed contour is also shown.

CP violation was first observed in the  $K^0\bar{K}^0$  system in 1964 [19]. Until 2001 this was the only system in which CP violation was observed, then BABAR [20] and BELLE [21] collaborations observed the effect in the  $B^0 - \bar{B}^0$  system. Even so, CP violation remains one of the least well investigated areas of the SM.

In B decays, CP violation can occur in three different forms:

- CP violation in decay (“direct CP violation”): this effect occurs in both charged and neutral decays, when the amplitude for a decay and its CP conjugate process have different magnitudes.
- CP violation in mixing (“indirect CP violation”): this effect occurs when the two neutral mass eigenstates cannot be chosen to be CP eigenstates.
- CP violation in the interference between decays with and without mixing (“CP violation in the interference between mixing and decay”): this effect occurs in decays into final state that are common to  $B$  and  $\bar{B}$  neutral mesons.

### 1.3.1 CP violation in decay

Direct CP violation occurs when the amplitude of a certain decay process and the amplitude of its CP conjugate process are not equal. It has been observed in K [22] and B decays [23].

Consider the decay  $B \rightarrow f$ , where  $f$  is any final state, and its CP conjugate  $\bar{B} \rightarrow \bar{f}$ . The amplitudes of these decays can be written in the following way:

$$A_f = \langle f | H | B \rangle = \sum_j |A_j| e^{i(\delta_j + \phi_j)} \quad \bar{A}_{\bar{f}} = \langle \bar{f} | H | \bar{B} \rangle = \sum_j |A_j| e^{i(\delta_j - \phi_j)} \quad (1.15)$$

where  $A_j$ ,  $\delta_j$  and  $\phi_j$  are respectively the amplitude, the strong (or CP conserving) phase and the weak (or CP violating) phase of a contributing process. The condition for CP violation is that  $|A_f|^2 \neq |\bar{A}_{\bar{f}}|^2$ . In order to satisfy this condition there must be a contribution from at least two processes with different weak and strong phases. In that case we have

$$|A_f|^2 - |\bar{A}_{\bar{f}}|^2 = -2 \sum_{i,j} |A_i| |A_j| \sin(\phi_i - \phi_j) \sin(\delta_i - \delta_j). \quad (1.16)$$

Any rate asymmetry in charged B decays of the form:

$$A_{CP}^{dir} = \frac{\Gamma(B^- \rightarrow f) - \Gamma(B^+ \rightarrow \bar{f})}{\Gamma(B^- \rightarrow f) + \Gamma(B^+ \rightarrow \bar{f})} = \frac{\frac{|\bar{A}_{\bar{f}}|^2}{|A_f|^2} - 1}{\frac{|\bar{A}_{\bar{f}}|^2}{|A_f|^2} + 1} \neq 0, \quad (1.17)$$

would be a clear signature of direct CP violation.

Direct CP violation can also occur for neutral meson decays, where it competes with the other two types of CP violation mechanisms described in the following subsection. Direct CP violation can be searched in rate asymmetries of decays to final states  $f$  that are self-tagging, i.e. are only accessible to either  $B^0$  or  $\bar{B}^0$ , but not to both. Following this method Babar, Belle and CDF II collaborations measured the rate asymmetry for the  $B^0 \rightarrow K^+ \pi^-$  decay [23] [6] [7].

### 1.3.2 CP violation in Mixing

The CP violation in mixing interests the neutral B system.

An arbitrary linear combination of the neutral B-meson flavor eigenstates  $a|B^0\rangle + b|\bar{B}^0\rangle$  is governed by the time-dependent Schrödinger equation:

$$i \frac{d}{dt} \begin{pmatrix} a \\ b \end{pmatrix} = H \begin{pmatrix} a \\ b \end{pmatrix} \equiv (M - \frac{i}{2}\Gamma) \begin{pmatrix} a \\ b \end{pmatrix} \quad (1.18)$$

for which  $M$  and  $\Gamma$  are  $2 \times 2$  Hermitian matrices.

The light  $B_L$  and heavy  $B_H$  mass eigenstates are given by:

$$\begin{aligned} |B_L\rangle &= p|B^0\rangle + q|\bar{B}^0\rangle \\ |B_H\rangle &= p|B^0\rangle - q|\bar{B}^0\rangle. \end{aligned} \quad (1.19)$$

The complex coefficients  $p$  and  $q$  obey the normalization condition  $|q|^2 + |p|^2 = 1$ .

Invariance under CPT implies that  $H_{11}$  and  $H_{22}$  are equal. Furthermore, CP asymmetry requires that  $H_{12}^* = H_{21}$ , which implies that the mass eigenstates are also CP eigenstates and  $|p| = |q|$ . Consequently if  $\frac{q}{p} \neq 1$  there is CP violation in mixing.

When CP is conserved, the mass eigenstates must be CP eigenstates. In that case the relative phase between  $M_{12}$  and  $\Gamma_{12}$  vanishes.

Since:

$$\left| \frac{q}{p} \right|^2 = \left| \frac{M_{12}^* - \frac{i}{2}\Gamma_{12}^*}{M_{12} - \frac{i}{2}\Gamma_{12}} \right| \quad (1.20)$$

$|q/p| \neq 1$  implies the CP violation.

The only source of CP violation in charged current semileptonic decays is CP violation in mixing and it can be measured via the asymmetry of “wrong sign” decays induced by oscillations, when  $B_q^0$  mesons are produced in pairs ( $B_q^0 \bar{B}_q^0$ ):

$$A_{SL}^q(t) = \frac{\Gamma(B_q^0(t) \rightarrow l^- \bar{\nu} x) - \Gamma(\bar{B}_q^0(t) \rightarrow l^+ \nu x)}{\Gamma(B_q^0(t) \rightarrow l^- \bar{\nu} x) + \Gamma(\bar{B}_q^0(t) \rightarrow l^+ \nu x)} = \frac{\left| \frac{q}{p} \right|^4 - 1}{\left| \frac{q}{p} \right|^4 + 1}. \quad (1.21)$$

The world average for this asymmetry is  $A_{SL} = -0.0030 \pm 0.0078$  [24].

### 1.3.3 CP Violation in the interference between decays with and without mixing

The last manifestation of CP violation arises from the interference between the mixing and decay processes. This can be observed in decays of  $B^0$  and  $\bar{B}^0$  mesons to the same final state, which must therefore be a CP eigenstate ( $f = \bar{f}$ ). Defining  $A_f$  as the amplitude for the decay  $B^0 \rightarrow f$  and  $\bar{A}_f$  as the amplitude for the decay  $\bar{B}^0 \rightarrow f$ , the quantity

$$\lambda_f = \frac{q}{p} \frac{\bar{A}_f}{A_f} \quad (1.22)$$

must be equal to the unity if CP is conserved. Furthermore the time-dependent asymmetry is found to be

$$\begin{aligned} A_{CP}(t) &= \frac{\Gamma(B \rightarrow f)(t) - \Gamma(\bar{B} \rightarrow f)(t)}{\Gamma(B \rightarrow f)(t) + \Gamma(\bar{B} \rightarrow f)(t)} = \\ &= \left( \frac{1 - |\lambda_f|^2}{1 + |\lambda_f|^2} \right) \cos \Delta m_B t - \left( \frac{2 \text{Im}(\lambda_f)}{1 + |\lambda_f|^2} \right) \sin \Delta m_B t. \end{aligned} \quad (1.23)$$

The cosine term arises from direct CP violation and vanishes if  $|\lambda_f| = 1$ , since together with the fact that  $\left| \frac{q}{p} \right| \sim 1$  it implies that  $\bar{A}_f = A_f$ . The sine term is due to the interference between decays with and without mixing and vanishes if  $\text{Im}(\lambda_f) = 0$ .



## 1.4 Motivation for Measuring $\gamma$

The measurement of the CKM matrix elements is one of the most stringent tests of the Standard Model and for this reason it represents also a window for New Physics. Intense experimental efforts are now underway in B-physics and for this program it is crucial to determine experimentally the angles of the Unitarity Triangle.

The  $\sin(2\beta)$  measurement has reached a good level of precision. The world average uses measurements from the decays  $B^0 \rightarrow J/\psi K_s^0$ ,  $J/\psi K_L^0$ ,  $\psi(2S)K_s^0$ ,  $\chi_{c1}K_s^0$ ,  $\eta_c K_s^0$  and  $J/\psi K^{*0}$  ( $K^{*0} \rightarrow K_s^0 \pi^0$ ) and gives:

$$\sin(2\beta) = 0.687 \pm 0.032[13]. \quad (1.24)$$

The angle  $\alpha$  can be measured from the study of charmless B decays such as  $\pi\pi$ ,  $\rho\pi$  and  $\rho\rho$ . The world average is:

$$\alpha = 99_{-8}^{+13}[13] \quad (1.25)$$

in good agreement with the value predicted by the CKM fits to the Unitarity Triangle constraints.

The angle  $\gamma$  is by far the most difficult to measure. Several methods have been proposed in the past for the measurement of  $\gamma$ . We will describe these methods in the next Section.

## 1.5 Methods for the measurement of the angle $\gamma$

There are various strategies to measure the angle  $\gamma$ . Some of them are theoretically clean, some suffer from hadronic uncertainties, some use the charged B decays and others use the  $B_s$  decays.

Using  $B^+ \rightarrow \bar{D}^0 K^+$  decays,  $\gamma$  could be extracted by exploiting the interference between the processes  $\bar{b} \rightarrow \bar{c}u\bar{s}$ , whose amplitude is proportional to  $V_{cb}V_{us}$  and  $\bar{b} \rightarrow \bar{u}c\bar{s}$ , whose amplitude is proportional to  $V_{ub}V_{cs}$ . In Fig. 1.3 the diagrams of these processes are shown, on the left the  $B^+ \rightarrow \bar{D}^0 K^+$  ( $\bar{b} \rightarrow \bar{c}u\bar{s}$ ) and on the right the  $B^+ \rightarrow D^0 K^+$  ( $\bar{b} \rightarrow \bar{u}c\bar{s}$ ).  $\gamma$  is the relative weak phase between the two diagrams, and in principle can be probed by measuring CP-violating effects in B-decays where the two amplitudes interfere.

Here we discuss the following methods:

- The GLW (Gronau-London-Wyler) method [25] [26], that uses the  $B^\pm \rightarrow DK^\pm$  decay with  $D_{CP}^0$  decay modes. The  $D_{CP+}^0$  modes are  $D^0 \rightarrow \pi\pi$ ,  $KK$  while the  $D_{CP-}^0$  modes are  $D^0 \rightarrow K_s^0 \pi^0$ ,  $K_s^0 \omega$ ,  $K_s^0 \phi$ .
- The ADS (Atwood-Dunietz-Soni) method [27] [28], that uses the  $B^\pm \rightarrow DK^\pm$  decay with  $D^0$  reconstructed in the doubly cabibbo suppressed  $D_{DCS}^0 \rightarrow K^+ \pi^-$  decay.

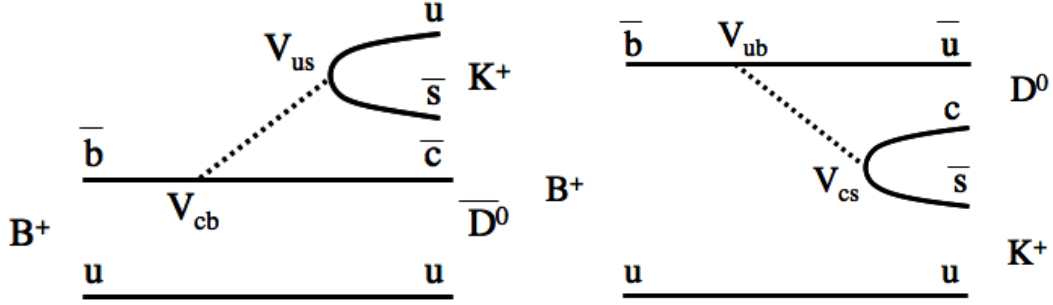


Figure 1.3: Diagrams contributing to  $B^\pm \rightarrow DK^\pm$  and related modes. The diagram on the left proceeds via  $V_{cb}$  transition, while the diagram on the right proceeds via  $V_{ub}$  transition and is color suppressed.

- The GGSZ (Giri-Grossmann-Soffer-Zupan) method [28] [29], that uses the  $B^\pm \rightarrow DK^\pm$  decay with the  $D^0$  and  $\bar{D}^0$  reconstructed into three-body final states. For example the  $D^0 \rightarrow K_s^0 \pi^+ \pi^-$  decay.

Also by using  $B_s$  decays the  $\gamma$  angle can be measured in a theoretically clean way. CP violation due to mixing can occur in the decay channels  $B_s(\bar{B}_s) \rightarrow D_s^\mp K^\pm$  due to the interference between the mixed and unmixed paths of a decay to one of the final states. In Fig. 1.4 the diagrams for  $\bar{B}_s$  decays are shown. Final states of both sign are accessible by both  $B_s$  mesons with similar size amplitudes ( $\sim \lambda^3$ ).

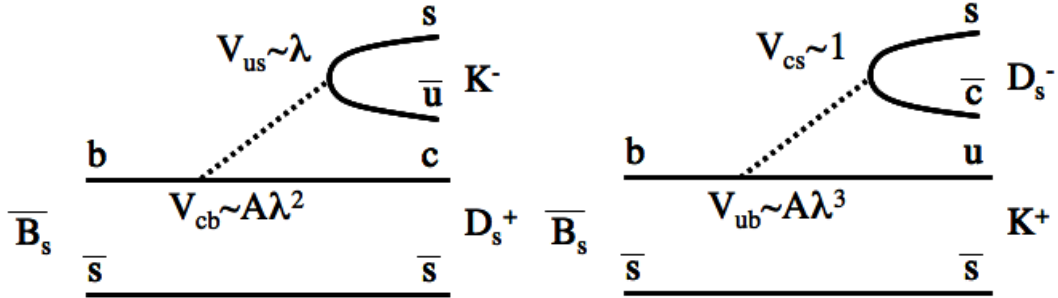


Figure 1.4: Diagrams relative to the  $\bar{B}_s$  decays. On the left the  $\bar{B}_s \rightarrow D_s^+ K^-$  decay and on the right the  $\bar{B}_s \rightarrow D_s^- K^+$  decay.

The CP asymmetry  $A_{CP}(D_s^+ K^-)(t)$  may be constructed [30]:

$$A_{CP}(D_s^+ K^-)(t) \equiv \frac{\Gamma(B_s \rightarrow D_s^+ K^-)(t) - \Gamma(\bar{B}_s \rightarrow D_s^+ K^-)(t)}{\Gamma(B_s \rightarrow D_s^+ K^-)(t) + \Gamma(\bar{B}_s \rightarrow D_s^+ K^-)(t)}. \quad (1.26)$$

This has the following dependence:

$$\begin{aligned}
A_{CP}(D_s^+ K^-)(t) &= \\
&= \frac{A_{CP}^{dir}(B_s \rightarrow D_s^+ K^-) \cos \Delta m_s t + A_{CP}^{mix}(B_s \rightarrow D_s^+ K^-) \sin \Delta m_s t}{\cosh(\Delta \Gamma_s t/2) - A_{\Delta \Gamma_s} \sinh(\Delta \Gamma_s t/2)} = \\
&= \frac{C_s \cos \Delta m_s t + S_s \sin \Delta m_s t}{\cosh(\Delta \Gamma_s t/2) - A_{\Delta \Gamma_s} \sinh(\Delta \Gamma_s t/2)}, \tag{1.27}
\end{aligned}$$

where  $\Delta m_s$  and  $\Delta \Gamma_s$  are the mass and lifetime differences between the heavy and light  $B_s$  eigenstates, which for the purpose of this discussion are assumed to be known. The three observables  $C_s$ ,  $S_s$  and  $A_{\Delta \Gamma_s}$ , can then be fitted from data. By performing an equivalent analysis for the  $D_s^- K^+$  final state three additional observables,  $\overline{C}_s$ ,  $\overline{S}_s$  and  $\overline{A}_{\Delta \Gamma_s}$ , can be obtained. The observables depend on the underlying physics parameters in the following manner:

$$\begin{aligned}
C_s, (\overline{C}_s) &= -(+)\left(\frac{1 - r_s^2}{1 + r_s^2}\right) \\
S_s, (\overline{S}_s) &= \frac{2r_s \sin(\phi_s + \gamma + (-)\delta_s)}{1 + r_s^2} \\
A_{\Delta \Gamma_s}, (\overline{A}_{\Delta \Gamma_s}) &= -\frac{2r_s \cos(\phi_s + \gamma + (-)\delta_s)}{1 + r_s^2}. \tag{1.28}
\end{aligned}$$

Here  $r_s$  is the ratio of amplitudes between the interfering tree diagrams,  $\delta_s$  is a possible CP conserving strong phase difference between the diagrams and  $\phi_s$  is the CP violating weak phase associated with the  $B_s^0 - \overline{B}_s^0$  oscillations, believed to be very small in the Standard Model. From the measurement of the six observables  $C_s$ ,  $\overline{C}_s$ ,  $S_s$ ,  $\overline{S}_s$ ,  $A_{\Delta \Gamma_s}$  and  $\overline{A}_{\Delta \Gamma_s}$  the parameters  $r_s$ ,  $\delta_s$  and  $\gamma$  can be determined.

Since CDF II measured  $\Delta m_s$  [5], now it is also possible the measurement of  $\gamma$  using these decays [31]. We expected about 200  $D_s K$  events in  $1 \text{ fb}^{-1}$  and since, up to now, the  $B_s \rightarrow D_s K$  has not been observed, also the measurement of the branching ratio  $\frac{BR(B_s^0 \rightarrow D_s^- K^+) + BR(\overline{B}_s^0 \rightarrow D_s^+ K^-)}{BR(B_s^0 \rightarrow D_s^- \pi^+) + BR(\overline{B}_s^0 \rightarrow D_s^+ \pi^-)}$  alone will be an important new result.

### 1.5.1 The Gronau-London-Wyler method

This method uses the CP asymmetry in  $B^\pm \rightarrow D_{CP+(-)}^0 K^\pm$ , where  $D_{CP+(-)}^0$  is a CP-even (odd) state. This state can be identified by its CP-even (odd) decay products. For instance, the states  $K_s \pi^0$ ,  $K_s \rho$ ,  $K_s \omega$ ,  $K_s \phi$  can identify a  $D_{CP-}^0$ , while  $\pi^+ \pi^-$ ,  $K^+ K^-$  represent a  $D_{CP+}^0$ . The CP eigenstates  $|D_{CP\pm}^0\rangle$  of the neutral D meson system with CP eigenvalues  $\pm 1$  are given by

$$|D_{CP\pm}^0\rangle = \frac{1}{\sqrt{2}}(|D^0\rangle \pm |\overline{D}^0\rangle), \tag{1.29}$$

so that the  $B^\pm \rightarrow D_{CP+}^0 K^\pm$  transition amplitudes can be expressed as [26]

$$\sqrt{2}A(B^+ \rightarrow D_{CP+}^0 K^+) = A(B^+ \rightarrow D^0 K^+) + A(B^+ \rightarrow \overline{D}^0 K^+) \tag{1.30}$$

$$\sqrt{2}A(B^- \rightarrow D_{CP+}^0 K^-) = A(B^- \rightarrow \overline{D}^0 K^-) + A(B^- \rightarrow D^0 K^-). \tag{1.31}$$

These relations, which are exact, can be represented as two triangles in the complex plane shown in Fig.1.5.

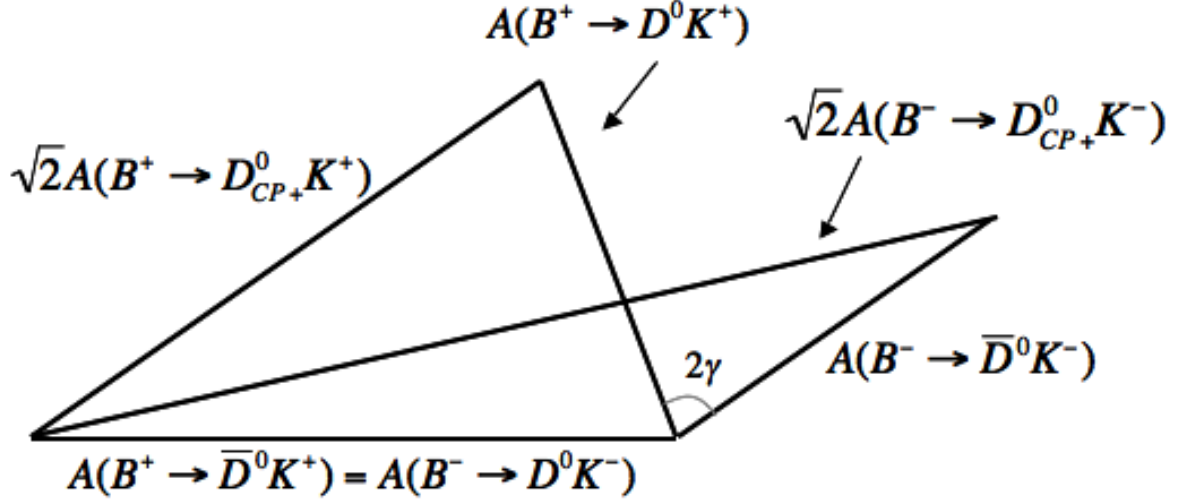


Figure 1.5: Triangle relations among the  $B^\pm \rightarrow DK^\pm$  decay amplitudes.

Taking into account that the  $B^+ \rightarrow DK^+$  decays originate from  $\bar{b} \rightarrow \bar{u}c\bar{s}$  and  $\bar{b} \rightarrow \bar{c}u\bar{s}$  quark-level transitions (see Fig. 1.3) we have:

$$A(B^+ \rightarrow D^0 K^+) = e^{i\gamma} \lambda |V_{cb}| R_B |a_h| e^{i\Delta_{a_h}} = e^{2i\gamma} A(B^- \rightarrow \bar{D}^0 K^-) \quad (1.32)$$

$$A(B^+ \rightarrow \bar{D}^0 K^+) = \lambda |V_{cb}| |A_h| e^{i\Delta_{A_h}} = A(B^- \rightarrow D^0 K^-), \quad (1.33)$$

where  $R_B = \frac{1-\lambda^2/2}{\lambda} \left| \frac{V_{ub}}{V_{cb}} \right|$  measures one side of the unitarity triangle. The quantities  $|a_h|$ ,  $|A_h|$  are the magnitudes of the hadronic matrix elements of current-current operators, and  $\Delta_{a_h}$ ,  $\Delta_{A_h}$  denote the corresponding CP-conserving strong phase. Assuming  $\gamma \neq 0$ , one finds

$$|A(B^+ \rightarrow D_{CP^+}^0 K^+)| \neq |A(B^- \rightarrow D_{CP^+}^0 K^-)|. \quad (1.34)$$

Combining all these considerations, the triangle relations (1.30) and (1.31) can be used to extract  $\gamma$  by measuring only the rates of the six processes.

This approach is theoretically clean and suffers from no hadronic uncertainties. Unfortunately the amplitude triangles are expected to be squashed since  $B^+ \rightarrow D^0 K^+$  is color-suppressed with respect to  $B^+ \rightarrow \bar{D}^0 K^+$  [32]:

$$r_B \equiv \frac{|A(B^+ \rightarrow D^0 K^+)|}{|A(B^+ \rightarrow \bar{D}^0 K^+)|} \approx \frac{|V_{ub} V_{cs}^*| a_2}{|V_{cb} V_{us}^*| a_1} \approx 0.1, \quad (1.35)$$

where  $\frac{a_2}{a_1} \approx 0.26$  is a color suppression factor estimated from the measured branching fractions of color-suppressed B decays and  $\frac{|V_{ub} V_{cs}^*|}{|V_{cb} V_{us}^*|} = 0.4 \pm 0.1$ .

This estimation for  $r_B$  is confirmed by recent experimental determinations published

by the BABAR and BELLE experiments:

$$\begin{aligned} r_B &= 0.12 \pm 0.09 & BABAR & [33] \\ r_B &= 0.21 \pm 0.09 & BELLE & [34]. \end{aligned}$$

The observables are the two direct CP asymmetries:

$$A_{CP\pm} \equiv \frac{BR(B^- \rightarrow D_{CP\pm}^0 K^-) - BR(B^+ \rightarrow D_{CP\pm}^0 K^+)}{BR(B^- \rightarrow D_{CP\pm}^0 K^-) + BR(B^+ \rightarrow D_{CP\pm}^0 K^+)} \quad (1.36)$$

and the two ratios of charge averaged branching fractions:

$$R_{\pm} \equiv \frac{\frac{BR(B^- \rightarrow D_{CP\pm}^0 K^-) + BR(B^+ \rightarrow D_{CP\pm}^0 K^+)}{BR(B^- \rightarrow D_{CP\pm}^0 \pi^-) + BR(B^+ \rightarrow D_{CP\pm}^0 \pi^+)}}{\frac{BR(B^- \rightarrow D^0 K^-) + BR(B^+ \rightarrow \bar{D}^0 K^+)}{BR(B^- \rightarrow D^0 \pi^-) + BR(B^+ \rightarrow \bar{D}^0 \pi^+)}}. \quad (1.37)$$

They are expressed in terms of  $\gamma$ ,  $r_B$  and  $\delta_B = \Delta_a - \Delta_A$  that is the strong phase difference between the  $V_{ub}$  and the  $V_{cb}$  mediated amplitudes, through the relations:

$$\begin{aligned} R_{\pm} \approx R_{CP\pm} &\equiv \frac{BR(B^- \rightarrow D_{CP\pm}^0 K^-) + BR(B^+ \rightarrow D_{CP\pm}^0 K^+)}{BR(B^- \rightarrow D^0 K^-) + BR(B^+ \rightarrow \bar{D}^0 K^+)} \equiv \\ &\equiv 1 + r_b^2 \pm 2r_B \cos \delta_B \cos \gamma \end{aligned} \quad (1.38)$$

$$A_{CP\pm} \equiv \frac{\pm 2r_B \sin \delta_B \sin \gamma}{R_{CP\pm}}. \quad (1.39)$$

The approximate equality  $R_{CP\pm} \approx R_{\pm}$  follows from the exact cancellation of  $D^0\pi$  phase-space factors in the double ratio  $R_{\pm}$  and from the approximation  $A(B^+ \rightarrow D_{CP\pm}^0 \pi^+) \approx A(B^- \rightarrow D_{CP\pm}^0 \pi^-) \approx \frac{1}{\sqrt{2}}A(B^- \rightarrow D^0 \pi^-)$ , where a term  $r_B \times |V_{us}V_{cd}/V_{ud}V_{cs}|$  is neglected.

As we can see from equations (1.38) and (1.39), however large the data sample, the sensitivity to  $\gamma$  is essentially proportional to the value of  $r_B$  and is therefore limited by the small value of  $r_B$ .

The current results of Babar and Belle experiments, regarding  $A_{CP\pm}$ , and  $R_{CP\pm}$  are summarized in Table 1.1 and 1.2 respectively.

Measurement	$A_{CP+}$	$A_{CP-}$
Babar [35]	$0.35 \pm 0.13 \pm 0.04$	$-0.06 \pm 0.13 \pm 0.04$
Belle [36]	$0.06 \pm 0.14 \pm 0.05$	$-0.12 \pm 0.14 \pm 0.05$

Table 1.1: Babar and Belle results regarding  $A_{CP\pm}$ .

Measurement	$R_{CP+}$	$R_{CP-}$
Babar [35]	$0.90 \pm 0.12 \pm 0.04$	$0.86 \pm 0.10 \pm 0.05$
Belle [36]	$1.13 \pm 0.16 \pm 0.08$	$1.17 \pm 0.14 \pm 0.14$

Table 1.2: Babar and Belle results regarding  $R_{CP\pm}$ .

### 1.5.2 The Atwood-Dunietz-Soni method

The Atwood-Dunietz-Soni (ADS) method is based on the reconstruction of charged B-decays to  $D^0 K$  where the  $D^0$  decays to a doubly-Cabibbo-suppressed (DCS) final state  $f$ , like for instance  $f = K^+ \pi^-$ . In this case a large interference is expected between the  $B^- \rightarrow D^0 K^-$ ,  $D^0 \rightarrow K^+ \pi^-$  amplitude, which proceeds through the color-allowed  $b \rightarrow c$  transition followed by the DCS  $D^0$  decay, and the  $B^- \rightarrow \bar{D}^0 K^-$ ,  $\bar{D}^0 \rightarrow K^+ \pi^-$  amplitude, where the color-suppressed  $b \rightarrow u$  transition is followed by a Cabibbo-allowed  $\bar{D}^0$  decay:

$$\begin{aligned}
|A(B^- \rightarrow D^0 K^-, D^0 \rightarrow K^+ \pi^-)| &= \\
&= |A(B^- \rightarrow D^0 K^-)| \times |A(D^0 \rightarrow K^+ \pi^-)| \propto |V_{cb} V_{us}^*| \times |V_{cd}^* V_{us}| \\
|A(B^- \rightarrow \bar{D}^0 K^-, \bar{D}^0 \rightarrow K^+ \pi^-)| &= \\
&= |A(B^- \rightarrow \bar{D}^0 K^-)| \times |A(\bar{D}^0 \rightarrow K^+ \pi^-)| \propto |V_{ub} V_{cs}^*| \frac{a_2}{a_1} \times |V_{cs} V_{ud}^*|
\end{aligned}$$

Using the expression (1.35) for  $r_B$  the ratio between the two amplitudes becomes:

$$\frac{|A(B^- \rightarrow \bar{D}^0 K^-, \bar{D}^0 \rightarrow K^+ \pi^-)|}{|A(B^- \rightarrow D^0 K^-, D^0 \rightarrow K^+ \pi^-)|} = r_B \left| \frac{V_{cs} V_{ud}}{V_{us} V_{cd}} \right| \approx r_B \lambda^{-2} \approx 2. \quad (1.40)$$

Accordingly, the (direct) CP asymmetries, in these decays, are potentially large, up to 40%, and the sensitivity to  $\gamma$ , which, like in the previous method, is proportional to the interference term, should be enhanced. Unfortunately, on the other hand, considering doubly-cabibbo-suppressed  $D^0$  decays instead of singly-Cabibbo-suppressed decays to CP eigenstates reduces the overall branching fractions by a factor  $\approx \lambda^2$  and a significantly larger statistics is needed to perform the measurement. With the same data sample, the sensitivities of this and of the previous methods are probably comparable.

To extract  $\gamma$  from these decays one needs to measure their branching fractions and CP asymmetries, which are related to  $\gamma$  through the relations:

$$\begin{aligned}
R_{ADS}(f = K\pi) &\equiv \frac{BR(B^- \rightarrow [K^+ \pi^-]_{D^0} K^-) + BR(B^+ \rightarrow [K^- \pi^+]_{D^0} K^+)}{BR(B^- \rightarrow [K^- \pi^+]_{D^0} K^-) + BR(B^+ \rightarrow [K^+ \pi^-]_{D^0} K^+)} = \\
&= r_D^2 + r_B^2 + 2r_D r_B \cos \gamma \cos(\delta_B + \delta_D) \quad (1.41)
\end{aligned}$$

$$\begin{aligned}
A_{ADS} &\equiv \frac{BR(B^- \rightarrow [K^+ \pi^-]_{D^0} K^-) - BR(B^+ \rightarrow [K^- \pi^+]_{D^0} K^+)}{BR(B^- \rightarrow [K^- \pi^+]_{D^0} K^-) + BR(B^+ \rightarrow [K^+ \pi^-]_{D^0} K^+)} = \\
&= \frac{2r_B r_D \sin \gamma \sin(\delta_B + \delta_D)}{r_B^2 + r_D^2 + 2r_B r_D \cos \gamma \cos(\delta_B + \delta_D)} \quad (1.42)
\end{aligned}$$

where  $\delta_B$  is the strong phase difference between the  $V_{ub}$  and the  $V_{cb}$  mediated amplitude and  $\delta_D$  is the strong phase in the  $D^0$  decay.  $r_D$  is the magnitude of the ratio of amplitudes of the  $D^0$  Cabibbo-suppressed with respect to the  $D^0$  Cabibbo allowed decay:

$$r_D \equiv \frac{|A(\overline{D}^0 \rightarrow K^- \pi^+)|}{|A(D^0 \rightarrow K^- \pi^+)|} = 0.060 \pm 0.002 \quad [24]. \quad (1.43)$$

The current measurements of  $R_{ADS}(K\pi)$  allow to put an upper limit on the value of  $r_B$ :

$$\begin{aligned} r_B &\leq 0.23 \quad (90\%C.L.) & BABAR & [37] \\ r_B &\leq 0.18 \quad (90\%C.L.) & BELLE & [38]. \end{aligned}$$

but do not allow a direct measurement of  $\gamma$ . In fact the number of unknowns (3) is greater than the number of observables (2). The unknown parameters  $r_B$ ,  $\gamma$  are in common with the GLW method, while in this case we have the unknown extra-parameter  $\delta = \delta_B + \delta_D$ . In any case the analysis can provide useful information once the results are combined with other  $\gamma$  related measurements.

### 1.5.3 The Giri-Grossmann-Soffer-Zupan method

The Giri-Grossmann-Soffer-Zupan (GGSZ) method is based on the reconstruction of  $B \rightarrow D^0 K$  and  $B \rightarrow \overline{D}^0 K$  decays with the  $D^0$  and  $\overline{D}^0$  reconstructed into three-body (or multi-body) self-conjugate final states. We consider here, as an example, the decay  $D^0 \rightarrow K_s^0 \pi^+ \pi^-$ .

Let us denote with  $m_-^2$  and  $m_+^2$  the squared invariant masses of the  $K_s^0 \pi^-$  and  $K_s^0 \pi^+$  combinations respectively, and

$$A(D^0 \rightarrow K_s^0 \pi^+ \pi^-) = f(m_-^2, m_+^2) = |f(m_-^2, m_+^2)| e^{i\Delta(m_-^2, m_+^2)}$$

the amplitude of the  $D^0 \rightarrow K_s^0 \pi^+ \pi^-$  decay to the point  $(m_-^2, m_+^2)$  of the Dalitz plot. Neglecting CP violation in  $D^0$  decays, the amplitude  $A(\overline{D}^0 \rightarrow K_s^0 \pi^+ \pi^-)$  to the same point of the Dalitz plot is

$$A(\overline{D}^0 \rightarrow K_s^0 \pi^+ \pi^-) = f(m_+^2, m_-^2) = |f(m_+^2, m_-^2)| e^{i\Delta(m_+^2, m_-^2)}.$$

The total  $B^-$  and  $B^+$  amplitudes for the process  $B \rightarrow [K_s^0 \pi^+ \pi^-]_{D^0} K$ , denoted with  $A_-$  and  $A_+$ , are:

$$\begin{aligned} A_-(m_-^2, m_+^2) &= A(B^- \rightarrow D^0 K^-) [f(m_-^2, m_+^2) + r_B e^{i(\delta_B - \gamma)} f(m_+^2, m_-^2)] \\ A_+(m_-^2, m_+^2) &= A(B^+ \rightarrow \overline{D}^0 K^+) [f(m_+^2, m_-^2) + r_B e^{i(\delta_B + \gamma)} f(m_-^2, m_+^2)]. \end{aligned}$$

The resulting bi-dimensional Dalitz  $(m_-^2, m_+^2)$  distributions for negative and positive B candidates, modulo reconstruction efficiency variations, are proportional to

$$\begin{aligned} |A_-(m_-^2, m_+^2)|^2 &= |A|^2 \times [|f(m_-^2, m_+^2)|^2 + r_B^2 |f(m_+^2, m_-^2)|^2 + \\ &\quad 2r_B |f(m_-^2, m_+^2)| |f(m_+^2, m_-^2)| \cos(\delta_B - \gamma + \delta_D(m_-^2, m_+^2))] \end{aligned} \quad (1.44)$$

and

$$|A_+(m_-^2, m_+^2)|^2 = |A|^2 \times [|f(m_+^2, m_-^2)|^2 + r_B^2 |f(m_-^2, m_+^2)|^2 + 2r_B |f(m_+^2, m_-^2)| |f(m_-^2, m_+^2)| \cos(\delta_B + \gamma - \delta_D(m_+^2, m_-^2))] \quad (1.45)$$

where  $|A| \equiv |A(B^- \rightarrow D^0 K^-)| = |A(B^+ \rightarrow \overline{D}^0 K^+)|$  and

$$\delta_D(m_-^2, m_+^2) \equiv \overline{\Delta}(m_-^2, m_+^2) - \Delta(m_-^2, m_+^2) = \Delta(m_+^2, m_-^2) - \Delta(m_-^2, m_+^2) \quad (1.46)$$

is the strong phase difference between the  $\overline{D}^0$  and  $D^0$  amplitudes at the point  $(m_-^2, m_+^2)$  of the  $K_s^0 \pi^+ \pi^-$  Dalitz plot.

If the Dalitz structure of the  $D^0 \rightarrow K_s^0 \pi^+ \pi^-$  decay is known, i.e.  $f(m_-^2, m_+^2)$  is known (for instance from charm factories), then the Dalitz distribution of the  $K_s^0 \pi^+ \pi^-$  candidates originating from  $B^+$  and  $B^-$  decays to  $D^0 K$  can be fitted to extract  $r_B$ ,  $\delta_B$  and  $\gamma$ .

The main advantage of this method is that the  $D^0$  decays that are considered are Cabibbo-allowed, therefore the branching fractions are about one order of magnitudes higher than in the GLW case.

On the other hand, the Dalitz plot  $(m_-^2, m_+^2)$  of the selected B candidates must be sufficiently populated to perform the fit, which requires a significant number of  $B \rightarrow [K_s^0 \pi^+ \pi^-]_{D^0} K$  decays to be reconstructed, and the  $D^0 \rightarrow K_s^0 \pi^+ \pi^-$  amplitude  $f(m_-^2, m_+^2)$  must be known.

Using this method Belle [39] and Babar [40] obtained  $\gamma = 68_{-15}^{+14} \pm 13 \pm 11^\circ$  and  $\gamma = 67 \pm 28 \pm 13 \pm 11^\circ$ , respectively, where the last uncertainty is due to the D decay modeling.

Combining the GLW, ADS and Dalitz analyses [13]  $\gamma$  is constrained as  $\gamma = (63_{-12}^{+15})^\circ$ .

We start with the measurements connected to the GLW method (BR and  $A_{CP}$  measurements for  $B \rightarrow DK$  decays) because in this way we also put the basis for the  $\gamma$  measurement using the  $B_s \rightarrow D_s K \rightarrow [\phi \pi] K$ .



## Chapter 2

# The Tevatron collider and the CDF-II Detector

Until the startup of Large Hadron Collider (LHC) at CERN, the Fermilab Tevatron Collider is the high energy frontier in particle physics and the source of the highest energy proton-antiproton ( $p\bar{p}$ ) collisions. The collisions occur at two points on an underground ring, which has a radius of about 1 km. At these collision points there are two detectors: the Collider Detector at Fermilab (CDF II) and D0.

Between 1997 and 2001, both the accelerator complex and the collider detectors underwent major upgrades, mainly aimed at increasing the instantaneous luminosity of the accelerator. The upgraded machine accelerates  $36 \times 36$  bunches of protons and antiprotons, whereas the previous version of the accelerator operated with only  $6 \times 6$  bunches. Consequently, the time between two consecutive bunch crossings has been decreased from  $3.5 \mu\text{s}$  for the previous version to 396 ns for the current collider.

By the fall of 2005, the anti-protons production chain has been improved introducing the electron cooling [41] in the Recycler (Section 2.1). In the year 2006 the  $2 \times 10^{32} \text{ cm}^{-2} \text{ s}^{-1}$  peak luminosity has been reached. Then, starting in the year 2007 and until the end of the Tevatron operations, the peak luminosity is expected to be  $3 \times 10^{32} \text{ cm}^{-2} \text{ s}^{-1}$ , with an expected total integrated luminosity of  $4 \text{ fb}^{-1}$  at the end of 2007 (Fig. 2.1).

Thanks to the Tevatron high luminosity and to the new SVT trigger (Section 2.8), large samples of b and c hadrons decays have been collected by the CDF II detector and are now available for the analysis.

The data sample used in this Thesis has been collected by the CDF II detector between March 2002 and February 2006, and it corresponds to an integrated luminosity of  $1.3 \text{ fb}^{-1}$  on tape<sup>1</sup>.

The new accelerator configuration required significant upgrades of the CDF II detector to ensure a maximum response time shorter than the time between two consecutive beam crossings. In the following pages, we will describe how the protons and antiprotons beams are produced, accelerated to the final energy of 980 GeV and collided. We

---

<sup>1</sup>The analysis described has been made with  $360 \text{ pb}^{-1}$  of data. The update of the analysis to  $1 \text{ fb}^{-1}$  of data is in progress at the time of the writing.

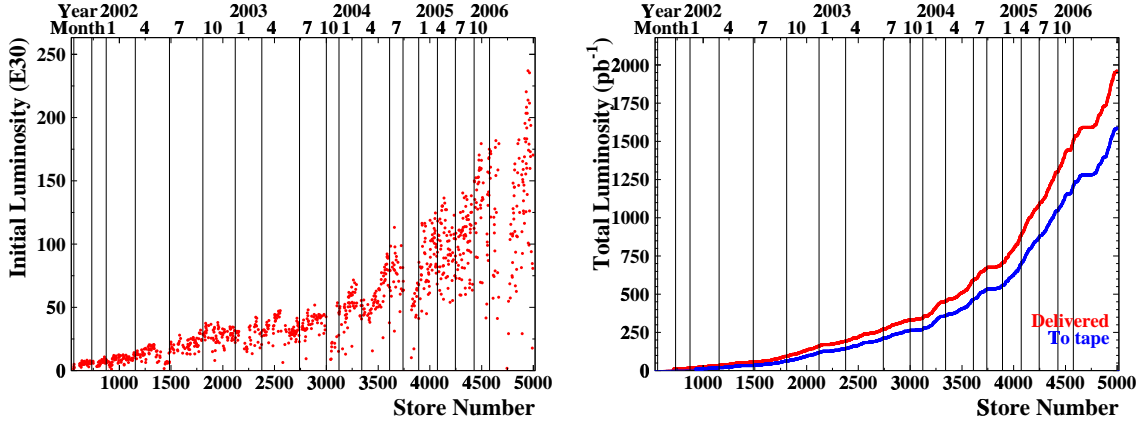


Figure 2.1: Left: Peak luminosity as a function of time, measured using the store number. Right: Integrated luminosity as a function of time, measured using the store number.

will then describe the CDF II components used to identify and measure the properties of the particles produced in the collision focusing on the detector components most relevant for this analysis.

## 2.1 $p\bar{p}$ acceleration and collisions

In order to create the particle beams Fermilab uses a series of accelerators. Fig. 2.2 shows the paths taken by protons and antiprotons from the initial acceleration to collision in the Tevatron.

The Cockcroft-Walton [42] pre-accelerator provides the first stage of the acceleration. Inside this device, hydrogen gas is ionized to create  $H^+$  ions, which are accelerated to 750 keV of kinetic energy. Next, the  $H^+$  ions enter a linear accelerator (Linac) [43], approximately 150 m long, where they are accelerated to 400 MeV. The acceleration in the Linac is done by a series of "kicks" from Radio Frequency (RF) cavities. The oscillating electric field of the RF cavities groups the ions into bunches.

The 400 MeV  $H^+$  ions are then injected into the Booster, a circular synchrotron [43] with a diameter of 7.45 m. A carbon foil strips the electrons from the  $H^+$  ions at injection, leaving bare protons. The intensity of the protons beam is increased by injecting new protons into the same orbit as the circulating ones. The protons are accelerated from 400 MeV to 8 GeV by a series of "kicks" applied by RF cavities. Each turn around the Booster, the protons accrue about 500 keV of kinetic energy.

Protons are extracted from the Booster into the Main Injector [44], which operates at 53 MHz. The Main Injector accelerates protons from 8 GeV to 150 GeV before injection into the Tevatron, it produces the 120 GeV protons used for antiprotons production, it receives antiprotons from the Antiproton Source and accelerates them to 150 GeV for injection into the Tevatron, and finally, it injects protons and antiprotons in the Tevatron.

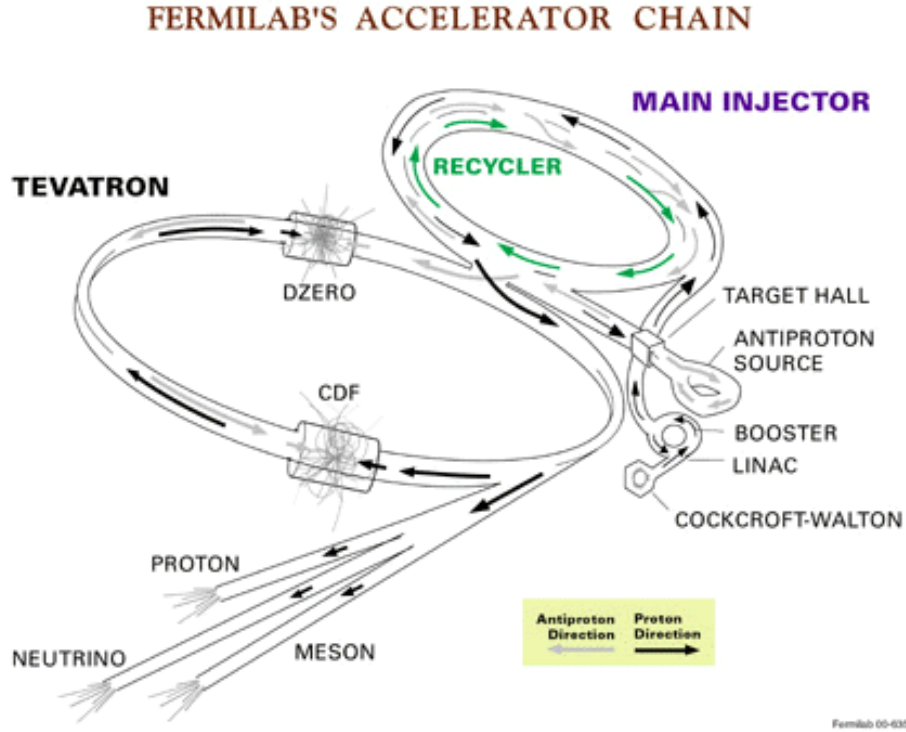


Figure 2.2: Layout of the Fermilab accelerator complex. The protons (black arrow) are accelerated at the Cockcroft-Walton, Linac, Booster, Main Injector and finally at the Tevatron. The anti-protons (grey arrow) from the anti-proton source are first accelerated by the Main Injector and then by the Tevatron.

The Main Injector replaced the Main Ring accelerator which was situated in the Tevatron tunnel. The Main Injector is capable of containing larger proton currents than its predecessor, which results in a higher rate of antiprotons production. The Main Injector tunnel also houses the Antiproton Recycler. Not all antiprotons in a given store are used for the collisions. Recycling the unused antiprotons and reusing them in the next store significantly reduces the stacking time. The task of the Antiproton Recycler is to receive antiprotons from a Tevatron store, cool them and re-integrate them into the stack, so that they can be used in the next store.

To produce antiprotons, 120 GeV protons from the Main Injector are directed into a nichel target. In the collisions, about 20 antiprotons are produced per one million protons, with a mean kinetic energy of 8 GeV. The antiprotons are focused by a lithium lens and separated from other particle species by a pulsed magnet. The antiprotons are stored in the Accumulator ring. Once a sufficient number of antiprotons have been produced, they are sent to the Main Injector and accelerated to 150 GeV. Finally both, the protons and antiprotons, are injected into the Tevatron.

The Tevatron is the last stage of the Fermilab accelerator chain, It receives 150 GeV protons and antiprotons from the Main Injector and accelerates them to 980 GeV. The

protons and antiprotons travel around the Tevatron in opposite directions. In the interaction points, where CDF II and D0 are located, the two beams are focused by quadrupole magnets that reduce the beam size increasing the luminosity. The instantaneous luminosity, to which the number of collisions per unit of time is proportional is approximately given by:

$$L = \frac{f N_B N_p N_{\bar{p}}}{2\pi(\sigma_p^2 + \sigma_{\bar{p}}^2)} \quad (2.1)$$

where  $f$  is the revolution frequency,  $N_B$  is the number of bunches,  $N_{p(\bar{p})}$  is the number of protons (antiprotons) per bunch, and  $\sigma_{p(\bar{p})}$  is the proton (antiproton) RMS beam size at the interaction point. The instantaneous luminosity degrades over the time as particles are lost and beams begin to heat up, mostly due to the long range beam-beam interaction.

## 2.2 The CDF II Detector

The Collider Detector at Fermilab (CDF) is a general purpose, azimuthally and forward-backward symmetric apparatus, designed to study  $p\bar{p}$  collisions at the Tevatron. Fig. 2.3 shows the detector and the different sub-systems in a solid cutaway view. The protons and antiprotons beams travel towards each other along the horizontal axis (beam line or beam axis). Any plane perpendicular to the beam line is called a transverse plane, and the intersection point between the beam line and the transverse plane is referred to as beam spot.

CDF II consists of five main subdetector systems: tracking, particle identification, calorimetry, muon identification and luminosity detector.

The innermost system is the integrated tracking system: a silicon microstrip detector and an open-cell wire drift chamber, the Central Outer Tracker (COT) that surrounds the silicon detector.

The tracking system is surrounded by the Time Of Flight system, designed to provide particle identification for low-momentum charged particles (momentum below to 2 GeV/c).

Both the tracking and the Time Of Flight detector are placed inside the superconducting coil, which generates a 1.4 T uniform horizontal magnetic field along the z axis inside the tracking volume. The trajectories of the charged particles inside the tracking volume are helices.

The tracking system is designed to measure the momentum and the trajectory of the charged particles. Multiple-track reconstruction allows to identify the vertices where either the  $p\bar{p}$  interaction took place (primary vertex) or the decay of a long-lived particle took place (secondary or displaced vertex).

The solenoid coil is surrounded by the calorimeters, which measure the energy of particles that shower when interacting with matter. The calorimeters are surrounded by the muon detectors. Muons are "minimally ionizing particles", they only deposit small amounts of ionization energy in the material. Therefore, they are able to penetrate both the tracking and calorimeter systems. The integrated material of the tracking

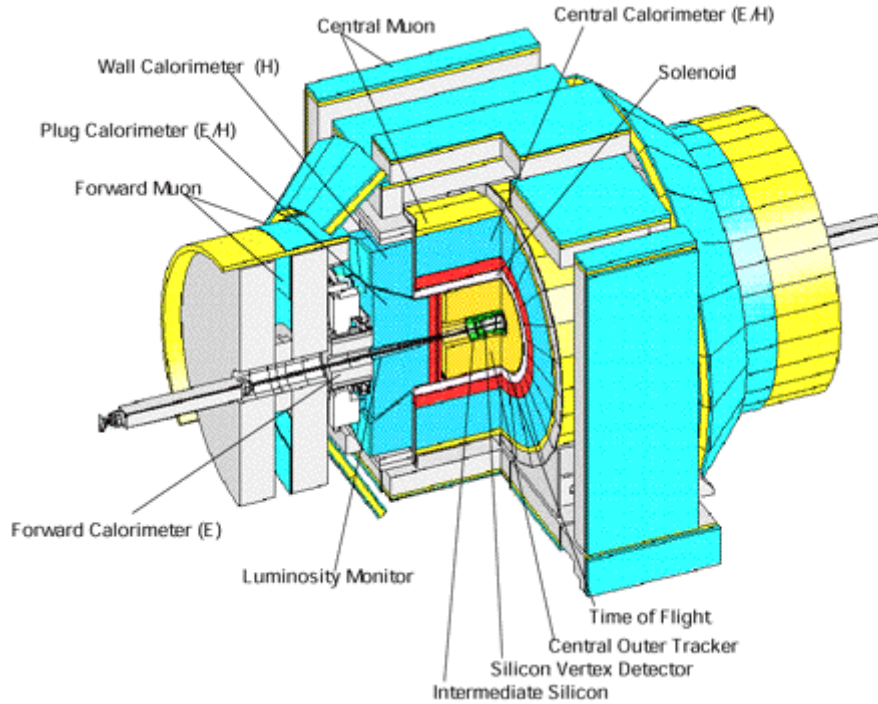


Figure 2.3: The CDF II detector with a quadrant cut to expose the different subdetectors.

system, of the TOF detector, of the solenoid and of the calorimeter serves as a particle filter. Particles which penetrate through all that material are mostly muons, and they are detected by the tracks in the muon chambers, located outside the calorimeter.

At the extreme forward region of the CDF II detector two modules of Cherenkov Luminosity Counters (CLC) [45] are placed. They point to the center of the interaction region to record the number of  $p\bar{p}$  interactions and determine the instantaneous luminosity.

The most important parts of the detector for this analysis are the tracking system, the particle identification detectors and the trigger, and these will be described in detail in the following section. The description of the remaining systems will be brief. More detailed information on all these systems can be found in the Technical Design Report of the CDF II Detector [46] [47].

## 2.3 Standard Definitions in CDF

Because of its barrel-like shape, the CDF II Detector uses a cylindrical coordinate system  $(r, \phi, z)$  with the origin at the center of the detector and the  $z$ -axis along the nominal direction of the protons beam.  $r$  is the radial distance from the origin and  $\phi$  the azimuthal angle. The  $r - \phi$  plane is called the transverse plane, since is perpendicular to the beam line. The polar angle,  $\theta$ , is the angle relative to the  $z$ -axis.

An alternative way of expressing  $\theta$  is the pseudorapidity  $\eta^2$ , defined as:

$$\eta \equiv -\ln \tan \left( \frac{\theta}{2} \right). \quad (2.2)$$

The coverage of each CDF II detector sub-system will be described using combinations of  $\eta$ ,  $r$ ,  $\phi$  and  $z$ .

Charged particles moving through a homogeneous solenoidal magnetic field along the  $z$  direction follow helical trajectories. To uniquely parameterize a helix in three dimensions, five parameters are needed:  $C$ ,  $\cot \theta$ ,  $d_0$ ,  $\phi_0$  and  $z_0$ . The projection of the helix on the  $r-\phi$  plane is a circle.  $C$  is the signed curvature of the circle, defined as  $C \equiv \frac{\text{sign}(Q)}{2\rho}$ , where  $\rho$  is the radius of the circle and the charge of the particle ( $Q$ ) determines the sign of  $C$ . Positive charged tracks curve counterclockwise in the  $r-\phi$  plane when looking along the  $z$  direction and negative charged tracks bend clockwise. The transverse momentum,  $p_T$ , depends on the curvature  $C$ , on the magnetic field ( $B_{\text{magnet}}$ ), and on the charge of the particle through the following formula:  $p_T = Q \cdot \frac{B_{\text{magnet}}}{2C}$ . Since  $\theta$  is the angle between the  $z$  axis and the particle momentum,  $\cot \theta = \frac{p_z}{p_T}$ , where  $p_z$  is the  $z$  component of the particle momentum.

The last three parameters,  $d_0$ ,  $\phi_0$  and  $z_0$ , are the  $r$ ,  $\phi$  and  $z$  coordinates of the point of closest approach of the helix to the beam line. See Fig.2.4 for the definition of  $d_0$  and  $\phi_0$ .  $d_0$  is a signed variable:

$$d_0 = Q \cdot \left( \sqrt{x_0^2 + y_0^2} - \rho \right), \quad (2.3)$$

where  $(x_0, y_0)$  is the center of the helix circle in the  $r-\phi$  plane.

Fig.2.5 shows the definition of  $d_0$  sign.

For decaying particles, we define the displacement  $L_{xy}$ :

$$L_{xy} = \frac{\widehat{x_V} \cdot \vec{p_T}}{|p_T|}, \quad (2.4)$$

where  $x_V$  is the decay length in the transverse plane. In the following we will call  $L_{xy}$  "transverse decay length".

---

<sup>2</sup>It is convenient because it is a purely geometrical quantity related to the polar angle, and, at the same time, it is a Lorentz invariant under a boost in  $z$  direction in ultra-relativistic limit. Since a lot of the physics at CDF is approximately ultra-relativistic this variable is useful for describing the geometry of the decay.

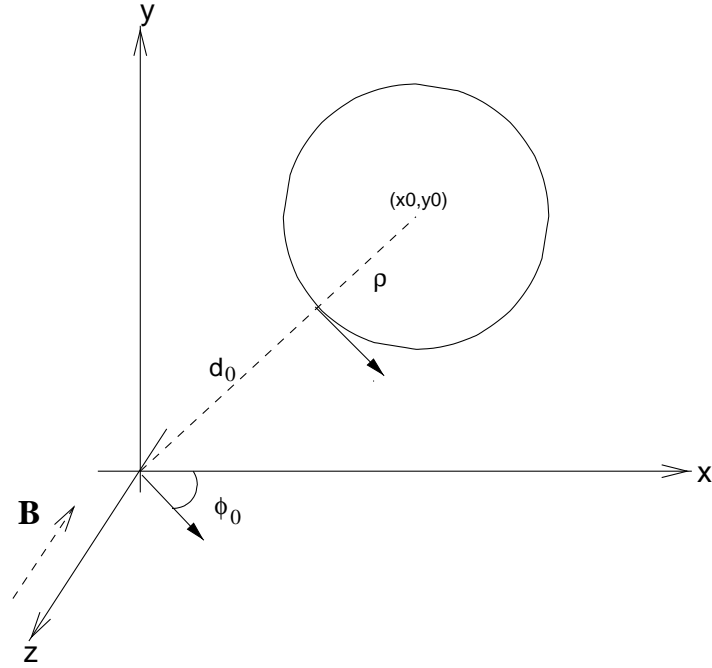
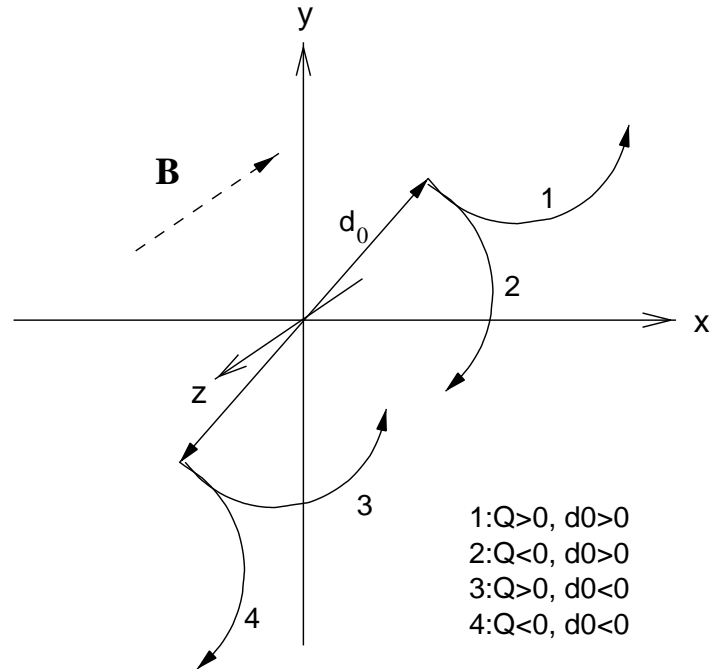
Figure 2.4: Definition of the  $d_0$  and  $\phi_0$  coordinates.

Figure 2.5: Tracks of particles with positive/negative charge and positive/negative impact parameters.

## 2.4 The CDF II Tracking System

The tracking system is immersed in a 1.4 T solenoidal magnetic field for the measurement of charged particles momenta. We will describe this system, shown in Fig.2.6, starting from the device closest to the beam and moving outwards. The innermost tracking device is a silicon detector, which consists of three subdetectors that cover the region  $|\eta| < 2$  and  $2\pi$  of azimuthal angle. The first layer of silicon sensors, called Layer 00 (L00) [48], is installed directly onto the beryllium beam pipe, with the sensors at radii 1.35 and 1.62 cm from the beam. The beam pipe is made of beryllium because this metal has the best mechanical qualities with the lowest nuclear interaction cross section.

The L00 is followed by SVX II [49], made of five concentric layers of silicon sensors located at radii between 2.45 and 10.6 cm. The Intermediate Silicon Layers (ISL) [50] are the outermost silicon detectors, with one layer of sensors at a radius of 22 cm in the central region and two layers at radii 20 and 28 cm in the forward region. Surrounding the silicon detectors is the Central Outer Tracker (COT) [51], a 3.1 m long cylindrical open-cell drift chamber covering the volume between 43.4 cm and 132.3 cm of radius and  $|\eta| < 1$ .

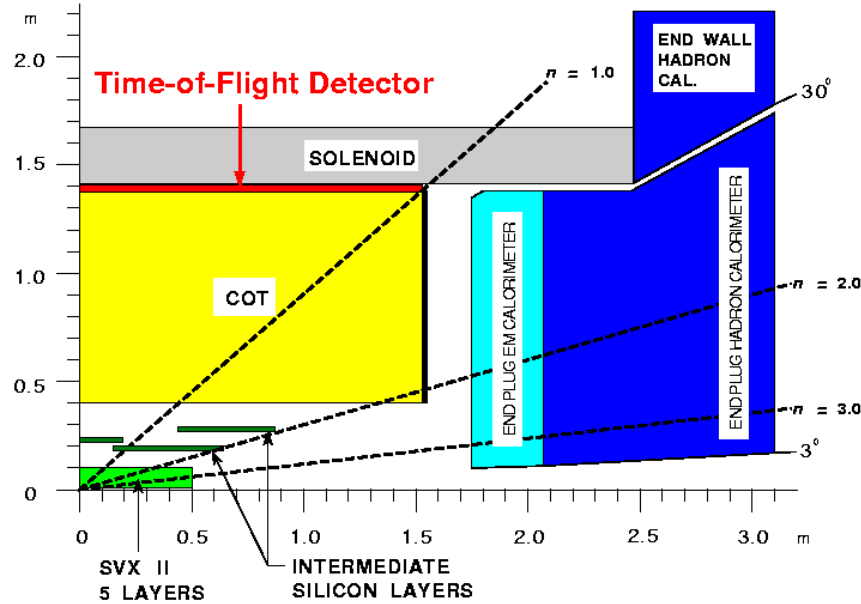


Figure 2.6: Longitudinal section of one quadrant of the CDF II tracking system and part of the calorimeter.



### 2.4.1 The Silicon Detectors

The silicon strip detectors [52] at CDF II provide a precise determination of the particle trajectory close to the beam line.

The impact parameter resolution measured in the transverse plane is of  $27\ \mu\text{m}$ .

A silicon detector is fundamentally a reverse-biased p-n junction. When a charged particle passes through the detector material, it causes ionization. For a semiconductor, this means that electron-hole pairs are produced. Electrons drift towards the anode, and holes drift towards the cathode, where the charge is gathered. The amount of charge is, to first order, proportional to the path length traversed in the detector material by the charged particle.

By segmenting the p or n side of the junction into "strips" and reading out the charge deposition separately on every strip, we obtain sensitivity to the position of the charged particle. All the CDF II silicon detectors are implemented as microstrip detectors. The typical distance between two strips is about  $60\ \mu\text{m}$ . Charge deposition from a single particle passing through the silicon sensor can be read out on one or more strips. This charge deposition is used to determine the hit position in the direction perpendicular to the strips.

There are two types of microstrip detectors: single and double-sided. In single-sided detectors only one (p) side of the junction is segmented into strips. Double-sided detectors have both sides of the junction segmented into strips. The benefit of double-sided detectors is that while one (p) side has strips parallel to the  $z$  direction, providing  $r - \phi$  position measurements, the (n) side can have strips at an angle (stereo angle) with respect to the  $z$  direction, and can provide  $z$  position information.

For SVX II, made of double sided silicon sensor, four silicon sensors are assembled into a "ladder" structure which is 29 cm long. The readout electronics are mounted directly to the surface of the silicon sensor at each end of the ladder. The ladders are organized in an approximately cylindrical configuration, creating "barrels". A SVX II barrel is segmented into 12 wedges, each covering approximately  $30^\circ$  in  $\phi$ , for each wedge there are five layers. Each layer provides one axial measurement on one side and a measurement at the stereo angle on the other side (see table 2.1). The resolution on the single hit is  $12\ \mu\text{m}$ . There are three SVX II barrels, mounted adjacent to each other along the  $z$ -axis, as shown in Fig.2.7, covering the nominal interaction region at the center of the CDF II Detector. The coverage of the silicon detector subsystem is shown in Fig. 2.8.

The innermost layer, L00, is made of single-sided silicon sensors which provide only  $r - \phi$  measurements, but also, being only at 1.5 cm from the interaction point, provides the best resolution on the transverse impact parameter.

The ISL is made of double-sided silicon sensors and it provides up to two additional tracking layers depending on pseudorapidity (Fig. 2.8). In particular ISL provides a higher tracking efficiency by connecting tracks in SVX with the ones in COT and allows to extend tracking beyond the COT limit ( $|\eta| < 1$ ), and up to  $|\eta| < 2$ .

All the silicon detectors are used in the Offline track reconstruction algorithm.

Property	Layer 0	Layer 1	Layer 2	Layer 3	Layer 4
number of $\phi$ strips	256	384	640	768	869
number of $z$ strips	256	576	640	512	869
stereo angle	$90^\circ$	$90^\circ$	$+1.2^\circ$	$90^\circ$	$-1.2^\circ$
$\phi$ strip pitch [ $\mu\text{m}$ ]	60	62	60	60	65
$z$ strip pitch [ $\mu\text{m}$ ]	141	125.5	60	141	65
active width [mm]	15.30	23.75	38.34	46.02	58.18
active length [mm]	72.43	72.43	72.38	72.43	72.43

Table 2.1: Relevant parameters for the layout of the sensors of the five SVX-II layers.

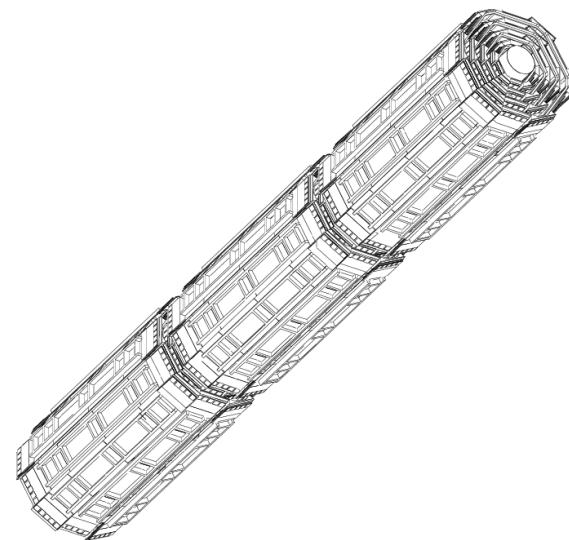


Figure 2.7: Isometric view of three SVX II barrels.

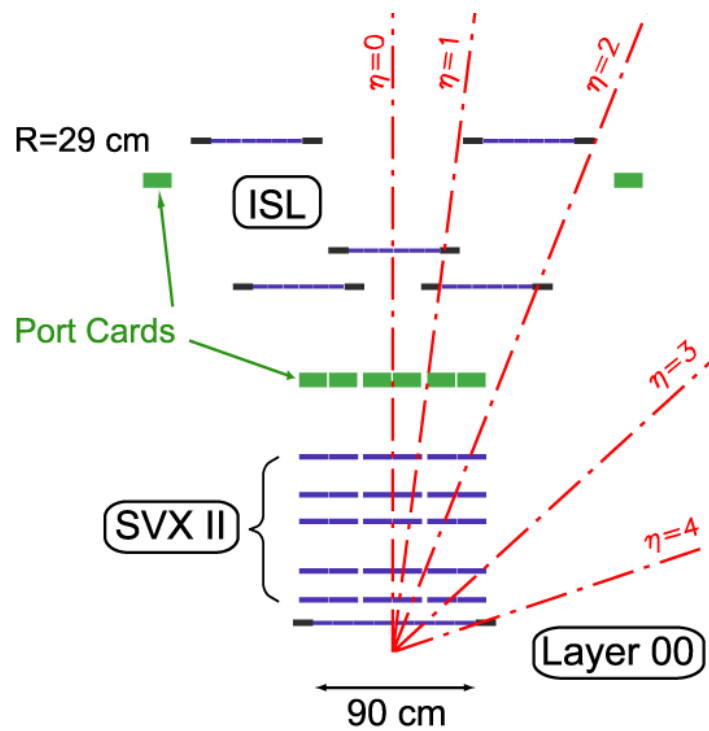


Figure 2.8: Coverage of the silicon detectors in the  $r-z$  plane. The  $r$  and  $z$  axes have different scales.

### 2.4.2 The Central Outer Tracker

The COT drift chamber provides the tracking of charged particles at large radii in the pseudorapidity region  $|\eta| < 1$ , giving an accurate information in the  $r - \phi$  plane for the measurement of the transverse momentum, and substantially less accurate information in the  $r - z$  plane for the measurement of the  $z$  component,  $p_z$ . The COT contains 96 sense wire layers, which are radially grouped into eight "superlayers". This can be seen from the end plate section shown in Fig. 2.9.

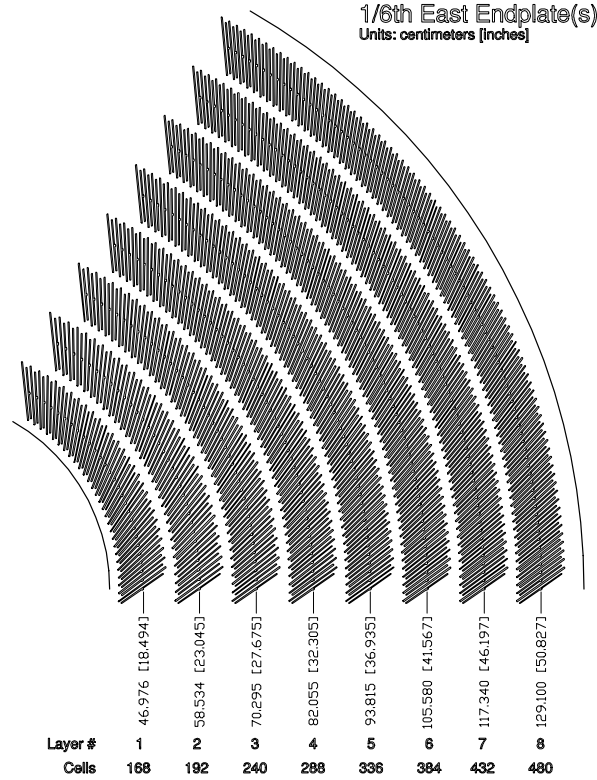


Figure 2.9: Layout of the wire planes on a COT endplate.

Each superlayer is divided into cells, and each cell contains 12 sense wires. The maximum drift distance is approximately the same for all superlayers. Therefore, the number of cells in a given superlayer scales approximately with the radius of the superlayer. The entire COT contains 30,240 sense wires spanning the entire length of the detector in  $z$ . Approximately half the wires run along  $z$  direction ("axial"). The other half are strung at a small angle ( $2^\circ$ ) with respect to the  $z$  direction ("stereo"). This allows to perform track reconstruction in the  $r - z$  plane. The active volume of the COT begins at a radius of 43.4 cm from the beamline and extends out to a radius of 132.3 cm. The chamber is 310 cm long. Particles originating from the interaction point with  $|\eta| < 1$  pass through all the 8 superlayers of the COT.

The cell layout, shown in Fig. 2.10 for superlayer 2, consists of a wire plane containing sense and potential wires (for field shaping) and a field (or cathode) sheet on

either side of the cell. Both the sense and potential wires are  $40\ \mu\text{m}$  diameter gold plated tungsten wires. The field sheet is  $6.35\ \mu\text{m}$  thick mylar with vapor-deposited gold on both sides. Each field sheet is shared with the neighboring cell.

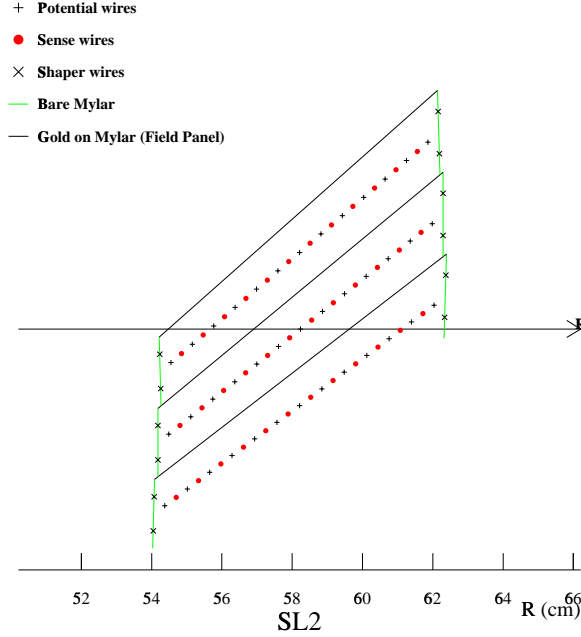


Figure 2.10: Layout of the wires in a COT cell.

The COT is filled with an Argon-Ethane gas mixture and Isopropyl alcohol (49.5:49.5:1). The gas mixture is chosen to have a constant drift velocity across the cell width. When a charged particle passes through the detector volume, the gas is ionized. Electrons drift towards the nearest sense wire. The electric field in a cylindrical system grows exponentially with decreasing radius. As a consequence, an avalanche multiplication of charge happens inside the high electric field region, in the vicinity of the wire, due to electron-atom collisions. The resulting charge reaches the wire and this so-called "hit" is read out by electronics. The avalanche discharge provides a gain of  $\sim 10^4$ . The maximum electron drift is approximately 100 ns. Due to the magnetic field electrons drift at a Lorentz angle of  $\sim 35^\circ$  with respect to the radius. The cell is tilted by  $\sim 35^\circ$  with respect to the radial direction to compensate for this effect.

Signals on the sense wires are processed by the ASDQ (Amplifier, Shaper, Discriminator with charge encoding) chip, which provides input projection, amplification, pulse shaping, baseline restoration, discrimination and charge measurement [53]. The pulse is sent through  $\sim 11$  m of micro-coaxial cable, via repeater cards to Time to Digital Converter (TDC) boards in the collision hall.

The pulse leading edge gives the arrival time information and the pulse width, in nanosecond, is related to the amount of charge collected by the wire. After calibrating

the width variations due to the COT geometry, to the path length of the associated track, to the gas gain differences for the 96 wires, the Landau associated to the track is determined, using the amount of the charge collected (in nanosecond) for each hit along the track path length. From the Landau the energy loss is measured and used for particle identification. A detailed description of the calibration is found in [54] [55]. The TDC boards contain also the buffer where the data are stored while waiting for the events to be accepted by the trigger. The TDC auxiliary card catch hits for the eXtremely Fast Tracker (XFT) track trigger processor (Section 2.8.1). Hit times are later processed by pattern recognition (tracking) software to form helical tracks. The hit resolution of the COT is about  $140 \mu\text{m}$ . The transverse momentum resolution has been measured using cosmic ray events to be:

$$\frac{\sigma_{p_T}}{p_T^2} = 0.0017 \quad [\text{GeV}/c]^{-1}. \quad (2.5)$$

The tracking algorithms reconstruct particle trajectories (helices) that best correspond to the observed hits. Reconstructed trajectories are referred to as “tracks”.

The tracks with available COT information are important for several reasons:

- they are fundamental for the trigger based on charged tracks and for the special level 2 trigger optimized for B-physics (Section 2.8) used to collect data analysed in this thesis;
- they form the basis of the TOF reconstruction to provide particle identification information for track parent particle;
- they can be used in the silicon reconstruction to match the hits in the SVX detector to the COT track trajectory;
- they, themselves, contain information about particle velocity through the measurement of the energy loss.

All the tracks that we use in the following are required to have the COT and the SVX II information.

### 2.4.3 Pattern Recognition Algorithms

As explained in the previous sections, charged particles leave small charge depositions as they pass through the tracking system. By following, or “tracking”, these depositions, pattern recognition algorithms can reconstruct the charged particle original trajectory.

There are several algorithms used to reconstruct tracks in the CDF II tracking system. Most tracks are reconstructed using “Outside-In” algorithms which will be described here. The name of this group of algorithms suggests that the track is followed from the outside of the tracking system inwards.

The track is first reconstructed using only COT information. The COT electronics reports hit time and integrated charge for every hit wire in an event. The hit time corresponds to the time when an avalanche occurred on a sense wire. The hit time can

be interpreted as the drift time of the charge in the gas, when it has been corrected for the particle time of flight. The hit time resolution is of the order of a few ns; this roughly corresponds to the average spread of the collision times. It is assumed that the collision time always happens at the same time in a cycle during a store. An average of collision times is done for many previous events and it is used as the event collision time. Hit times corrected for the collision time are interpreted as drift times and are used for pattern recognition. To perform the final track fit, an additional time of flight correction is performed assuming massless particles.

The helical track, when projected onto the  $r - \phi$  plane, is a circle. This simplifies pattern recognition, so the first step of pattern recognition in the COT looks for circular paths in the radial superlayers of the COT. Cells in the radial superlayers are searched for sets of 4 or more hits that can be fit to a straight line. These sets are called “segments”. A straight-line fit of a segment gives sufficient information to extrapolate rough measurements of curvature and  $\phi_0$ . Once segments are found, there are two approaches to track finding. One approach is to link together the segments for which the measurements of curvature and  $\phi_0$  are consistent. The other approach is to improve the curvature and  $\phi_0$  measurement of a segment reconstructed in superlayer 8 by constraining its circular fit to the beamline, and then adding hits consistent with this path. Once a circular path is found in the  $r - \phi$  plane, segments and hits in the stereo superlayers are added by their proximity to the circular fit. This results in a three-dimensional track fit. Typically, if one algorithm fails to reconstruct a track, the other algorithm will not. This results in a high track reconstruction efficiency ( $\sim 95\%$ ) in the COT for tracks which pass through all 8 superlayers ( $P_T \geq 400$  MeV/c). The track reconstruction efficiency mostly depends on how many tracks are reconstructed in the event. If there are many tracks close to each other, hits from one track can shadow hits from the other track, resulting in efficiency losses.

Once a track is reconstructed in the COT, it is extrapolated inward to the SVX-II. Based on the estimated errors on the track parameters, a three dimensional “road” is formed around the extrapolated track. Starting from the outermost layer, and working inwards, silicon clusters found inside the road are added to the track. As a cluster gets added, the road gets narrowed according to the knowledge of the updated track parameters. Reducing the width of the road reduces the chance of adding a wrong hit to the track, and also reduces the computation time. In the first pass of this algorithm,  $r - \phi$  clusters are added. In the second pass, clusters with stereo information are added to the track.

## 2.5 The Time Of Flight Detector

The Time Of Flight detector (TOF) [56] is the primary system used for K/ $\pi$  particle separation at low momenta. The TOF detector measures the time taken by the particle to travel from the collision point to the TOF system. Combining this information with the quantities measured by the COT (flight length  $L$  and particle momentum  $p$ ) one

can estimate the particle mass as

$$m = \frac{p}{c} \sqrt{\left(\frac{ct}{L}\right)^2 - 1}. \quad (2.6)$$

The TOF detector consists of 216 bars of scintillator of dimensions  $4 \times 4 \times 279 \text{ cm}^3$  forming a thin cylinder in the space available between the COT detector and the solenoid cryostat, as shown in Fig. 2.6. Bars are located at roughly equal distances in  $\phi$  at the radius of 140 cm and the full system covers the region  $|\eta| < 1$  and the entire region in  $\phi$ .

Interaction of a charged particle with the detector material is called a hit. When a charged particle traverses the scintillator material, photons are emitted, and these photons propagate towards the ends of the scintillator bar. The photo-multiplier tubes (PMTs) installed at the both ends of the bar collect the light and the front-end electronics measures the arrival time of the PMT pulse and the amount of charge collected (which is related to the number of photons produced). The physical location of the bar where the hit was registered provides the  $\phi$  location of the hit. By comparing the arrival times of the pulses at the two ends of the bar it is possible to determine the  $z$  position of the hit. The COT tracks are then extrapolated to the TOF system location to find the matches between the track trajectories and the hits in the TOF system. This associates the timing information from the TOF with the tracking information from the COT.

Fig. 2.11 shows the overview of the electronics read-out system for one TOF channel. It starts with the photo-multiplier tube where the light is collected and converted to a charge pulse. The pre-amplifier receives a nearly differential pulse from the PMT base and drives it to the discriminator. The pre-amplifier is designed to have a bilinear gain, the gain is reduced for bigger pulses which increases the dynamic range and makes it possible to measure the charges from very large pulses produced by heavy slow particles. The discriminator, which has an adjustable threshold, selects the signals to be processed by effectively filtering out the noise. After the discriminator the signal path is split and the signal is sent to the time and charge measurement circuits.

The discriminator provides a start signal to the Time-to-Amplitude Converter, or TAC, which is later stopped by the CDF common stop signal. The TAC read-out is converted into a digitized time reading by a 12-bit Analog-to-Digital Converter chip (ADC). The digitized time is buffered in the VME module called an ADMEM for the ultimate read-out by the data acquisition system. The charge measurement circuit converts the received signal into a current that is passed to a charge sensitive ADC that is also located on the ADMEM module. The primary purpose of measuring the pulse charge is to perform the correction for the variation in the timing measurement of the pulses with varying amplitudes (so called time-slewing correction).

The TOF electronics also provides the operations for configuration, monitoring, calibration and testing of the system. A more comprehensive description of the TOF front-end electronics can be found in [57]. The timing resolution of the electronic read-out itself is 20 ps and contributes very little to the overall timing resolution of the TOF detector.



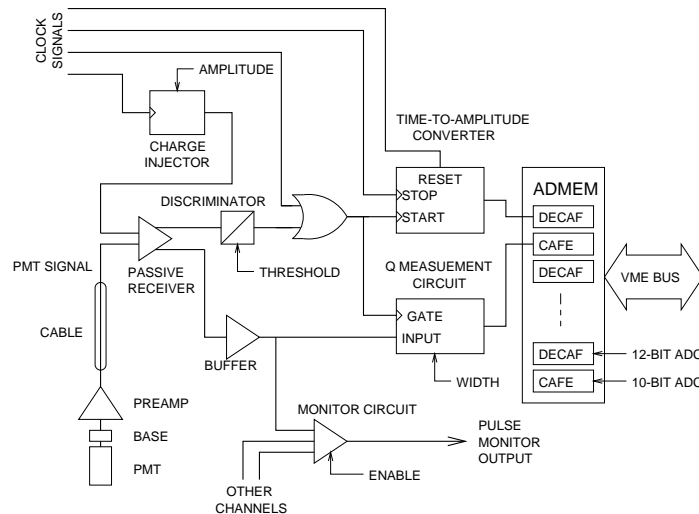


Figure 2.11: Electronic read-out chain of one TOF channel.

The TOF electronics measures the time of the PMT pulse with respect to the CDF common stop signal. In order to calculate the actual flight time of the particle, the direct measurement has to be corrected by the time it takes the photons to reach the PMTs, by the time-slewing correction, by the time it takes the signals to travel the length of the cables in the data acquisition system, and so on. The main contributions to the TOF timing resolution include physics effects such as the random variations in the number of photoelectrons in the photo-multipliers and the variations in the electron transit time inside the PMT. In addition, the variations in the shapes of the PMT pulses make impossible a precise determination of the pulse arrival time based on a threshold crossing time. The situations where more than one particle produces a hit in the scintillator bar cannot always be detected and contribute significantly to the TOF resolution. Extrapolation of the measured particle trajectories to the TOF detector is itself imprecise and also makes a contribution to the timing uncertainty. In the end, we achieve an overall time of flight timing resolution of 100-150 ps for most particles.

The expected separation power<sup>3</sup> for the various particle species that is achievable with TOF alone, assuming 100 ps for the time of flight resolution, as a function of momentum is shown in Fig. 2.12. For comparison, the expected  $K/\pi$  separation from the COT dE/dx measurement is also shown to illustrate the complementary power of COT with respect to the TOF particle identification.

Measuring the arrival times of the charged particles with respect to the CDF common stop signal is not sufficient to deduce particle masses because the time of the  $p\bar{p}$  interaction  $t_0$  with respect to the common stop signal can vary significantly from event to event<sup>4</sup>. However the combined TOF timing measurements for all the particles

<sup>3</sup>The expected separation power is defined as  $\frac{TOF_i(p) - TOF_j(p)}{\sigma_{TOF}}$ , where  $TOF_i(p) = \frac{L}{c} \sqrt{\frac{m_i^2 c^2}{p^2} + 1}$  is the expected time of flight of the  $i$  particle of mass  $m_i$  and momentum  $p$ .  $\sigma_{TOF}$  is the time of flight resolution.

<sup>4</sup>This is mostly due to the relatively large size of the protons and antiprotons bunches resulting in a long

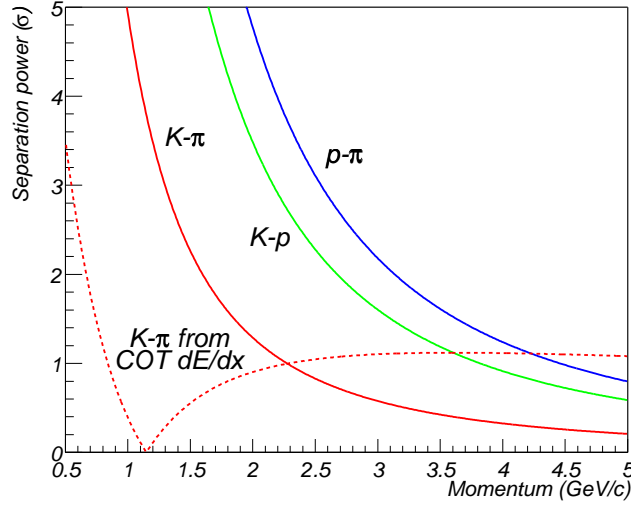


Figure 2.12: Expected separation power of the TOF particle identification. The dashed line is relative to the  $K-\pi$  separation power obtained with the COT  $dE/dx$ .

in the event can be used to estimate the value of  $t_0$  by assuming that these particles consist of known mixture of pions, kaons and protons and estimating the value of  $t_0$  that is most consistent with all the observed particles. In most events the  $t_0$  can be determined with a resolution of roughly 50 ps which is significantly smaller than the intrinsic timing resolution of the TOF measurement. In conclusion, the combination of the particle identification information deriving from the COT and TOF detectors allows to separate the particles based on their mass in almost all the momentum range relevant for B-physics at CDF.

## 2.6 The Calorimeters

Outside the solenoid, the scintillator-based calorimetry covers the region  $|\eta| < 3$  with separate electromagnetic and hadronic measurements. The CDF calorimeters have an important role in the physics program by measuring electron and photon energies, jet energies and net transverse energy flow.

Since this analysis does not use calorimetry information, this system will be described briefly. A detailed description can be found in the CDF II Technical Design Report [47].

The CDF II calorimeter has a "projective tower" geometry. This means that it is segmented in  $\eta$  and  $\phi$  "towers" pointing to the interaction region. The coverage of the calorimetry system is  $2\pi$  in  $\phi$  and  $|\eta| < 3$  in pseudorapidity.

The calorimeter consists of an electromagnetic (EM) section followed by a hadronic section. In both sections the active elements are scintillator tiles read out by wavelength

---

time window during which a  $p\bar{p}$  interaction can occur.

shifting (WLS) fibers embedded in the scintillator. The WLS fibers are spliced to clear fibers, which carry the light out to photomultiplier tubes (PMT) located on the back plane of each endplug.

The EM calorimeter is a lead/scintillator sampling device with a unit layer composed of 4.5 mm lead and 4 mm scintillator. There are 23 layers in depth for a total thickness of about  $21 X_0$  (radiation lengths) at normal incidence. The energy resolution of the EM section is approximately  $16\%/\sqrt{E}$  with a 1% constant term.

The hadron calorimeter is a 23 layer iron and scintillator sampling device with a unit layer composed of 2 inch iron and 6 mm scintillator.

## 2.7 The Muon detector

Muons are particles which interact with matter only by ionization. For the energies typical of this experiment, they do not cause showers in the electromagnetic or hadronic calorimeters. As a result, if a muon is produced and it has enough momentum, it will pass through the calorimeter with minimal interaction with the internal material. Therefore, the calorimeter can be considered as a filter which retains particles that shower when interacting with matter. Muon detection systems are therefore placed outside the calorimeters.

The CDF II Detector has four independent muon systems: the Central Muon Detector (CMU), the Central Muon Upgrade Detector (CMP), the Central Muon Extension Detector (CMX) and the Intermediate Muon Detector (IMU) [58]. The CMU and the CMP detectors are made of drift cells, and the CMX detector is made of drift cells and scintillation counters, used to reject background based on timing information. Using the timing information from the drift cells of the muon systems, short tracks (called "stubs") are reconstructed. Tracks reconstructed in the COT are extrapolated to the muon systems. Based on the track trajectory extrapolated to the muon system, the estimated errors on the tracking parameters and the position of the muon stub, a  $\chi^2$  value of the track-stub match is computed. To ensure good muon quality, an upper limit is placed on the value of  $\chi_\phi^2$ , the  $\chi^2$  of the track-stub match in the  $\phi$  coordinate.

Most particles passing through the calorimeter without showering are muons, but this is also possible for pions or kaons. These particles can then fake muon signals in the muon chambers. Typically, these fake rates are at the percent level.

## 2.8 The Trigger

The trigger plays an important role in a detector at a  $p\bar{p}$  collider, as the Tevatron, for two main reasons. First, the collision rate is about 2.5 MHz, which is much higher than the rate at which CDF data can be stored on tape, 100 Hz. Second, the total hadronic cross section (including the elastic, inelastic, and diffractive processes) is about 100 mb while interesting physics signals have a much lower cross-section. The  $b\bar{b}$  cross-section, as an example, is about 1000 times smaller, 0.1 mb. Even if the bandwidth to write on tape would be much larger, extracting online the most interesting physics events from the large number of normal events would be required to reduce the cost and the time

necessary to reconstruct data.

This is achieved by the pipelined data acquisition system and the three level trigger of CDF II that is shown in Fig. 2.13.

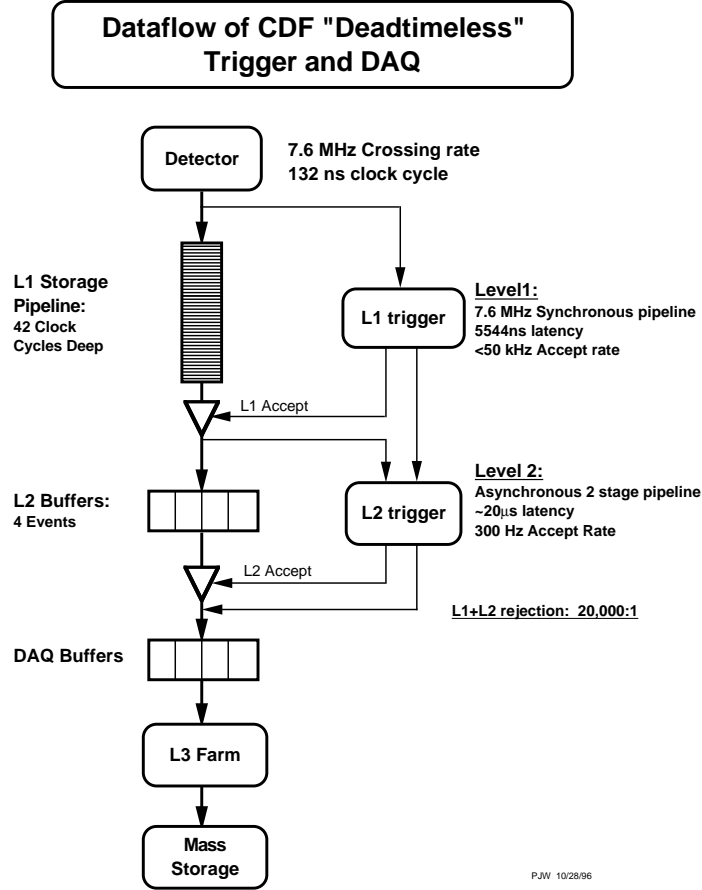


Figure 2.13: Diagram of the CDF II trigger architecture.

With this architecture the global trigger decision is performed in several steps. Each level provides a rate reduction sufficient to allow processing in the next level. Each level performs selection reconstructing physics quantities with increasing resolution than the preceding. The typical rates of events accepted by each trigger level are reported in Table 2.2<sup>5</sup>.

The Level 1 trigger (L1) is organized as a synchronous pipeline that processes events at the bunch crossing rate and takes trigger decision within a latency of  $5.5 \mu\text{s}$ . For every event all the detectors store the data in a 42 stage pipeline and send them to the L1. After 42 Bunch Crossings the L1 takes the decision on the event. Upon a L1 trigger accept, the data on each front-end card are transferred to one of four local Level 2 (L2) buffers. The L2 performs a more accurate analysis of the event in few tens of

<sup>5</sup>The table is relative to the rate at the moment of the collection of the first  $360 \text{ pb}^{-1}$  of data. With recent upgrades we obtain a Level 1 Accept of 30 kHz, and a Level 2 Accept of 900 Hz.

Level 1 Accept	25 kHz
Level 2 Accept	350 Hz
Event Builder	75 MB/s
Level 3 Accept	80 Hz
Rate of Storage	20 MB/s

Table 2.2: Rate of events accepted by each trigger level. The bandwidth accepted by the Event Builder and the Data-Logging systems are also reported.

microseconds.

Data relative to events that satisfy L2 requirements, are read out by the EEvent Builder (EVB) [59] system and are stored in the DAQ buffers. There, the event fragments obtained from different subsystem are organized into a properly ordered sequence, flagged with the event number and fed to the computing farm which performs the Level 3 functions. The EVB is able to process 75 MB/s of data.

Fig. 2.14 shows the block diagram of the CDF II trigger system with the Level 1 and Level 2 subsystem along with their interconnections. The structure of both L1 and L2 are similar. Physical objects are reconstructed by the subprocessors, which feed data to the global decision hardware, which combines this information and takes the trigger decision. The eXtremely Fast Tracker (XFT), at Level 1, and the Silicon Vertex Tracker (SVT), at Level 2, provide tracking information fundamental to reject background events.

The third trigger level (L3) [59] is a farm of parallel processors, each fully analyzing a single event running off-line reconstruction code on it. The L3 uses the full detector resolution to reconstruct the whole event. The L3 performs a three dimensional reconstruction of all the tracks and vertices. Events are selected by repeating the L2 selections on the better reconstructed quantities.

Events accepted by the L3 are sent by the Data-Logging to mass storage and to online monitoring processes to verify that the detector, trigger and data acquisition systems are functioning correctly. The output rate of the third level is approximately 80 Hz.

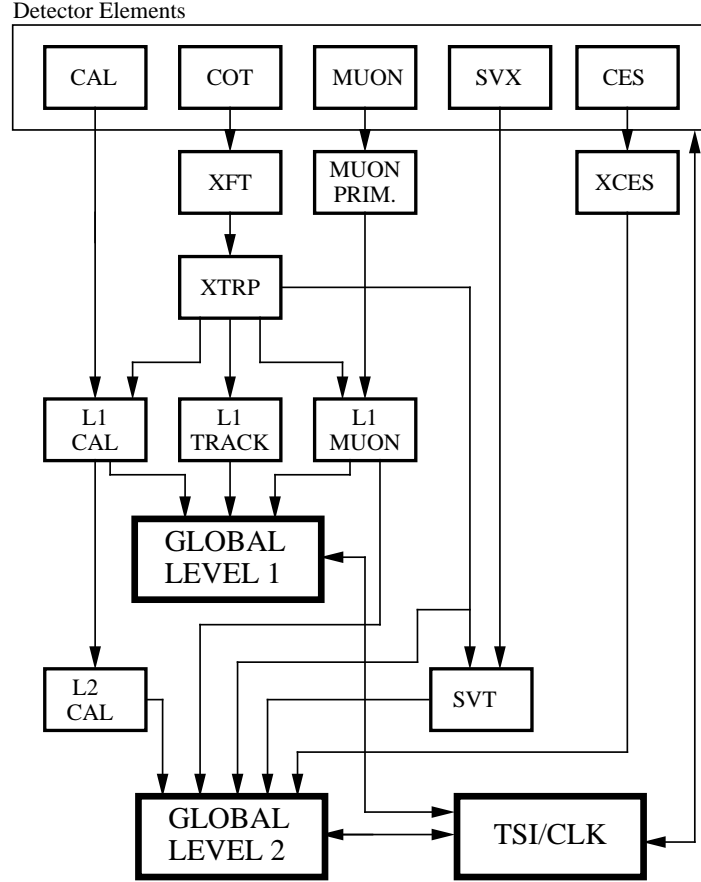
A detailed description of the CDF trigger system can be found in [60]. In the following we will describe the three trigger levels.

### 2.8.1 Level 1 trigger

The Level 1 consists of three parallel synchronous processing streams. The first stream finds calorimeter based objects, the second one finds muons, while the third one finds tracks in the COT. Up to 64 different triggers can be formed using simple ANDs and ORs of objects from these streams.

The eXtremely Fast Tracker (XFT) identifies tracks with  $p_T$  of the order of 1.5 GeV/c in the  $r - \phi$  view using the information provided by four axial superlayers of the COT. As mentioned earlier, the superlayers are arranged in cells of 12 wires each,

## **RUN II TRIGGER SYSTEM**



PJW 9/23/96

Figure 2.14: Functional block diagram of the CDF II first and second level triggers.

oriented at an angle of  $\sim 35^\circ$  relative to the radial direction. There are a total of 16,128 axial wires, and the hits on each wire are classified as prompt or delayed, for a total of 32,256 bits of information. A charged track passing through an axial superlayer will generate a maximum of 12 "hits" of prompt or delayed hits. The definition of a prompt or a delayed hit will depend upon the maximum drift time in the COT. For a bunch spacing of 396 ns, the maximum drift time is  $\sim 121$  ns, and so a prompt hit occurs whenever there is a hit in the time window 0-44 ns, and a delayed hit is defined as a hit falling in the window 44-121 ns.

Track identification is accomplished in two processes by the Finder and the Linker boards. The Finder searches for high  $p_T$  track segments in each of the four axial superlayers of the Central Tracker. The Linker searches for a four-out-of-four match

among segments in the 4 layers, consistent with a prompt high- $p_T$  track. If no track is found, the Linker searches for a three-out-of-three match among segments in the innermost 3 layers.

Using this algorithm the track  $p_T$  and  $\phi$  are measured with a resolution of  $0.0174 p_T^2$  GeV/c and 6 mrad, respectively.

Transition modules drive found track information from the Linker modules to the XTRP (eXTRaPolation unit) system, which extrapolate the tracks to the calorimeter and the muon chambers, applies trigger momentum thresholds and distributes the track data to the Level 1 and Level 2 trigger system.

### 2.8.2 Level 2 trigger

The Level 2 trigger consists of several asynchronous subsystems which provide input data to the Global Level 2 crate that evaluates whether any of the L2 triggers is satisfied.

Processing for a L2 trigger decision starts after the event is written into one of the four L2 buffers on all front-end and trigger modules by a L1 accept. While L2 is analyzing the event that buffer cannot be used to store additional L1 accepts.

Data are collected from the L2 buffers of the Level 1 trigger systems (XFT and L1 MUON) and from the calorimeter shower maximum detector (XCES). Simultaneously a hardware cluster finder (L2CAL) processes the calorimeter data and SVT (Silicon Vertex Tracker) [61] [62], described in the next Section, finds tracks in SVX-II.

Once the objects are available, the Global Level 2 processes the data and takes the decision.

#### The Online Silicon Vertex Tracker (SVT)

The Online Silicon Vertex Tracker (SVT) is part of the Level 2 trigger. It receives the list of the COT tracks reconstructed by the XFT processor (for each track the curvature  $C$  and the azimuthal angle  $\phi$  are measured) and the digitized pulse heights on the silicon layers ( $10^5$  channels). The SVT links the XFT tracks to the silicon hits and reconstructs tracks with offline-like quality. The resolution of the SVT is  $\delta\phi \simeq 1$  mrad,  $\delta p_T \simeq 0.003 \cdot p_T^2$  GeV/c and  $\delta d \simeq 35 \mu\text{m}$ , where  $d$  is the track impact parameter, the distance of closest approach of the particle trajectory helix to the z-axis of the CDF reference system.

By providing a precise measurement of the impact parameter of charged particle tracks, SVT allows triggering on events containing long lived particles. B hadrons in particular have a decay length of the order of  $500 \mu\text{m}$  and tracks which come out of the B decay vertices have an impact parameter on average greater than  $100 \mu\text{m}$ . The opportunity offered by the SVT of triggering directly on B hadron decay vertices is available for the first time at a hadron collider.

The SVT has a widely parallelized design: it is made of 12 identical slices ("wedges") working in parallel. Each wedge receives and processes data only from tracks in the plane perpendicular to the beamline (stereo info from SVX II is dropped) and only with  $p_T$  above 2 GeV/c.

The tracking process is performed in two steps:

- Pattern recognition: candidate tracks are searched among a list of precalculated low resolution patterns ("roads");
- Track fitting: a full resolution fit of the hit coordinates found within each road is performed using a linearized algorithm.

The pattern recognition step is performed in a completely parallel way by the Associative Memory (AM) system which uses full custom VLSI chips (AMchips [63]). The AM system compares all the silicon clusters and XFT tracks with the set of precalculated patterns. A pattern is defined as a combination of six bins ("SuperStrips"): five SuperStrips correspond to the position coordinates of the particle trajectory on five silicon layers, which can be chosen among the five SVX II layers, the sixth SuperStrip corresponds to the azimuthal angle of the particle trajectory at a distance of 12 cm from the beam line. The output of AM system is the list of patterns ("roads") for which at least one hit has been found on each SuperStrip. Each SVT wedge uses 32K patterns which cover more than 95% of the phase space for  $p_T \geq 2$  GeV/c.

The track fitting method is based on linear approximations and principal components analysis [64].

Figure 2.15 shows the SVT track impact parameter resolution for tracks with  $p_T > 2$  GeV/c. The width of the Gaussian fit for the distribution in Fig. 2.15 is  $55 \mu\text{m}$ . This is a combination of the intrinsic SVT impact parameter resolution, and the transverse size of the beam line:  $\sigma_{fit} = \sigma_{SVT} \oplus \sigma_{beam}$ , where  $\sigma_{beam}$  is about  $30 \mu\text{m}$ . Therefore, the intrinsic SVT resolution is about  $35 \mu\text{m}$ .

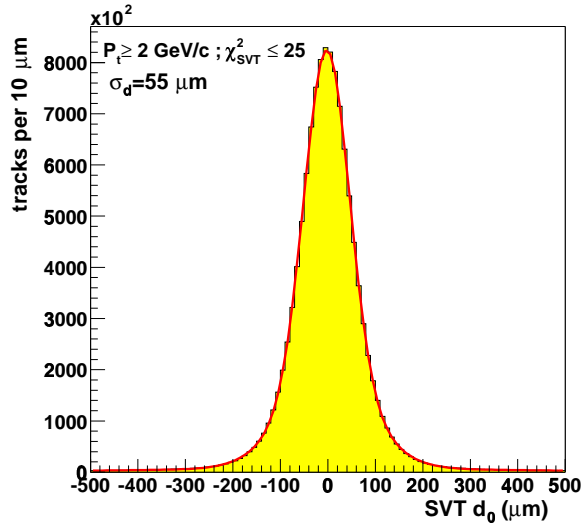


Figure 2.15: Impact parameter resolution of the SVT track.

For the first time at an Hadron Collider, thanks to SVT, it is possible to trigger directly on hadronic B decay vertices.



### 2.8.3 Level 3 trigger

The third level of the CDF trigger is implemented on a PC farm. Every CPU in the farm provides a processing slot for one event. With roughly 300 CPUs, and an input rate of  $\sim 300$  Hz, this allocates approximately 1 second to perform event reconstruction and take a trigger decision.

Fig. 2.16 shows the implementation of the Level 3 farm. The detector readout from the Level 2 buffers is received via an Asynchronous Transfer Mode (ATM) switch and distributed to 16 “converter” node PCs, shown in Fig. 2.16 in light blue. The main task of these nodes is to assemble all the pieces of the same event as they are delivered from different subdetectors through the ATM switch. The event is then passed via an ethernet connection to a “processor” node. There are about 150 nodes in the farm as shown in Fig. 2.16. Each processor node is a separate dual-processor PC. Each of the two CPUs on the node processes a single event at a time. The Level 3 decision is based on near-final quality reconstruction performed by a “filter” executable. If the executable decides to accept an event, it is then passed to the “output” nodes of the farm. These nodes send the event onward to the Consumer Server/Data Logger (CSL) system for storage first on disk, and later on tape.

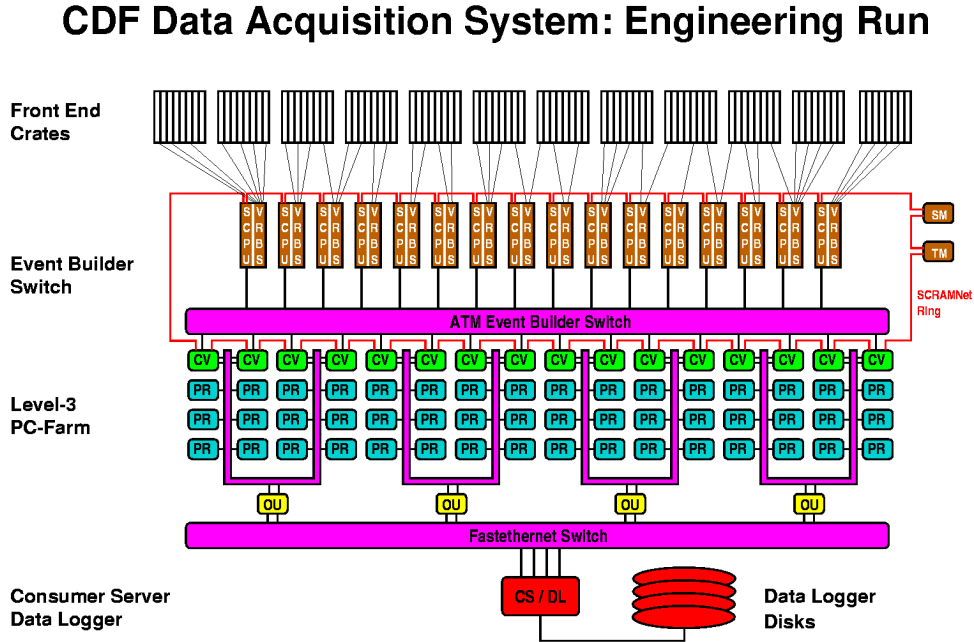


Figure 2.16: Principle of Event Building and Level 3 Filtering. Data from the front end crates is prepared by Scanner CPUs (SCPU) and fed into the ATM switch. On the other side of the switch, converter nodes (CV) assemble events and pass them to processor nodes (PR). Accepted events are passed to output nodes (OU) which send them to the Consumer Server and Data Logging system (CS/DL).

### 2.8.4 Organization of a Trigger Table

The trigger system described above is able to use the information of quite any detector subsystem. Combining all the measurements of the various subsystems it is possible to efficiently record, at the same time, events characterized by different signatures. Indeed the data collected by CDF II can be used to study the properties of the top quark and weak bosons as well as the decays of b and c hadrons, or to search evidence of physics beyond the Standard Model.

Each signature requires certain selections at each trigger level, to efficiently collect the data. The combination of these selections define a Trigger Path.

All the Trigger Paths are listed in the Trigger Table. The Trigger Table is organized in such a way that the rates at each level don't exceed the limits listed in table 2.2.

### 2.8.5 The Two Track Trigger Path (TTT)

In the following we will describe the TTT trigger path used for the analysis described in this Thesis. The term Two Track Trigger (TTT) is used within CDF to indicate two kind of triggers that require at least two charged tracks in the event, with some kinematical constraint that we are going to describe in the following. These triggers are able to extract fully hadronic decays from a large background of tracks, just using the tracks reconstructed by SVT. The two triggers differ by the fact that one is meant to collect two-body decays, like  $B_s^0 \rightarrow h^+ h'^-$  (B\_PIPi), while the other is sensitive to multi-body decays, like  $B^+ \bar{D}^0 \pi^+ \rightarrow [K^+ \pi^-] \pi^+$  (B\_CHARM).

### 2.8.6 The Two Track Trigger selection

#### Level 1

The Level 1 selections are common to the B\_CHARM and B\_PIPi trigger paths. At least two XFT tracks with opposite charge are required in the event. The minimum transverse momenta of the tracks have to be higher than 2.04 GeV/c and their scalar sum has to be greater than 5.5 GeV/c. Finally the azimuthal opening angle between them, calculated at the radial distance of the COT superlayer 6 ( $R = 105.575$  cm),  $\Delta\phi_6^6$ , must be  $0 \leq \Delta\phi_6 \leq 135^\circ$ .

#### Level 2

At Level 2 the B\_PIPi and B\_CHARM are splitted. Both trigger paths require two SVT tracks with opposite charge. Then the kinematical cuts are different because for the B\_CHARM path, the events are not fully reconstructed by the trigger. The cuts relative to the two trigger path are reported in table 2.3.

The impact parameter ( $d_{CV}$ ) and transverse decay length ( $L_{xy}$ ) of the B candidate vertex are calculated starting from the parameters of the two SVT tracks using the

---

<sup>6</sup> $\phi_6$  is the azimuthal angle of the tracks measured at the COT superlayer 6. It is related to  $\phi_0$  by the relation:  $\phi_6 = \phi_0 + \sin^{-1}(r \cdot C)$ , where  $r = 105.575$  and  $C$  is the track's curvature.

Cuts	B_PIP1	B_CHARM
$Min(p_T) \geq$	2 GeV/c	2 GeV/c
$p_{T1} + p_{T2} \geq$	5.5 GeV/c	5.5 GeV/c
$\Delta\phi_0 \geq$	20°	2°
$\Delta\phi_0 \leq$	135°	90°
$ d_0  \geq$	100 $\mu\text{m}$	120 $\mu\text{m}$
$ d_0  \leq$	1 mm	1 mm
$ L_{xy}  \geq$	200 $\mu\text{m}$	-
$L_{xy} \geq$	-	200 $\mu\text{m}$
$ d_{CV}  \leq$	140 $\mu\text{m}$	-

Table 2.3: Level 2 cuts applied by the B\_PIP1 and B\_CHARM triggers.  $d_0$  is the impact parameter of the track.  $d_{CV}$  and  $L_{xy}$  are respectively the impact parameter and transverse decay length of the candidate vertex. They are calculated starting from the quantities measured by SVT as described in the text.

following equations:

$$p_x = p_{T1} \cos \phi_1 + p_{T2} \cos \phi_2 \quad p_y = p_{T1} \sin \phi_1 + p_{T2} \sin \phi_2 \quad (2.7)$$

so, the flight direction of the B candidate vertex is given by:

$$\cos \phi_V = \frac{p_x}{p_T} \quad \sin \phi_V = \frac{p_y}{p_T}, \quad (2.8)$$

where

$$p_T = \sqrt{p_x^2 + p_y^2} \quad (2.9)$$

and the coordinates of the B candidate vertex are

$$x_V = \frac{d_1 \cos \phi_2 - d_2 \cos \phi_1}{\cos \phi_1 \sin \phi_2 - \cos \phi_2 \sin \phi_1} \quad y_V = \frac{d_1 \sin \phi_2 - d_2 \sin \phi_1}{\cos \phi_1 \sin \phi_2 - \cos \phi_2 \sin \phi_1} \quad (2.10)$$

therefore

$$L_{xy} = \frac{x_V \cdot p_x + y_V \cdot p_y}{p_T} \quad d_{CV} = x_V \sin \phi_V - y_V \cos \phi_V. \quad (2.11)$$

### Level 3

The third trigger level performs selection on tracks that are reconstructed using the offline algorithm and matched to SVT tracks. The matching is done in  $\phi$  and curvature. The tolerances are respectively 15 mrad and  $1.5 \times 10^{-4} \text{ cm}^{-1}$ . The same cuts as in Level 2 are performed on hybrid tracks. The cut on the impact parameter requires the knowledge of the exact beam position. Within CDF the most accurate online measurement of the beam position, in each barrel, is provided by SVT. The Level 3

calculates the impact parameter transverse to the three dimensional beam position, which is calculated starting from the SVT measurement.

Level 3 applies a fiducial geometric cut on the tracks pseudo-rapidity:  $|\eta_{1,2}| \leq 1.2$ . In the B.PIPI a cut on the reconstructed invariant mass of the track pairs assigning the  $\pi$  mass to both tracks is applied as well:  $4 \text{ GeV}/c^2 \leq M_{\pi\pi} \leq 7 \text{ GeV}/c^2$ . There is not an analogous cut for B.CHARM because the events are not fully reconstructed by the trigger.

## 2.9 Standard data processing

The events accepted by the trigger and stored to tape are not optimal for physics analysis because the up-to-date calibrations of the detectors are usually not available for online event reconstruction. CDF uses a standard software package called "Production" for final quality reconstruction of the data. The Production gives the highest precision measurement of physical quantities (based on the best available detector calibrations, beam-line position measurements and so on) and separates the data into different datasets based on the different trigger-paths that accepted events. In our case, for example, we have two different datasets, one for the events that passed the B.CHARM trigger and one for the events that passed the B.PIPI trigger. Each dataset can have more secondary datasets corresponding to different data periods.

## 2.10 Luminosity Measurement

At hadron collider experiments the beam luminosity can be measured using the inelastic  $p\bar{p}$  scattering. It has a large cross section,  $\sigma_{in} \sim 60 \text{ mb}$ . The rate of inelastic  $p\bar{p}$  interactions is given by:

$$\mu \cdot f_{bc} = \sigma_{in} \cdot L, \quad (2.12)$$

where  $L$  is the instantaneous luminosity,  $f_{bc}$  is the rate of bunch crossings in the Tevatron and  $\mu$  is the average number of  $p\bar{p}$  interactions per bunch crossing.

To detect inelastic  $p\bar{p}$  events efficiently a dedicated detector at small angles, operating at high rate and occupancy, is required. The Cherenkov Luminosity Counters (CLC) have been designed to measure  $\mu$  accurately (within a few percent) all the way up to the high luminosity regime  $L \sim 3 \times 10^{32} \text{ cm}^{-2} \text{ s}^{-1}$ . The CLC modules and the luminosity measurement method are described in detail in [45].

There are two CLC modules in the CDF detector, installed at small angles in the proton (East) and antiproton (West) directions with pseudorapidity coverage between 3.75 and 4.75. Each module consists of 48 thin, long, gas-filled, Cherenkov counters. The counters are arranged around the beam pipe in three concentric layers, with 16 counters each, and pointing to the center of the interaction region. The cones in the two outer layers are about 180 cm long and the inner layer counters (closer to the beam pipe) have a length of 110 cm. The Cherenkov light is detected with fast, 2.5 cm diameter, photomultiplier tubes. The tubes have a concave-convex, 1 mm thick,

quartz window for efficient collection of the ultraviolet part of Cherenkov spectrum and operate at a gain of  $2 \cdot 10^5$ .

The counters are mounted inside a thin pressure vessel made of aluminum and filled with isobutane. The Cherenkov angle is  $3.1^\circ$  and the momentum threshold for light emission is 9.3 MeV/c for electrons and 2.6 GeV/c for pions.

The number of  $p\bar{p}$  interactions in a bunch crossing follows a Poisson distribution with mean  $\mu$ , where the probability of empty crossing is given by  $P_0(\mu) = e^{-\mu}$ . An empty crossing is observed when there are fewer than two tubes with signal above threshold in either module of the CLC. The measured fraction of empty bunch crossings is corrected for the CLC acceptance and the value of  $\mu$  is calculated. The measured value of  $\mu$  is combined with the inelastic  $p\bar{p}$  cross section to determine the instantaneous luminosity using (2.12).

The CLC has been one of the upgrades of the CDF II Detector. It provides an improved measurement of the luminosity with respect to the Run I device. The luminosity measured by the CLC is used to monitor the Tevatron performance.



## Chapter 3

# Combined Particle Identification

The CDF II detector provides two independent measurements used for charged particle identification. The first one is the  $dE/dx$  measurement performed by the central outer tracker (COT); the second one is the measurement of the time of flight with the TOF detector.

In this chapter we describe how to combine TOF and  $dE/dx$  measurements in a single optimized quantity, used to determine, in a statistical approach, the ID (where ID can be proton, kaon, pion, muon or electron) of one or more charged tracks in the same event.

The Particle IDentification (PID) tools have been developed in two different cases:

1. Single track case (Section 3.5.1). Useful when the user wants distinguish a particle (signal) from others different particles (background). For example, muons from a background of pions and kaons.
2. Two or more tracks case (Section 3.5.3). Useful when the user wants distinguish a decay into  $n$ -charged particles with defined masses from a background of  $n$ -tracks with different masses, in the same event. As example of track pairs case, the  $\phi \rightarrow K^+ K^-$  decay from a background of  $\pi\pi$ ,  $\pi K$ ,  $\pi p$ ,  $pK$  and  $pp$ .

The performance of a PID tool are characterize by:

- the experimental separation power, that is the capability to distinguish a particle from another particle, for example a pion from a kaon, this is mainly related to detector performance;
- the ability, in the “multiple track” case, to correctly take into account the PID-correlations between particles in the same event. This item is very important because, neglecting these correlations, it can produce a bias in the result of a Likelihood fit, making use of PID information.

In Fig. 2.12 of Section 2.5 was shown the expected separation power  $K$ - $\pi$  separately for TOF and  $dE/dx$  assuming known values of TOF resolution ( $\sigma_{TOF} \sim 100$  ps) and  $dE/dx$  resolution ( $\sigma_{dE/dx} \sim 1.5$  ns). In this chapter (Section 3.5.1), we describe the measurement of the experimental separation power  $K$ - $\pi$  and  $p$ - $\pi$ , combining the PID

measurements (dE/dx and TOF) in a single optimized quantity. In particular, we measured a very good separation in all the momentum range, reaching a  $\pi$ -K separation of at least  $1.5 \sigma$  and a p- $\pi$  separation of at least  $2.4 \sigma$  for track momenta up to 5 GeV, with larger values in the lower momentum range.

In Fig. 3.1 the K- $\pi$ <sup>1</sup> separation power as a function of the momentum of the particle is shown. The black curve represents the TOF separation, the red one the dE/dx separation and the blue one represents the combined PID (TOF+dE/dx) separation. The procedure used to obtain this plot is described in Section 3.5.1.

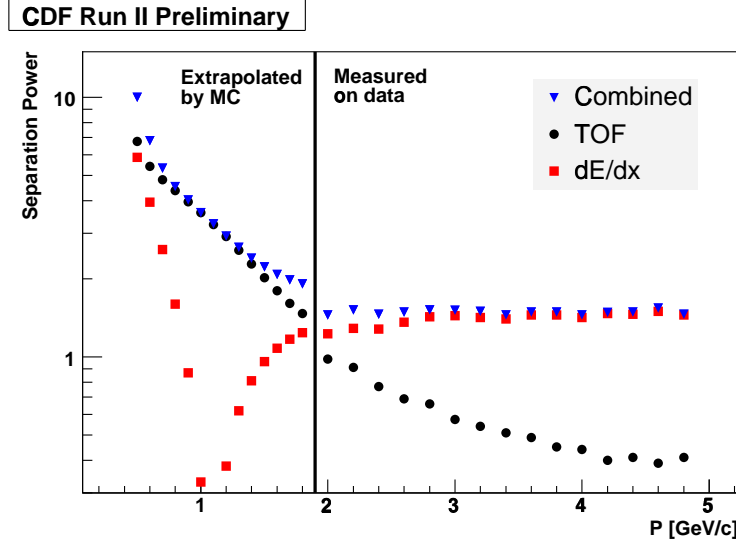


Figure 3.1: K- $\pi$  separation power vs momentum. Black: TOF separation. Red: dE/dx separation. Blue: combined PID (TOF+dE/dx) separation.

In this chapter we also describe:

- the data sample used for the PID parameterization (Section 3.1);
- the parameterization of the TOF and dE/dx distributions: particle residuals and correlation distributions (Section 3.3);
- the treatment of the systematic uncertainty on a measurement making use of PID (Section 3.4).

We implemented a public code for CDF II users containing all the PID functions [65]: Likelihoods for single track and track pairs, for TOF, dE/dx and Combined PID, that can be used to make cuts or to perform Likelihood fits to distinguish particles or decay modes. In the code is also implemented the treatment of systematics.

Finally, in Section 3.6, the most important CDF II analysis that use the Combined Particle IDentification are briefly described.

<sup>1</sup>The achievable experimental separation power K- $\pi$  is the fundamental ingredient for the measurement described in this thesis.



### 3.1 Data sample used for PID studies

In this section, the selection of a pure samples of  $D^0 \rightarrow K^- \pi^+$  and of  $\Lambda \rightarrow p \pi^-$  decays is described.

We reconstructed a signal of  $D^{*+} \rightarrow D^0 \pi_s^+ \rightarrow [K^- \pi^+] \pi_s^+$  (and charge conjugate) decays. This sample has been collected by the B\_CHARM trigger path described in Section 2.8.5. The good run requirements are applied. The excluded runs were marked bad by the CDF data Quality Monitoring Group, for either known detectors problems (i.e. SVX, COT) or trigger problems (XFT, SVT). This data correspond to an integrated luminosity of  $360 \text{ pb}^{-1}$ .

Two tracks  $D^0$  candidates are picked requiring the combinations to be neutral in charge. The trigger confirmation has been performed by requiring K and  $\pi$  from the  $D^0$  candidate to match the SVT track. This means that K and  $\pi$  have transverse momentum higher than 2 GeV/c and impact parameter such as  $120 \text{ } \mu\text{m} < |d_0| < 1 \text{ mm}$ , as described in Section 2.8.2. The reconstructed  $D^0$  candidates are then combined with a third soft pion track to reconstruct the final  $D^{*+} \rightarrow D^0 \pi_s^+$  candidate. The sign of the soft pion  $\pi_s$  tags the flavor of the  $D^0$  and hence the identity of its decay products. Some cuts have been applied in order to purify the  $D^0$  signal [66]:

- Difference between the mass of  $D^{*+}$  and  $D^0$ :  $M(K\pi\pi_s) - M(K\pi) < 0.147 \text{ GeV}/c^2$ ;
- $D^0$  decay lenght:  $L_{xy}(D^0) > 300 \text{ } \mu\text{m}$ ;
- $D^0$  transverse momentum:  $p_T(D^0) > 5.5 \text{ GeV}/c$ ;
- $D^0$  impact parameter:  $I.P.(D^0) < 140 \text{ } \mu\text{m}$ ;
- product between the impact parameters of the  $D^0$  daughters:  $d_0(K) \times d_0(\pi) < 0 \text{ } \mu\text{m}^2$ .

As shown in Fig. 3.2, where the difference between the invariant mass of  $D^{*+}$  and  $D^0$  ( $M(K\pi\pi_s) - M(K\pi)$ ) is reported, a lot of background is removed requiring  $M(K\pi\pi_s) - M(K\pi) < 0.147 \text{ GeV}/c^2$ .

In Fig. 3.3 the  $D^0$  invariant mass distribution of the selected sample is reported. We obtained  $\sim 760,000$   $D^0$  with a  $\frac{S}{B} \sim 64$ .

We also reconstructed a signal of  $\Lambda \rightarrow p \pi^-$  (and charge conjugate) decays in  $360 \text{ pb}^{-1}$ . This sample has been collected by the B\_PIPi trigger path described in Section 2.8.5 and the good run requirements are applied.

Track pairs which make the  $\Lambda$  candidate must pass the following cuts:

- Sum of transverse momenta:  $|P_{t1}| + |P_{t2}| > 1.1 \text{ GeV}/c$ ;
- Difference between the two  $z$  coordinates:  $|z_{01} - z_{02}| < 2 \text{ cm}$ ;
- Bidimensional vertex quality  $\chi^2$ :  $\chi^2 \text{ vertex}_{2D} < 10$ ;
- $\Lambda$  decay lenght:  $L_{xy} > 0.5 \text{ cm}$ ;

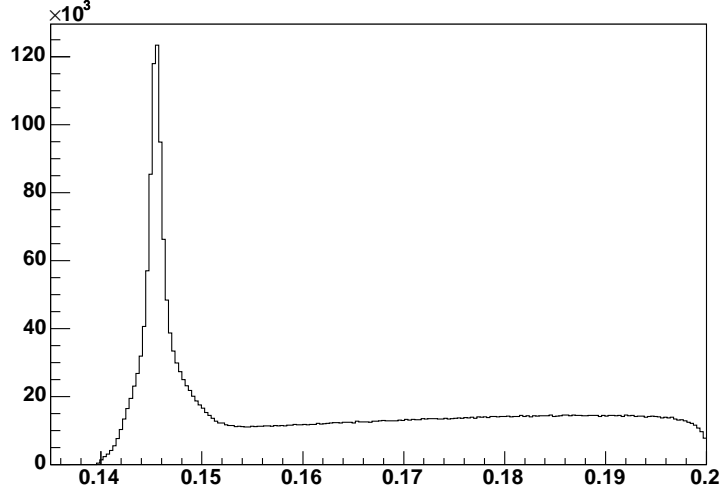


Figure 3.2: Difference between the  $D^{*+}$  mass and the  $D^0$  mass ( $M(K\pi\pi_s) - M(K\pi)$ ).

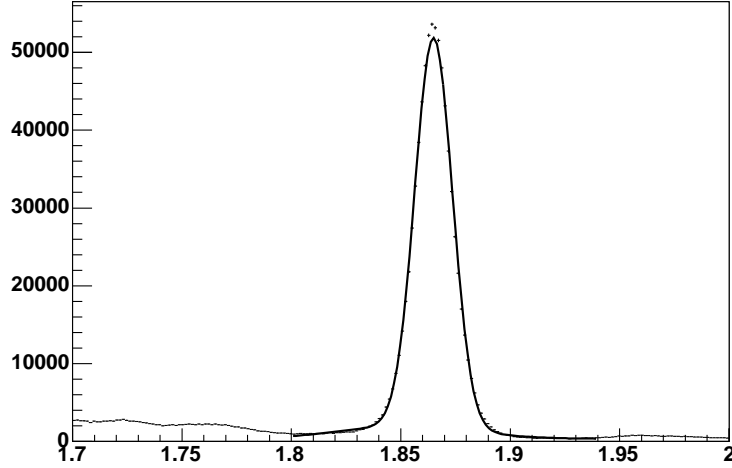


Figure 3.3:  $D^0 \rightarrow \pi^+ K^-$  invariant mass distribution. We obtained  $\sim 760,000$   $D^0$ , with  $\frac{S}{B} \sim 64$ .

- $0.1 \text{ GeV}/c^2 < M_{\pi\pi} < 1.5 \text{ GeV}/c^2$  ( $M_{\pi\pi}$  is the invariant mass of the track pair assuming that both tracks are pions).

In addition to purify the signal some additional cuts, obtained through an optimization procedure [67], are applied:

- A harder cut on the  $\Lambda$  decay length:  $L_{xy}(\Lambda) > 0.85 \text{ cm}$ ;

- $\Lambda$  impact parameter:  $|I.P.(\Lambda)| < 0.007$  cm;
- A cut on a variable (win) relative to the correlation between the proton and the pion impact parameters:  $\text{win} < 0.0051$  cm;

In Fig. 3.4 the  $\Lambda \rightarrow p\pi^-$  invariant mass distribution of the selected sample is reported. We obtained  $\sim 120,000$   $\Lambda$  with a  $\frac{S}{B} \sim 9$ .

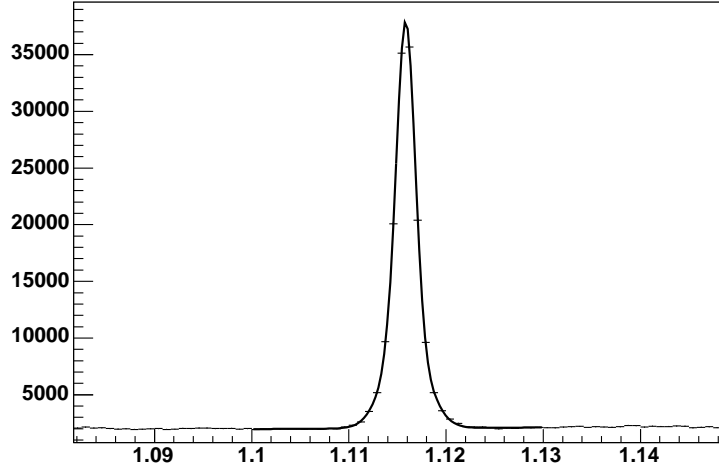


Figure 3.4:  $\Lambda \rightarrow p\pi^-$  invariant mass distributions. We obtained  $\sim 120,000$   $\Lambda$ , with  $\frac{S}{B} \sim 9$ .

### 3.2 Method to combine PID: ingredients and recipes

Before describing the used method to combine PID measurements, we need to define some quantities that will be largely used in this Chapter.

First of all, the  $dE/dx$  and TOF residuals.

The  $dE/dx$  and TOF residuals of a particle ("part" can be  $\pi$ , K, p, e,  $\mu$ ) are defined respectively as:

$$\frac{dE^{part}}{dx_{Res}} = \frac{dE}{dx_{measured}} - \frac{dE^{part}}{dx_{expected}} \quad (3.1)$$

$$TOF_{Res}^{part} = TOF_{measured} - TOF_{expected}^{part} \quad (3.2)$$

The  $\frac{dE^{part}}{dx_{expected}}$  is known from the experimental determination of the Universal curve ( $dE/dx$  as a function of  $\beta\gamma^2$ ). In Fig. 3.5 [68] is shown the experimental  $dE/dx$  as a

---

<sup>2</sup> $\gamma = \frac{1}{\sqrt{1-\beta^2}}$

function of  $\beta\gamma$  for positive (on the left) and negative (on the right) tracks, obtained using very pure samples of electrons from  $\gamma$  conversion, muons from  $J/\Psi \rightarrow \mu\mu$ , kaons and pions from  $D^{*+} \rightarrow D^0\pi^+$  with  $D^0 \rightarrow K^-\pi^+$ , and protons from  $\Lambda \rightarrow p\pi^-$  decays. The fit on the experimental data (continuous line in Fig. 3.5) gives the Universal expected curve for positive and negative tracks. Making a change of variable ( $\beta\gamma m_{part} = p$ ), we obtain the expected  $dE/dx$  of each particle (of mass  $m$ ) as a function of the momentum.

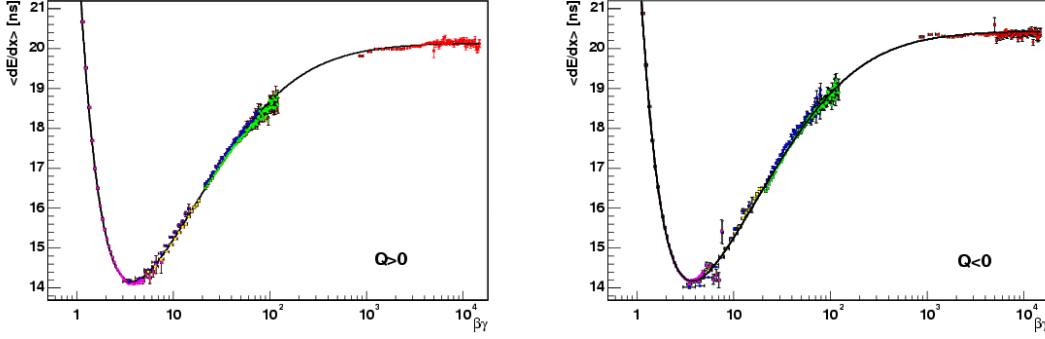


Figure 3.5: Experimental  $dE/dx$  as a function of  $\beta\gamma$  with superimposed the fitting function (continuous line). Left: positive tracks. Right: negative tracks. The electrons are red, the muons green, the kaons yellow, the pions blue and the protons magenta.

The  $TOF_{expected}^{part} = \frac{L}{pc} \sqrt{p^2 + m_{part}^2 c^2}$ , where  $L$  is the flight path of the charged track,  $p$  and  $m_{part}$  are respectively the momentum and the mass of the particle.

The TOF and  $dE/dx$  residuals are affected by common-mode fluctuations, responsible of PID correlations between particles in the same event. The origins of common-mode fluctuations are different for  $dE/dx$  and TOF.

- Common-mode fluctuations of the  $dE/dx$  response.

In this case, common-mode fluctuations are due to a certain number of factors, as an example COT gain and pressure variations. As a consequence of that, the residual measured for a specific particle (mass hypothesis "part") is:

$$\frac{dE}{dx}_{measured} - \frac{dE^{part}}{dx}_{expected} = \frac{dE}{dx}_{measured\ ideal} + \Delta_{dE/dx} - \frac{dE^{part}}{dx}_{expected} \quad (3.3)$$

where  $\frac{dE}{dx}_{measured\ ideal}$  is the response in absence of common mode fluctuations and  $\Delta_{dE/dx}$  is the common mode fluctuations for  $dE/dx$ .  $\Delta_{dE/dx}$  is a function of run and event number.

The last equation (3.3) can be written:

$$\frac{dE^{part}}{dx_{Res}} = \frac{dE^{part}}{dx_{Res\ ideal}} + \Delta_{dE/dx} \quad (3.4)$$

- Common mode fluctuations of the TOF response.

In this case the common mode fluctuations are due to the  $t_0$  (collision time)

resolution distribution. As before, the residual measured in mass hypothesis "part" is:

$$TOF_{measured} - TOF_{expected}^{part} = TOF_{measured\ ideal} + \Delta_{TOF} - TOF_{expected}^{part} \quad (3.5)$$

where  $TOF_{measured\ ideal}$  is the response in absence of common mode fluctuations and  $\Delta_{TOF}$  is the common mode fluctuation due to the  $t_0$  resolution distribution. The last equation (3.5) can be written:

$$TOF_{Res}^{part} = TOF_{Res\ ideal}^{part} + \Delta_{TOF} \quad (3.6)$$

Notice that both,  $\Delta_{dE/dx}$  and  $\Delta_{TOF}$ , are the same for all the tracks in the same event. So, the residuals of two track in the same event are correlated. From here we will use the terms "correlation" and "common mode fluctuations" to indicate the same thing:  $\Delta_{PID}$  (PID=TOF or dE/dx).

The method used to combine dE/dx and TOF information can be applied in both case of single track and of multiple tracks. The method makes use of Likelihoods respectively for one or more charged tracks. The Likelihood are constructed using the measured dE/dx and TOF residuals and they take into account the PID-correlation (due to the common-mode fluctuations) between particles in the same event.

We need to combine the Likelihood which uses TOF with the Likelihood which uses dE/dx. First of all, we have to define those Likelihoods.

In the single track case, the Likelihood for a single track in the mass hypothesis "part" can be written:

$$L_{PID}(PID_{Res}, part) = p(PID_{Res}|part) \quad (3.7)$$

where  $PID_{Res}$  is the dE/dx (PID = dE/dx) or TOF (PID = TOF) measured residual and  $p(PID_{Res}|part)$  is the probability density function (pdf) obtained fitting the residuals distribution in the mass hypothesis "part".

Then, we can combine the dE/dx and the TOF Likelihood obtaining the combined Likelihood for a single track.

The combined PID Likelihood is:

$$L_{combined\ PID}\left(\frac{dE}{dx}_{Res}, TOF_{Res}, part\right) = L_{dE/dx}\left(\frac{dE}{dx}_{Res}, part\right) \cdot L_{TOF}(TOF_{Res}, part). \quad (3.8)$$

We defined the Likelihood function as the product of the dE/dx and TOF Likelihoods, assuming no correlation between dE/dx and TOF residuals. This assumption is justified by the scatter plot of the TOF residual vs the dE/dx one (Fig. 3.6) for a pure sample of kaons (Section 3.1). In this plot the two measurements appear completely uncorrelated. Similar plots have been obtained for protons and pions.

In case of two or more tracks in the same event, it is very important to consider the correlation between particles, because, neglecting the correlations, we can have a large bias in the result of a Likelihood fit which makes use of PID measurements. We

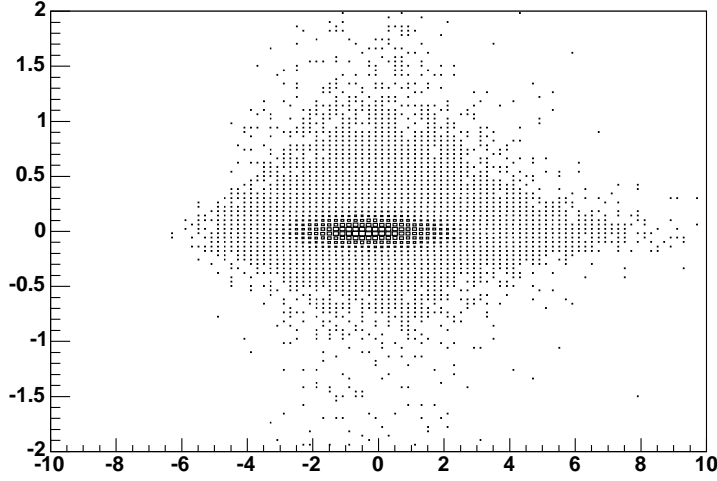


Figure 3.6: TOF residual distribution vs dE/dx residual distribution. It seems that there is no correlation between the two distributions.

can make an example with two tracks.

The Likelihood for track pairs assumes the following form:

$$\begin{aligned}
 L_{PID}^{track\ pairs}(PID_1, PID_2, part_1, part_2) &= p(PID_{Res}^1, PID_{Res}^2 | part_1, part_2) = \\
 &\int p(PID_{Res\ ideal}^1, PID_{Res\ ideal}^2, \Delta_{PID} | part_1, part_2) d\Delta_{PID} = \\
 &\int p(PID_{Res\ ideal}^1, PID_{Res\ ideal}^2 | \Delta_{PID}, part_1, part_2) \cdot p(\Delta_{PID}) d\Delta_{PID} = \\
 &\int p(PID_{Res\ ideal}^1 | \Delta_{PID}, part_1, part_2) \cdot p(PID_{Res\ ideal}^2 | \Delta_{PID}, part_1, part_2) \cdot p(\Delta_{PID}) d\Delta_{PID}
 \end{aligned} \tag{3.9}$$

where  $p(\Delta_{PID})$  is the pdf of  $\Delta_{PID}$ .

As in the case of single track, the combined Likelihood for track pairs is:

$$\begin{aligned}
 L_{combined\ PID}^{track\ pairs}\left(\frac{dE^1}{dx_{Res}}, \frac{dE^2}{dx_{Res}}, TOF_{Res}^1, TOF_{Res}^2, part_1, part_2\right) &= \\
 &= L_{dE/dx}^{track\ pairs}\left(\frac{dE^1}{dx_{Res}}, \frac{dE^2}{dx_{Res}}, part_1, part_2\right) \cdot L_{TOF}^{track\ pairs}(TOF_{Res}^1, TOF_{Res}^2, part_1, part_2).
 \end{aligned} \tag{3.10}$$

After the description of almost all the ingredients of PID entering in the expression of the combined Likelihood for one or more track, we notice that we must determine the unknown distributions  $p(\frac{dE}{dx_{Res\ ideal}}, part_i, \Delta_{dE/dx})$ ,  $p(TOF_{Res\ ideal}, part_i, \Delta_{TOF})$ ,  $p(\Delta_{dE/dx})$  and  $p(\Delta_{TOF})$ .

In the Section 3.3 we will make use of the measured residual distributions  $p(\frac{dE}{dx}_{Res}, K)$ ,  $p(TOF_{Res}, K)$ ,  $p(\frac{dE}{dx}_{Res}, \pi)$  and  $p(TOF_{Res}, \pi)$  using a pure sample of kaons and pions from  $D^0 \rightarrow K^- \pi^+$  decays, to determine the distributions of ideal residuals of kaons and pions and the distribution of  $\Delta_{PID}$ . Then in the same way, we will use the measured residual distributions  $p(\frac{dE}{dx}_{Res}, p)$  and  $p(TOF_{Res}, p)$ , using a pure sample of protons from  $\Lambda \rightarrow p \pi^-$  decays, to obtain the proton ideal residual distribution.

### 3.3 Parameterization of Particle IDentification distributions

To determine the necessary unknown distributions for kaons, pions and protons, we used the pure sample of  $D^0 \rightarrow K^- \pi^+$  and of  $\Lambda \rightarrow p \pi^-$  decays described in Section 3.1. The unknown distribution are  $p(\Delta_{PID})$ , where  $\Delta_{PID}$  can be the  $dE/dx$  or TOF common-mode fluctuations,  $p(\frac{dE}{dx}_{Res\ ideal}|part)$  and  $p(TOF_{Res\ ideal}|part)$ , where "part" can be kaon, pion or proton.

To determine these distributions we used the SUM and the DIFFERENCE of residuals distribution. we defined:

- $dE/dx$  case:  $SUM_{dE/dx} = \frac{dE}{dx}_{Res}^{\pi} + \frac{dE}{dx}_{Res}^K$ ,  $DIFF_{dE/dx} = \frac{dE}{dx}_{Res}^{\pi} - \frac{dE}{dx}_{Res}^K$
- TOF case:  $SUM_{TOF} = TOF_{Res}^{\pi} + TOF_{Res}^K$ ,  $DIFF_{TOF} = TOF_{Res}^{\pi} - TOF_{Res}^K$

where from Section 3.2:

$$\begin{aligned} \frac{dE^{part}}{dx_{Res}} &= \frac{dE^{part}}{dx_{Res\ ideal}} + \Delta_{dE/dx} \\ TOF_{Res}^{part} &= TOF_{Res\ ideal}^{part} + \Delta_{TOF}. \end{aligned}$$

The SUM and the DIFFERENCE can also be written in the following way:

$$\begin{aligned} SUM_{PID} &= PID_{Res\ ideal}^{\pi} + PID_{Res\ ideal}^K + 2\Delta_{PID} \\ DIFF_{PID} &= PID_{Res\ ideal}^{\pi} - PID_{Res\ ideal}^K. \end{aligned}$$

where we observe the presence of the ideal residual  $PID_{Res\ ideal}$  and of the correlation  $\Delta_{PID}$ , whose distributions are unknown.

Defining  $p_i^{PID}(x)$  the distribution of the unknown ideal residuals of particle  $i$  ( $i = \pi, K$ ), using  $\frac{dE}{dx}$  (PID= $\frac{dE}{dx}$ ) or TOF (PID=TOF), the  $SUM_{PID}$  and the  $DIFF_{PID}$  distributions are given by:

$$\begin{aligned} p(SUM_{PID}) &= \int \int p_{\pi}^{PID}(x) \cdot p_K^{PID}(y-x) \cdot p_{\Delta_{PID}}((SUM_{PID}-y)/2) dx dy \\ p(DIFF_{PID}) &= \int p_{\pi}^{PID}(x) \cdot p_K^{PID}(DIFF_{PID}+x) dx \end{aligned} \quad (3.11)$$

From equations (3.11), the  $SUM_{PID}$  distribution  $p(SUM_{PID})$  is the convolution of  $p_{\pi}^{PID}(x)$ ,  $p_K^{PID}(x)$  and  $p_{\Delta_{PID}}(2x)$ , and the  $DIFF_{PID}$  distribution  $p(DIFF_{PID})$  is the convolution of  $p_{\pi}^{PID}(x)$  and  $p_K^{PID}(-x)$ .

We parameterized the ideal residuals ( $p_i^{PID}(x)$ ) of pions and kaons as sums of Gaussian functions:

$$p_\pi^{PID}(x = PID_{Res}^\pi ideal) = f'(x) + g'(x) + h'(x) \quad (3.12)$$

$$p_K^{PID}(x = PID_{Res}^K ideal) = f''(x) + g''(x) + h''(x). \quad (3.13)$$

In a similar way we parameterized the correlation distribution as:

$$p_{\Delta_{PID}}(\Delta_{PID} = x) = c_1(x) + c_2(x). \quad (3.14)$$

where  $c_1$  and  $c_2$  are two gaussian functions.

With the above parameterization we can write the distributions of the residuals, of the  $SUM_{PID}$  ( $PID_{Res}^\pi + PID_{Res}^K$ ) and of the  $DIFF_{PID}$  ( $PID_{Res}^\pi - PID_{Res}^K$ ):

$$\begin{aligned} p(PID_{Res}^\pi = x) &= (f'(x) + g'(x) + h'(x)) * (c_1(x) + c_2(x)) \\ p(PID_{Res}^K = x) &= (f''(x) + g''(x) + h''(x)) * (c_1(x) + c_2(x)) \\ p(SUM_{PID} = x) &= (f'(x) + g'(x) + h'(x)) * (f''(x) + g''(x) + h''(x)) * (c_1(2x) + c_2(2x)) \\ p(DIFF_{PID} = x) &= (f'(x) + g'(x) + h'(x)) * (f''(-x) + g''(-x) + h''(-x)) \end{aligned} \quad (3.15)$$

where the symbol  $*$  indicates the convolution operation.

To obtain the ideal residuals distributions and the correlation distribution we used an iterative procedure. First we fit the residuals, then we go through the fit of  $SUM_{PID}$  distribution to come back to the residual. The  $DIFF_{PID}$  distribution is used as a test of convergence of the algorithm: if it does not describe the data well enough, a new iteration is performed.

So we can divide the procedure of the parameterization in steps:

1. Fit of the residuals distributions using:

$$\begin{aligned} p(PID_{Res}^\pi = x) &= (f'(x) + g'(x) + h'(x)) * G_{\mu=0.0, \sigma=0.5}(x) \\ p(PID_{Res}^K = x) &= (f''(x) + g''(x) + h''(x)) * G_{\mu=0.0, \sigma=0.5}(x) \end{aligned} \quad (3.16)$$

where at the first iteration the correlation  $p(\Delta_{PID})$  is fixed to be a single Gaussian centered in the origin and with  $\sigma = 0.5$ .

2. Fit of the  $SUM_{PID}$  distribution using:

$$\begin{aligned} p(SUM_{PID}) &= p(PID_{Res}^\pi + PID_{Res}^K) = \\ &= (f'(x) + g'(x) + h'(x)) * (f''(x) + g''(x) + h''(x)) * (c_1(2x) + c_2(2x)) \end{aligned} \quad (3.17)$$

where the  $f'(x)$ ,  $g'(x)$ ,  $h'(x)$ ,  $f''(x)$ ,  $g''(x)$  and  $h''(x)$  parameters are fixed from the previous fit (step 1). In this way, we obtained the parameters of the two Gaussians describing the correlation distribution.



3. Fit of the residuals distributions using:

$$\begin{aligned} p(PID_{Res}^{\pi} = x) &= (f'(x) + g'(x) + h'(x)) * (c_1(x) + c_2(x)) \\ p(PID_{Res}^K = x) &= (f''(x) + g''(x) + h''(x)) * (c_1(x) + c_2(x)) \end{aligned} \quad (3.18)$$

where the  $c_1(x)$  and  $c_2(x)$  distributions are fixed from the previous fit (step 2). In this way, we obtained the parameters of  $f'(x)$ ,  $g'(x)$ ,  $h'(x)$ ,  $f''(x)$ ,  $g''(x)$  and  $h''(x)$  that describe the ideal residuals.

4. Crosscheck on the  $p(DIFF_{PID})$ . We superimposed the function  $(f'(x) + g'(x) + h'(x)) * (f''(-x) + g''(-x) + h''(-x))$ , as it has been determined in step 3, to the experimental difference distributions of data. From equation (3.15), if the parameterization is good there must be a good agreement between the data and the function.

We determined the parameterization using pions and kaons from  $D^0$  (trigger tracks) and we used the soft pions from  $D^{*+}$  to check that the extracted PID functions describe also the soft tracks ( $P < 2 \text{ GeV}/c$ ).

In the  $dE/dx$  case we adopted a different parameterization for each particle type and charge. As an example, Fig. 3.7 (residuals for positive charges) and Fig. 3.8 (residuals for negative charges) show that the pion residuals (in red) are significantly different from the kaon residuals (in black).

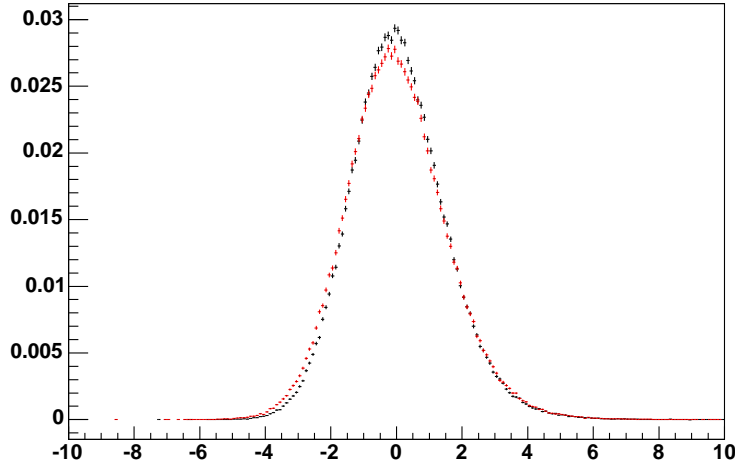


Figure 3.7:  $dE/dx$  residuals. Black:  $K^+$  from  $D^0$ . Red:  $\pi^+$  from  $D^0$ . The two residuals are different so we adopted a different parameterization for each particle type.

We have extracted residuals distributions for protons and antiprotons by using the  $\Lambda \rightarrow p\pi^-$  sample described in Section 3.1.

The protons from  $\Lambda$  are not required to confirm the B\_PIPi trigger (are not required to be "trigger tracks") and protons momentum range is extended down to  $1.5 \text{ GeV}/c$ .

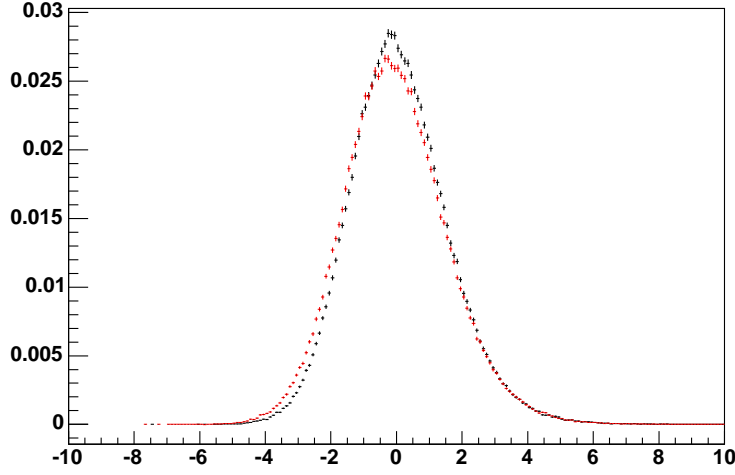


Figure 3.8:  $dE/dx$  residuals. Black:  $K^-$  from  $D^0$ . Red:  $\pi^-$  from  $D^0$ . The two residuals are different so we adopted a different parameterization for each particle type.

In the TOF case, instead, we extract an unique parameterization for all the particle types and charges.

### 3.3.1 $dE/dx$ parameterization

In this Section we describe the steps of the parameterization procedure for the  $dE/dx$  case.

Fig. 3.9 and Fig. 3.10 show the resulting curve fitting, on the sample  $D^0 \rightarrow K^- \pi^+$ , the residuals for positive pions and negative kaons respectively using the first step fit functions of the iterative procedure (equations (3.16)). From these fits, we obtained the parameters of the ideal residuals that we used in the fit of the sum distribution ( $\frac{dE}{dx}_{Res}^{\pi^+} + \frac{dE}{dx}_{Res}^{K^-}$ ) with the function (3.17) (second step). In Fig. 3.11 the fit of the  $SUM_{dE/dx}$  distribution is shown. The correlation distribution ( $p(\Delta_{dE/dx})$ ) parameters, obtained from the fit of the  $SUM_{dE/dx}$  distribution, are summarized in Table 3.1 where for each Gaussians is indicated: A the relative weight,  $\mu$  the mean value and  $\sigma$  the standard deviation.

The correlation distribution for  $dE/dx$  ( $p(\Delta_{dE/dx})$ ) is shown in Fig. 3.12. We verified that, repeating the iterative procedure for negative pions and positive kaons, instead of positive pions and negative kaons, we obtained the same  $p(\Delta_{dE/dx})$  parameters within the errors.

Then we fitted the residuals distributions for positive and negative pions and kaons with the functions (3.18)(third step). Fig. 3.13 shows the fit of the pion residuals (on the top we reported positive pions and on the bottom negative pions) and Fig. 3.14 the fit of the kaon residuals (on the top we reported positive kaons and on the bottom negative kaons). The ideal residual parameters are summarized in Table 3.2 and Table

Parameters	Value	Error
$A_{c_1}$	0.248	0.102
$\mu_{c_1}$	0.125	0.05
$\sigma_{c_1}$	0.877	0.098
$A_{c_2}$	0.752	0.102
$\mu_{c_2}$	-0.0436	0.0096
$\sigma_{c_2}$	0.272	0.083

Table 3.1: Correlation distribution ( $p(\Delta dE/dx)$ ) parameters.

3.3 for pions and kaons respectively.

Positive pions			Negative pions		
Parameters	Value	Error	Parameters	Value	Error
$A_{f'}$	0.64	0.12	$A_{f'}$	0.726	0.1
$\mu_{f'}$	-0.339	0.038	$\mu_{f'}$	-0.377	0.041
$\sigma_{f'}$	1.206	0.035	$\sigma_{f'}$	1.275	0.026
$A_{g'}$	0.34	0.14	$A_{g'}$	0.2563	0.0098
$\mu_{g'}$	0.523	0.283	$\mu_{g'}$	0.79	0.38
$\sigma_{g'}$	1.53	0.07	$\sigma_{g'}$	1.583	0.072
$A_{h'}$	0.024	0.031	$A_{h'}$	0.017	0.024
$\mu_{h'}$	2.03	2.05	$\mu_{h'}$	2.495	1.889
$\sigma_{h'}$	2.182	0.488	$\sigma_{h'}$	2.093	0.412

Table 3.2: Ideal residuals parameters for positive (left) and negative (right) pions.

Positive kaons			Negative kaons		
Parameters	Value	Error	Parameters	Value	Error
$A_{f''}$	0.70	0.12	$A_{f''}$	0.69	0.12
$\mu_{f''}$	-0.327	0.058	$\mu_{f''}$	-0.337	0.053
$\sigma_{f''}$	1.133	0.015	$\sigma_{f''}$	1.166	0.019
$A_{g''}$	0.27	0.12	$A_{g''}$	0.28	0.12
$\mu_{g''}$	0.84	0.37	$\mu_{g''}$	0.88	0.40
$\sigma_{g''}$	1.279	0.097	$\sigma_{g''}$	1.364	0.104
$A_{h''}$	0.029	0.018	$A_{h''}$	0.0297	0.0178
$\mu_{h''}$	2.547	0.825	$\mu_{h''}$	2.553	0.784
$\sigma_{h''}$	1.745	0.199	$\sigma_{h''}$	1.85	0.19

Table 3.3: Ideal residuals parameters for positive (left) and negative (right) kaons.

At this point, we can evaluate the difference distribution  $(p(\frac{dE}{dx}_{Res}^{\pi^+} - \frac{dE}{dx}_{Res}^{K^-}))$  and compare it to data (fourth step). In Fig. 3.15 we superimposed the functions  $p(\frac{dE}{dx}_{Res}^{\pi^+} - \frac{dE}{dx}_{Res}^{K^-}) = (f'(x) + g'(x) + h'(x)) * (f''(-x) + g''(-x) + h''(-x))$  in blue, on data in black. There is a good agreement between the function, extracted from residuals parameterization, and data, the corresponding  $\chi^2$  is  $\chi^2 = 169/160$ .

In order to verify that the parameterization of the correlation is valid also for the other charges we checked that the curves obtained from the parameterization of the  $SUM_{dE/dx}$  and the  $DIFF_{dE/dx}$  distributions of the negative pions residuals and of the positive kaons residuals are in good agreement with the data. In Fig. 3.16 we reported, in black the  $\frac{dE}{dx}_{Res}^{\pi^-} + \frac{dE}{dx}_{Res}^{K^+}$  from data and in blue the curve obtained from the parameterization, the corresponding  $\chi^2$  is  $\chi^2 = 181/160$ . In Fig. 3.17 instead we reported, in black the  $\frac{dE}{dx}_{Res}^{\pi^-} - \frac{dE}{dx}_{Res}^{K^+}$  from data and in blue the curve obtained from the parameterization, the corresponding  $\chi^2$  is  $\chi^2 = 201/160$ .

Using the sample of  $\Lambda \rightarrow p\pi^-$  decay, we obtained also the parameters of the ideal residuals of protons and antiprotons. In Fig. 3.18, the fit of protons residual on the top and of antiprotons residual on the bottom are shown. The correlation distribution  $p(\Delta_{dE/dx})$  was set to the function found from kaons and pions from  $D^0$  decay (see the discussion on the “next event” correlation in the next section). The ideal residual parameters for protons and anti-protons are summarized in Table 3.4.

Protons			Anti-Protons		
Parameters	Value	Error	Parameters	Value	Error
$A_{f''}$	0.85	0.06	$A_{f''}$	0.736	0.077
$\mu_{f''}$	-0.066	0.076	$\mu_{f''}$	-0.012	0.12
$\sigma_{f''}$	1.206	0.028	$\sigma_{f''}$	1.206	0.048
$A_{g''}$	0.09	0.08	$A_{g''}$	0.19	0.05
$\mu_{g''}$	1.986	0.407	$\mu_{g''}$	1.64	0.33
$\sigma_{g''}$	1.004	0.297	$\sigma_{g''}$	1.712	0.093
$A_{h''}$	0.053	0.087	$A_{h''}$	0.067	0.067
$\mu_{h''}$	2.814	2.502	$\mu_{h''}$	-1.582	0.399
$\sigma_{h''}$	1.826	0.682	$\sigma_{h''}$	0.85	0.19

Table 3.4: Ideal residuals parameters for protons (left) and anti-protons (right).

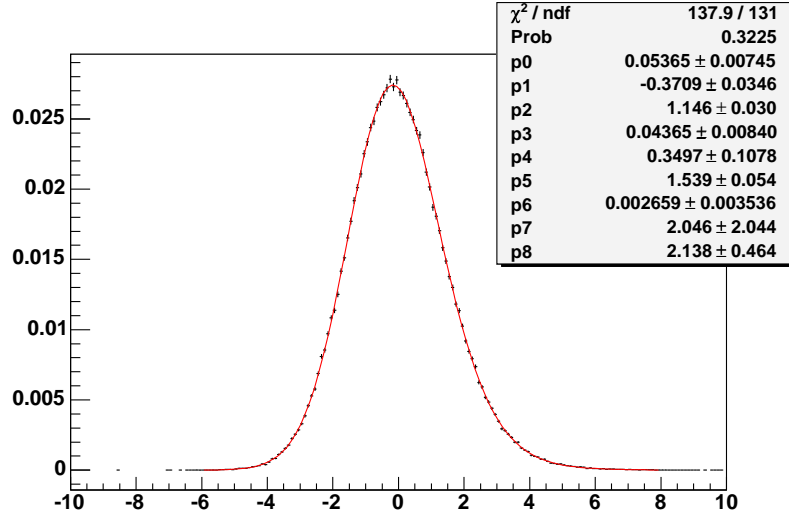


Figure 3.9: Fit of the  $\pi^+$  residual using the function  $(f'(x) + g'(x) + h'(x)) * G_{\mu=0.0, \sigma=0.5}(x)$  (first step). The parameters of  $f'$ ,  $g'$  and  $h'$  are left free to vary in the fit.

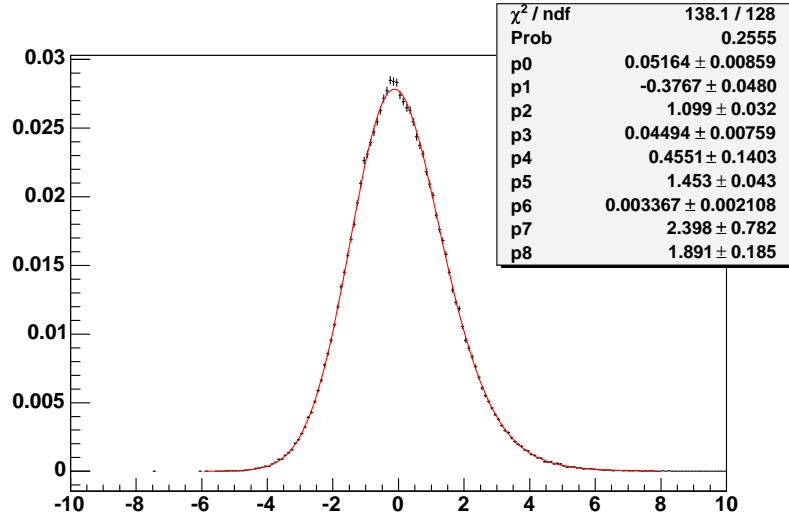


Figure 3.10: Fit of the  $K^-$  residual using the function  $(f''(x) + g''(x) + h''(x)) * G_{\mu=0.0, \sigma=0.5}(x)$  (first step). The parameters of  $f''$ ,  $g''$  and  $h''$  are left free to vary in the fit.

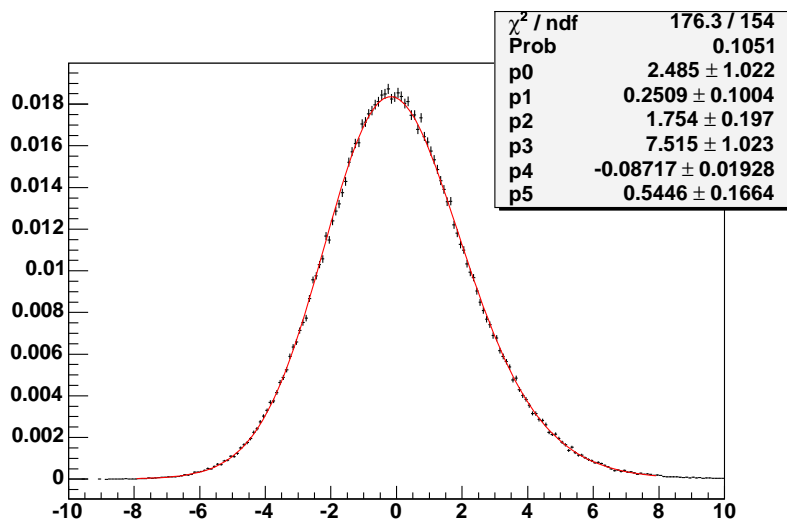


Figure 3.11: Fit of  $SUM_{dE/dx}$  distribution  $\frac{dE}{dx}_{\pi^+} + \frac{dE}{dx}_{K^-}$  using the function  $(f'(x) + g'(x) + h'(x)) * (f''(x) + g''(x) + h''(x)) * (c_1(2x) + c_2(2x))$  (second step). The parameters of  $c_1$  and  $c_2$  are left free to vary in the fit, while all others are fixed.

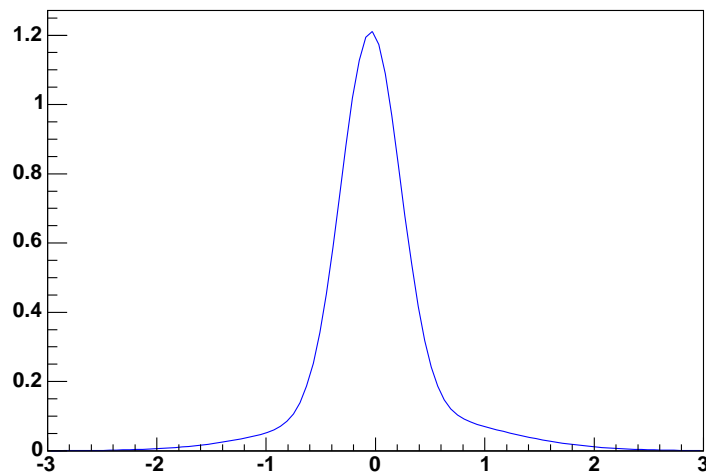


Figure 3.12: Correlation distribution,  $c_1(x) + c_2(x)$ .

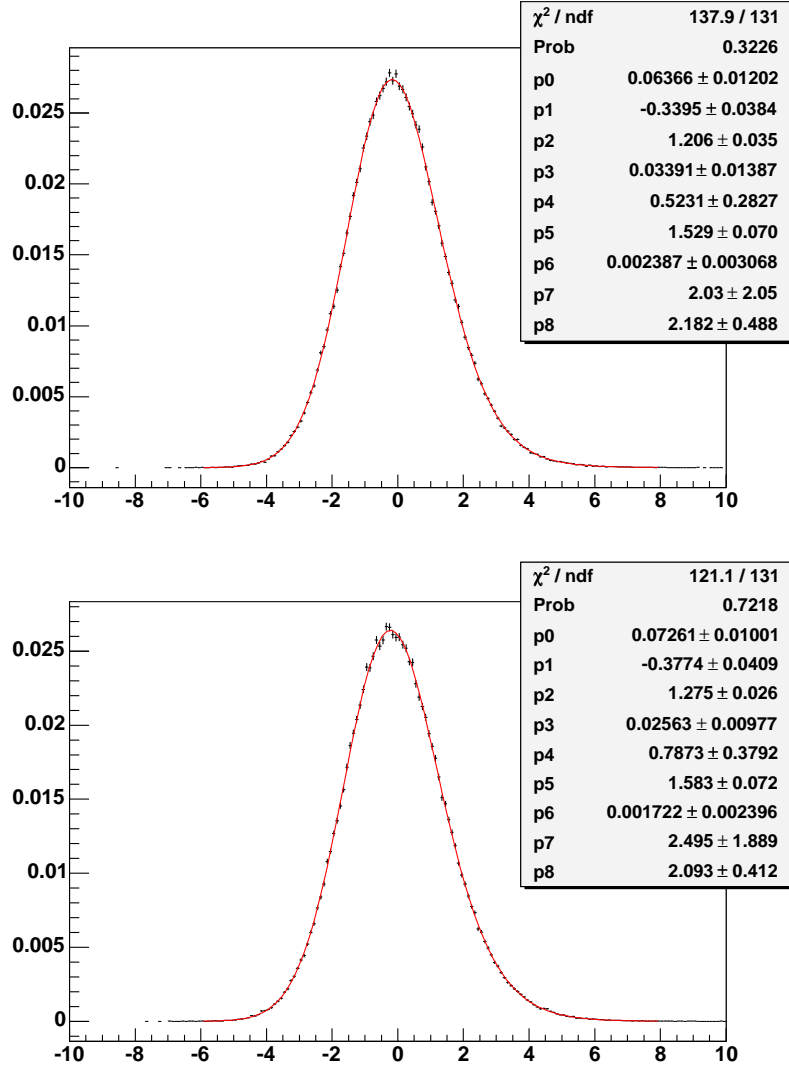


Figure 3.13: Fit of the pion residuals using the function  $(f'(x) + g'(x) + h'(x)) * (c_1(x) + c_2(x))$  (third step). On the top positive pions and on the bottom negative pions.

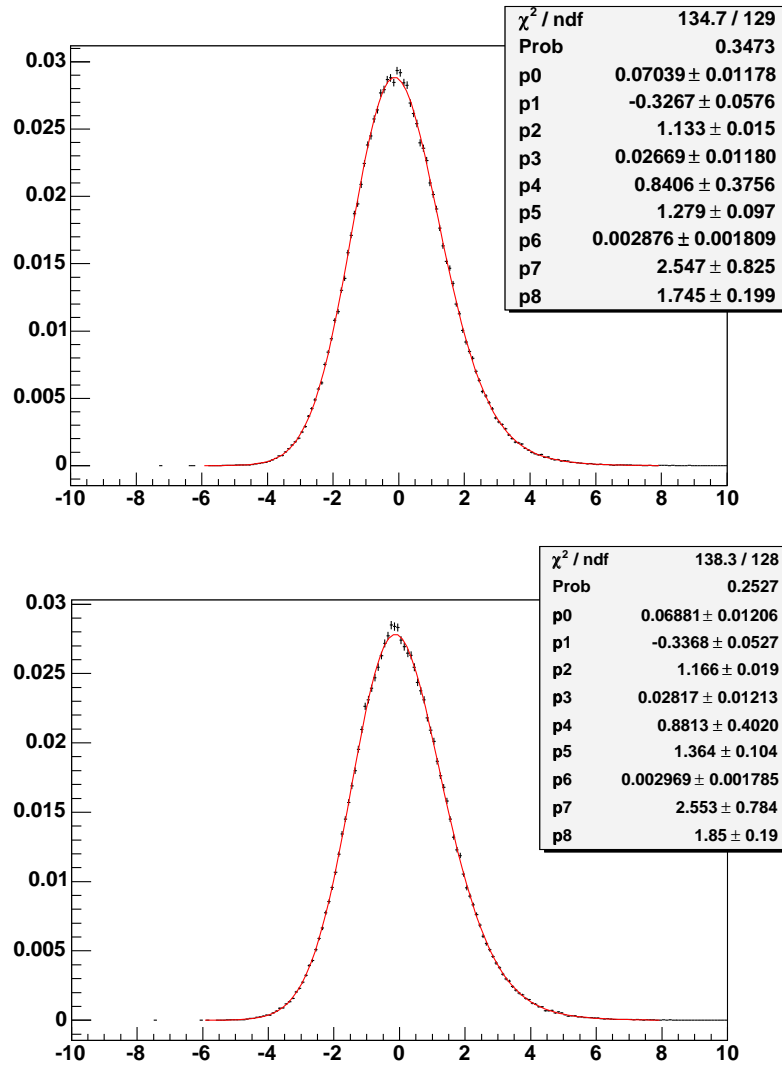


Figure 3.14: Fit of the kaon residuals using the function  $(f''(x) + g''(x) + h''(x)) * (c_1(x) + c_2(x))$  (third step). On the top positive kaons and on the bottom negative kaons.



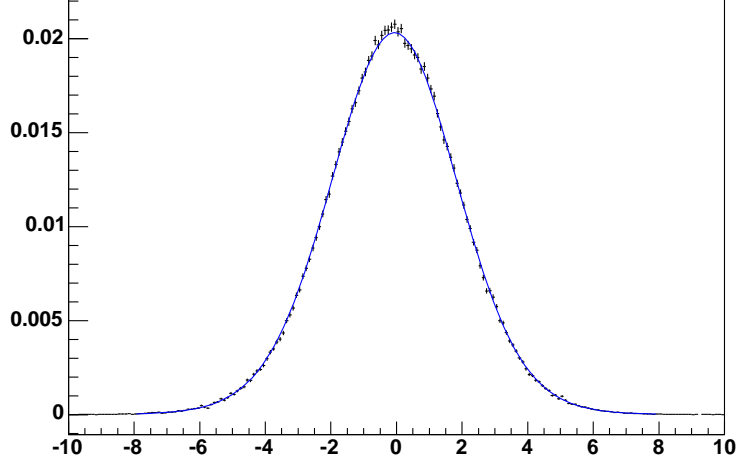


Figure 3.15: Parameterization crosscheck. Black: difference distribution (data)  $\frac{dE}{dx}_{Res}^{\pi^+} - \frac{dE}{dx}_{Res}^{K^-}$ . Blue: curve obtained from residuals and  $p(\Delta_{dE/dx})$  parameterization.  $\chi^2 = 169/160$ .

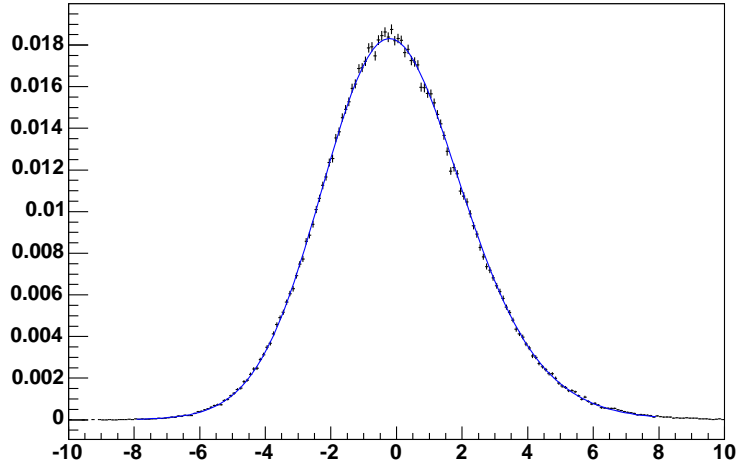


Figure 3.16: Parameterization crosscheck. Black: sum distribution (data)  $\frac{dE}{dx}_{Res}^{\pi^-} + \frac{dE}{dx}_{Res}^{K^+}$ . Blue: curve obtained from residuals and  $p(\Delta_{dE/dx})$  parameterization.  $\chi^2 = 181/160$ .

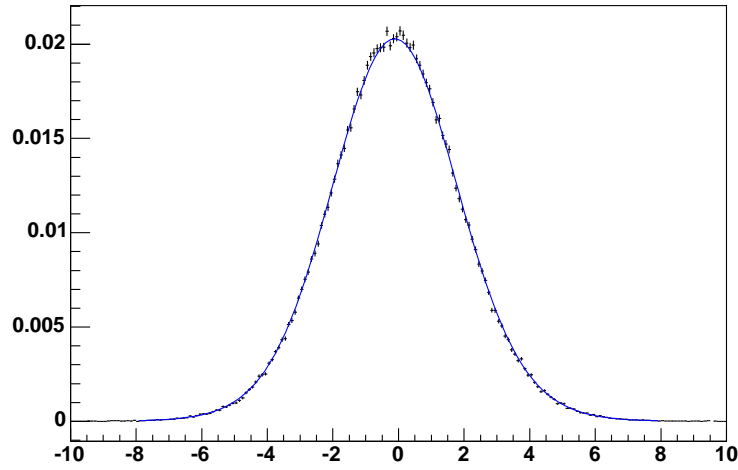


Figure 3.17: Parameterization crosscheck. Black: difference distribution (data)  $\frac{dE}{dx}_{Res}^{\pi^-} - \frac{dE}{dx}_{Res}^{K^+}$ . Blue: curve obtained from residuals and  $p(\Delta_{dE/dx})$  parameterization.  $\chi^2 = 201/160$ .

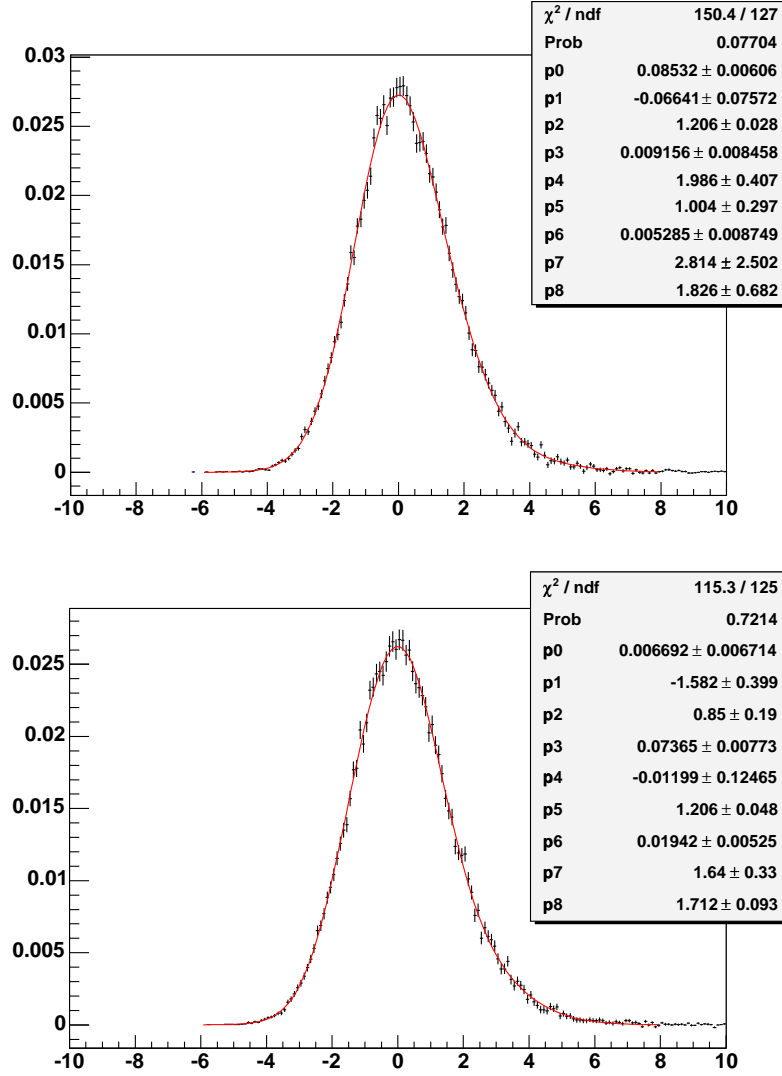


Figure 3.18: Fit of the proton residuals with  $(f'(x) + g'(x) + h'(x)) * (c_1(x) + c_2(x))$ . On the top protons and on the bottom antiprotons.

**“Next-event” correlation**

In order to test our understanding of the correlation between tracks belonging to the same event, we looked also at the same distributions for an artificial “next-event” sample, where we paired a kaon from one event with a pion from the previous one. Using this artificial sample, we extracted the correlation distribution with the same method used for tracks in the same event described above. In Fig. 3.19 the fit of the sum distribution with the function  $(f'(x) + g'(x) + h'(x)) * (f''(x) + g''(x) + h''(x)) * (c_1(2x) + c_2(2x))$  is shown. The parameters of  $c_1$  and  $c_2$  are left free to vary in the fit, while all the other parameters are fixed from the residual fits in the “same event” sample. This is due to the fact that the ideal residuals are the same in the “next-event” and in the “same-event” sample. In this way we obtained an alternative set of correlation parameters (“next-event set”) summarized in Table 3.5.

Parameters	Value	Error
$A_{c_1}$	0.39	0.22
$\mu_{c_1}$	0.011	0.037
$\sigma_{c_1}$	0.588	0.146
$A_{c_2}$	0.61	0.22
$\mu_{c_2}$	-0.007	0.017
$\sigma_{c_2}$	0.14	0.30

Table 3.5: “Next-event” correlation distribution parameters.

In Fig. 3.20 we reported  $p(\Delta_{dE/dx})$  for “next-event” sample (in blue) and  $p(\Delta_{dE/dx})$  for “same-event” sample (in red). As expected the “next-event” correlation is narrower than the one we found for tracks in the same event.

We have checked that this difference in correlation is not due to different kinematics of “same-event” and “next-event”.

To do that, we reweighted the  $\Delta\eta$  and the  $\Delta\phi$  distributions of “next-event” sample in a way to make them similar to the distributions of the “same-event”.

In Fig. 3.21 the  $\Delta\eta$  (on the left) and  $\Delta\phi$  (on the right) distributions for the “same-event” sample are shown; the same distributions for the “next-event” sample are shown in Fig. 3.22.

We compared the “next-event”  $SUM_{dE/dx}$  distribution with  $\Delta\eta$  and  $\Delta\phi$  of the “next-event” sample and the “next-event”  $SUM_{dE/dx}$  distribution reweighted in according to  $\Delta\eta$  and  $\Delta\phi$  of “same-event” sample.

In Fig. 3.23, the “next-event” sum distribution (in black) and the “next-event” sum distribution reweighted (in red) are shown. They show no significant differences.

So we can conclude that the correlation doesn’t depend on  $\Delta\eta$  and  $\Delta\phi$  distributions, and we can use the correlation calculated for the  $D^0$  also for other decays where the tracks have a different opening angle.

For example we used the  $p(\Delta_{dE/dx})$  obtained with  $D^0 \rightarrow K^-\pi^+$  decay, in the fit of the protons residuals from  $\Lambda \rightarrow p\pi^-$ .

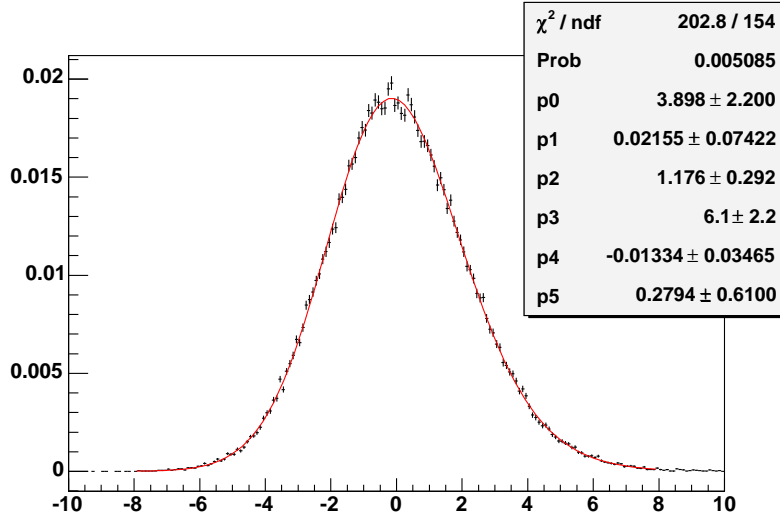


Figure 3.19: Fit of the “next-event”  $SUM_{dE/dx}$  distribution using the function  $(f'(x) + g'(x) + h'(x)) * (f''(x) + g''(x) + h''(x)) * (c_1(2x) + c_2(2x))$ . The parameters of  $f'$ ,  $g'$ ,  $h'$ ,  $f''$ ,  $g''$  and  $h''$  are fixed from the residual fit in the “same event” sample. We obtained the “next-event” correlation distribution parameters (the parameters of  $c_1$  and  $c_2$ ).

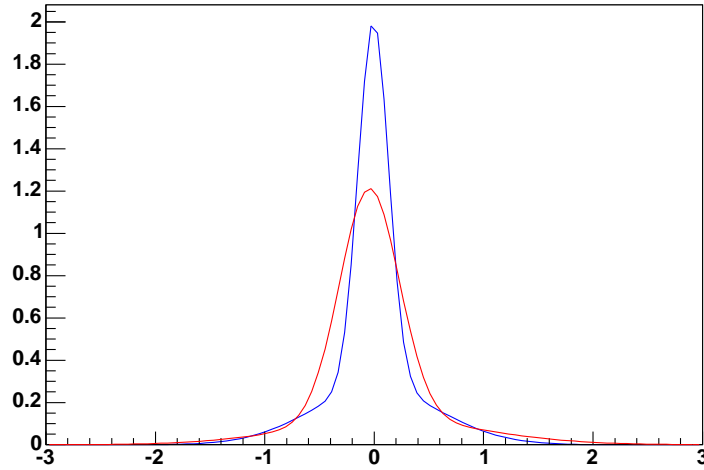


Figure 3.20: In blue the “next-event”  $p(\Delta_{dE/dx})$ . In red the “same-event”  $p(\Delta_{dE/dx})$ . The next event correlation is narrower than the one we found for tracks in the same event.

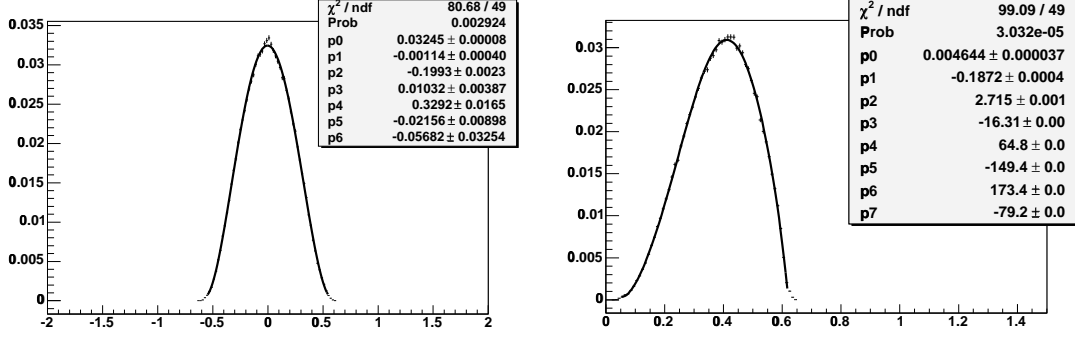


Figure 3.21: Left:  $\Delta\eta$  distribution for the "same-event" sample. Right:  $\Delta\phi$  distribution for the "same-event" sample.

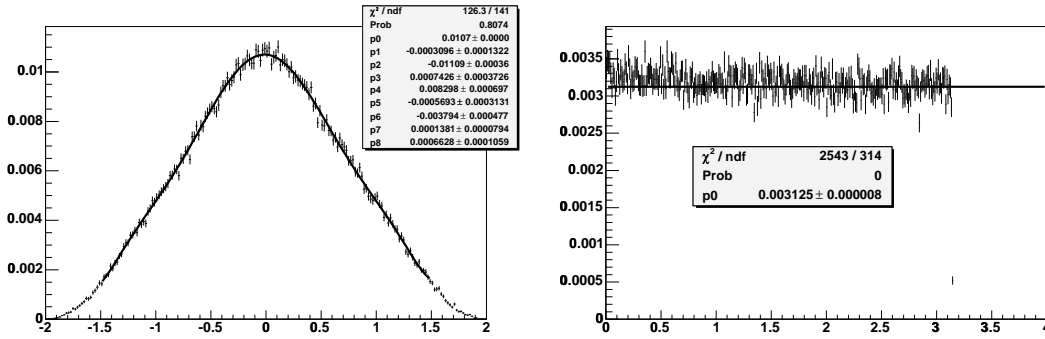


Figure 3.22: Left:  $\Delta\eta$  distribution for the "next-event" sample. Right:  $\Delta\phi$  distribution for the "next-event" sample.

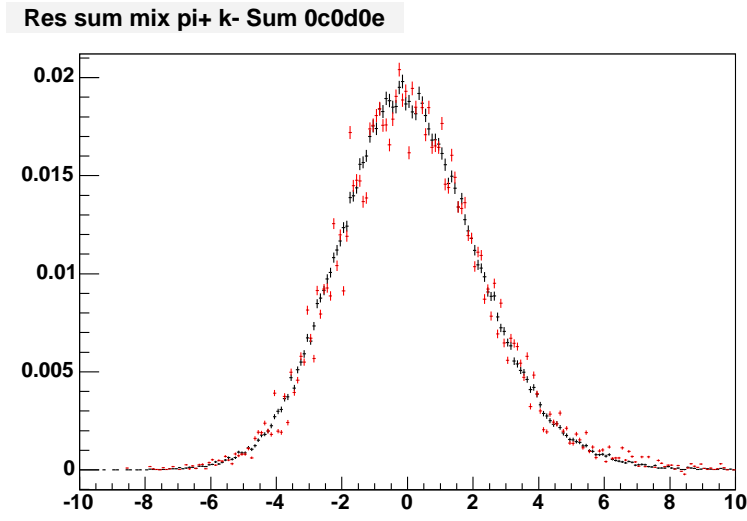


Figure 3.23: In black the “next-event”  $SUM_{dE/dx}$  distribution. In red the “next-event”  $SUM_{dE/dx}$  distribution reweighted with “same-event”  $\Delta\eta$  and  $\Delta\phi$  distributions. They show no significant differences.

### dE/dx residuals for soft pion

In the previous Section, we described the dE/dx parameterization considering pions and kaons from  $D^0$  decay, that are trigger tracks ( $p_T > 2$  GeV/c). To check that the parameterization is suitable also for the tracks with lower momenta we looked at soft pions from  $D^{*+}$  decay.

Fig. 3.24 shows the residuals of positive soft pions (in black) in momentum bins of 0.1 GeV/c starting from 0.4 GeV/c. The parameterization obtained using the trigger tracks is superimposed (in blue). We notice that there is a discrepancy for momentum between 0.4 and 0.6 GeV/c.

Fig. 3.25 shows the same plots for negative pions. The discrepancy is larger and survives up to 0.9 GeV/c.

In the public code for CDF II users we implemented two functions. One takes into account the discrepancy in the systematic uncertainty, the other uses ad hoc parameterization for this momentum range.

The parameters of the ad hoc parameterization are obtained by fitting the residuals in this momentum range, assuming as correlation distribution the one obtained with the trigger tracks from  $D^0$  decay. The fit of the positive pions residuals and of the negative pions residuals are shown respectively in Fig. 3.26 and Fig. 3.27.

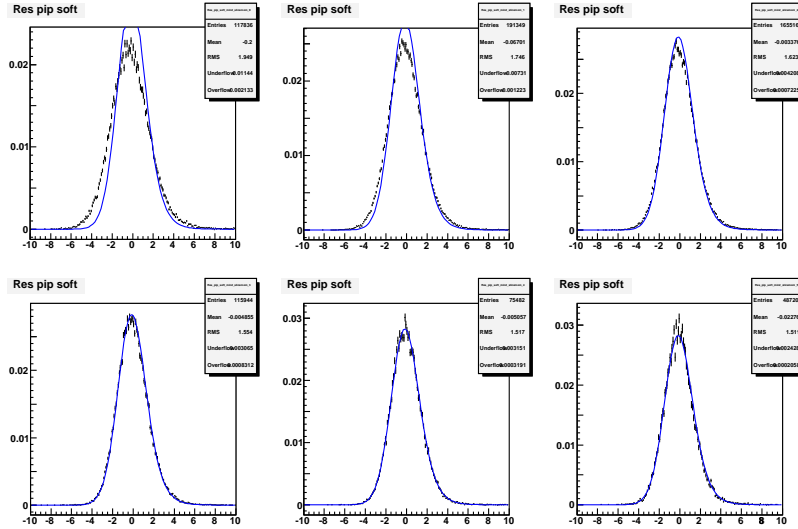


Figure 3.24: In black the positive soft pions residual in momentum bins. In blue the parameterization obtained with the trigger tracks. (Momentum bin = 0.1 GeV/c starting from 0.4 GeV/c).



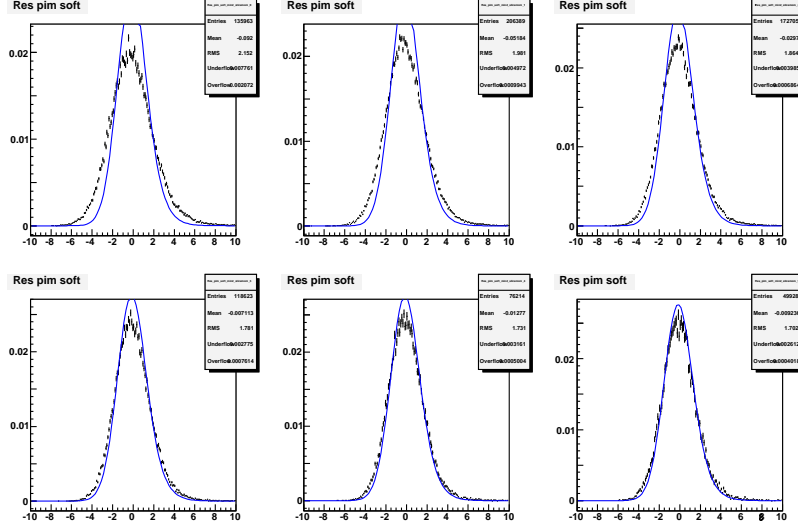


Figure 3.25: In black the negative soft pions residuals in momentum bins. In blue the parameterization obtained with the trigger tracks. (Momentum bin = 0.1 GeV/c starting from 0.4 GeV/c).

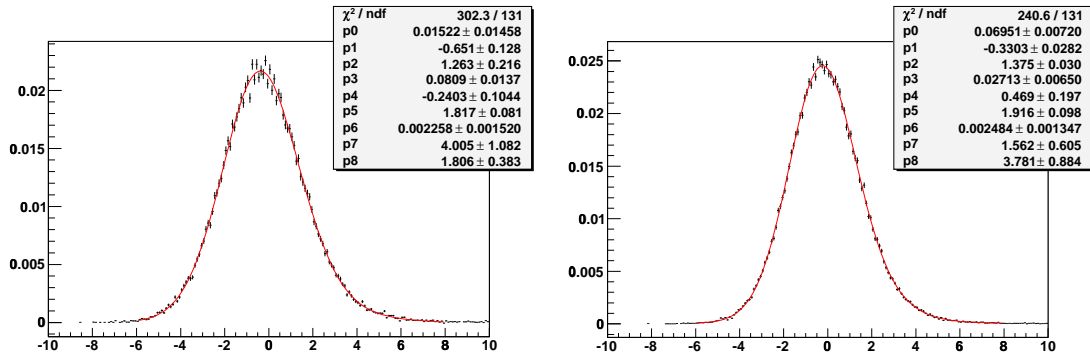


Figure 3.26: Fit of the positive soft pions residuals in momentum bins. Left: ( $0.4 \leq p < 0.5$ ) GeV/c. Right: ( $0.5 \leq p < 0.6$ ) GeV/c.

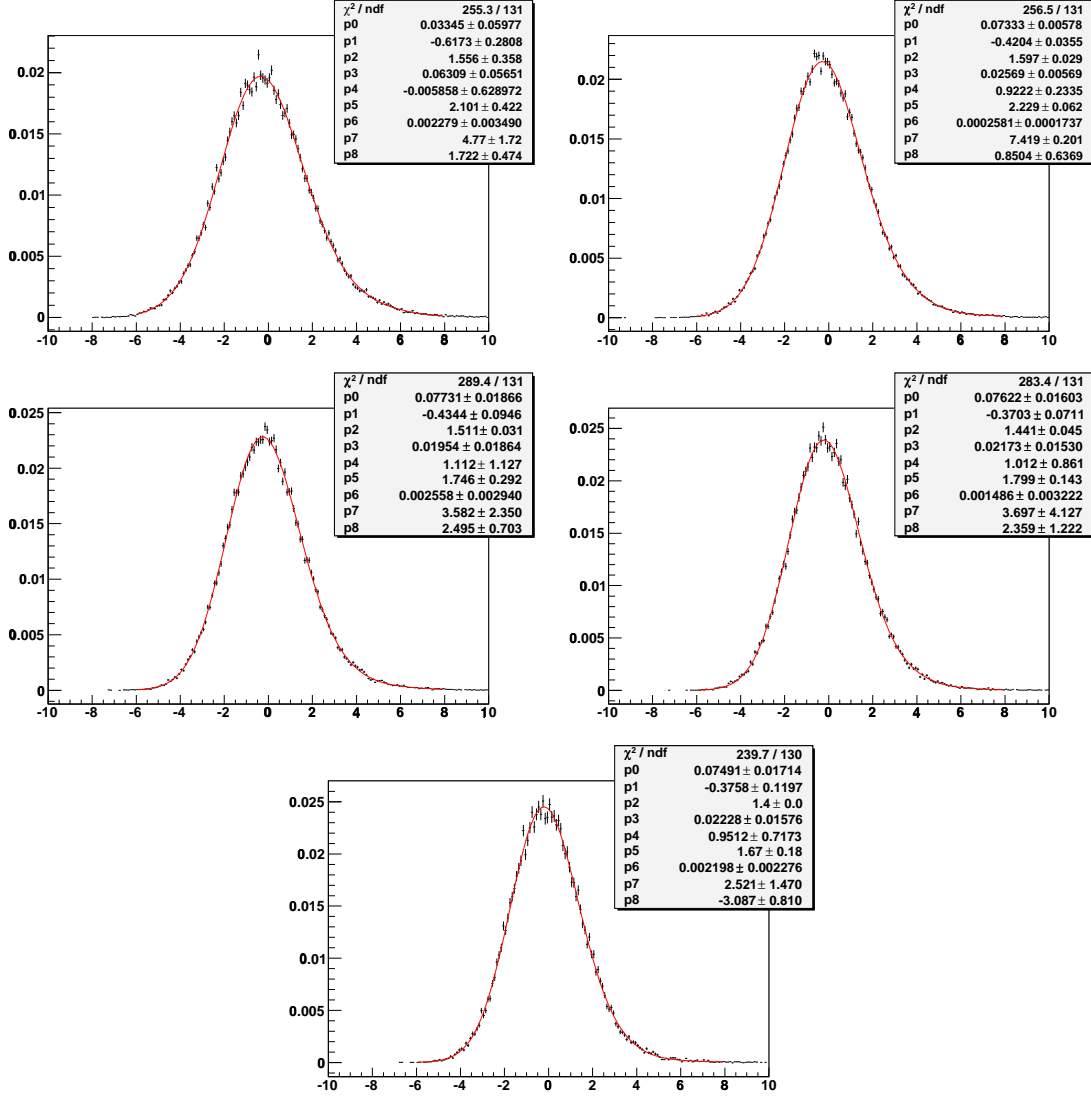


Figure 3.27: Fit of the negative soft pions residuals in momentum bins. From the Top left: (0.4 ≤ p < 0.5) GeV/c, (0.5 ≤ p < 0.6) GeV/c, (0.6 ≤ p < 0.7) GeV/c, (0.7 ≤ p < 0.8) GeV/c, (0.8 ≤ p < 0.9) GeV/c.

### 3.3.2 TOF parameterization

In this Section we describe the steps of the parameterization procedure used in the TOF case.

We found that, unlike the  $dE/dx$  case, a single gaussian is sufficient to describe the time of flight correlation  $p(\Delta_{TOF})$ . So  $p(\Delta_{TOF} = x) = c(x)$  where  $c(x)$  is a gaussian.

In Fig. 3.28 and Fig. 3.29 we reported the fits of the residuals respectively for negative pions and positive kaons performed using the fit functions  $(f'(x) + g'(x) + h'(x)) * G_{\mu=0.0, \sigma=0.0048}(x)$  and  $(f''(x) + g''(x) + h''(x)) * G_{\mu=0.0, \sigma=0.0048}(x)$  (first step). From these fits the parameters of the ideal residuals are determined to be used in the fit of the  $SUM_{TOF}$  distribution ( $TOF_{Res}^{\pi^-} + TOF_{Res}^{K^+}$ ) using the function  $p(TOF_{Res}^{\pi^-} + TOF_{Res}^{K^+}) = (f'(x) + g'(x) + h'(x)) * (f''(x) + g''(x) + h''(x)) * c(2x)$ . From the fit of  $SUM_{TOF}$  distribution we obtain  $p(\Delta_{TOF})$ , the parameters are equivalent to a very narrow Gaussian. This is not unexpected, as the TOF correlation is expected to be limited. Then we tried to fit the data in the assumption that the correlation function is a Dirac delta function, and found that this allows to describe the data very well as we can see from Fig. 3.30 where the fit of the sum distribution is shown. In Table 3.6 the correlation distribution parameters are shown.

Parameters	Value	Error
$A_{c1}$	1.0	0.004
$\mu_{c1}$	0.0005	0.0003
$\sigma_{c1}$	0.0	0.0

Table 3.6: Correlation distribution ( $p(\Delta_{TOF})$ ) parameters. It is a Dirac delta function.

In the TOF case, we use an universal residual parameterization for all particles, in fact there are not differences between pions and kaons and between positive and negative charges. So in the third step we fit only the negative pion residual (Fig. 3.31) and we determine the parameters relative to the ideal TOF residual.

The ideal TOF residual parameters are summarized in Table 3.7.

As a crosscheck, we verified that the curve obtained from the parameterization is in agreement with the difference distributions  $TOF_{Res}^{\pi^-} - TOF_{Res}^{K^+}$  (Fig. 3.32,  $\chi^2 = 160/100$ ) and  $TOF_{Res}^{\pi^+} - TOF_{Res}^{K^-}$  (Fig. 3.33,  $\chi^2 = 158/100$ ) and with the sum distribution  $TOF_{Res}^{\pi^+} + TOF_{Res}^{K^-}$  (Fig. 3.34,  $\chi^2 = 141/100$ ).

Parameters	Value	Error
$A_f$	0.75	0.015
$\mu_f$	-0.0022	0.0005
$\sigma_f$	0.0902	0.0009
$A_g$	0.185	0.015
$\mu_g$	0.0218	0.0039
$\sigma_g$	0.1812	0.0076
$A_h$	0.055	0.04
$\mu_h$	0.1874	0.0114
$\sigma_h$	0.431	0.012

Table 3.7: Ideal TOF residual parameters.

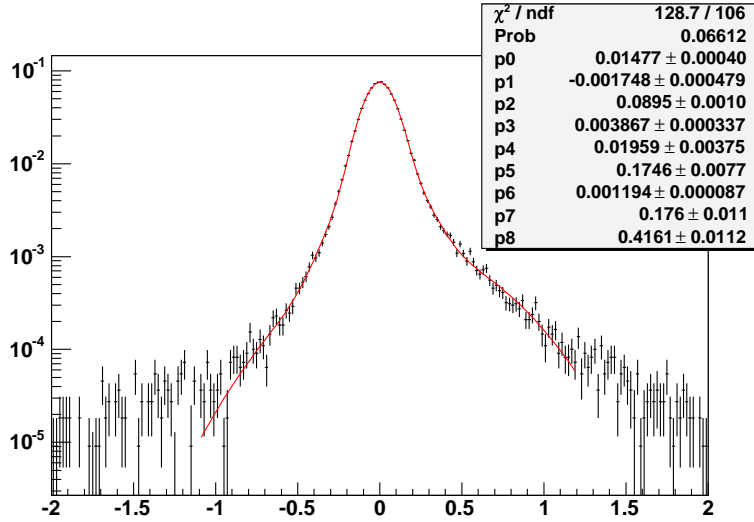


Figure 3.28: Fit of the  $\pi^-$  residual with  $(f'(x) + g'(x) + h'(x)) * G_{\mu=0.0, \sigma=0.0048}(x)$  (first step). The parameters of  $f'$ ,  $g'$  and  $h'$  are left free to vary in the fit.

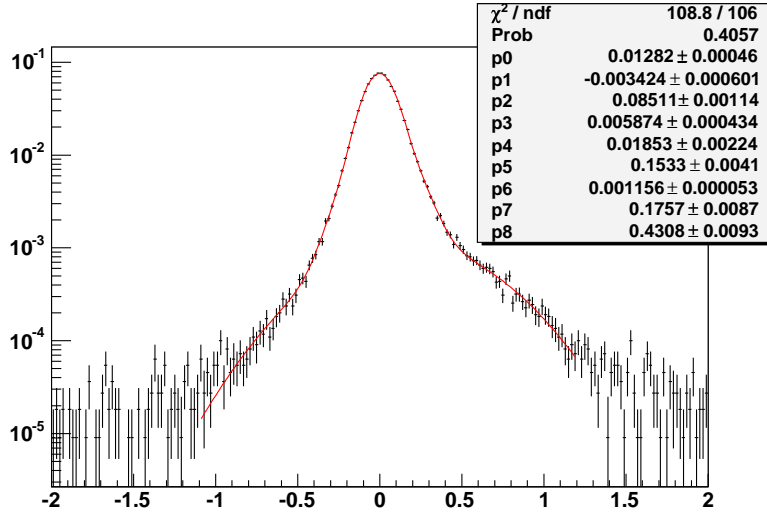


Figure 3.29: Fit of the  $K^+$  residual with  $(f''(x) + g''(x) + h''(x)) * G_{\mu=0.0, \sigma=0.0048}(x)$  (first step). The parameters of  $f''$ ,  $g''$  and  $h''$  are left free to vary in the fit.

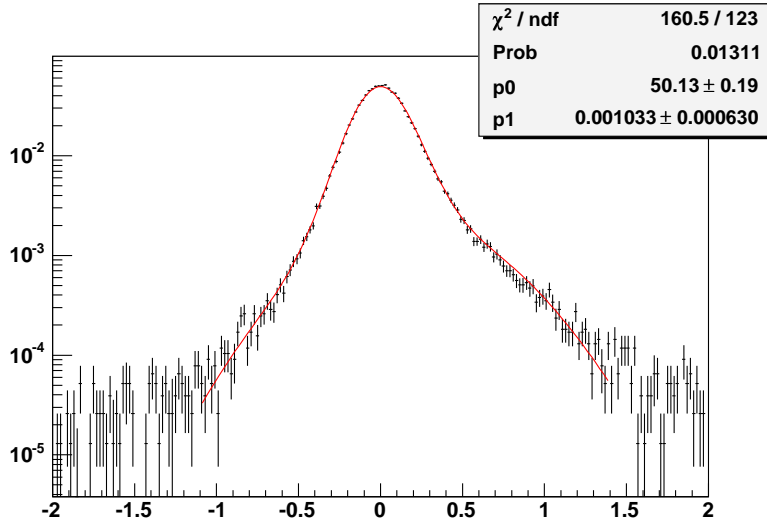


Figure 3.30: Fit of the  $SUM_{TOF}$  distribution  $TOF_{Res}^{\pi^-} + TOF_{Res}^{K^+}$  with  $(f'(x) + g'(x) + h'(x)) * (f''(x) + g''(x) + h''(x)) * c(2x)$  (second step). The parameters of  $c(2x)$  are left free to vary in the fit, while all the others are fixed.

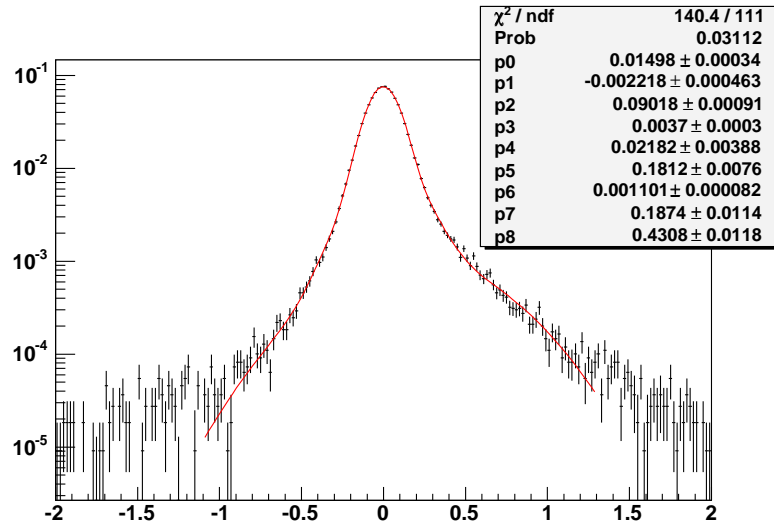


Figure 3.31: Fit of the pion residuals with  $(f'(x) + g'(x) + h'(x)) * c(x)$  (third step).

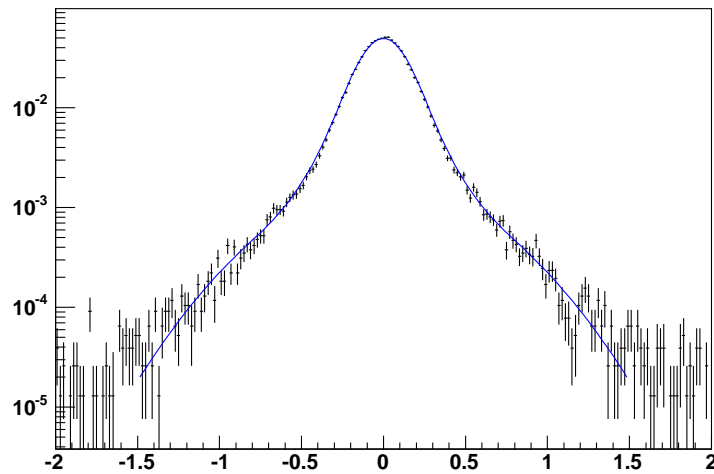


Figure 3.32: Parameterization crosscheck. Black: difference distribution (data)  $TOF_{Res}^{\pi^-} - TOF_{Res}^{K^+}$ . Blue: curve obtained from residuals and  $p(\Delta_{TOF})$  parameterization.  $\chi^2 = 160/100$ .

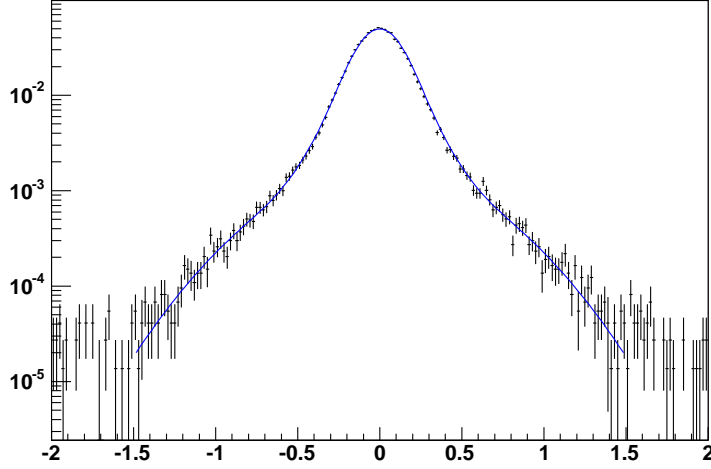


Figure 3.33: Parameterization crosscheck. Black: difference distribution (data)  $TOF_{Res}^{\pi^+} - TOF_{Res}^{K^-}$ . Blue: curve obtained from residuals and  $p(\Delta_{TOF})$  parameterization.  $\chi^2 = 158/100$ .

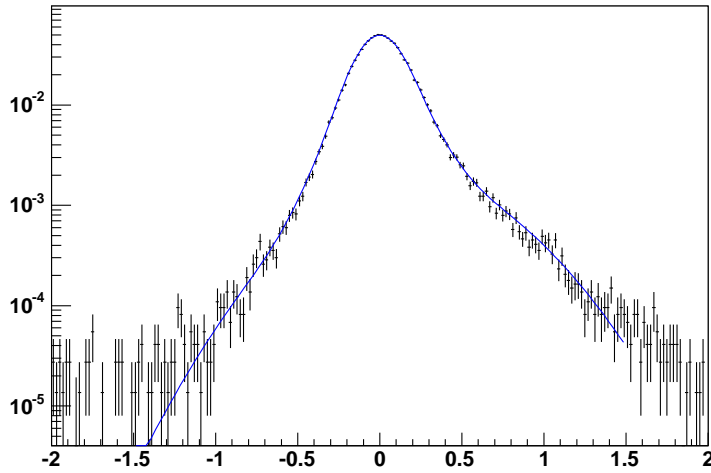


Figure 3.34: Parameterization crosscheck. Black: sum distribution (data)  $TOF_{Res}^{\pi^+} + TOF_{Res}^{K^-}$ . Blue: curve obtained from residuals and  $p(\Delta_{TOF})$  parameterization.  $\chi^2 = 141/100$ .

### TOF residuals for soft pions

Using the soft pions from the  $D^{*+}$  decay, we checked the validity of our parameterization for tracks with low momenta. In Fig. 3.35 the soft pions residuals in momentum bins of 0.1 GeV/c starting from 0.4 GeV/c are shown. The curve is obtained with the algorithm described above and there is a good agreement between data and parameterization.

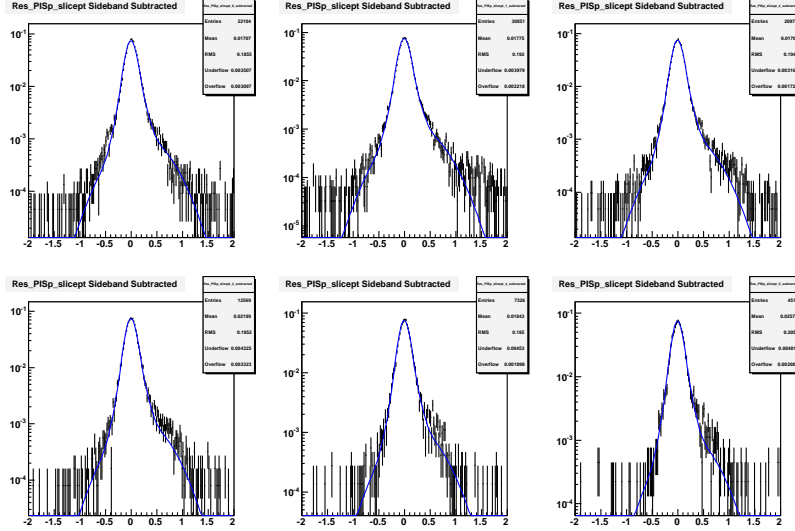


Figure 3.35: In black the soft pions residual distributions in momentum bins. (Momentum bin = 0.1 GeV/c starting from 0.4 GeV/c). In blue the parameterization obtained from trigger tracks.

## 3.4 Systematics treatment

Due to the large number of parameters used to describe the PID functions, the important question of the systematic uncertainty on a measurement making use of PID may be quite complicated to answer in practice.

We should vary the parameters of the PID functions in all the possible way. This is hard to do due to the large number of parameters. So we decided to generate the parameters shifts in a random way.

We take the multidimensional sphere, in the space of parameters, of radius  $n\sigma$  (number of standard deviation from the “default response”), and we randomly varied the parameters in this sphere.

In order to statistically sample a sufficient number of “directions” in the large space of systematic parameter shifts, we have to repeat the analysis for various seed values. For each seed value the PID functions change in a different way and we can obtain a measurement of the effect of systematic uncertainties on the analysis results.

To generate randomly a list of parameter shifts we used the congruence method [69]



( $i = 0, 1, \dots, npar$  where  $npar$  is the number of parameter of the function):

$$X[i + 1] = (a * X[i] + c) \bmod m \quad (3.19)$$

where  $a$ ,  $c$  and  $m$  are fixed by choosing one of the most used tern for the congruence method, we had choosen  $a = 40$ ,  $c = 3641$  and  $m = 729$  [69].  $X[0]$  is the seed value. The generated numbers are included in an interval  $[0, m - 1]$ , so to have a number between 0 and 1 we have to divide by  $m - 1$ .

We want to have shifts in all the directions, so we make a change of variables to have a generated number between -1 and 1.

Indicating with  $S[i]$  the shift vector we have:

$$S[i + 1] = \frac{\sqrt{npar} \cdot X[i + 1] \cdot n\sigma}{\sqrt{mod_X}} \quad (3.20)$$

where  $X[i]$  is the vector of the random generated numbers and  $mod_X$  is its modulus. So we shifted the PID functions parameters:

$$P_i = P_i + err_i \cdot S[i + 1]. \quad (3.21)$$

The base uncertainties ( $err_i$ ) on each parameter are determined either by finite statistics in the calibration sample (the errors in Tables 3.2, 3.3 and 3.4 for pions, kaons and protons respectively), or by the systematic shifts between alternative parameterizations.

For example, for  $dE/dx$  we have two alternative parameterizations. The one obtained using the trigger tracks and the ad hoc parameterization for low momentum tracks (Figs. 3.26 and 3.27). In this case the uncertainties are defined as  $err_i = \frac{P_i - P'_i}{\sqrt{12}}$ , where  $P_i$  and  $P'_i$  are the parameters of the two different parameterizations respectively. Considering these  $err_i$  we take into account the difference between the parameterization obtained from trigger tracks and the residuals of low momenta tracks, in the systematics.

In Fig. 3.36 the pion  $dE/dx$  residual (in black) is shown. The red curves are the curves obtained using the systematics described above. We used 20 different seeds and we obtained 20 different curves that produce a band around data and an uncertainty of about 0.1-0.2 ns (Fig. 3.36).

The code for the CDF II users accepts two variables relative to the systematics: the number of standard deviations from the “default” response ( $n\sigma$ ), and a seed value ( $X[0]$ ). If the first value is set to zero the code returns the “default” or “central” PID response. If a non-zero value is provided, the code generates the shifts of all parameters starting from the provided seed.

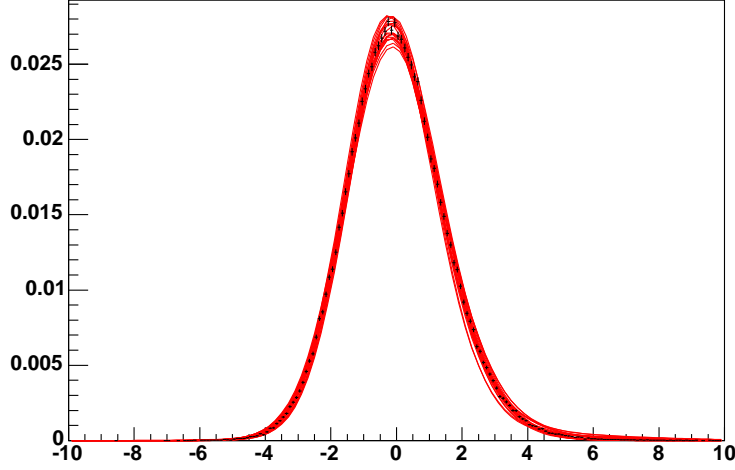


Figure 3.36: In black the pion  $dE/dx$  residual distribution. In red the 20 curves obtained using the systematics given by different seed values.

### 3.5 Combined PID performance

In this Section we show the performance of the Combined PID for both single track and track pairs case. For single track we measure the separation power  $K$ - $\pi$  and  $p$ - $\pi$  as a function of momentum.

For track pairs we apply Combined PID to select an optimized signal of  $\phi \rightarrow K^+ K^-$  decay. Moreover we check the validity of the treatment of correlation between particles in the same event.

In both case we use the Likelihood Ratio variable (LR) that is the optimal variable to cut on to separate the signal from the background.

From the Neyman-Pearson test [70]:

in separating two classes of events, A and B, of perfectly known distributions, applying a cut, the minimal contamination, for any value of the cut, is achieved by cutting on the Likelihood Ratio (LR)

$$\frac{L(A)}{L(B)}.$$

To use this method we must have a good knowledge of the properties of both signal and background.

For example, to separate kaons (signal) from a background of protons and pions we can cut on:

$$LR = \frac{L(signal)}{L(background)} = \frac{L(K)}{f_p \cdot L(p) + f_\pi \cdot L(\pi)} \quad (3.22)$$

where  $f_p$  and  $f_\pi$  are the fractions of protons and of pions in the background, and the Likelihood are defined in the Section 3.2.

The LR is correctly evaluated only if we know very well the fraction of the particle in the background; in the example we assumed a background of only protons and pions.

### 3.5.1 Single track

We used the Likelihood Ratio variable to give a statistical separation between protons and pions and between pions and kaons. Kaons and pions come from  $D^0 \rightarrow K^- \pi^+$  decay and protons from  $\Lambda \rightarrow p \pi^-$  decay. These data samples are described in Section 3.1.

For the p- $\pi$  separation the LR is

$$\frac{L_{combined\ PID}(\frac{dE}{dx}_{Res}, TOF_{Res}, \pi)}{L_{combined\ PID}(\frac{dE}{dx}_{Res}, TOF_{Res}, p)} = \frac{p(\frac{dE}{dx}_{Res}|\pi) \cdot p(TOF_{Res}|\pi)}{p(\frac{dE}{dx}_{Res}|p) \cdot p(TOF_{Res}|p)}. \quad (3.23)$$

We calculated this Likelihood Ratio for both pions and protons obtaining two curves shown in Fig.3.37, where the protons are in red and the pions are in black. These curves are relative to momenta higher than 2 GeV/c and the separation power obtained is 2.3  $\sigma$ . The method to compute the separation is described in Section 3.5.2.

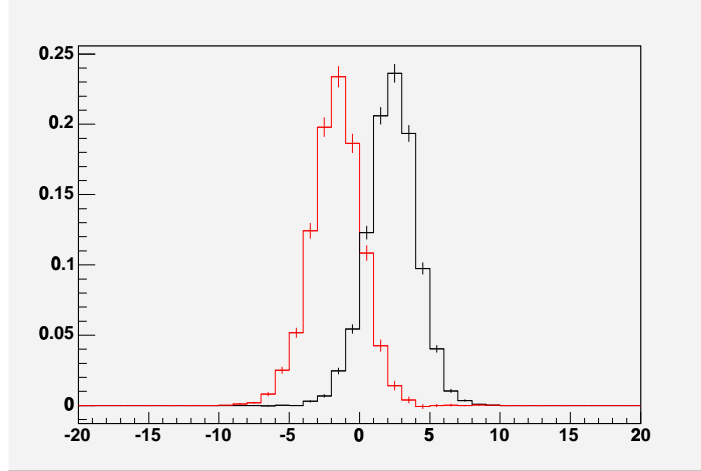


Figure 3.37: Combined PID.  $\frac{L_{combined\ PID}(\frac{dE}{dx}_{Res}, TOF_{Res}, \pi)}{L_{combined\ PID}(\frac{dE}{dx}_{Res}, TOF_{Res}, p)}$  calculated for protons (in red) and for pions (in black). The separation power obtained is 2.3  $\sigma$ .

To check the validity of the LR method we also look at the  $dE/dx$  and at the TOF separately. We used the  $dE/dx$  and the TOF residual distributions calculated in pion hypothesis:

$$\frac{dE}{dx}_{Res\ hyp\ \pi} = \frac{dE}{dx}_{measured} - \frac{dE}{dx}_{expected} \quad (3.24)$$

$$TOF_{Res\ hyp\ \pi} = TOF_{measured} - TOF_{expected}^{\pi} \quad (3.25)$$

Since we used the pion hypothesis, for the pions we obtained a curve centered in zero. For the protons instead, a curve shifted with respect to zero. These curves are shown

in Fig. 3.38, the  $dE/dx$  on the left and the TOF on the right, the protons in red and the pions in black.

In the  $dE/dx$  case the protons are at the left of the pions, in fact from the Universal Curve reported in Fig. 3.5, the  $dE/dx$  of the protons with momentum higher than 2 GeV/c ( $\beta\gamma > 1.8$ ) is lower than the  $dE/dx$  of the pions with the same momentum ( $\beta\gamma > 24$ ).

In the TOF case instead the protons are at the right of the pions, in fact the protons are heavier than pions and so they need more time to arrive at the TOF detector.

The separation power obtained using  $dE/dx$  is  $1.7 \sigma$  and using TOF is  $1.25 \sigma$ .

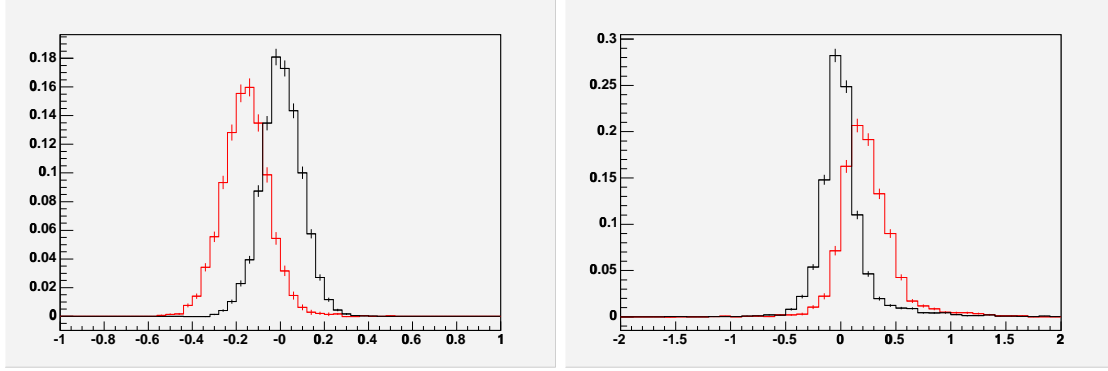


Figure 3.38: Left:  $dE/dx$  residual in pion hypothesis calculated for protons (in red) and for pions (in black). We obtained a separation of  $1.7 \sigma$ . Right: TOF residual in pion hypothesis calculated for protons (in red) and for pions (in black). We obtained a separation of  $1.25 \sigma$ .

Fig. 3.39 shows the  $p$ - $\pi$  separation as a function of the momentum of the particle. This plot was obtained computing the separation power in momentum bins. To do that we made the same curves of Figs. 3.37 and 3.38, for pions and protons, of Combined Likelihood Ratio  $\frac{L_{combined\ PID}(\frac{dE}{dx}_{Res}, TOF_{Res}, \pi)}{L_{combined\ PID}(\frac{dE}{dx}_{Res}, TOF_{Res}, p)}$  and of  $dE/dx$  and TOF residuals in pion hypothesis, in momentum bins. For each bin we computed the separation power between pions and protons.

The black curve is relative to the TOF, the red one is relative to the  $dE/dx$  and the green one is relative to the combined PID (TOF+ $dE/dx$ ). In blue we have the theoretical curve obtained adding in quadrature the TOF and the  $dE/dx$  separation:

$$C_{theo} = \sqrt{(TOF_{sep})^2 + (dE/dx_{sep})^2}. \quad (3.26)$$

The separation obtained with the combined PID, around  $2.5 \sigma$ , is very close to the theoretical maximum. This confirms the validity of the LR method and also the correctness of the parameterization of both TOF and  $dE/dx$  distributions, described in Section 3.3, and the absence of spurious correlation between the two PIDs.

We used the LR method also for the  $K$ - $\pi$  separation. In this case the LR is defined:

$$\frac{L_{combined\ PID}(\frac{dE}{dx}_{Res}, TOF_{Res}, \pi)}{L_{combined\ PID}(\frac{dE}{dx}_{Res}, TOF_{Res}, K)} = \frac{p(\frac{dE}{dx}_{Res}|\pi) \cdot p(TOF_{Res}|\pi)}{p(\frac{dE}{dx}_{Res}|K) \cdot p(TOF_{Res}|K)}. \quad (3.27)$$

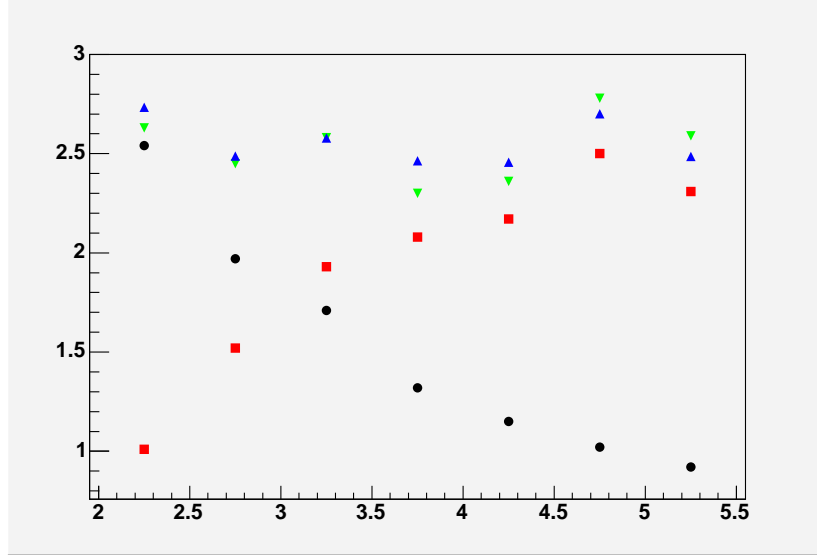


Figure 3.39:  $p$ - $\pi$  separation power vs momentum. Black: TOF separation. Red:  $dE/dx$  separation. Green: combined separation obtained with the LR. Blue:  $\sqrt{(TOF_{sep})^2 + (dE/dx_{sep})^2}$ .

The  $K$ - $\pi$  separation power as a function of the momentum of the particle is reported in Fig. 3.1 at the beginning of this Chapter.

For momentum greater than 2 GeV/c the time of flight is not very useful, it increases the  $dE/dx$  separation of only 0.1-0.2  $\sigma$  for momentum lower than 3 GeV/c and higher than 2 GeV/c. We can see the TOF effect for lower momentum. The  $K$ - $\pi$  separation at low momentum was obtained through a Toy MC, described in the following, using the parameterization of  $dE/dx$  and TOF residuals obtained from data.

The black vertical line in Fig. 3.1 separates the value of separation power obtained from data to the value obtained from Toy MC.

For momentum below 0.8 GeV/c we have a good separation both for TOF and  $dE/dx$ , so we obtain a very good combined separation from 4 up to 10  $\sigma$ .

The importance of TOF at lower momentum will be also evidenced in the case of the track pairs with the  $\phi \rightarrow K^+ K^-$  decay (Section 3.5.3).

### Toy MC for low momentum

This Toy MC was developed to have an idea of the PID separation ( $dE/dx$ , TOF and Combined PID separation) for low momentum particles since the PID parameterization was made using tracks with momentum higher than 2 GeV/c.

To calculate the separation between particles with momentum lower than 2 GeV/c we need their measured  $dE/dx$  and TOF values.

We randomly generated  $dE/dx$  and TOF residual values using the residual parameterization obtained from data (tracks with momentum higher than 2 GeV/c), described in Section 3.3. We obtained  $\frac{dE}{dx}_{Res}^i$  and  $TOF_{Res}^i$ ,  $i = K, \pi$ .

We calculated the expected  $dE/dx$  for pions and kaons ( $\frac{dE}{dx}_{expected}^i$ ) with momentum between 0.4 and 2 GeV/c using the Universal Curve, giving as input the momentum, the mass and the charge of the particle. To calculate the expected TOF ( $TOF_{expected}^i$ ) we used the formula  $t_{exp} = \frac{L}{c} \sqrt{1 + \frac{m^2 c^2}{p^2}}$ , obtained inverting the eq. (2.6), where  $L$  is the flight length,  $p$  is the particle momentum and  $m$  the particle mass.

The measured values of  $dE/dx$  and TOF,  $\frac{dE}{dx}_{measured}^i = \frac{dE}{dx}_{Res}^i + \frac{dE}{dx}_{expected}^i$  and  $TOF_{measured}^i = TOF_{Res}^i + TOF_{expected}^i$ , of pions and kaons allow to have the Likelihood Ratio curve of Combined PID, from which we can compute the separation.

The results of this Toy MC are the separation vs momentum curves for momentum lower than 2 GeV/c of Fig. 3.1.

### 3.5.2 Separation compute

The separation depends on the variable used to measure it. Once chosen the variable ( $x$ ), for example the LR variable, one plots the distribution of such a variable for the two classes of which the separation have to be estimated (i.e. K and  $\pi$  or p and  $\pi$  in our case).

The probability distribution of  $x$  for our sample of two classes is:

$$P_{tot}(x|f_1) = f_1 \cdot p_1(x) + (1 - f_1) \cdot p_2(x) \quad (3.28)$$

where  $p_i(x)$  is the pdf of  $x$  for events of type  $i$  and  $f_1$  is the fraction of events of type 1. Since the sum of the fractions of the different classes present in the sample must be 1 in order for the overall distribution to be correctly normalized,  $f_2 = 1 - f_1$ .

The most basic information one wishes to extract from the sample of data at hand is the value of the fraction  $f_1$ ; we can therefore take the resolution in extracting  $f_1$  as the measure of the separating power of the observable  $x$ .

Instead of setting up a Maximum Likelihood fit and repeating it on a sufficient number of pseudo-experiment, the Minimum Variance Bound (MVB) [70] estimates rather quickly the upper bound of the achievable resolution  $\sigma$  on the fraction  $f_1$ . For the simple case of two classes of events the MVB is written as:

$$\sigma^2(f_1) = \frac{1}{N} \left( \int \frac{(p_1(x) - p_2(x))^2}{f_1 \cdot p_1(x) + (1 - f_1) \cdot p_2(x)} dx \right)^{-1} \quad (3.29)$$

where  $N$  is the total number of events. This is the quantity you want to minimize in order to achieve the best possible statistical separation. In the limiting case the chosen variable is distributed in the two classes as two Gaussians infinitely spaced apart (events totally separated). The only uncertainty in assigning an event to one of the two classes comes from the Binomial fluctuation due to finite sample size  $\sigma_{best}^2 = f_1(1 - f_1)/N$ .

It is particularly convenient [71] to use the ratio of the resolution (equation (3.29)) to the limit resolution  $\sigma_{best}$ , in order to quote the separation power of the observable  $x$  as an adimensional quantity:

$$s = \frac{\sigma_{best}}{\sigma(f_1)} = \sqrt{f_1(1 - f_1) \int \frac{(p_1(x) - p_2(x))^2}{f_1 \cdot p_1(x) + (1 - f_1) \cdot p_2(x)} dx} \quad (3.30)$$

This estimate is independent of the sample size and tells us the power of  $x$  in separating the samples, from 0 (no separation), to 1 (absolute maximum achievable with the given sample). It is convenient to quote  $s$ , by convention, for  $f_1 = \frac{1}{2}$ . Such a way to quote separation has the advantage of being valid whatever the shape and the dimensionality of the distribution involved. In addition, it is possible to quote the separation in the conventional way (“ $n$ - $\sigma$  separation”) by converting analitically any value of “ $s$ ” into an “equivalent  $\sigma$  separation” calculated as if the distribution of the considered variable  $x$  were Gaussian.

### 3.5.3 Test of the combined Likelihood for track pairs: $\phi \rightarrow K^+K^-$ decay

To test the combined Likelihood for track pairs and the correctly inclusion of the correlation we used the  $\phi \rightarrow K^+K^-$  decay from B\_PIP1 trigger path described in Section 2.8.5.

In Fig. 3.40 the  $\phi$  invariant mass distribution obtained with the following cuts is shown:

- $\Delta\phi$  between tracks  $< 0.1$
- Both tracks have associated TOF measurement (TOF efficiency<sup>3</sup> = 28%, 53% for each track)[65][67].

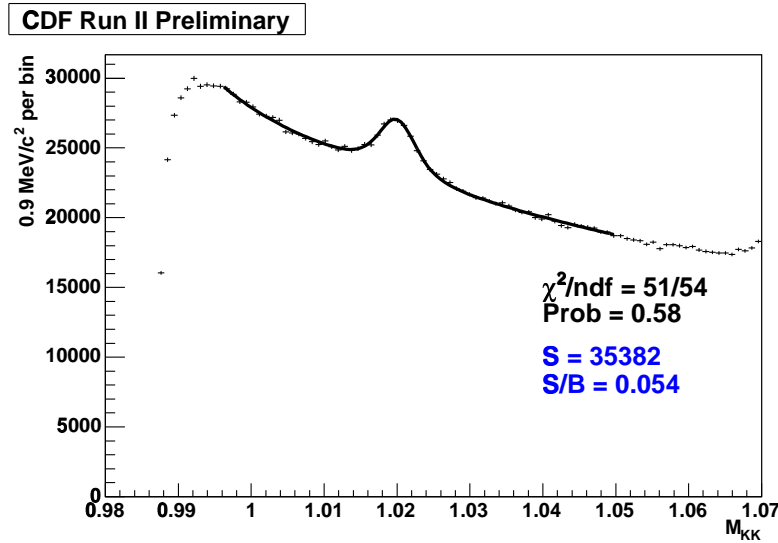


Figure 3.40: Invariant mass distribution of  $\phi \rightarrow K^+K^-$ , both tracks have the TOF information.

We fitted the observed spectrum using for the signal shape the convolution of a Breit Wigner with a gaussian resolution function, and for the combinatorial background a threshold function:  $a \cdot (M_{KK} - 2 \cdot M_K)^b e^{c \cdot (M_{KK} - 2M_K)}$  where  $a$ ,  $b$  and  $c$  are free parameters

<sup>3</sup>The TOF inefficiency is due to the high TOF occupancy, that is  $\sim 30\%$

[72]. From the fit we obtained 35,382  $\phi \rightarrow K^+K^-$  with a signal over background  $\frac{S}{B} = 0.054$ .

At first we checked the inclusion of the correlation between particles in the same event in the Likelihood. We considered the TOF Likelihood including correlation  $L_{\text{TOF corr}}$  and the TOF Likelihood without correlation  $L_{\text{TOF no corr}}$ . In Fig. 3.41 the rejection vs efficiency, varying the cut on LR, is shown, the red curve is relative to a cut on LR that includes correlation and the green one is relative to a cut on LR without the correlation.

The efficiency is defined as:

$$eff = \frac{\text{Signal after cut}}{\text{Signal before cut}} \quad (3.31)$$

and the rejection as:

$$rej = \frac{\frac{S}{B} \text{ after cut}}{\frac{S}{B} \text{ before cut}}. \quad (3.32)$$

We observe that the rejection improves, as expected, with the inclusion of the correlation.

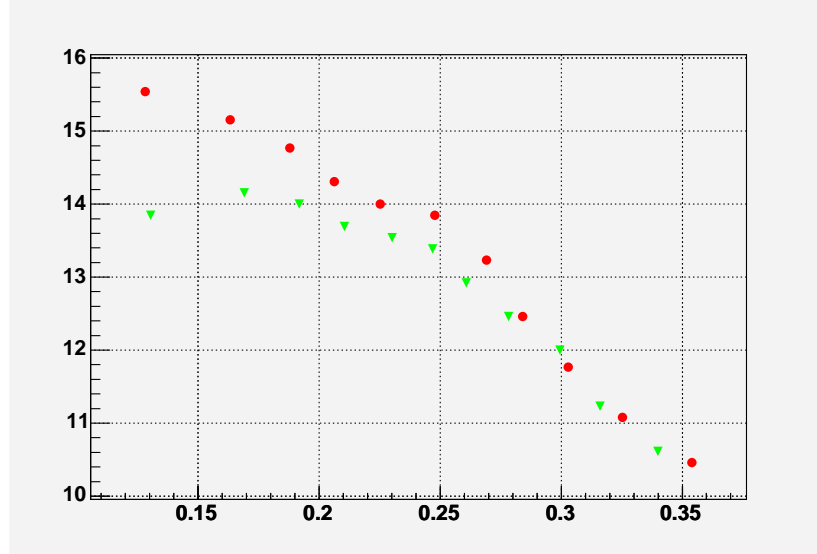


Figure 3.41: Red curve: rejection vs efficiency varying the cut on LR considering the correlation. Green curve: rejection vs efficiency varying the cut on LR without the correlation. The rejection improves with the inclusion of the correlation.

Including correlation we improve the rejection and moreover we remove the BIAS in a fit making use of the PID information. As an example of the BIAS we can consider the  $B_{(s)}^0 \rightarrow h^+h'^-$  analysis at CDF II [6]. The result of  $\frac{f_s}{f_d} \frac{BR(B_s \rightarrow KK)}{BR(B_d \rightarrow K\pi)}$  obtained using a maximum Likelihood fit including the PID information, changes if the correlation was



considered or not<sup>4</sup>:

- no correlation  $\frac{f_s}{f_d} \frac{BR(B_s \rightarrow KK)}{BR(B_d \rightarrow K\pi)} = 0.74 \pm 0.20(stat) \pm 0.22(sys)$ ;
- with correlation  $\frac{f_s}{f_d} \frac{BR(B_s \rightarrow KK)}{BR(B_d \rightarrow K\pi)} = 0.50 \pm 0.08(stat) \pm 0.09(sys)$ .

We used the  $L_{\text{combined PID}}^{\text{track pairs}}$  described in Section 3.2, to make a cut on Likelihood Ratio (LR) and extract the  $\phi \rightarrow K^+ K^-$  decay from background. We have to define the LR as the signal Likelihood over the background Likelihood. In this case the signal is the pair KK and the background are the pairs that we can obtain combining protons, pions and kaons. So the LR is defined as:

$$LR = \frac{L_{\text{sign}}}{L_{\text{back}}} = \frac{L_{KK}}{f_K f_K L_{KK} + f_\pi f_\pi L_{\pi\pi} + f_p f_p L_{pp} + f_K f_\pi L_{K\pi} + f_K f_p L_{Kp} + f_\pi f_p L_{\pi p}} \quad (3.33)$$

where we assumed that in the background the particle IDs are uncorrelated, so for example  $f_{KK} = f_K \cdot f_K$ .

We estimated, roughly, the background fractions  $f_K$ ,  $f_\pi$  and  $f_p$  from the TOF residual distributions in the sidebands of the  $\phi$  invariant mass. The  $\phi$  signal window is defined as  $\pm 2.5\sigma$  around the reconstructed  $\phi$  mass peak and the sidebands window is between 4 and 6.5  $\sigma$  from the mean value,  $(M - 6.5\sigma, M - 4\sigma) \cup (M + 4\sigma, M + 6.5\sigma)$ . We obtained:

- $f_p = 10\%$
- $f_K = 20\%$
- $f_\pi = 70\%$ .

In Fig. 3.42 the invariant mass distribution of  $\phi \rightarrow K^+ K^-$  after a cut on the LR is shown. The continuous line is the fit, we obtained 10,234  $\phi \rightarrow K^+ K^-$ , corresponding to an efficiency of 30%, and a signal over background of  $\frac{S}{B} = 1.1$ , corresponding to a rejection of 20.

In Fig. 3.43 the rejection vs efficiency varying the LR cut, is shown. Three curves are plotted, the blue one is relative to the combined PID, the red one to the dE/dx and the black one to the TOF. This means that three different LR were used to cut on:

- blue curve: cut on the combined PID LR that uses  $L_{\text{combined PID}}^{\text{track pairs}}$ ;
- red curve: cut on the dE/dx LR that uses  $L_{\text{dE/dx}}^{\text{track pairs}}$ ;
- black curve: cut on the TOF LR that uses  $L_{\text{TOF}}^{\text{track pairs}}$ .

From the plot we observe that the combined PID permits to obtain a very good rejection at high efficiency.

We can also see that the TOF contribution is higher than the dE/dx contribution, this is due to the low momentum spectrum of kaons from  $\phi \rightarrow K^+ K^-$  decay, shown in Fig. 3.44.

---

<sup>4</sup>The first result (without correlation) is relative to 65  $pb^{-1}$ , the second one (with correlation) is relative to 180  $pb^{-1}$ .

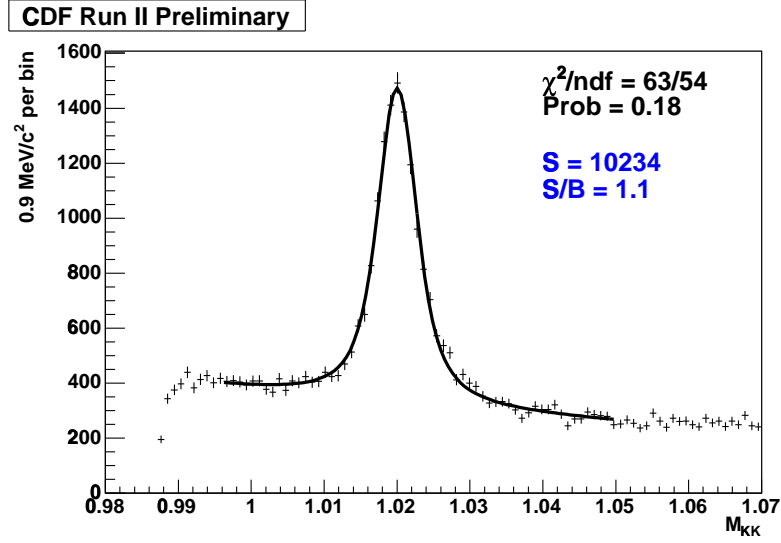
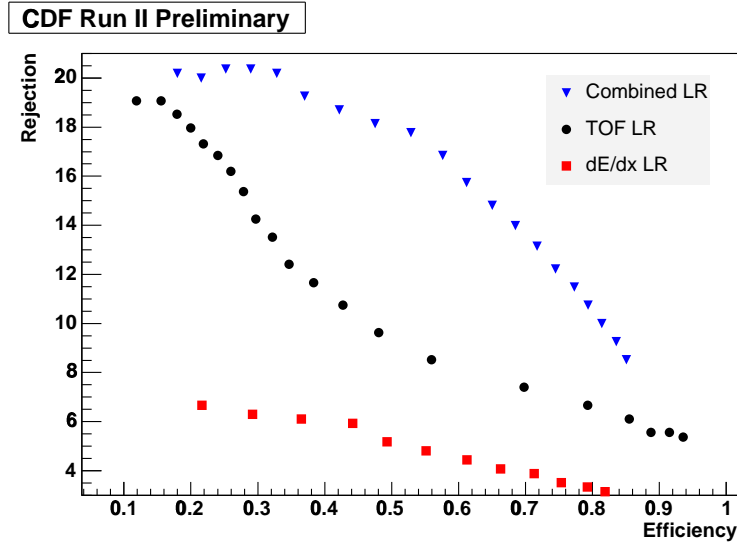
Figure 3.42: Invariant mass distribution of  $\phi \rightarrow K^+ K^-$  after the cut on LR.

Figure 3.43: Rejection vs efficiency varying the LR cut. Blue curve: cut on the combined PID LR that uses  $L_{\text{combined PID}}^{\text{track pairs}}$ . Red curve: cut on the dE/dx LR that uses  $L_{dE/dx}^{\text{track pairs}}$ . Black curve: cut on the TOF LR that uses  $L_{TOF}^{\text{track pairs}}$ . The combined PID permits to obtain a very good rejection at high efficiency.

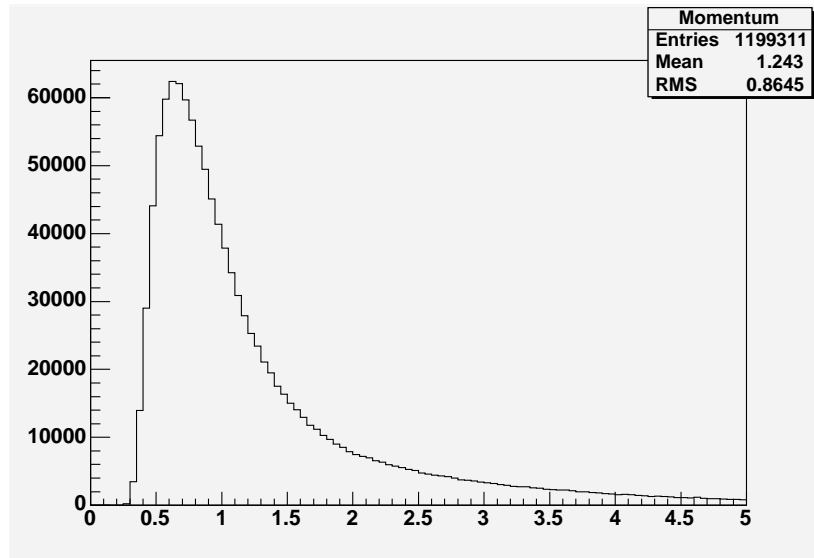


Figure 3.44: Momentum spectrum of kaons from  $\phi \rightarrow K^+ K^-$  decay.

### 3.6 Combined PID applications

The TOF, dE/dx and Combined (TOF+dE/dx) Likelihoods, for single track and for track pairs, are implemented in a public code for CDF II users.

The code was used in several CDF analysis, the most relevant are:

- $B_{(s)}^0 \rightarrow h^+ h'^-$  analysis;
- $B_s$  mixing;
- $B^+ \rightarrow \bar{D}^0 K^+$  modes for the  $\gamma$  angle measurement (argument of this thesis, see next Chapter).

In the case of  $B_{(s)}^0 \rightarrow h^+ h'^-$  analysis [6] the dE/dx Likelihood for track pairs is the crucial ingredient of the Unbinned Maximum Likelihood Fit used to distinguish all the contributes present in the peak.

Thanks to PID the fit can distinguish between  $KK$ ,  $\pi K$  and  $\pi\pi$ . In Fig. 3.45 the  $B_{(s)}^0 \rightarrow h^+ h'^-$  invariant mass distribution in  $\pi\pi$  hypothesis, obtained using  $360 \text{ pb}^{-1}$ , is shown. The point are data, the black curve is the total fit projection and the color areas are the various contributions ( $B^0 \rightarrow K\pi$ ,  $B_s^0 \rightarrow KK$ ,  $B^0 \rightarrow \pi\pi$  and  $B_s^0 \rightarrow K\pi$ ) to the experimental invariant mass spectrum.

In the case of  $B_s$  mixing the Particle IDentification has been crucial to determine the  $B_s$  flavor at the production [5]. At the production the  $B_s$  is accompanied by a K; using the combined PID Likelihood for single track it has been possible to identify the Kaons associated with the  $B_s$  production. The PID is the fundamental ingredient of the Same Side Kaon Tagging, that is the tagger with the largest effectiveness.

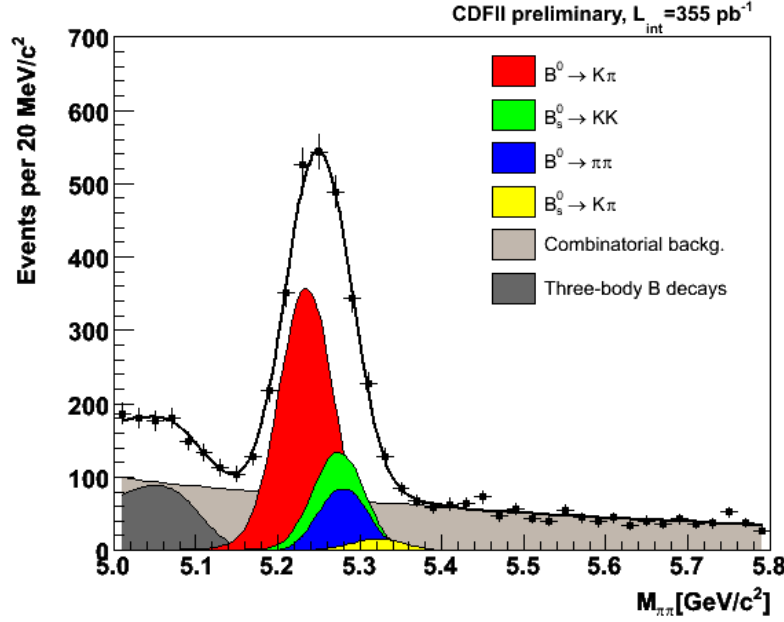


Figure 3.45:  $B_{(s)}^0 \rightarrow h^+ h'^-$  peak using  $360 \text{ pb}^{-1}$ . Point: data. Black curve: total fit projection. Color areas: various contributions to the experimental invariant mass spectrum.

The effectiveness  $Q \equiv \epsilon D^2$  is quantified with an efficiency  $\epsilon$ , the fraction of signal candidates with a flavor tag, and a dilution  $D \equiv 1 - 2w$ , where  $w$  is the probability that the tag is incorrect. For the Same Side Kaon Tagging the effectiveness pass from  $Q \sim 2\%$  without PID to  $Q \sim 3.5\%$  using the Combined PID [5].

Regarding the  $B^+ \rightarrow \bar{D}^0 K^+$ , in the next Chapter (Chapter 4) we will describe the implementation of an Unbinned Maximum Likelihood Fit using PID information, to separate statistically  $B^+ \rightarrow \bar{D}^0 K^+$  from  $B^+ \rightarrow \bar{D}^0 \pi^+$ .

In order to demonstrate the PID capability of CDF we show here an application of the Combined PID at the  $B^+ \rightarrow \bar{D}^0 K^+$  decay.

We used the  $B^+ \rightarrow \bar{D}^0 \pi^+$  candidates sample described in Section 4.1. In Fig. 3.46 this sample selected without the use of a PID tool is shown. The signal of  $B^+ \rightarrow \bar{D}^0 K^+$ , in light blue, is obtained from simulation assuming  $\frac{BR(B^+ \rightarrow \bar{D}^0 K^+)}{BR(B^+ \rightarrow \bar{D}^0 \pi^+)} = 0.083$  [13]. It is overlaid of background and cannot be distinguished from the  $B^+ \rightarrow \bar{D}^0 \pi^+$ .

We then apply a cut, to the track from B, on the Combined (TOF+dE/dx) LR defined as  $\frac{L_{\text{combined PID}}(\frac{dE}{dx}_{Res}, TOF_{Res}, K)}{L_{\text{combined PID}}(\frac{dE}{dx}_{Res}, TOF_{Res}, \pi)}$  to select kaons ( $B^+ \rightarrow \bar{D}^0 K^+$ ) and reject pions ( $B^+ \rightarrow \bar{D}^0 \pi^+$ ). In Fig. 3.47 the invariant mass distribution of  $B^+ \rightarrow \bar{D}^0 K^+$ , after the LR cut ( $LR > 0.6$ ), is shown. A fit of the invariant mass spectrum making use of two gaussians for the signal (one describing the  $B^+ \rightarrow \bar{D}^0 K^+$  signal shape and the other describing the  $B^+ \rightarrow \bar{D}^0 \pi^+$  signal shape) and of an exponential plus a constant for the

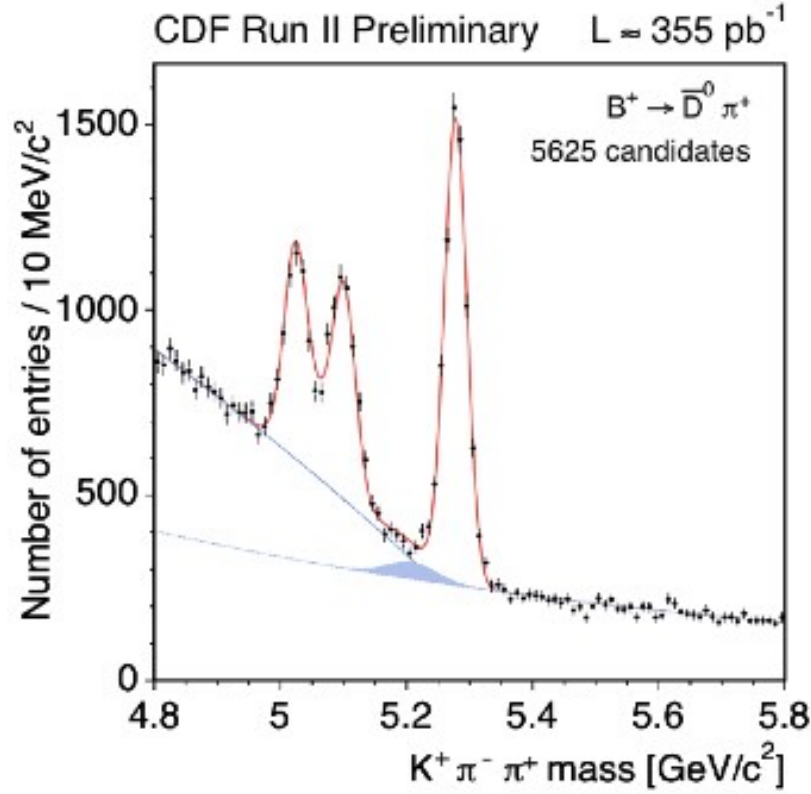


Figure 3.46:  $B^+ \rightarrow \bar{D}^0 \pi^+$  invariant mass. In light blue the  $B^+ \rightarrow \bar{D}^0 K^+$ , obtained from simulation assuming that  $\frac{BR(B^+ \rightarrow \bar{D}^0 K^+)}{BR(B^+ \rightarrow \bar{D}^0 \pi^+)} = 0.083$ .

background, is done in the range of mass  $[5.2, 5.8] \text{ GeV}/c^2$ .

The two signal yields are free to vary in the fit, while the means and the widths of the gaussians that describe the  $B \rightarrow \bar{D}^0 K^+$  (red curve) and  $B \rightarrow \bar{D}^0 \pi^+$  (blue curve) signals, are fixed by simulation. The background, in green, is an exponential plus a constant. We obtained  $\sim 85 \bar{D}^0 K^+$  and  $\sim 245 \bar{D}^0 \pi^+$ . We can see the powerfull of the Combined PID that makes visible the two peaks.

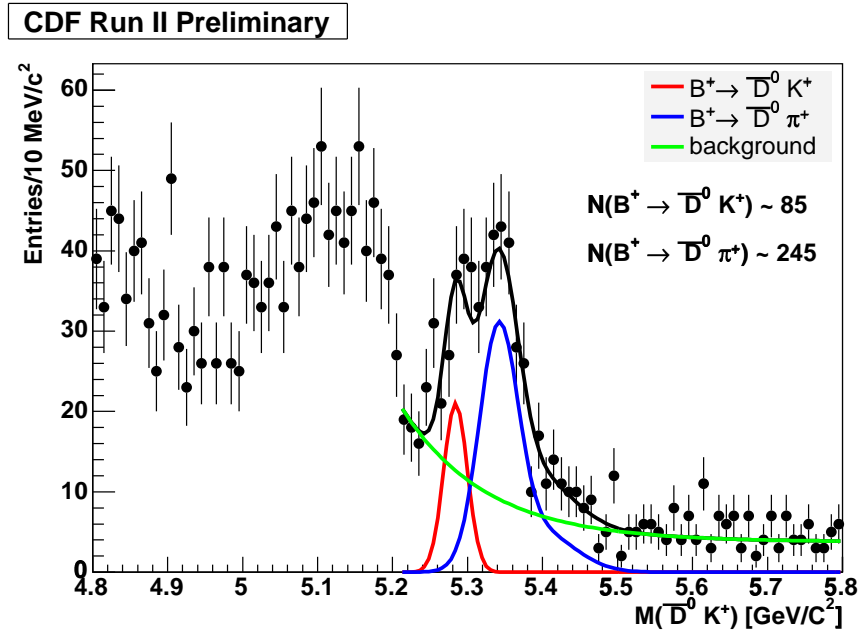


Figure 3.47:  $B \rightarrow \bar{D}^0 K^+$  invariant mass after the cut on  $LR = \frac{L_{\text{combined PID}}(\frac{dE}{dx}_{Res}, TOF_{Res}, K)}{L_{\text{combined PID}}(\frac{dE}{dx}_{Res}, TOF_{Res}, \pi)}$  ( $LR > 0.6$ ). The Combined PID makes visible the two peaks.

## Chapter 4

# Measurement of $\frac{BR(B^+ \rightarrow \overline{D}^0 K^+)}{BR(B^+ \rightarrow \overline{D}^0 \pi^+)}$

As pointed out in Section 1.5 there are several methods to measure the angle  $\gamma$ . In this Chapter we describe the first step of the GLW method, that is the measurement of the ratio

$$R = \frac{BR(B^+ \rightarrow \overline{D}^0 K^+)}{BR(B^+ \rightarrow \overline{D}^0 \pi^+)} = \frac{BR(B^+ \rightarrow [K^+ \pi^-] K^+)}{BR(B^+ \rightarrow [K^+ \pi^-] \pi^+)}. \quad (4.1)$$

The CDF mass resolution and Particle IDentification capability do not allow an event-by-event separation of the decay modes  $\overline{D}^0 K^+$  and  $\overline{D}^0 \pi^+$ , and a different approach, aiming to obtain a statistical separation, is required.

We used an Unbinned Maximum Likelihood Fit which combines the small kinematics differences between the  $\overline{D}^0 \pi^+$  and the  $\overline{D}^0 K^+$  decay modes and the Particle IDentification information provided by the specific ionization ( $dE/dx$ ) in the drift chamber. This technique was used, in CDF, also for the  $B_{(s)}^0 \rightarrow h^+ h'^-$  analysis [6].

In the last part of the Chapter we will also describe the fit results on the DCP modes ( $B^+ \rightarrow D_{CP^+} K^+ \rightarrow [K^+ K^-] K^+$  and  $B^+ \rightarrow D_{CP^+} K^+ \rightarrow [\pi^+ \pi^-] K^+$ ).

### 4.1 Data sample

We want to reconstruct the decays of  $B^+ \rightarrow \overline{D}^0 \pi^+$  and of  $B^+ \rightarrow \overline{D}^0 K^+$ . The proper decay length  $c\tau$  of a  $B^+$  is about  $460 \mu\text{m}$ . The  $c\tau$  of  $D^0$ ,  $D^+$ ,  $D_s^+$  and  $\Lambda_c^+$  are about 120, 150, 300 and  $60 \mu\text{m}$ . Long lived  $K_s^0$  and  $\Lambda$  have much longer lifetime, 2-8 cm. Therefore, a minimum requirement on the distance between the beamline (primary vertex) and the secondary vertex reconstructed in the transverse plane ( $L_{xy}$ ), reduces the contamination due to short lived charmed hadrons. Moreover, the particles produced in the B decay also tend to have a larger impact parameter in the transverse plane ( $d_0$ ) than the tracks produced in the primary vertex, as illustrated in Fig. 4.1, but smaller  $d_0$  than the daughters particles of  $K_s^0$  and  $\Lambda$ . Consequently, a minimum and a maximum cut on the track  $d_0$  rejects the background from the primary tracks,  $K_s$  and  $\Lambda$ , or secondary tracks generated by the particle interaction with the material.

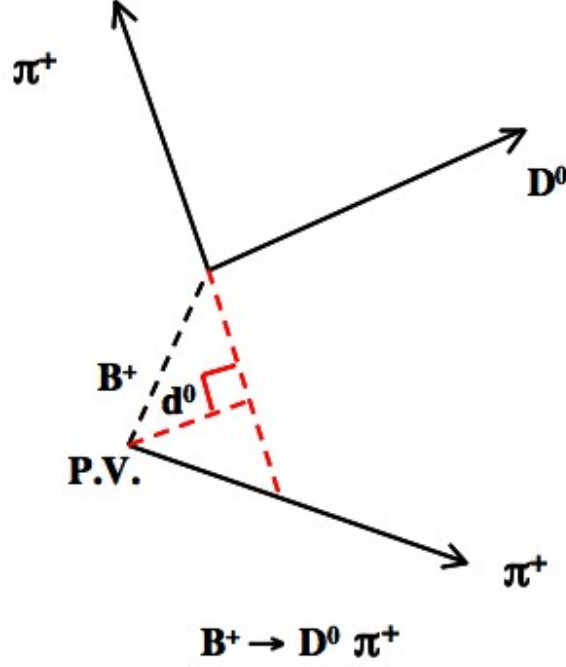


Figure 4.1: Example of a  $B^+$  decay:  $\pi^+$  from the  $B^+$  decay has a larger impact parameter  $d_0$  than that of the track produced at the primary vertex.

The data used for this analysis have been collected with the upgraded CDF II detector, between April 2001 and August 2004 by the trigger path B\_CHARM described in Section 2.8.5. We used events collected in runs where the following systems were declared good by the CDF Data Quality Monitoring Group: SVX, COT, CLC and all the trigger levels. We excluded the runs when SVX was off and when there were a high voltage problems in the COT. Moreover, requirements on the online and offline data quality were applied. The final sample corresponds to an integrated luminosity of  $360 \text{ pb}^{-1}$ .

The  $B^- \rightarrow D^0 \pi^-$  decay with  $D^0 \rightarrow K^- \pi^+$  (flavour eigenstate) and the  $B^- \rightarrow D_{CP+}^0 \pi^-$  decay with  $D_{CP+}^0 \rightarrow \pi^+ \pi^-$  and  $D_{CP+}^0 \rightarrow K^+ K^-$  (CP-even eigenstate) were reconstructed.

We begin the reconstruction of the B signals by identifying the  $D^0$  candidates:  $D^0 \rightarrow K^- \pi^+$ ,  $D_{CP+}^0 \rightarrow K^+ K^-$  and  $D_{CP+}^0 \rightarrow \pi^+ \pi^-$ .

We first cut on the raw mass of the charm candidate. The raw mass is calculated using the track momentum at the point of closest approach to the beam line. We determined the charmed candidate (tertiary) vertex by performing a vertex fit using the CTVMFT algorithm [73]. This algorithm determines the decay vertex by varying the track parameters of the daughters particles within their errors, so that a  $\chi^2$  between the track trajectory and the points is minimized. We then applied a constraint of mass on the charmed candidate mass determining the momenta of the daughters tracks.

The charmed candidate is then combined with an additional track to form the B can-



didate (secondary vertex), using the same vertexing algorithm used to reconstruct the  $D^0 \rightarrow K^-\pi^+$  signal (CTVMFT). We required that two of the three tracks from the reconstructed B hadron candidate each matches a SVT track. We confirm the trigger by requiring the matched SVT tracks to pass the B\_CHARM cuts listed in Section 2.8.5.

After applying the requirements discussed above we further require [74]:

- B decay length significance:  $\frac{L_{xy}}{\sigma_{L_{xy}}} > 8$ ;
- D decay length measured with respect to the B decay vertex:  $L_{xy}(D)_B > -0.0015$  cm;
- B impact parameter:  $|d_0(B)| < 0.008$  cm;
- transverse momentum of the track from B:  $p_T > 1$  GeV/c;
- $\Delta R = \sqrt{\Delta\phi^2 + \Delta\eta^2}$  between the track from B and the  $D^0$ :  $\Delta R < 2$ ;
- tridimensional vertex quality  $\chi_{3D}^2$ :  $\chi_{3D}^2 < 15$ ;
- B isolation:  $\text{Isol} > 0.5$ .

The B isolation is defined as  $\frac{p_T(B)}{p_T(B) + \sum p_T}$ , where the sum on the transverse momentum is extended to the tracks contained in a cone with radius = 1 in the  $\eta - \phi$  space around the B meson flight direction, excluding the tracks from the B decays. The B isolation cut has been optimized for B meson in [75], where is shown that b hadron prefers to be produced quite isolated with respect to the background.

The cuts on the tridimensional vertex quality  $\chi_{3D}^2$  and on the B isolation are very important to suppress the combinatorial background.

The resulting invariant mass distributions, with pion mass assignment to the track from B, were reported in Figs. 4.2, 4.3 and 4.4, respectively the invariant mass distribution of  $B^+ \rightarrow \bar{D}^0 \pi^+ \rightarrow [K^+\pi^-]\pi^+$ , the one of  $B^+ \rightarrow D_{CP+}^0 \pi^+ \rightarrow [K^+K^-]\pi^+$  and the one of  $B^+ \rightarrow D_{CP+}^0 \pi^+ \rightarrow [\pi^+\pi^-]\pi^+$ .

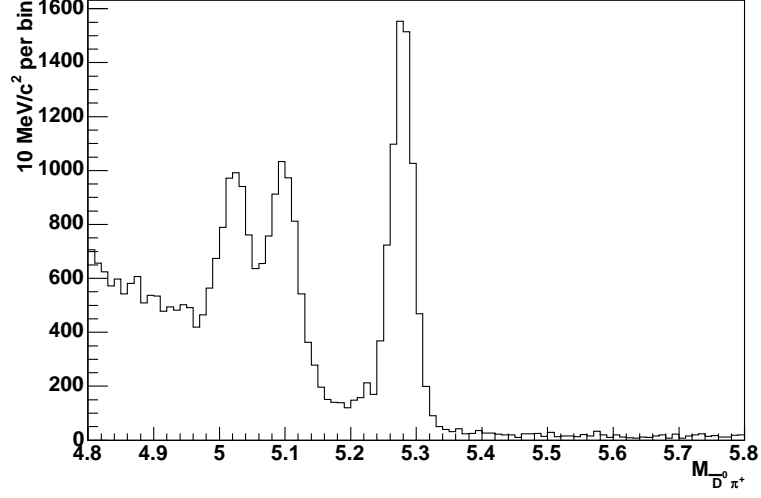


Figure 4.2: Invariant mass distribution of  $B^+ \rightarrow \bar{D}^0 \pi^+$  with  $D^0 \rightarrow K^- \pi^+$  (flavour eigenstate).

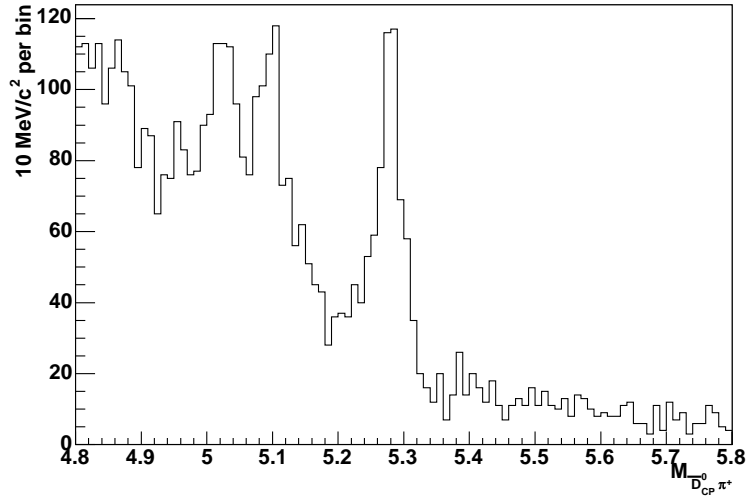


Figure 4.3: Invariant mass distribution of  $B^+ \rightarrow D_{CP+}^0 \pi^+$  with  $D_{CP+}^0 \rightarrow K^+ K^-$  (CP-even eigenstate).

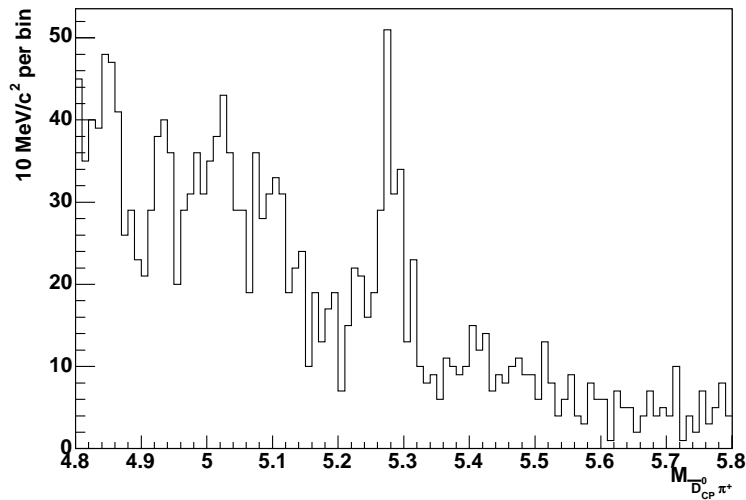


Figure 4.4: Invariant mass distribution of  $B^+ \rightarrow D_{CP+}^0 \pi^+$  with  $D_{CP+}^0 \rightarrow \pi^+ \pi^-$  (CP-even eigenstate).

## 4.2 Monte Carlo Simulation

Monte Carlo simulations are an essential tool for data analysis. They represent a fast and tuned interface between the predicted model and the collected data, allowing a better understanding of the data.

A Monte Carlo simulation can be summarized in a three step procedure: particle generation, particle decay and detector simulation. The particle generation is based on Bgenerator [76], a Monte Carlo program based on NLO calculations [77]. In fact Bgenerator, dedicated to B physics, is able to generate B or D mesons only, without care of fragmentation products that naturally come from hadron collisions.

A b quark<sup>1</sup> is generated following the NDE input spectrum [77] and then it is fragmented into a B meson according to the Peterson fragmentation function [77] with the Peterson fragmentation parameter set at its default value of  $\epsilon_B = 0.006$ . For our analysis the generated quark was limited within the spatial region  $|\eta| < 1.3$  and with a minimum momentum greater than 5 GeV/c. These settings reflect the fact that the b quarks can be generated within the fiducial volume of the detector and that a minimum energy is needed in order to fire the trigger.

The mesons decay relies on EvtGen program [78], a decayer tool extensively tuned by B factory experiments.

Then the geometry and the behavior of active volumes of the CDF II detector are simulated using a dedicated software based on the third version of GEANT package [79]. GEANT is a wide spread program able to simulate the response of High Energy

---

<sup>1</sup>For our simulation only a single quark was generated

Physics detectors at hit level.

Finally, the trigger effects are simulated by TRGSim++, a software that implements the details of the trigger logic used by CDF II. The TRGSim++ appends to each simulated event trigger banks and trigger bits as for data. A particular trigger path can be selected by requiring the corresponding trigger bit.

Since the CDF II detector underwent several hardware and trigger modifications during the data taking period, the actual dataset can be rather inhomogeneous. To properly reflect the different running conditions that occurred, the Monte Carlo samples have been generated for a set of representative runs weighted by their luminosity.

We generated 6,000,000 of  $B^+$  events, requiring that  $D^0 \rightarrow K^- \pi^+$ . In Fig. 4.5 the  $B^+$  invariant mass distribution from simulation is reported.

Our goal is to measure the relative yields of  $B^+ \rightarrow \bar{D}^0 K^+$  to  $B^+ \rightarrow \bar{D}^0 \pi^+$ . Other channels contribute to background as we can observe from Fig. 4.5:  $B^+ \rightarrow \bar{D}^{*0} \pi^+$ ,  $B^0 \rightarrow D^{*-} \pi^+$ ,  $B^+ \rightarrow \bar{D}^{*0} K^+$  and other decays.

However, as we can see from Fig. 4.6 where a zoom of the MC invariant mass is shown, the principal background contribution to the mass region of the  $\bar{D}^0 K^+$  signal is the  $B^+ \rightarrow \bar{D}^{*0} \pi^+$ . We choose as fit window the range of mass between 5.17 and 5.60  $\text{GeV}/c^2$ ; in this region the only significant physical backgrounds are  $B^+ \rightarrow \bar{D}^0 \pi^+$  and  $B^+ \rightarrow \bar{D}^{*0} \pi^+$ .

In this way we can avoid, in the mass part of the Likelihood fit, the two structures on the left of  $B^+ \rightarrow \bar{D}^0 K^+$  particularly difficult to parameterize.

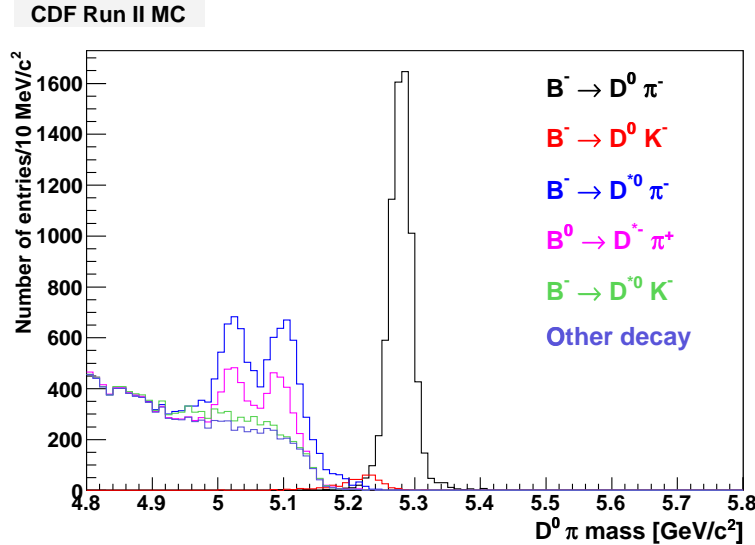


Figure 4.5:  $B^+$  MC. Black:  $B^+ \rightarrow \bar{D}^0 \pi^+$ . Red:  $B^+ \rightarrow \bar{D}^0 K^+$ . Blue:  $B^+ \rightarrow \bar{D}^{*0} \pi^+$ . Magenta:  $B^0 \rightarrow D^{*-} \pi^+$ . Green:  $B^+ \rightarrow \bar{D}^{*0} K^+$  and in violet other decay.

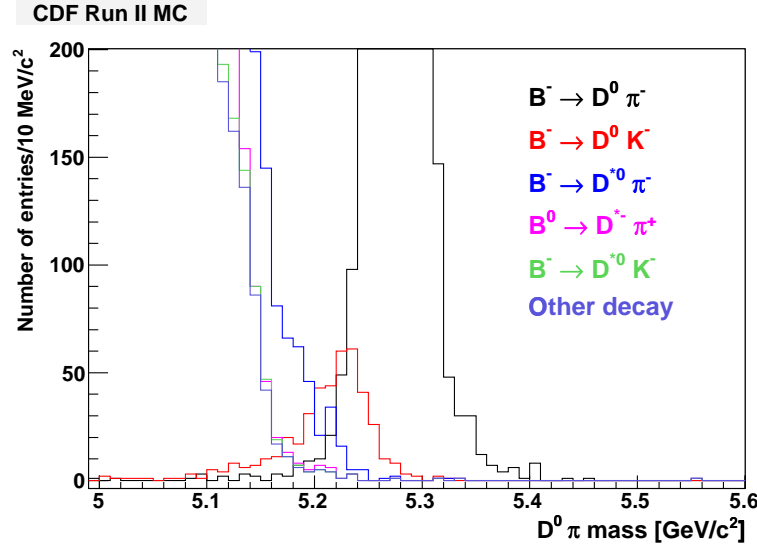


Figure 4.6: Zoom of the  $B^+$  MC. Black:  $B^+ \rightarrow \bar{D}^0 \pi^+$ . Red:  $B^+ \rightarrow \bar{D}^0 K^+$ . Blue:  $B^+ \rightarrow \bar{D}^{0*} \pi^+$ . Magenta:  $B^0 \rightarrow D^{*-} \pi^+$ . Green:  $B^+ \rightarrow \bar{D}^{0*} K^+$  and in violet other decay. The principal background contribution to the mass region of the  $\bar{D}^0 K^+$  signal is the  $B^+ \rightarrow \bar{D}^{0*} \pi^+$ .

### 4.3 Likelihood anatomy

We implemented a maximum Likelihood fit which combines  $M_{D^0 \pi}$ , the invariant mass assigning the pion mass to the track from B, the momenta and the Particle IDentification information.

We started out by writing  $B^+$  masses with different particle assignments at the track from  $B^+$ , as function of a single mass ( $M_{D^0 \pi}$ ) plus an appropriate kinematic variable  $\underline{\alpha}$ .

The difference between the squared invariant masses reconstructed in the pion hypothesis (that is the reference mass) and in particle "b" hypothesis is given by:

$$M_{D^0 b}^2 - M_{D^0 \pi}^2 = \left( \sqrt{m_{D^0}^2 + p_{D^0}^2} + \sqrt{m_b^2 + p_{tr}^2} \right)^2 - \left( \sqrt{m_{D^0}^2 + p_{D^0}^2} + \sqrt{m_\pi^2 + p_{tr}^2} \right)^2 \quad (4.2)$$

where  $m_{D^0}$ ,  $m_b$  and  $m_\pi$  are respectively the  $D^0$  mass, the mass of the particle b and the pion mass;  $p_{D^0}$  and  $p_{tr}$  are respectively the  $D^0$  momentum and the momentum of the track from B.

If we expand this shift at the first order in  $(m_b/\pi/p_{tr})^2$ , we obtain:

$$M_{D^0 b}^2 - M_{D^0 \pi}^2 \sim (m_b^2 - m_\pi^2) \cdot (1 + \sqrt{m_{D^0}^2 + p_{D^0}^2}/p_{tr}) = (m_b^2 - m_\pi^2) \cdot (1 + E_{D^0}/p_{tr}) \quad (4.3)$$

where  $E_{D^0} = \sqrt{m_{D^0}^2 + p_{D^0}^2}$  is the  $D^0$  energy.

Defining  $\underline{\alpha} = E_{D^0}/p_{tr}$  we can write the mass of the B in the kaon hypothesis as:

$$M^2(\underline{\alpha}) = M_{B^+}^2 + (m_K^2 - m_\pi^2) \cdot (1 + \underline{\alpha}). \quad (4.4)$$

In Fig. 4.7 the  $B^+$  invariant mass distribution as a function of  $\underline{\alpha}$ , using the simulation, is shown. In black the  $M_{D^0\pi}$  and in red the  $M_{D^0K}$ . In green the theoretical curve obtained using the formula (4.4) is shown.

We observe a discrepancy between the red curve obtained from the simulation and the theoretical one, in fact from  $\alpha \sim 12$  the green curve tend to move away from the red one.

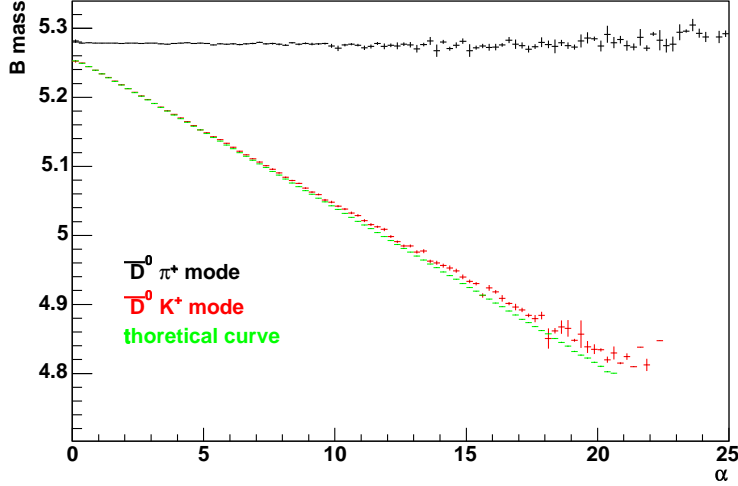


Figure 4.7:  $B^+$  mass vs  $\underline{\alpha}$  using simulation of  $B^+ \rightarrow \bar{D}^0 \pi^+$  and of  $B^+ \rightarrow D^0 K^+$ . Black:  $M_{D^0\pi}$ . Red:  $M_{D^0K}$ . Green: theoretical curve obtained using the formula (4.4) (expansion at the first order in  $m_b/\pi/p_{tr}$ ).

To obtain a better agreement between the two curves we tried to go to a second-order expansion. In Fig. 4.8 the  $B^+$  invariant mass distribution as a function of  $\underline{\alpha}$  is shown again. Now, the theoretical curve (green curve) is in a reasonable agreement with the red one (obtained from the simulation). The theoretical curve, in this case, goes over the red one remaining very close to it. The problem is that the mass is not anymore function of  $\underline{\alpha}$  only, in the formula is also present the momentum of the track from  $B^+$ :

$$M^2(\underline{\alpha}) = M_{B^+}^2 + (m_K^2 - m_\pi^2)(1 + \underline{\alpha} - \frac{1}{2}\underline{\alpha} \cdot (m_K^2 + m_\pi^2)/p_{tr}^2) \quad (4.5)$$

Since we need to use two kinematical variables to describe the invariant mass shift, we decide to keep the full analytical formula without any approximation. We also define the kinematical variables, the momentum balance  $\alpha$  and the total momentum  $P_{tot}$ , like in the  $B_{(s)}^0 \rightarrow h^+ h'^-$  analysis [6][7]:

- if  $p_{tr} < P_{D^0}$        $\alpha = 1 - p_{tr}/p_{D^0} > 0$
- if  $p_{tr} \geq P_{D^0}$        $\alpha = -(1 - p_{D^0}/p_{tr}) \leq 0$

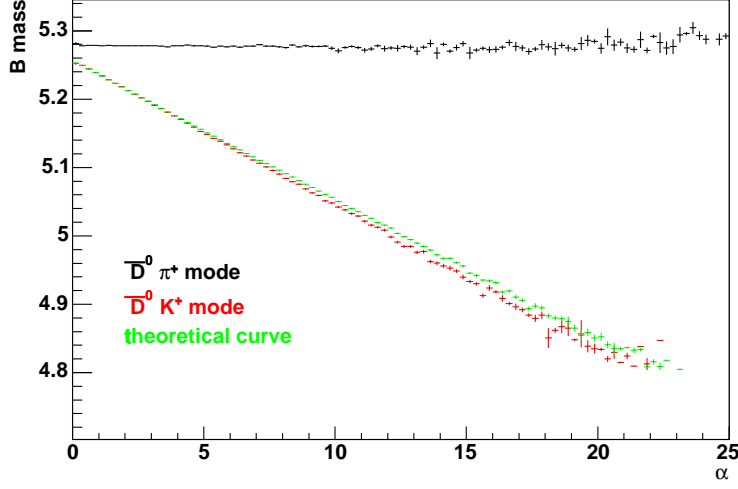


Figure 4.8:  $B^+$  mass vs  $\alpha$  using simulation of  $B^+ \rightarrow \bar{D}^0 \pi^+$  and of  $B^+ \rightarrow D^0 K^+$ . Black:  $M_{D^0 \pi}$ . Red:  $M_{D^0 K}$ . Green: theoretical curve obtained using the formula (4.5) (expansion at the second order in  $m_b/\pi/p_{tr}$ ).

- $P_{tot} = p_{tr} + p_{D^0}$ .

The expression of the  $B$  mass, in the kaon hypothesis, as function of these two kinematical variables is then:

- if  $\alpha > 0$

$$M^2(\alpha, P_{tot}) = M_{B^+}^2 + m_\pi^2 - m_K^2 + 2 \cdot \sqrt{m_{D^0}^2 + (P_{tot}/(2 - \alpha))^2} \cdot \left( \sqrt{(m_\pi^2 + (P_{tot}(1 - \alpha)/(2 - \alpha))^2)} - \sqrt{m_K^2 + (P_{tot}(1 - \alpha)/(2 - \alpha))^2} \right) \quad (4.6)$$

- if  $\alpha \leq 0$

$$M^2(\alpha, P_{tot}) = M_{B^+}^2 + m_\pi^2 - m_K^2 + 2 \cdot \sqrt{m_{D^0}^2 + (P_{tot}(1 + \alpha)/(2 + \alpha))^2} \cdot \left( \sqrt{(m_\pi^2 + (P_{tot}/(2 + \alpha))^2)} - \sqrt{m_K^2 + (P_{tot}/(2 + \alpha))^2} \right) \quad (4.7)$$

In Fig. 4.9 the  $B^+$  invariant mass distribution as a function of  $\alpha$  is shown. Now we observe a perfect agreement between the simulation (black curve) and the theoretical curve (in red).

The expression of the Likelihood used for the Unbinned Maximum Likelihood Fit

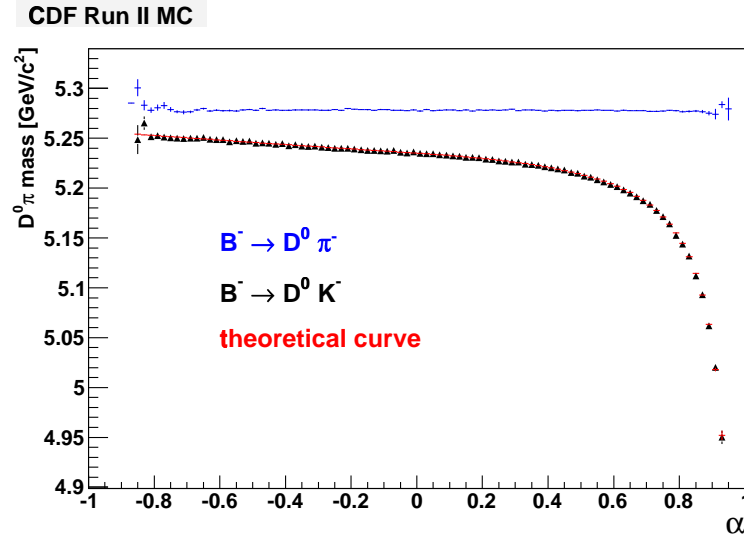


Figure 4.9:  $B^+$  mass vs  $\alpha$  using simulation of  $B^+ \rightarrow \bar{D}^0 \pi^+$  and of  $B^+ \rightarrow D^0 K^+$ . Blue:  $M_{D^0 \pi}$ . Black:  $M_{D^0 K}$ . Red: theoretical curve obtained using the full analytical formula.

is:

$$L = \prod_k^{N_{events}} ((1 - b) \cdot (f_\pi \cdot F_\pi(\alpha, P_{tot}, M_{D^0 \pi}, ID) + (1 - f_\pi) \cdot F_K(\alpha, P_{tot}, M_{D^0 \pi}, ID)) + b \cdot (f_D \cdot BG_D(\alpha, P_{tot}, M_{D^0 \pi}, ID) + (1 - f_D) \cdot BG_{comb}(\alpha, P_{tot}, M_{D^0 \pi}, ID)). \quad (4.8)$$

where  $b$  is the fraction of background measured with respect to all the events (as a consequence, the fraction of signal is  $1 - b$ ),  $f_\pi$  the fraction of  $B^+ \rightarrow \bar{D}^0 \pi^+$  with respect to the total signal (as a consequence, the fraction of  $B^+ \rightarrow \bar{D}^0 K^+$  is  $f_K = 1 - f_\pi$ ) and  $f_D$  the fraction of the physical background  $B^+ \rightarrow \bar{D}^{0*} \pi^+$  with respect to the total background (the fraction of combinatorial background is then  $f_{comb} = 1 - f_D$ ).

$F_\pi(\alpha, P_{tot}, M_{D^0 \pi}, ID)$  and  $F_K(\alpha, P_{tot}, M_{D^0 \pi}, ID)$  are the signal probability density function (pdf) respectively of  $B^+ \rightarrow \bar{D}^0 \pi^+$  and  $B^+ \rightarrow \bar{D}^0 K^+$ . The expression of these pdf is given by:

$$F_i(\alpha, P_{tot}, M_{D^0 \pi}, ID) = G(M_{D^0 \pi} - M(\alpha, P_{tot}))p(\alpha, P_{tot})p(ID) \quad (4.9)$$

where  $G(M_{D^0 \pi} - M(\alpha, P_{tot}))$  is the part of the pdf that describes the mass,  $p(\alpha, P_{tot})$  is the 2-dimensional distribution that describes the kinematical variables  $\alpha$  and  $P_{tot}$ , and  $p(ID)$  is the distribution of the particle identification variable  $ID$  that will be defined in the Section 4.7.

$BG_D(\alpha, P_{tot}, M_{D^0 \pi}, ID)$  and  $BG_{comb}(\alpha, P_{tot}, M_{D^0 \pi}, ID)$  are the background pdf respectively of the physical background ( $B^+ \rightarrow \bar{D}^{0*} \pi^+$ ) and of the combinatorial back-



ground. The expression of these pdf is given by:

$$BG_i(\alpha, P_{tot}, M_{D^0\pi}, ID) = BG(M_{D^0\pi})p(\alpha, P_{tot})p(ID). \quad (4.10)$$

In the following Sections we will consider the pdf piece by piece and we will describe the parameterization used for the kinematical variables and for the PID variable.

## 4.4 Kinematics vs trigger

We reconstructed the  $B^+$  candidate by requiring that at least two tracks are trigger tracks as we discussed in Section 4.1. This means that the two tracks have a transverse momentum higher than 2 GeV/c and an impact parameter such as  $120 \mu\text{m} < |d_0| < 1 \text{ mm}$ , as described in Section 2.8.2.

There are two possibilities:

1. The two tracks from  $D^0$  are trigger tracks;
2. The track from B and one track from  $D^0$  are trigger tracks.

In Fig. 4.10 the  $\alpha$  distributions from  $B^+ \rightarrow \overline{D}^0 \pi^+$  simulation, for the two types of trigger (on the left the track from B and one track from  $D^0$  are trigger track, on the right the two  $D^0$  tracks are trigger tracks) are shown. For each trigger possibility the kinematics is different: when the  $D^0$  tracks are trigger tracks the  $D^0$  momentum is almost always higher than the momentum of the track from B so  $\alpha > 0$  (right plot in Fig. 4.10).

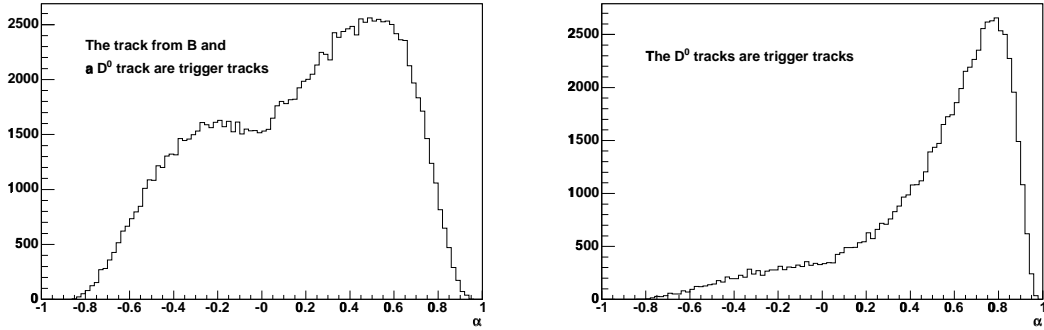


Figure 4.10:  $\alpha$  from  $B^+ \rightarrow \overline{D}^0 \pi^+$  simulation. Left: the track from B and one track from  $D^0$  are trigger tracks. Right: the two tracks from  $D^0$  are trigger tracks. For each trigger possibility the kinematics is different and a different parameterization of  $p(\alpha, P_{tot})$  is needed.

The different kinematics is confirmed by the 2-dimensional distributions  $p(\alpha, P_{tot})$  obtained using the same  $B^+ \rightarrow \overline{D}^0 \pi^+$  simulation. In Fig. 4.11  $p(\alpha, P_{tot})$ , for the total sample (top-left), for the sample where the track from B and a  $D^0$  track are trigger tracks (top-right), for the sample where the two tracks from  $D^0$  are trigger tracks

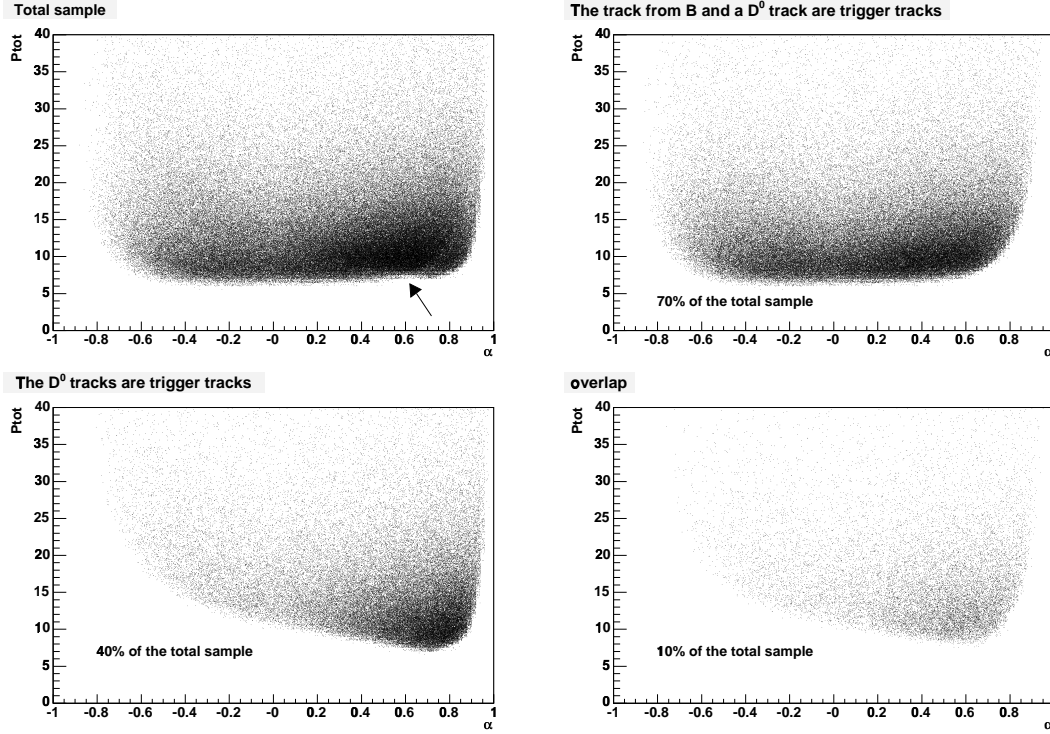


Figure 4.11:  $P_{tot}$  vs  $\alpha$  from  $B^+ \rightarrow \bar{D}^0 \pi^+$  simulation. Top-left: total sample. Top-right: sample where the track from  $B$  and a  $D^0$  track are trigger tracks. Bottom-left: sample where the two tracks from  $D^0$  are trigger tracks. Bottom-right: overlap sample where all the three tracks are trigger tracks.

(bottom-left) and finally for the overlap sample where all the three tracks are trigger tracks (bottom-right), are shown.

If we look at the total sample 2-dimensional distribution, we observe a notch in the vicinity of  $\alpha = 0.6$ , revealing the presence of two subsamples with different kinematics. The sample where the track from  $B$  and a  $D^0$  track are trigger tracks amounts to  $\sim 70\%$  of the total sample, while the events where both  $D^0$  tracks are trigger tracks make for  $\sim 40\%$  of the sample. The two samples have an overlap of  $\sim 10\%$ .

To make two different kinematical parameterizations of  $p(\alpha, P_{tot})$  we needed two samples without any overlap.

We decide to split the total sample in the two non-overlapping samples:

1. The track from  $B$  and a  $D^0$  track are trigger tracks ( $\sim 70\%$  of the total sample).
2. The two tracks from  $D^0$  tracks are trigger tracks and the track from  $B$  is not, it has  $P_t < 2 \text{ GeV}/c$  ( $\sim 10\%$  of the total sample).

We concentrate our analysis only on the larger sample, all parameterization are relative to the  $\sim 70\%$  of the total sample where the track from  $B$  and a  $D^0$  track are trigger tracks.

## 4.5 Mass probability density function

### 4.5.1 Signal pdf

For each decay we need  $G(M_{D^0\pi} - M(\alpha, P_{tot}))$ , present in the signal pdf (equation (4.9)), that is the sum of three gaussians:

$$G = \sum_{i=1}^3 \frac{A_i}{\sqrt{2\pi}\sigma_i} \cdot \exp\left(-\frac{1}{2} \cdot \left(\frac{M_{D^0\pi} - M(\alpha, P_{tot})}{\sigma_i}\right)^2\right). \quad (4.11)$$

The resolutions  $\sigma_i$  and the relative fractions  $A_i$  are obtained by fitting the "correct" invariant mass distribution from  $B^+ \rightarrow \bar{D}^0\pi^+$  and  $B^+ \rightarrow \bar{D}^0K^+$  simulation. We have defined the "correct mass" as  $M_{corr} = M_{D^0\pi} - \delta(\alpha, P_{tot})$ , where  $\delta(\alpha, P_{tot}) = M(\alpha, P_{tot}) - M_{B^+}$  is the mass shift due to the incorrect mass assignment ( $M(\alpha, P_{tot})$  is defined in the equations (4.6) and (4.6)). Clearly for  $B^+ \rightarrow \bar{D}^0\pi^+$ ,  $\delta(\alpha, P_{tot}) = 0$ .

In Fig. 4.12 the invariant mass distributions of the signal modes are shown, with a superimposed fit of a three-gaussians model.

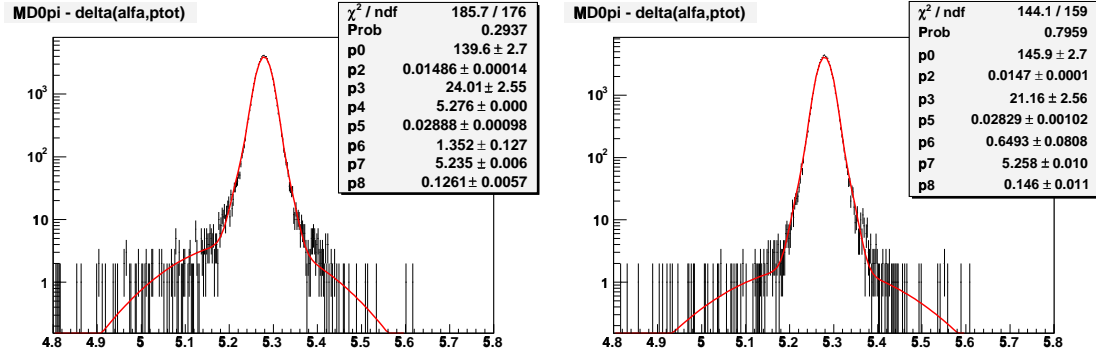


Figure 4.12:  $B^+$  Invariant mass distributions of signal decays. On the left the  $\bar{D}^0\pi^+$  and on the right the  $\bar{D}^0K^+$ . The continuous lines are the fit using a three-gaussians model.

In order to avoid relying on the absolute resolution predicted by the simulation, we introduced a free scale parameter in our likelihood fit, multiplying the width of the three gaussians. This parameter is fitted together with all the "physics parameters".

### 4.5.2 Background pdf

For each source of background, the physical one and the combinatorial one, we need the mass shape  $BG(M_{D^0\pi})$  to write the pdfs defined in equation (4.10).

#### Physical background pdf

As discussed in the section 4.2 we have defined a fit window that goes from 5.17 to 5.6  $\text{GeV}/c^2$  to have as physical background only the  $B^+ \rightarrow \bar{D}^{*0}\pi^+$ . In Fig. 4.13 we have

reported the invariant mass distribution of  $\bar{D}^{0*} \pi^+$  (log-scale), from simulation, fitted in the window  $[5.06, 5.6]$   $\text{GeV}/c^2$  with three gaussians plus an exponential. We made the fit in a larger window than the one used in the maximum likelihood fit to be sure to parameterize  $\bar{D}^{0*} \pi^+$  in the right way.

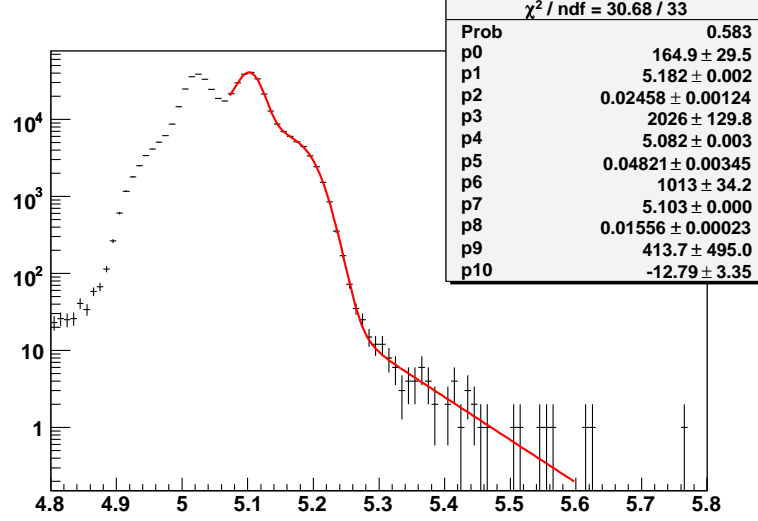


Figure 4.13: Invariant mass distributions of physical background  $\bar{D}^{0*} \pi^+$ . The continuous line is the fit using three gaussians plus an exponential.

### Combinatorial background pdf

For the combinatorial background we determined the mass shape from data themselves. We decided to use the events which pass the same selection (the selection cuts are described in the Section 4.1), with the only difference of having  $L_{xy}(B^+) < -300 \mu\text{m}$  instead of the requirement on the  $L_{xy}$  significance. In this way we can have an idea of the combinatorial background under the peak. We have verified that the shape obtained using the negative  $L_{xy}$  sample is in agreement with the one obtained with the standard selection cuts in the right sideband (between  $5.4$  and  $5.8 \text{ GeV}/c^2$ ), as it is shown in Fig.4.14, where the  $B^+$  invariant mass distribution between  $5.4$  and  $5.8 \text{ GeV}/c^2$  is shown. The candidates with  $L_{xy} > 0$  are in black and the candidates with  $L_{xy} < 0$  are in red.

In Fig. 4.15 the  $B^+$  invariant mass distribution from data requiring  $L_{xy}(B_u) < -300 \mu\text{m}$  is shown. The mass shape is described using an exponential. The parameters of this exponential (slope and normalization) are left free to float in the main fit.

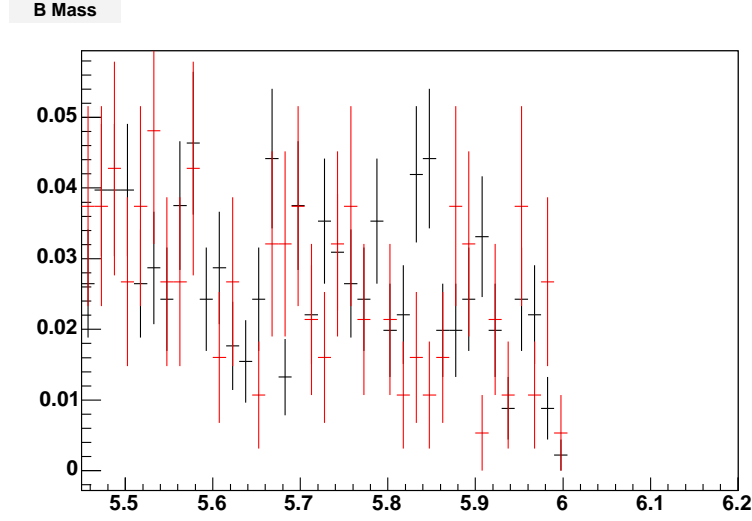


Figure 4.14:  $B^+$  Invariant mass distributions between 5.4 and 5.8  $\text{GeV}/c^2$ . In red the events with  $L_{xy} < 0$  and in black the events with  $L_{xy} > 0$ .

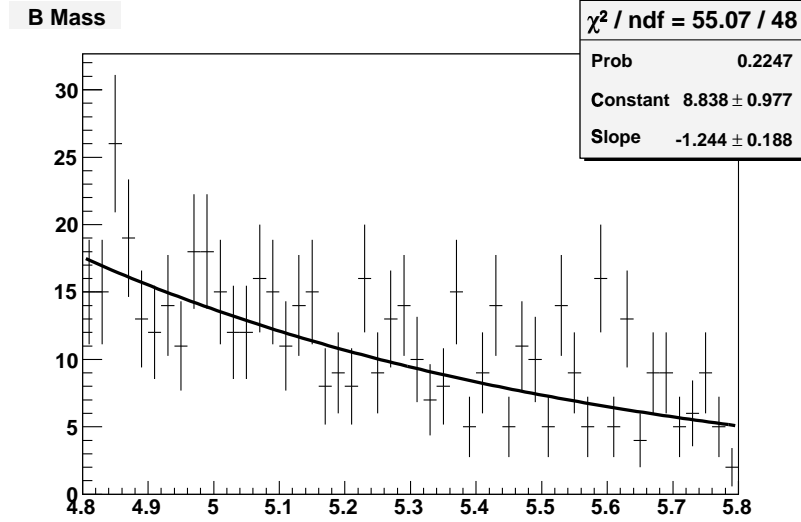


Figure 4.15:  $B^+$  Invariant mass distributions requiring  $L_{xy} < -300 \mu\text{m}$ . The continuous line is the fit using an exponential.

## 4.6 Kinematical parameterization

For each decay, we need the 2-dimensional function  $p(\alpha, P_{tot})$  that describes the 2-dimensional distribution  $P_{tot}$  vs  $\alpha$ . Starting from some considerations on the kinematics

of the decay, we defined the kinematical domain of our fit.

When  $p_{tr} < p_{D^0}$ ,  $\alpha = 1 - \frac{p_{tr}}{p_{D^0}}$ . Resolving  $\alpha$  for  $p_{D^0}$ , we obtain  $p_{D^0} = \frac{p_{tr}}{1-\alpha}$ . Since  $P_{tot} = p_{tr} + p_{D^0}$  we have  $P_{tot} = p_{tr} + \frac{p_{tr}}{1-\alpha} = p_{tr} \cdot \frac{2-\alpha}{1-\alpha}$ . With  $p_{tr} > 2$  GeV/c we obtain  $P_{tot} > 2 \cdot \frac{2-\alpha}{1-\alpha}$ .

When  $p_{tr} > p_{D^0}$ ,  $\alpha = -(1 - \frac{p_{D^0}}{p_{tr}})$ . Resolving  $\alpha$  for  $p_{tr}$ , we obtain  $p_{tr} = \frac{p_{D^0}}{1+\alpha}$ . In this case we have  $P_{tot} = p_{tr} + p_{D^0} = \frac{p_{D^0}}{1+\alpha} + p_{D^0} = p_{D^0} \cdot \frac{2+\alpha}{1+\alpha}$ . Since at least one  $D^0$  tracks is a trigger track we have  $p_{D^0} > 2$  GeV/c. So, we obtain  $P_{tot} > 2 \cdot \frac{2+\alpha}{1+\alpha}$ .

There are other two conditions  $P_{tot} > 7$  GeV/c and  $\alpha > -0.8$  that we have extracted directly from the  $P_{tot}$  vs  $\alpha$  distribution.

The distribution of  $P_{tot}$  vs  $\alpha$  is shown in Fig. 4.16, where the colored curves represent the kinematical domain, in red  $P_{tot} > 2 \cdot \frac{2-\alpha}{1-\alpha}$ , in blue  $P_{tot} > 2 \cdot \frac{2+\alpha}{1+\alpha}$ , in green  $P_{tot} > 7$  and in magenta  $\alpha > -0.8$ .

Summarizing, the kinematical domain for our fit is:

- $P_{tot} > 2 \cdot \frac{2-\alpha}{1-\alpha}$
- $P_{tot} > 2 \cdot \frac{2+\alpha}{1+\alpha}$
- $P_{tot} > 7$
- $\alpha > -0.8$

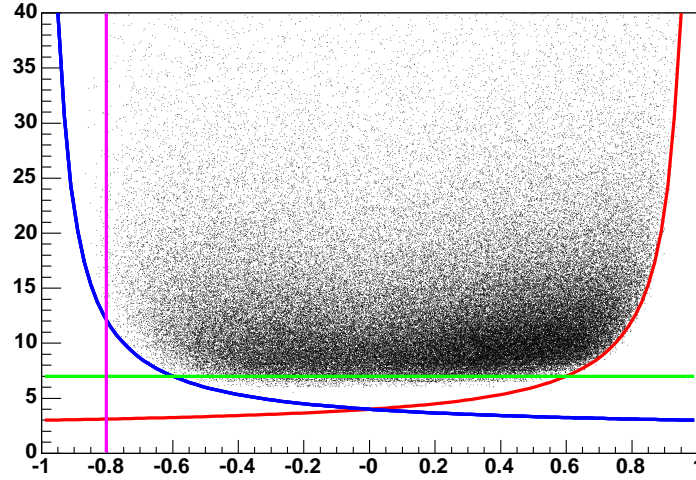


Figure 4.16:  $P_{tot}$  vs  $\alpha$  distribution for the  $\bar{D}^0 \pi^+$  mode obtained from simulation. The curves indicate the kinematical domain of the fit. Red curve:  $P_{tot} > 2 \cdot \frac{2-\alpha}{1-\alpha}$ . Blue curve:  $P_{tot} > 2 \cdot \frac{2+\alpha}{1+\alpha}$ . Green curve:  $P_{tot} > 7$ . Magenta curve:  $\alpha > -0.8$

### 4.6.1 Signal pdf

We parameterized  $p(\alpha, P_{tot})$  for the signal decays using the simulated samples of  $B^+ \rightarrow \bar{D}^0 \pi^+$  and of  $B^+ \rightarrow \bar{D}^0 K^+$ .

To make the 2-dimensional fit we use an interpolation technique. As an example we describe the complete procedure for the  $\bar{D}^0 \pi^+$  mode.

First of all, we fitted the  $\alpha$  distribution in slices of  $P_{tot}$  (bin = 1 GeV/c) using a sixth degree polynomial. In Fig. 4.17 the fits of these  $\alpha$  distributions are shown.

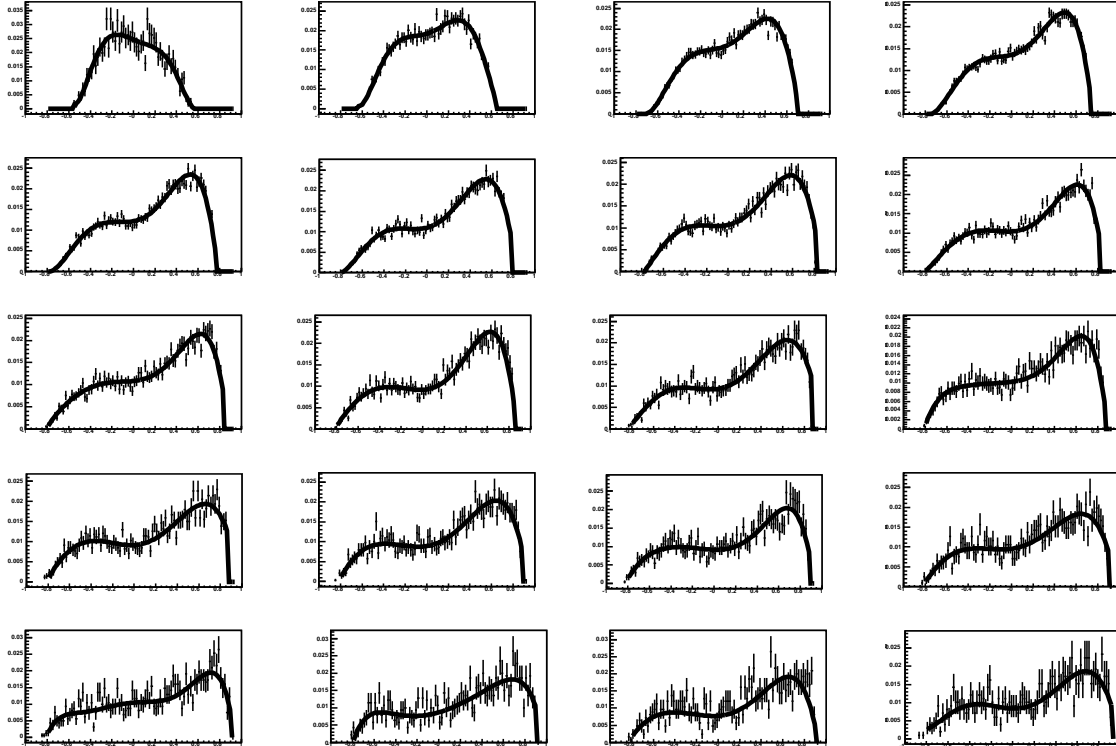


Figure 4.17: Fits of  $\alpha$  distributions in slices of  $P_{tot}$  (bin = 1 GeV/c) using a sixth degree polynomial ( $\bar{D}^0 \pi^+$  decay). The plot on the top left is the  $\alpha$  distribution for  $7 < P_{tot} < 8$  GeV/c, the second plot on the top is the  $\alpha$  distribution for  $8 < P_{tot} < 9$  GeV/c, and so on.

For each parameter of the sixth degree polynomial, we plotted the “parameter value” vs  $P_{tot}$  and we fitted it with a polynomial. In Fig. 4.18 the seven plots (one for each parameter of the sixth degree polynomial used to fit the  $\alpha$  distribution) “parameter value” vs  $P_{tot}$  are shown. In each plot the red curve is the fitting curve, for the first parameter we used a fifth degree polynomial, for the second parameter a second degree polynomial, for the third parameter a fourth degree polynomial, for the fourth parameter a first degree polynomial, finally for the fifth, the sixth and the seventh parameter we used a third degree polynomial.

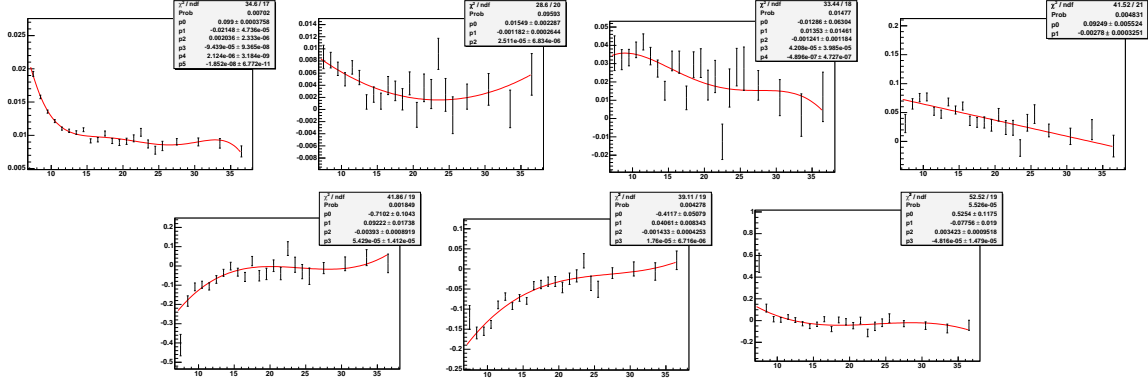


Figure 4.18: Plots of “parameter value” vs  $P_{tot}$  for  $\bar{D}^0 \pi^+$  candidates. One plot for each parameter of the sixth degree polynomial used to fit the  $\alpha$  distribution. The red curve is the fitting curve obtained using a polynomial.

Then we fitted the  $P_{tot}$  distribution using a Chebyshev polynomial of second kind [80] times an exponential. In particular the Chebyshev polynomials used are:

$$\begin{aligned}
 U_0 &= 1 \\
 U_1 &= 2x \\
 U_2 &= 4x^2 - 1 \\
 U_3 &= 8x^3 - 4x \\
 U_4 &= 16x^4 - 12x^2 + 1 \\
 U_5 &= 32x^5 - 32x^3 + 6x \\
 U_6 &= 64x^6 - 80x^4 + 24x^2 - 1.
 \end{aligned} \tag{4.12}$$

In Fig.4.19 the fit result of the  $P_{tot}$  distribution for  $\bar{D}^0 \pi^+$  mode, is shown.

The 2-dimensional function describing  $p(\alpha, P_{tot})$  is:

$$\sum_{i=0}^6 a_i U_i(P_{tot}) \cdot \exp(a_7 P_{tot}) \cdot \sum_{j=0}^6 b_j(P_{tot}) \alpha_j \tag{4.13}$$

where  $U_i$  are the Chebyshev polynomial (equations (4.12)) and  $b_j(P_{tot})$  are the polynomials used to fit the plots “parameter value” vs  $P_{tot}$  (Fig. 4.18).

In Fig. 4.20, the 2-dimensional distribution  $P_{tot}$  vs  $\alpha$  for simulated  $\bar{D}^0 \pi^+$  (on the left) and the 2-dimensional fit function (on the right) are shown. In Fig. 4.21 the projections of the 2-dimensional fit function (black curve) on the  $\alpha$  distribution in slices of  $P_{tot}$  are shown. We observe a good agreement between the parameterization and the simulation.

We used the same procedure for the simulated  $\bar{D}^0 K^+$  sample. In Fig. 4.22 the fit result of  $P_{tot}$  distribution with Chebyshev polynomial of second kind times an exponential is shown. In Fig. 4.23, the 2-dimensional distribution  $P_{tot}$  vs  $\alpha$  for a simulated



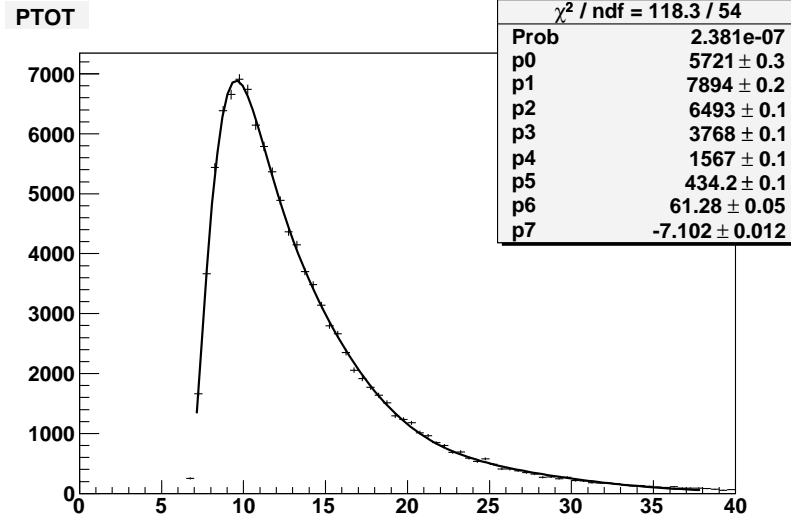


Figure 4.19: Fit of the  $P_{tot}$  distribution of the  $\bar{D}^0 \pi^+$  mode using a Chebyshev polynomial of second kind times an exponential.

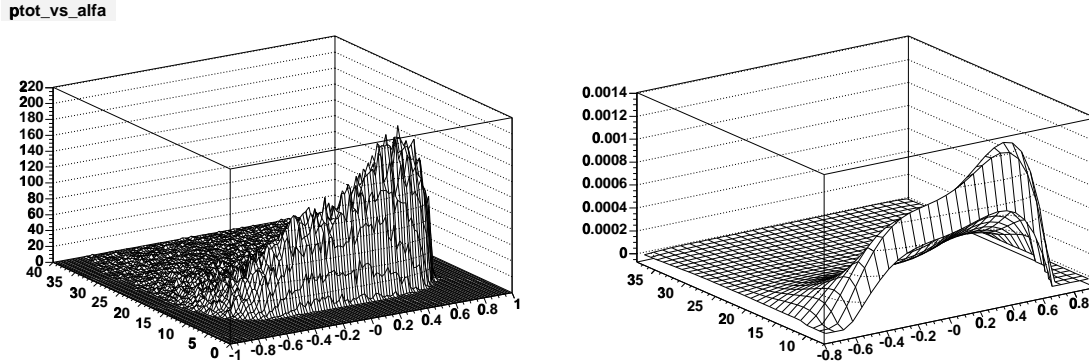


Figure 4.20: Left: 2-dimensional distribution  $P_{tot}$  vs  $\alpha$  from  $\bar{D}^0 \pi^+$  simulation. Right: 2-dimensional fit function.

$\bar{D}^0 K^+$  sample (on the left) and the 2-dimensional fit function (on the right) are shown. In Fig. 4.24 the projections of the 2-dimensional fit function (black curve) on the  $\alpha$  distribution in slices of  $P_{tot}$  are shown.

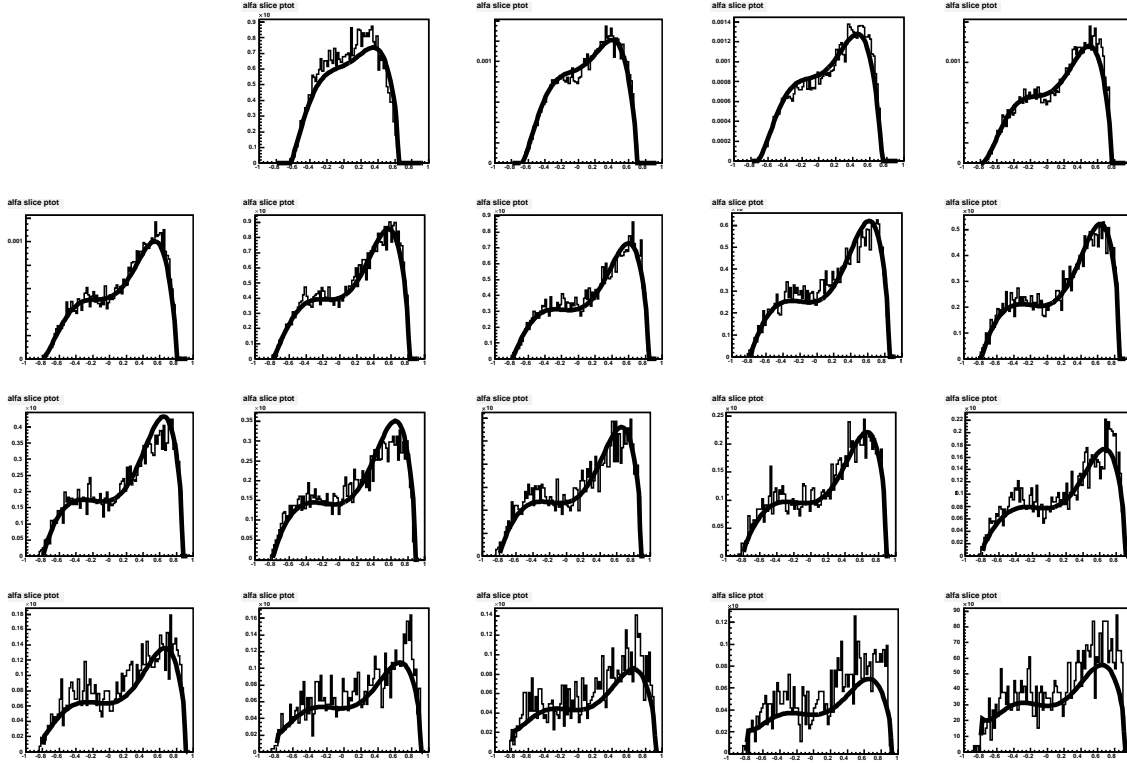


Figure 4.21: Projections of the 2-dimensional fit function (black curve) on the  $\alpha$  distribution in slices of  $P_{tot}$  ( $\bar{D}^0 \pi^+$  mode).

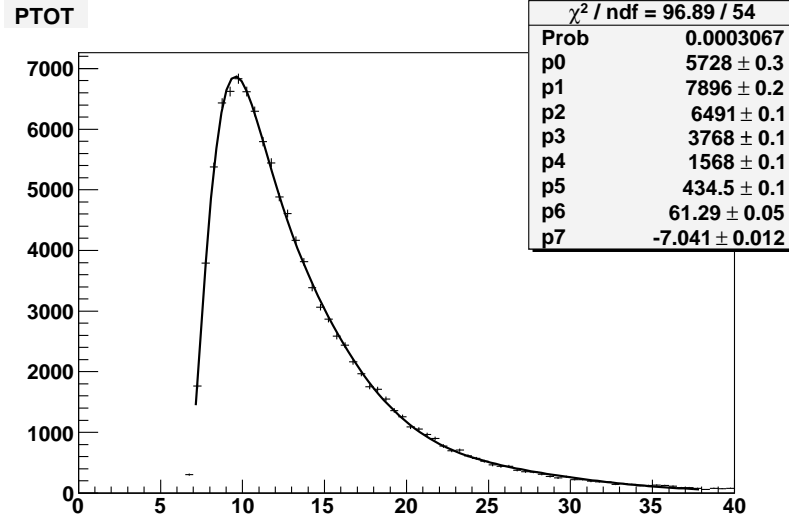


Figure 4.22: Fit of the  $P_{tot}$  distribution of the  $\bar{D}^0 K^+$  mode using a Chebyshev polynomial of second kind time an exponential.

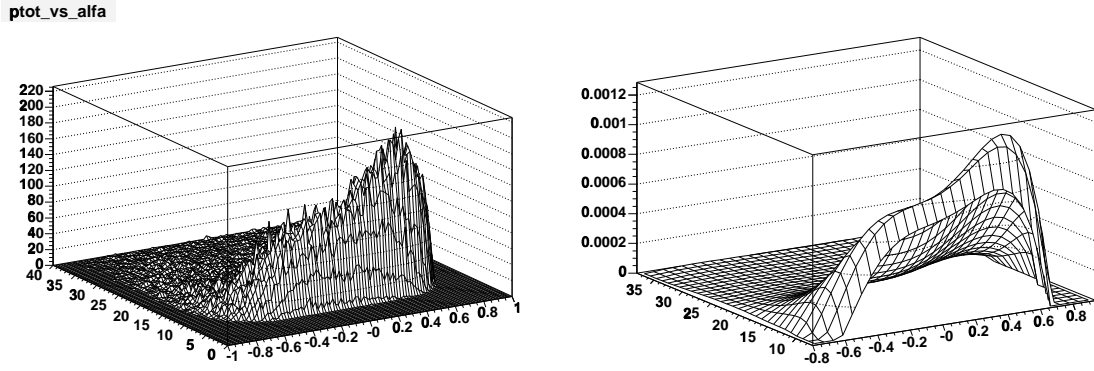


Figure 4.23: Left: 2-dimensional distribution  $P_{tot}$  vs  $\alpha$  from  $\bar{D}^0 K^+$  simulation. Right: 2-dimensional fit function.

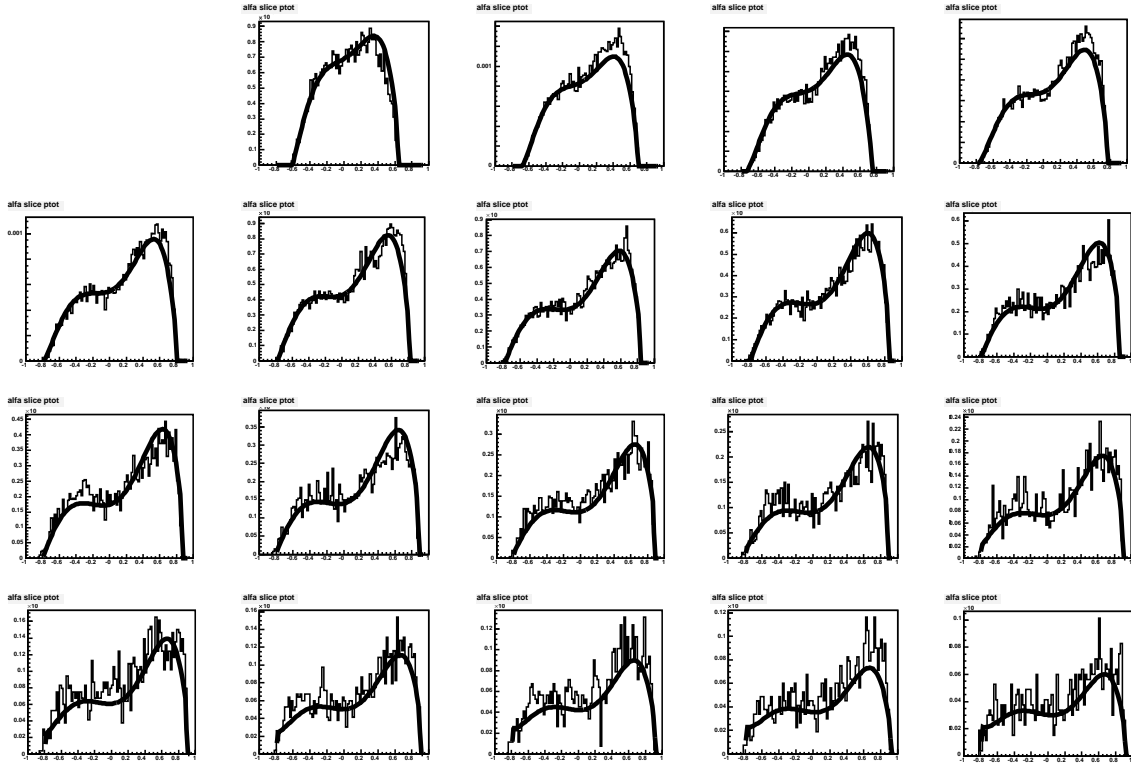


Figure 4.24: Projections of the 2-dimensional fit function (black curve) on the  $\alpha$  distribution in slices of  $P_{tot}$  ( $\bar{D}^0 K^+$  mode).

### 4.6.2 Physical background pdf

We used the interpolation technique also for the physical background. The only difference from the signal parameterization is the function used to fit the  $P_{tot}$  distribution. In fact for the  $\bar{D}^{0*} \pi^+$  mode we used a fifth degree polynomial times an exponential. In Fig. 4.25 the fit of  $P_{tot}$  distribution is shown. In Fig. 4.26, the 2-dimensional distribution  $P_{tot}$  vs  $\alpha$  from simulated  $\bar{D}^{0*} \pi^+$  sample (on the left) and the 2-dimensional fit function (on the right) are shown. In Fig. 4.27 the projections of the 2-dimensional fit function (black curve) on the  $\alpha$  distribution in slices of  $P_{tot}$  are shown.

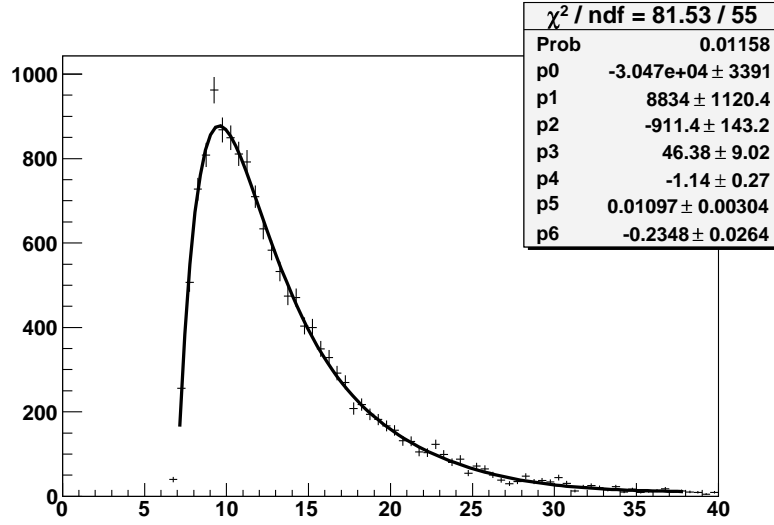


Figure 4.25: Fit of the  $P_{tot}$  distribution of the  $\bar{D}^{0*} \pi^+$  mode using a fifth degree polynomial times an exponential.

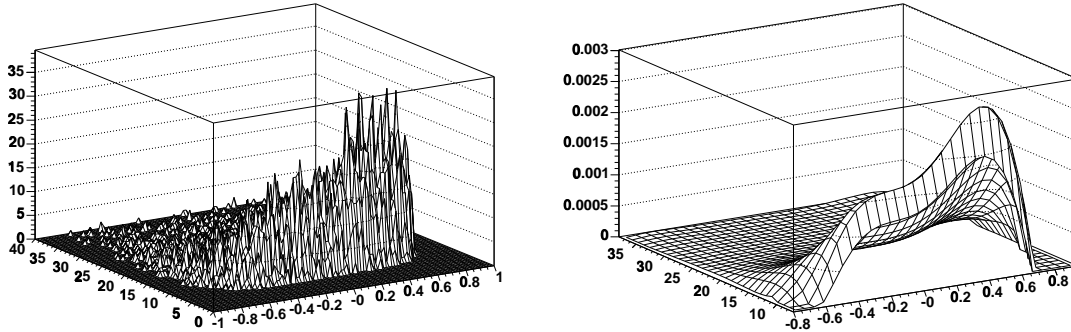


Figure 4.26: Left: 2-dimensional distribution  $P_{tot}$  vs  $\alpha$  from  $\bar{D}^{0*} \pi^+$  simulation. Right: 2-dimensional fit function.

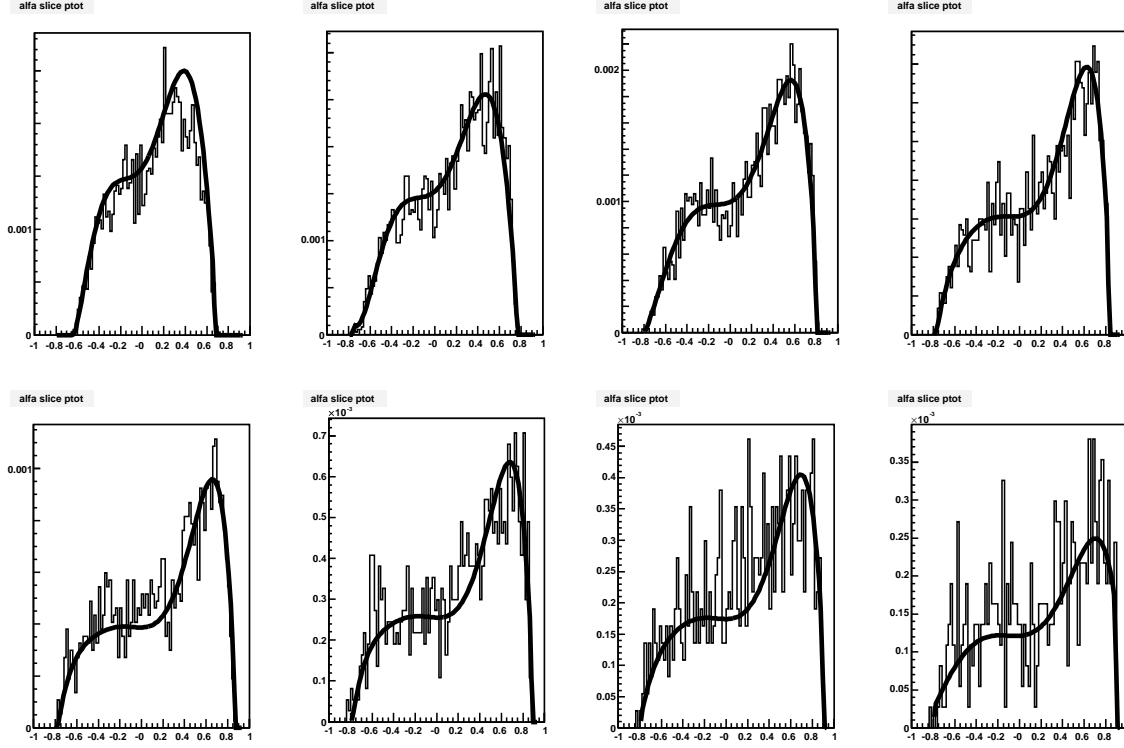


Figure 4.27: Projections of the 2-dimensional fit function (black curve) on the  $\alpha$  distribution in slices of  $P_{tot}$  ( $\overline{D}^{0*} \pi^+$  mode).

#### 4.6.3 Combinatorial background pdf

To parameterize the combinatorial background we used the data of the right sideband between 5.4 and 5.8  $GeV/c^2$ . We applied the interpolation technique and the function used to fit the  $P_{tot}$  distribution was the Pearson Type IV function [81] defined as:

$$Pearson(x) = (1 + ((-x - p0)/p1)^2)^{p2} \cdot \exp(-p3 \cdot \arctan((-x - p0)/p1)) \cdot p4. \quad (4.14)$$

As it is shown in Fig. 4.28, where the fit of  $P_{tot}$  is reported, the Pearson function allows to take in the right way the sharpened peak of the  $P_{tot}$  distribution.

In Fig. 4.29, the 2-dimensional distribution  $P_{tot}$  vs  $\alpha$  from data (on the left) and the 2-dimensional fit function (on the right) are shown. In Fig. 4.30 the projections of the 2-dimensional fit function (black curve) on the  $\alpha$  distribution in slices of  $P_{tot}$  are shown. Due to the low statistics, the slices of  $\alpha$  in  $P_{tot}$  are bigger, the bin width is equal to 2  $GeV/c$  instead of 1  $GeV/c$ , that is the bin width for the signal parameterization.

As it is shown in Fig. 4.30 for  $\alpha > 0.8$  there is a peak in the function used to parameterize the background. We have decided to remove this region to avoid possible problems in the maximum likelihood fit. So, the fit range in  $\alpha$  is  $[-0.8, 0.8]$ .

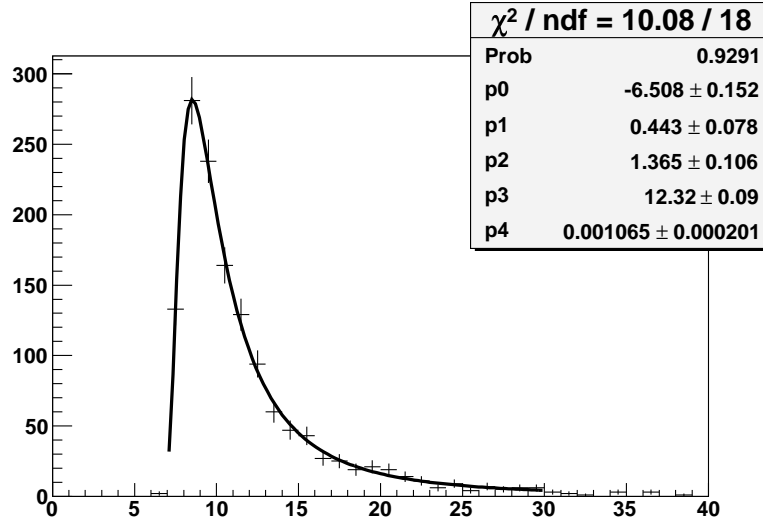


Figure 4.28: Fit of the  $P_{tot}$  distribution of the combinatorial background using a Pearson function.

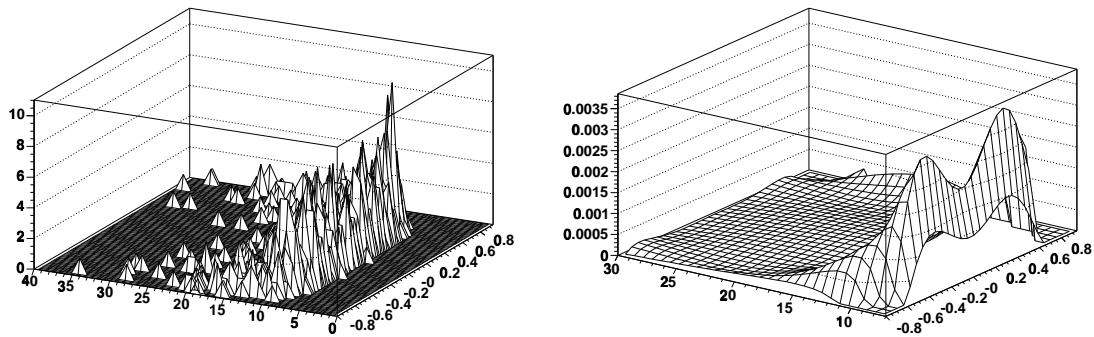


Figure 4.29: Left: 2-dimensional distribution  $P_{tot}$  vs  $\alpha$  from data (right sideband). Right: 2-dimensional fit function.

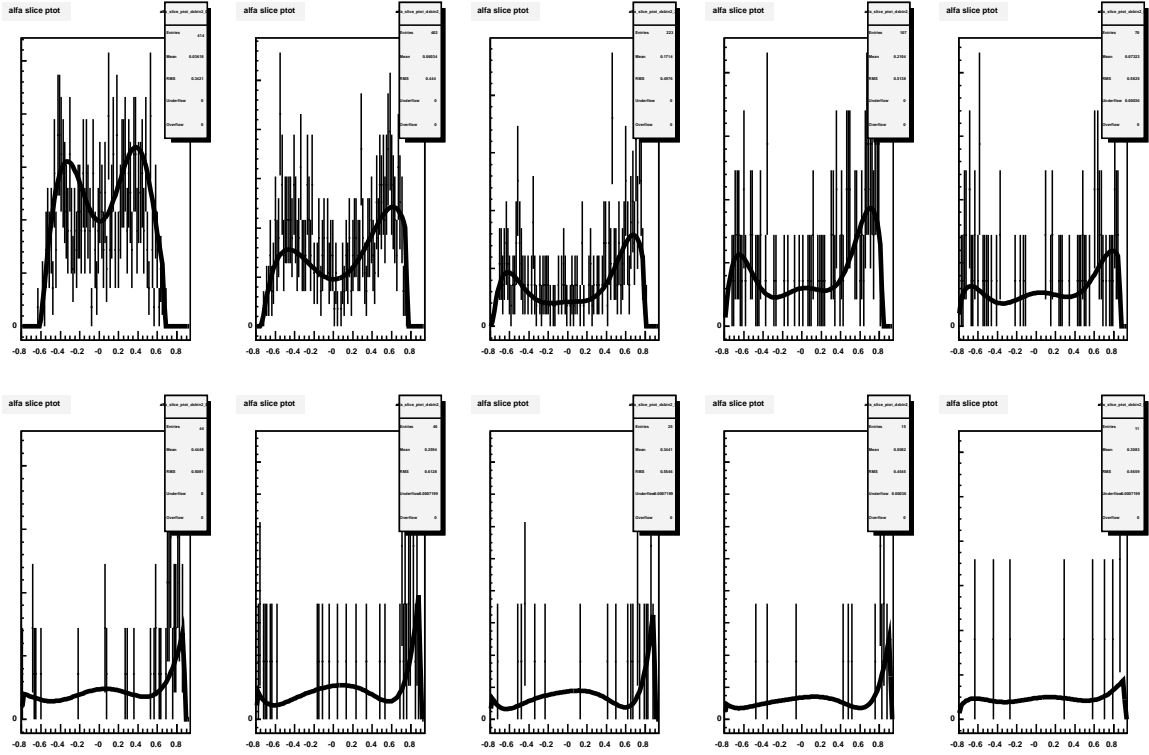


Figure 4.30: Projections of the 2-dimensional fit function (black curve) on the  $\alpha$  distribution in slices of  $P_{tot}$  (combinatorial background).

## 4.7 PID parameterization

We apply the particle identification to the track from B with the aim of distinguish between  $B^+ \rightarrow \bar{D}^0 K^+$  and  $B^+ \rightarrow \bar{D}^0 \pi^+$  mode.

To represent the PID information we chosen a single observable called "ID" defined as:

$$ID = \frac{\frac{dE}{dx} \text{ measured} - \frac{dE}{dx} \pi}{\frac{dE}{dx} K - \frac{dE}{dx} \pi}. \quad (4.15)$$

In particular  $\langle ID \rangle = 0$  if the track is a pion and  $\langle ID \rangle = 1$  if the track is a kaon.

We use only the  $dE/dx$  information because in the sample that we are considering the track from B has  $P_t > 2$  GeV/c, as we discussed in Section 4.4. In a near future we will consider also the other sample where the two tracks from  $D^0$  are trigger tracks and the track from B has  $P_t < 2$  GeV/c. For this sample we will introduce the Time Of Flight that will be very important due to the very good K- $\pi$  separation at low momenta.

As parameterization of the ID variable we used the functions of the combined PID package, for single track, described in the previous chapter (Chapter 3) with a variable

changing. In fact, the pdf of the Combined PID package describes the residual distribution of  $dE/dx$ , but we need a pdf for the ID variable.

We have:

$$\begin{aligned} \frac{dE}{dx}_{Res} &= \frac{dE}{dx}_{meas} - \frac{dE^{part}}{dx}_{exp} = \frac{dE}{dx}_{meas} - \frac{dE^\pi}{dx}_{exp} + \left( \frac{dE^\pi}{dx}_{exp} - \frac{dE^{part}}{dx}_{exp} \right) = \\ &= \left( \frac{\frac{dE}{dx}_{meas} - \frac{dE^\pi}{dx}_{exp}}{\frac{dE^K}{dx}_{exp} - \frac{dE^\pi}{dx}_{exp}} - \frac{\frac{dE^{part}}{dx}_{exp} - \frac{dE^\pi}{dx}_{exp}}{\frac{dE^K}{dx}_{exp} - \frac{dE^\pi}{dx}_{exp}} \right) \cdot \left( \frac{dE^K}{dx}_{exp} - \frac{dE^\pi}{dx}_{exp} \right) = (ID - \langle ID \rangle) \cdot \Delta \end{aligned} \quad (4.16)$$

where  $\Delta = \frac{dE^K}{dx}_{exp} - \frac{dE^\pi}{dx}_{exp}$ .

So the ID distribution is  $p(ID) = p\left(\frac{dE}{dx}_{Res}(ID)\right) \left| \frac{d(\frac{dE}{dx}_{Res})}{dID} \right| = p((ID - \langle ID \rangle) \cdot \Delta) \cdot |\Delta|$ .

For the PID pdf of combinatorial background we have assumed that the background is composed only of pions and kaons. The PID pdf has the form:

$$a \cdot pdf_\pi(ID) + (1 - a) \cdot pdf_K(ID) \quad (4.17)$$

where  $a$  is the fraction of pions in the combinatorial background. This fraction is *left free* to float in the maximum likelihood fit.  $pdf_\pi$  and  $pdf_K$  are the PID pdf of pions and kaons respectively, obtained using the functions of the combined PID package [65].

## 4.8 Fit implementation and test on toy MC

We implemented the fit using mass, kinematics and PID parameterizations described above and we tested it on Toy MC. We generated 1000 pseudoexperiments of 10000 events each. The fractions used to generate these Toys MC are:

- Background fraction with respect to the total event:  $b = 0.26$
- $\bar{D}^0 \pi^+$  fraction with respect to the total signal:  $f_\pi = 0.94$
- $\bar{D}^{*0} \pi^+$  fraction with respect to the total background:  $f_D = 0.18$
- Pion fraction in the combinatorial background:  $f_\pi$  in combinatorial background = 0.8

The proof that the fit is working well is the pull distribution of each fraction ( $b$ ,  $f_\pi$ ,  $f_D$  and  $f_\pi$  in combinatorial background). The pull of each fraction is defined as the ratio of the difference between the fitted value and the true value of the fraction, over the uncertainty on the fitted value. In Fig. 4.31, the pull distributions are shown. On the top left the pull relative to the  $\bar{D}^0 \pi^+$  fraction, on the top right the one relative to the fraction of pions in the combinatorial background, on the bottom left the one relative to the  $\bar{D}^{*0} \pi^+$  and finally on the bottom right the one relative to the background fraction  $b$ . The pulls of the background fractions ( $b$  and  $f_D$ ) have a small bias, but the important thing is that the pull of the  $\bar{D}^0 \pi^+$  fraction, that is the fraction used to calculate the ratio  $\frac{N(B^+ \rightarrow \bar{D}^0 K^+)}{N(B^+ \rightarrow \bar{D}^0 \pi^+)}$ , is centered in zero.



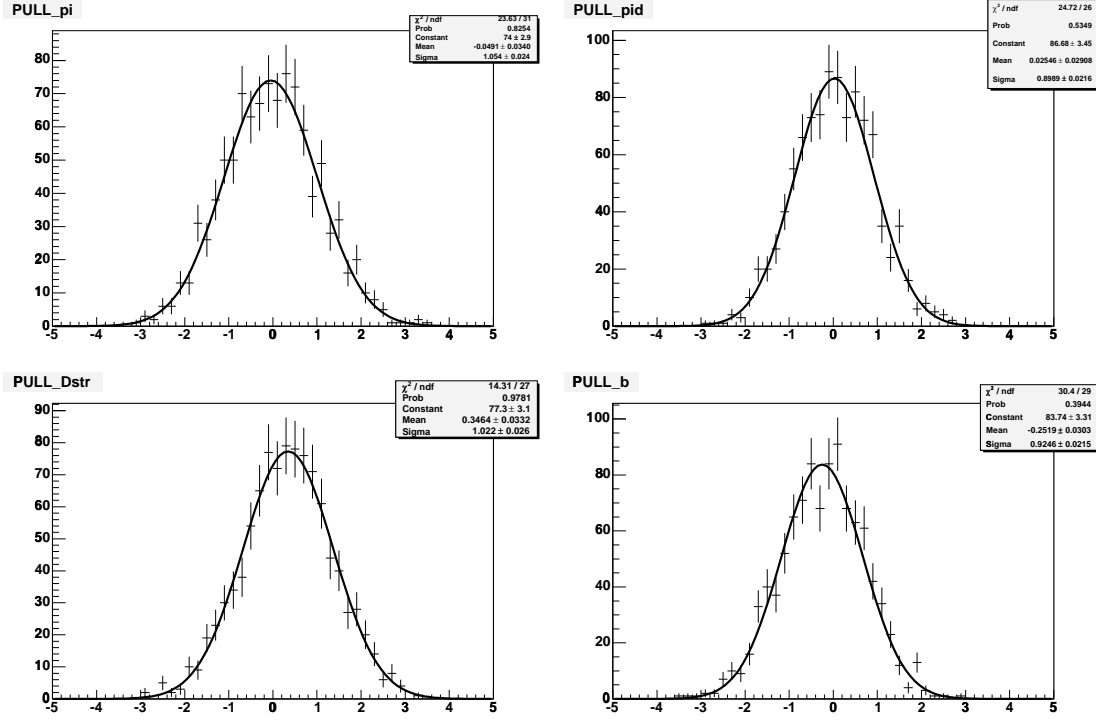


Figure 4.31: Pull distributions. Top left:  $\overline{D}^0 \pi^+$  fraction. Top right: fraction of pions in the combinatorial background. Bottom left:  $\overline{D}^{*0} \pi^+$  fraction. Bottom right: background fraction.

## 4.9 Fit results

The fit is performed on the events of  $B^+ \rightarrow \overline{D}_{flav}^0 \pi^+$  with the requirement that the track from  $B^+$  and a  $D^0$  track are trigger tracks. The fit windows are  $[5.17, 5.6]$  GeV/ $c^2$  in mass,  $[7, 30]$  GeV/ $c$  in  $P_{tot}$ ,  $[-0.8, 0.8]$  in  $\alpha$  and  $[-4, 4]$  in ID.

We are interested in the measurement of

$$R = \frac{BR(B^+ \rightarrow \overline{D}^0 K^+ \rightarrow [K^+ \pi^-] K^+)}{BR(B^+ \rightarrow \overline{D}^0 \pi^+ \rightarrow [K^+ \pi^-] \pi^+)}. \quad (4.18)$$

The raw fit results are summarized in the table 4.1. We label with “raw” the fit output which has not yet been corrected for the relative efficiencies.

The background fraction,  $f(B^+ \rightarrow \overline{D}^0 \pi^+)$  and  $f(B^+ \rightarrow \overline{D}^{*0} \pi^+)$  are respectively  $b$ ,  $f_\pi$  and  $f_D$  present in the Likelihood expression (4.8) described in the Section 4.3. The parameter “pion fraction in the combinatorial background” was introduced to express the particle identification pdf of combinatorial background as was described in section 4.7. We assumed a combinatorial background composed only of pions and kaons; the fraction of pions is left free to float in the main fit.

The parameter “scale” allows to correct the difference between data and MC about

Parameter	Value
background fraction	$0.187 \pm 0.009$
$f(B^+ \rightarrow \bar{D}^0 \pi^+)$	$0.936 \pm 0.006$
$f(B^+ \rightarrow \bar{D}^{*0} \pi^+)$	$0.16 \pm 0.03$
pion fraction in the combinatorial background	$0.74 \pm 0.04$
scale	$1.06 \pm 0.02$
Slope of the combinatorial background	$-3.4 \pm 0.5$

Table 4.1: Raw results from the maximum likelihood fit.

the width peak (section 4.5.1).

The last parameter is the slope of the combinatorial background mass shape that was left free in the fit as discussed in section 4.5.2.

From these values we can extract other interesting information:

- $f(B^+ \rightarrow \bar{D}^0 K^+) = 1 - f(B^+ \rightarrow \bar{D}^0 \pi^+) = 0.064 \pm 0.006$
- Combinatorial background fraction =  $0.84 \pm 0.03$
- Number of  $B^+ \rightarrow \bar{D}^0 \pi^+ = 3265 \pm 38$
- Number of  $B^+ \rightarrow \bar{D}^0 K^+ = 224 \pm 22$
- Number of  $B^+ \rightarrow \bar{D}^{*0} \pi^+ = 132 \pm 22$

Finally we can extract the raw result of the ratio R:

$$R|_{RAW} = \frac{N(B^+ \rightarrow \bar{D}^0 K^+)}{N(B^+ \rightarrow \bar{D}^0 \pi^+)} \Big|_{RAW} = 0.069 \pm 0.007. \quad (4.19)$$

Comparing our result with the Belle result,  $\frac{BR(B^+ \rightarrow \bar{D}^0 K^+)}{BR(B^+ \rightarrow \bar{D}^0 \pi^+)} = 0.077 \pm 0.005(stat.) \pm 0.006(sys.)$  [82] obtained with 6000 events of  $B^+ \rightarrow \bar{D}^0 \pi^+$ , the statistical errors are very similar, considering that we have 3300  $B^+ \rightarrow \bar{D}^0 \pi^+$ . We cannot do a true comparison with Babar result, because to calculate this ratio they used also the  $D^0 \rightarrow K^- \pi^+ \pi^+ \pi^-$  and  $D^0 \rightarrow K^- \pi^+ \pi^0$  obtaining more statistics and a smaller statistical error.

#### 4.9.1 Efficiency corrections

In order to translate the raw result of the fit into measurement of the ratio R we need to apply corrections for the relative efficiency. The raw fraction output by the fit is corrected with an efficiency factor  $\epsilon$ :

$$\epsilon = \epsilon_{trig} * \epsilon_{reco} * \epsilon_{cuts} * C_{XFT} \quad (4.20)$$

where  $\epsilon_{trig}$  is the trigger efficiency,  $\epsilon_{reco}$  is the reconstruction efficiency,  $\epsilon_{cuts}$  is the analysis cut efficiency and  $C_{XFT}$  is a correction that accounts for the fact that simulation does not reproduce the difference of the XFT efficiency between charged kaons and pions observed in data.

The product  $\epsilon_{trig} * \epsilon_{reco} * \epsilon_{cuts}$  is the kinematical efficiency ( $\epsilon_{kin}$ ) that can be estimated using MC signal samples. The XFT correction factor  $C_{XFT}$ , instead, has been measured on data [66].

Below we show how the efficiency corrections are applied to the raw result of the fit in order to extract the final value of relative BR:

$$\frac{BR(B^+ \rightarrow \bar{D}^0 K^+)}{BR(B^+ \rightarrow \bar{D}^0 \pi^+)} = \frac{N(B^+ \rightarrow \bar{D}^0 K^+)}{N(B^+ \rightarrow \bar{D}^0 \pi^+)} \Big|_{RAW} \cdot \frac{\epsilon_{kin}(B^+ \rightarrow \bar{D}^0 \pi^+)}{\epsilon_{kin}(B^+ \rightarrow \bar{D}^0 K^+)} \cdot \frac{C_{XFT}(B^+ \rightarrow \bar{D}^0 \pi^+)}{C_{XFT}(B^+ \rightarrow \bar{D}^0 K^+)} \quad (4.21)$$

Using the simulation of  $B^+ \rightarrow \bar{D}^0 \pi^+$  and of  $B^+ \rightarrow \bar{D}^0 K^+$  we obtained:

$$\frac{\epsilon_{kin}(B^+ \rightarrow \bar{D}^0 \pi^+)}{\epsilon_{kin}(B^+ \rightarrow \bar{D}^0 K^+)} = 0.919 \pm 0.006. \quad (4.22)$$

$C_{XFT}$  is the correction needed to account for the different XFT efficiency between charged kaons and pions, this is due to the different specific ionization in the COT volume, in fact the charged pions tend to ionize more than charged kaons. The consequence is a larger pulse width for pions compared to kaons and then a larger number of hits in the COT chamber. Due to the requirements on the number of Axial COT hits imposed by the XFT trigger (Section 2.8.1), this can reflect in a different efficiency for kaons and pions. This effect, is not well reproduced in the simulation, and will not cancels in the acceptance ratios estimates, resulting in a bias in the measurement of the relative branching fractions. This different XFT efficiency has been measured by an accurate study using  $D^+ \rightarrow K^- \pi^+ \pi^+$  decays [66].

The correction is:

$$\frac{C_{XFT}(B^+ \rightarrow \bar{D}^0 \pi^+)}{C_{XFT}(B^+ \rightarrow \bar{D}^0 K^+)} = 1.02 \pm 0.06 \quad (4.23)$$

After applying the corrections we obtained the following result:

$$R = \frac{N(B^+ \rightarrow \bar{D}^0 K^+)}{N(B^+ \rightarrow \bar{D}^0 \pi^+)} \cdot \frac{\epsilon_{kin}(B^+ \rightarrow \bar{D}^0 \pi^+)}{\epsilon_{kin}(B^+ \rightarrow \bar{D}^0 K^+)} \cdot \frac{C_{XFT}(B^+ \rightarrow \bar{D}^0 \pi^+)}{C_{XFT}(B^+ \rightarrow \bar{D}^0 K^+)} = 0.065 \pm 0.007(stat). \quad (4.24)$$

#### 4.9.2 Fit projection

In order to visualize the agreement between the fit and the data we reported the plots of fit projections. A projection of the generic probability density function  $pdf(x, \vec{y} | \vec{m})$  on the observable  $x$  is the plot of the function  $\int_{all \vec{y}} pdf(x, \vec{y} | \vec{m}) d\vec{y}$ , which can be

overlaid to the experimental data with the appropriate normalization.

In Fig. 4.32, 4.33, 4.34 and 4.35 the projections, respectively, on the mass, on the  $\alpha$  variable, on  $P_{tot}$  and on the ID variable are shown.

The points are data and the solid line are the fit projections.

In particular in red we have the total projection, in green the projection relative to the  $B^+ \rightarrow \bar{D}^0 \pi^+$ , in blue the one relative to the  $B^+ \rightarrow \bar{D}^0 K^+$ , in magenta the one relative to the  $B^+ \rightarrow \bar{D}^{*0} \pi^+$  and finally in black the one relative to the combinatorial background.

For each projection the plot of the difference between projection and data (second plot from the top) and the corresponding residual distributions (third plot from the top) are shown. The resulting  $\chi^2$  are:

- $\chi^2 = \frac{53}{56}$  for the mass distribution;
- $\chi^2 = \frac{156}{98}$  for the  $\alpha$  distribution;
- $\chi^2 = \frac{174}{99}$  for the  $P_{tot}$  distribution;
- $\chi^2 = \frac{63}{70}$  for the ID distribution.

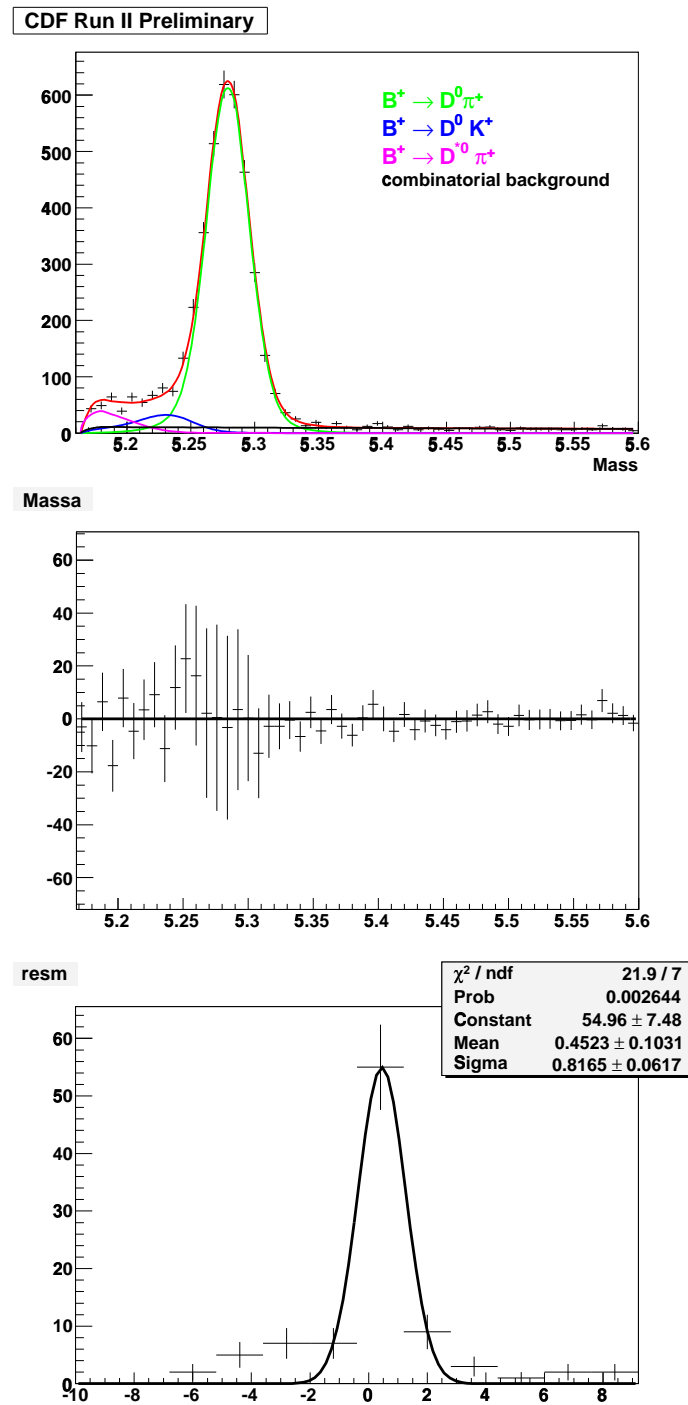


Figure 4.32: First plot: Fit projection on the mass. Second plot: Difference between projection and data. Third plot: Residual relative to the difference between projection and data.  $\chi^2 = 53/56$

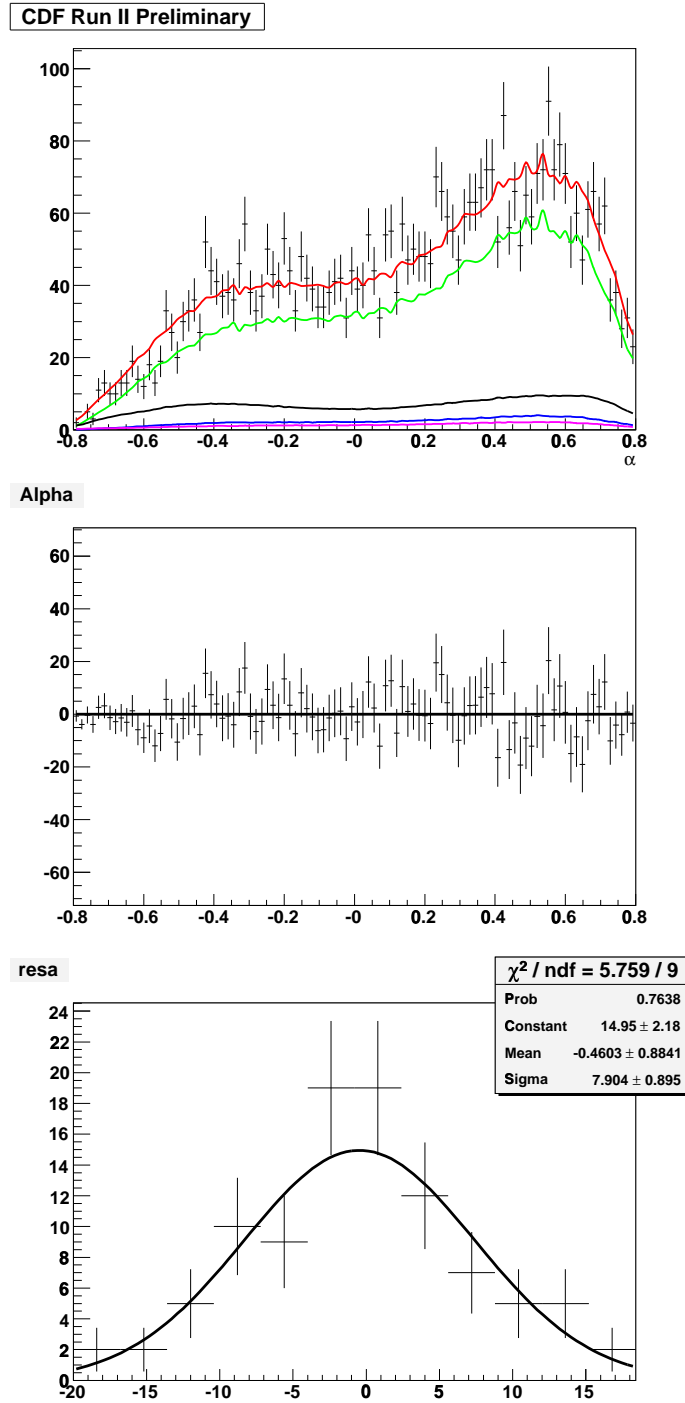


Figure 4.33: First plot: Fit projection on  $\alpha$ . Second plot: Difference between projection and data. Third plot: Residual relative to the difference between projection and data.  $\chi^2 = 156/98$

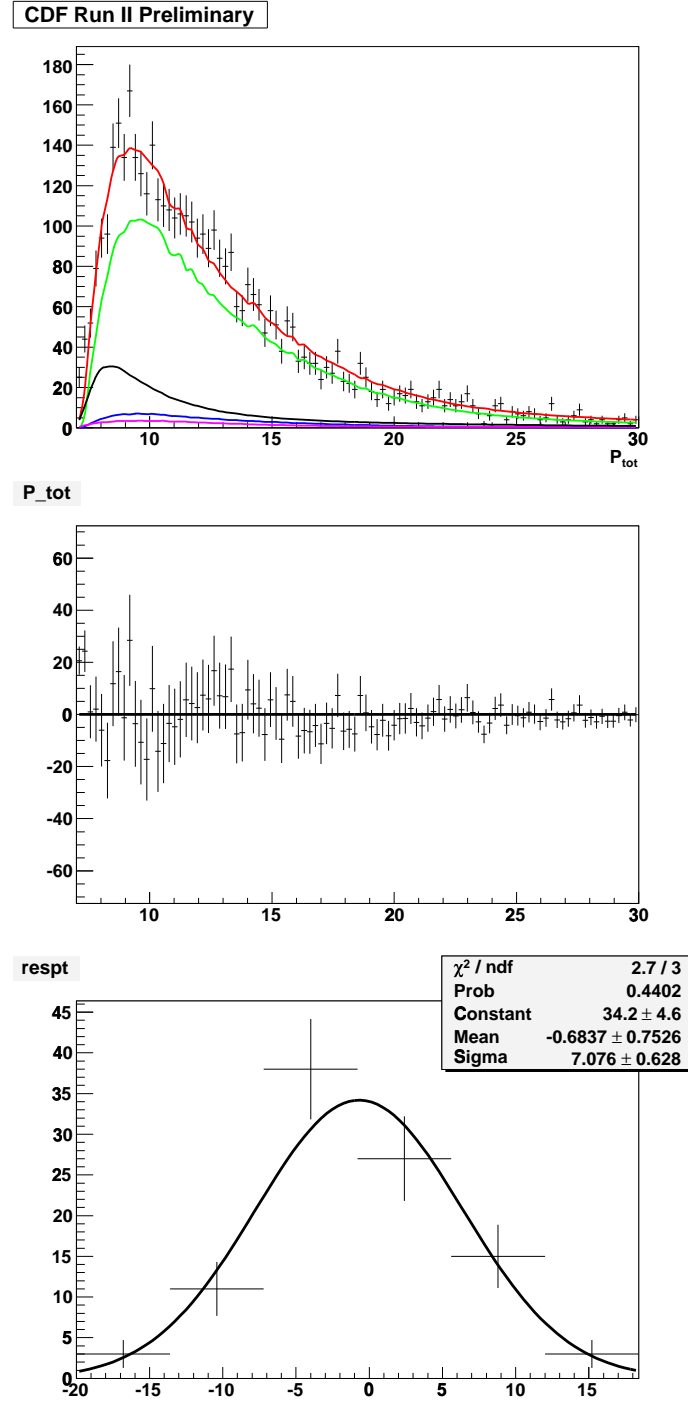


Figure 4.34: First plot: Fit projection on  $P_{tot}$ . Second plot: Difference between projection and data. Third plot: Residual relative to the difference between projection and data.  $\chi^2 = 174/99$

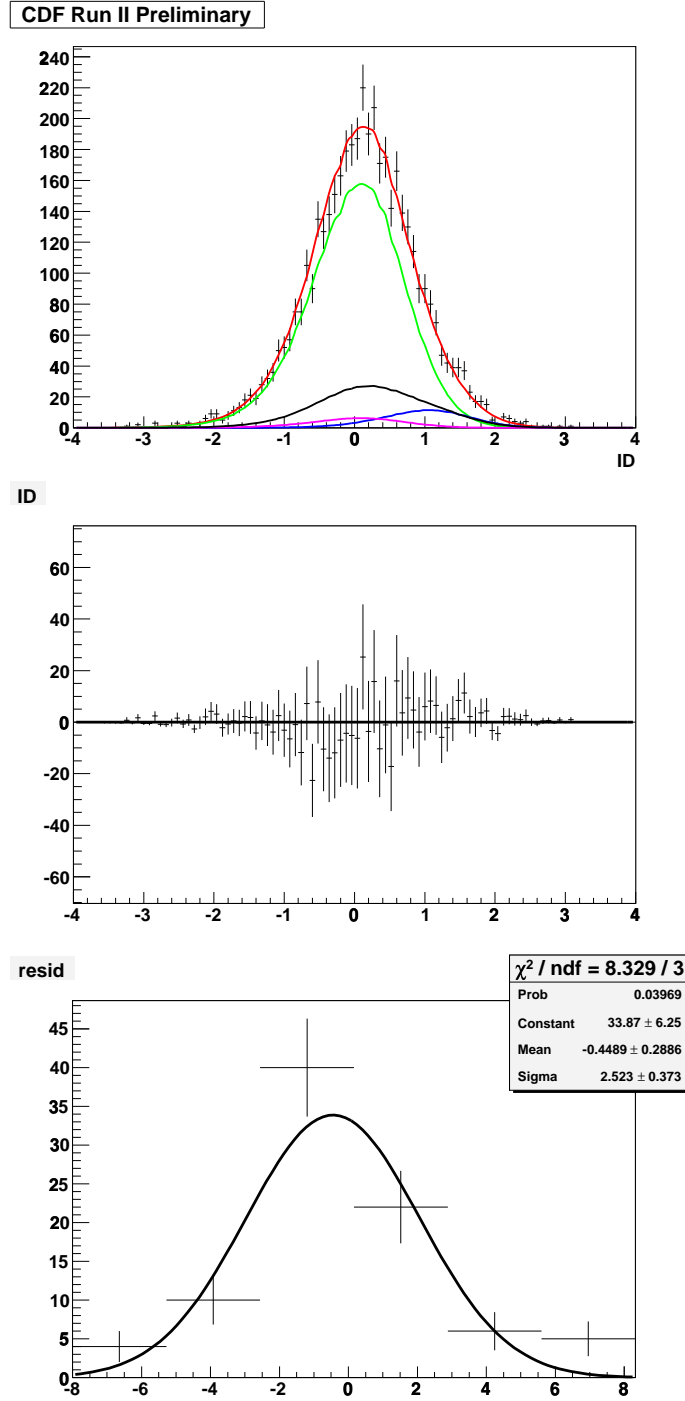


Figure 4.35: First plot: Fit projection on ID. Second plot: Difference between projection and data. Third plot: Residual relative to the difference between projection and data.  $\chi^2 = 63/70$



## 4.10 Systematics

In the following sections we will describe the main sources of systematic uncertainties:

- Mass resolution tails in  $\overline{D}^0 \pi^+$  and  $\overline{D}^0 K^+$  decays;
- Value of the input mass  $B^+$ ;
- Systematics associated with  $\frac{dE}{dx}$  distribution;
- Combinatorial background systematics due to the mass model, to the kinematical parameterization and to the PID assumptions;
- $\overline{D}^{*0} \pi^+$  mass model;
- Montecarlo statistics and XFT efficiency.

### 4.10.1 Mass resolution tails

In the simulation the invariant mass distribution of  $\overline{D}^0 \pi^+$  and  $\overline{D}^0 K^+$  samples present some tails that we can parameterize adding a constant to the three gaussians. In Fig. 4.36 the invariant mass distributions and the new fitting curves are shown. On the left the  $\overline{D}^0 \pi^+$  mass and on the right the  $\overline{D}^0 K^+$  one. We repeated the fit using these new fitting curves and the resulting systematics is 0.001.

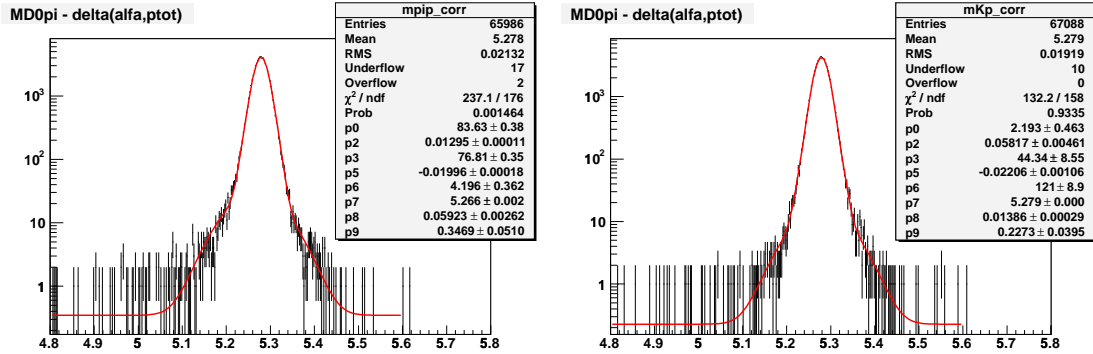


Figure 4.36:  $B^+$  Invariant mass distributions of signal decays. On the left the  $\overline{D}^0 \pi^+$  and on the right the  $\overline{D}^0 K^+$ . The continuous lines are the fit using three gaussians plus a constant.

### 4.10.2 Input mass

The  $B^+$  mass is an input parameter to the fit through the analytic expression of  $M(\alpha, P_{tot})$  (equations (4.6) and (4.7)). As  $B^+$  mass value we used  $5279.10 \pm 0.41(stat.) \pm 0.36(sys.) \text{ MeV}/c^2$  measured with the CDF II detector [83]. We repeated the fit varying the input mass of  $\pm 1\sigma$  and the resulting systematics is 0.001.

### 4.10.3 dE/dx induced systematics

To evaluate the systematics associated with dE/dx measurement we repeated the fit varying the parameters of the Likelihood functions randomly in a  $1\sigma$ -radius multidimensional sphere in the space of the parameters of dE/dx calibrations. This method was described in Section 3.4. The resulting systematics is 0.0015.

### 4.10.4 Combinatorial background systematics

#### Mass model

The central fit assumes a mass-shape of the combinatorial background events distributed as an exponential function. To evaluate the systematics we have changed the mass shape, looking at the sample obtained requiring  $L_{xy} < -300\mu m$ . We repeated the fit using as mass shape different polynomial functions of increasing degree, up to the third. In Fig. 4.37 the fits of the mass-shape using the polynomial are shown: on the top left a first degree polynomial was used, on the top right a second degree polynomial and on the bottom a third degree polynomial. The resulting systematics is 0.001.

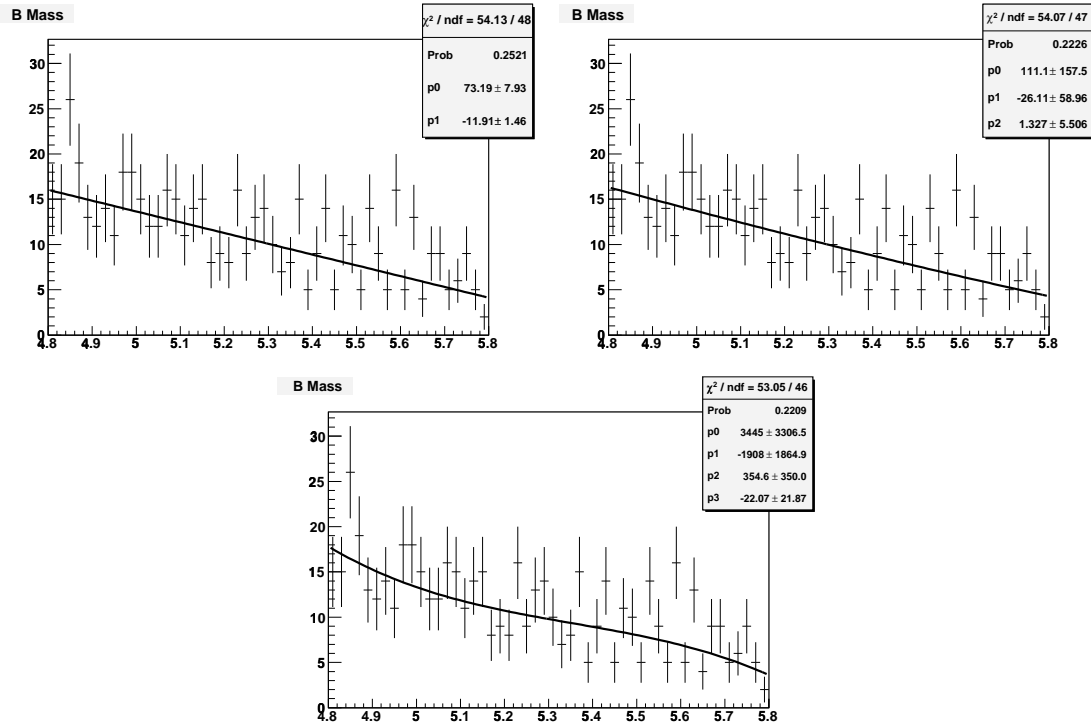


Figure 4.37: Fit of the combinatorial background mass using polynomial.

### Kinematical parameterization

To evaluate the systematics associated to the kinematical parameterization of the combinatorial background we repeated the fit using the  $p(\alpha, P_{tot})$  distributions of  $\bar{D}^0 \pi^+$  and of  $\bar{D}^0 K^+$  for the background. The resulting systematics is 0.001.

### Particle Identification

In the main fit we assumed that the fraction of pions in combinatorial background is not mass dependent. To verify that, we fitted two distinct pions fractions, one in the mass window  $[5.17-5.4] \text{ GeV}/c^2$  and one in the mass window  $[5.4,5.6] \text{ GeV}/c^2$ . We obtained:

- fraction of pions in  $[5.17-5.4] \text{ GeV}/c^2 = 0.76 \pm 0.05$
- fraction of pions in  $[5.4-5.6] \text{ GeV}/c^2 = 0.72 \pm 0.05$

that are in agreement within the error.

Another assumption is relative to the composition of the combinatorial background. We assumed a background of only pions and kaons. To evaluate the systematics associated with ignoring protons and electrons we made 100 toy MC with also protons and electrons in the background. The background composition of each toy is 70% of pions, 10% of protons, 2% of electrons and 18% of kaons. We fitted the toy MC with the main fit and, observing the residual distribution of the ratio  $\frac{N(B^+ \rightarrow \bar{D}^0 K^+)}{N(B^+ \rightarrow \bar{D}^0 \pi^+)}$  (difference between the fitted value and the true value) in Fig. 4.38, centered in zero, we confirm that the fit is not sensitive to the electrons and protons contribution.

#### 4.10.5 $\bar{D}^{*0} \pi^+$ mass model

To evaluate this systematics we left free to float in the main fit some parameters of the  $\bar{D}^{*0} \pi^+$  mass parameterization. We parameterized the  $\bar{D}^{*0} \pi^+$  mass with three gaussians plus an exponential in the range of mass  $[5.06,5.6] \text{ GeV}/c^2$  as described in section 4.5.2. The idea is to see how the result (the ratio  $\frac{N(B^+ \rightarrow \bar{D}^{*0} K^+)}{N(B^+ \rightarrow \bar{D}^{*0} \pi^+)}$ ) change letting free to float in the main fit the parameters of the exponential or of the gaussian that falls in the fit window  $[5.17,5.6] \text{ GeV}/c^2$ . We made some test:

- We left free to vary in the main fit the slope of the exponential and we obtained  $\frac{N(B^+ \rightarrow \bar{D}^{*0} K^+)}{N(B^+ \rightarrow \bar{D}^{*0} \pi^+)} = 0.069 \pm 0.007$ .
- We left free to vary the mean of the gaussian obtaining  $\frac{N(B^+ \rightarrow \bar{D}^{*0} K^+)}{N(B^+ \rightarrow \bar{D}^{*0} \pi^+)} = 0.066 \pm 0.007$ .
- We left free to vary, simultaneously, the slope of the exponential and the mean of the gaussian obtaining  $\frac{N(B^+ \rightarrow \bar{D}^{*0} K^+)}{N(B^+ \rightarrow \bar{D}^{*0} \pi^+)} = 0.066 \pm 0.007$ .

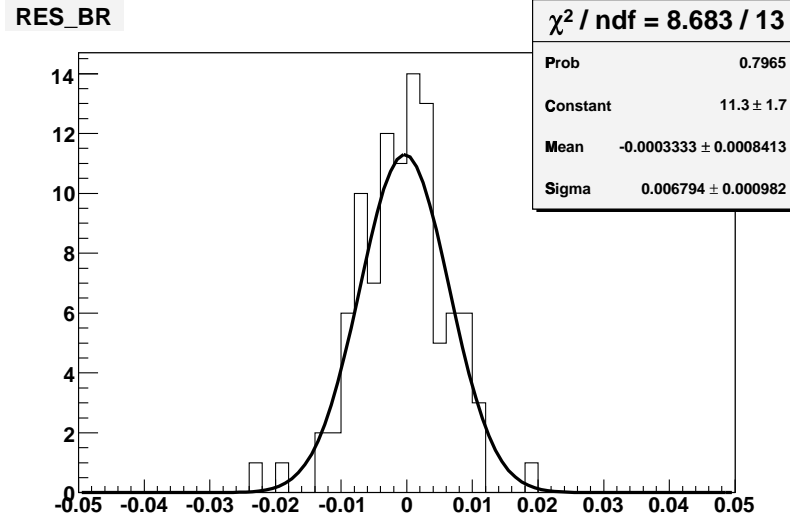


Figure 4.38: Residual distribution of the ratio  $\frac{N(B^+ \rightarrow \bar{D}^0 K^+)}{N(B^+ \rightarrow \bar{D}^0 \pi^+)}$  (difference between the fitted value and the true value) obtained fitting with the main fit a toy MC where besides kaons and pions are present protons and electrons. The residual is centered in zero, so the fit is not sensitive to the electron and the proton contribution.

The resulting systematics is 0.003.

We also make the fit with another parameterization for the  $D^{*0} \pi$  mass (Fig. 4.39). The resulting systematics is 0.001.

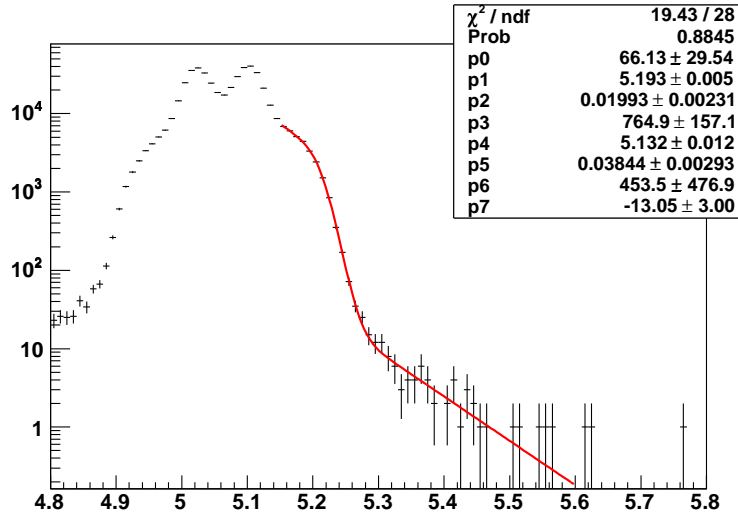


Figure 4.39: Fit of the  $\bar{D}^{*0} \pi^+$  mass with 2 gaussians plus an exponential in the mass range  $[5.15, 5.6] \text{ GeV}/c^2$ .

#### 4.10.6 Check of $\overline{D}^{*0}\pi^+$ mass model

To check the validity of treatment of the  $\overline{D}^{*0}\pi^+$  decay, we compare the result with the simulation.

In Fig.4.40 data and prediction are overlaid. The points are data, the red curve from 5.17 to 5.6  $\text{GeV}/c^2$  is the projection obtained from the main fit, the blue curve is the sum of the MonteCarlo sample and of the combinatorial background. In magenta and in green we can see the two components separately, respectively the MonteCarlo sample and the combinatorial background.

The combinatorial background is normalized to the number of events of background fitted in the window  $[5.17, 5.6] \text{ GeV}/c^2$ . The MonteCarlo sample is normalized to the number of  $\overline{D}^{*0}\pi^+$  fitted in the window  $[5.17, 5.6] \text{ GeV}/c^2$ . From the plot, we observe that the prediction is lower than the data.

Since the fit returns a fraction of  $\overline{D}^{*0}\pi^+$  with an uncertainty, we made the same plot normalizing the MonteCarlo sample to the number of  $\overline{D}^{*0}\pi^+$  fitted in the window  $[5.17, 5.6] \text{ GeV}/c^2$  plus  $1\sigma$  (we used  $f_D + 1\sigma$ ). We obtained the plot shown in Fig.4.41 where there is a good agreement between the prediction and the data.

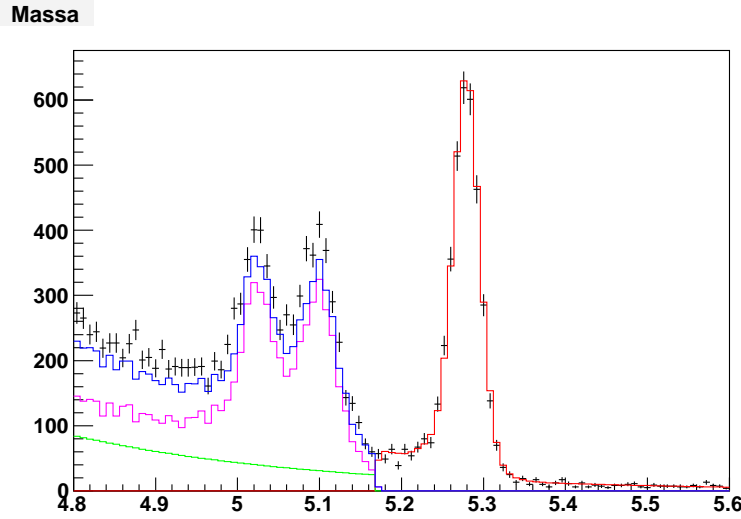


Figure 4.40: Invariant mass of  $\overline{D}^{*0}\pi^+$  candidates. Prediction (continuous lines) superimposed to data (points). The red curve is the projection obtained from the main fit. The blue curve is the sum of the MonteCarlo sample (in magenta) and of the combinatorial background (in green). We normalized the combinatorial background to the number of events of background fitted in the window  $[5.17, 5.6] \text{ GeV}/c^2$ . We normalized the MonteCarlo sample to the number of  $\overline{D}^{*0}\pi^+$  fitted in the window  $[5.17, 5.6] \text{ GeV}/c^2$ . The prediction is lower than the data.

We also attempt a fit in a wider mass window, from 5.11 to 5.6  $\text{GeV}/c^2$ . In this fit window besides the  $\overline{D}^{*0}\pi^+$  there are other physical backgrounds to consider as we observed in Fig.4.5 where the invariant mass spectrum of  $B^+ \rightarrow \overline{D}^0\pi^+$  from simulation

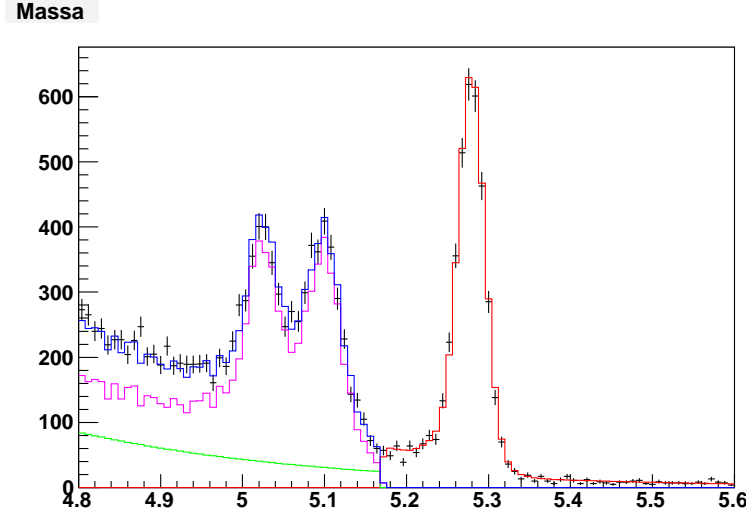


Figure 4.41: Invariant mass of  $\bar{D}^0 \pi^+$  candidates. Prediction (continuous lines) superimposed to data (points). The red curve is the projection obtained from the main fit. The blue curve is the sum of the MonteCarlo sample (in magenta) and of the combinatorial background (in green). We normalized the combinatorial background to the number of events of background fitted in the window  $[5.17, 5.6]$   $\text{GeV}/c^2$ . We normalized the MonteCarlo sample to the number of  $\bar{D}^{*0} \pi^+$  fitted in the window  $[5.17, 5.6]$   $\text{GeV}/c^2$  plus  $1\sigma$  (we used  $f_D + 1\sigma$ ). The prediction and the data are in agreement.

is shown.

To add these decays to the unbinned maximum likelihood fit we have to parameterize their mass shape. We parameterized the mass shape of these other physical background, the  $D^{*+} \pi^-$ , the  $\bar{D}^{*0} K^+$  and “other decay” with a gaussian plus an exponential. In Fig.4.42 the fits are shown. On the top left the  $D^{*+} \pi^-$ , on the top right the  $\bar{D}^{*0} K^+$  and on the bottom “other decay”. We need also a parameterization of the 2-dimensional distribution  $\alpha$  vs  $P_{tot}$ . As  $p(\alpha, P_{tot})$  distribution we used the one of the  $\bar{D}^0 \pi^+$  for all the three other physical background.

The result of the fit is  $0.072 \pm 0.007$  (remind that the central fit value is  $0.069 \pm 0.007$ ). The two results differ of 0.003, that is of the same order of the systematics that we put on the  $\bar{D}^{*0} \pi^+$  model.

In Fig.4.43 the fit projections are shown.

After all these checks we can conclude that the systematics on the  $\bar{D}^{*0} \pi^+$  is evaluated in the correct way.

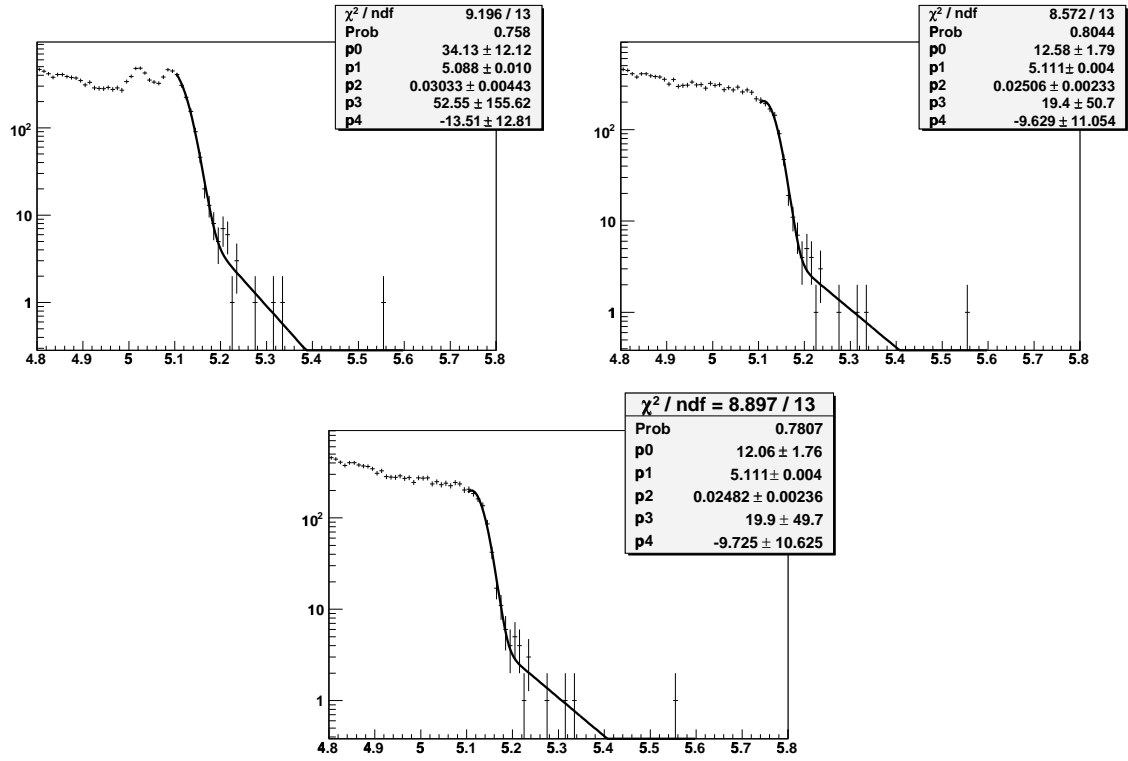


Figure 4.42: Fit of the mass shapes of the other physical background using a gaussian plus an exponential. On the top left the  $D^{*+}\pi^-$ , on the top right the  $\bar{D}^{*0}K^+$  and on the bottom “other decay”.

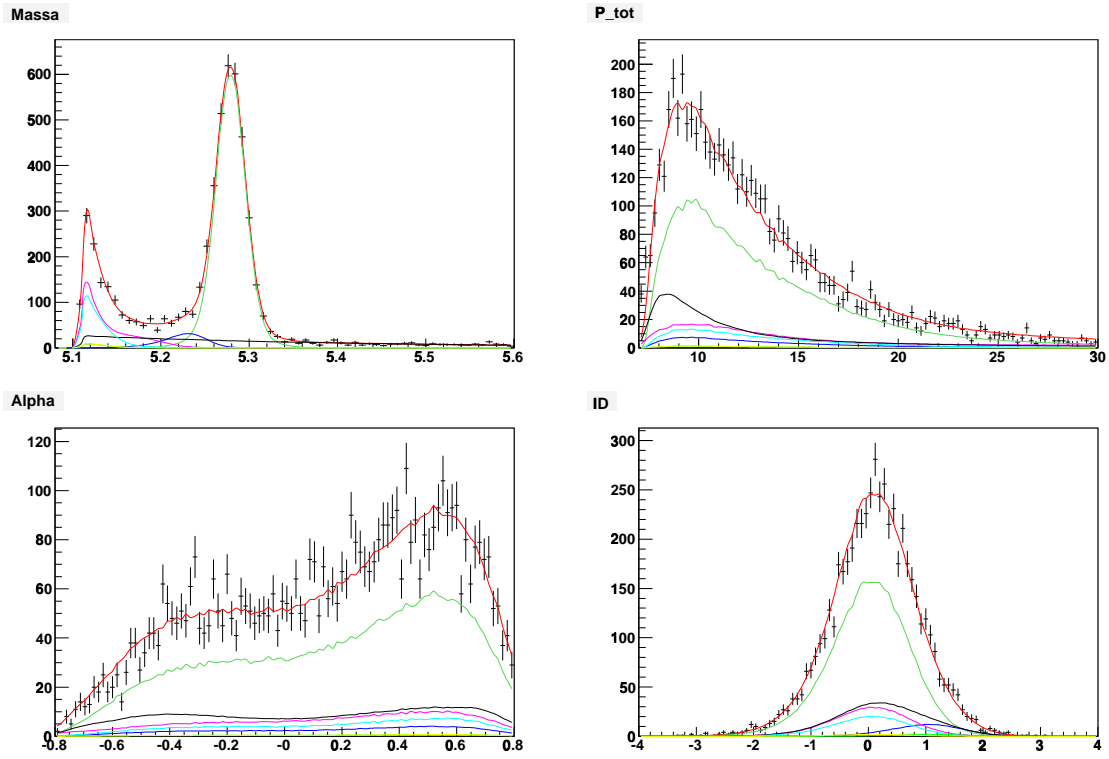


Figure 4.43: Projections of the fit in the window  $[5.11-5.6] \text{ GeV}/c^2$ . On the top left the mass projection, on the top right the  $P_{tot}$  projection, on the bottom left the  $\alpha$  projection and finally on the bottom right the ID projection.



#### 4.10.7 Monte Carlo statistics and XFT efficiency

This is the uncertainty deriving from the limited statistics of the Monte Carlo samples used to estimate the relative efficiencies and from the error on the XFT efficiency (equation (4.23)) that dominates this systematics. The resulting systematics is 0.002.

#### 4.10.8 Total systematic uncertainties

A summary of the all systematics is reported in table 4.2. The total systematic uncertainty has been determined as the sum in quadrature of the single systematic uncertainty.

Source	Shift wrt central fit
Mass resolution tails	0.0006
Input mass	0.001
dE/dx	0.0015
combinatorial background model	0.001
$D^{*0}\pi$ left free in the fit	0.003
changing $D^{*0}\pi$ mass model	0.001
MC statistics+XFT eff	0.002
Total(sum in quadrature)	0.004

Table 4.2: Systematics summary.

### 4.11 Final result

We measured the ratio

$$R = \frac{BR(B^+ \rightarrow \bar{D}^0 K^+ \rightarrow [K^+ \pi^-] K^+)}{BR(B^+ \rightarrow \bar{D}^0 \pi^+ \rightarrow [K^+ \pi^-] \pi^+)} = 0.065 \pm 0.007(stat) \pm 0.004(sys). \quad (4.25)$$

The world average for this ratio is  $0.083 \pm 0.0035$ . This result comes out from the combined measurement of Belle ( $0.077 \pm 0.005(stat.) \pm 0.006(sys.)$  [82]), Babar ( $0.0831 \pm 0.0035(stat.) \pm 0.002(sys.)$  [84]) and Cleo ( $0.099^{+0.014}_{-0.012}(stat.)^{+0.007}_{-0.006}(sys.)$  [85]).

#### 4.12 Fit of $B^+ \rightarrow D_{CP+}^0 \pi^+$ with $D_{CP+}^0 \rightarrow K^- K^+, \pi^- \pi^+$

We also make the Unbinned Maximum Likelihood Fit on the  $D_{CP+}^0 \pi^+$  decays. We separated the  $B^+$  and  $B^-$  because we have to calculate the  $A_{CP+}$  asymmetry defined in equation (1.36).

The raw fit results for  $B \rightarrow D_{CP+}^0 \pi$  with  $D_{CP+}^0 \rightarrow K^+ K^-, \pi^+ \pi^-$  are summarized in the table 4.3 both for  $B^-$  and  $B^+$ . The parameter of scale, that multiply the widths of the

Parameter	$B^-$	$B^+$
background fraction	$0.61 \pm 0.03$	$0.59 \pm 0.03$
$f(B \rightarrow D_{CP+}^0 \pi)$	$0.90 \pm 0.04$	$0.89 \pm 0.04$
$f(B \rightarrow D^{*0} \pi)$	$0.07 \pm 0.03$	$0.07 \pm 0.03$
pion fraction in the combinatorial background	$0.75 \pm 0.05$	$0.62 \pm 0.05$
Slope of the combinatorial background	$-2.2 \pm 0.7$	$-2.1 \pm 0.7$

Table 4.3: Raw results from the maximum likelihood fit on the DCP sample ( $D_{CP+} \rightarrow K^+ K^-$ ).

gaussians that describe the mass resolution, to take in account the differences between data and MC, is fixed by the fit on the flavor sample.

From these values we can extract other interesting information for  $B^-$ :

- $f(B^- \rightarrow D_{CP+}^0 K^-) = 1 - f(B^- \rightarrow D_{CP+}^0 \pi^-) = 0.10 \pm 0.04$
- Combinatorial background fraction =  $0.93 \pm 0.03$
- Number of  $B^- \rightarrow D_{CP+}^0 \pi^- = 206 \pm 16$
- Number of  $B^- \rightarrow D_{CP+}^0 K^- = 22 \pm 9$
- Number of  $B^- \rightarrow D^{*0} \pi^- = 24 \pm 12$

and for  $B^+$

- $f(B^+ \rightarrow D_{CP+}^0 K^+) = 1 - f(B^+ \rightarrow D_{CP+}^0 \pi^+) = 0.11 \pm 0.04$
- Combinatorial background fraction =  $0.93 \pm 0.03$
- Number of  $B^+ \rightarrow D_{CP+}^0 \pi^+ = 210 \pm 16$
- Number of  $B^+ \rightarrow D_{CP+}^0 K^+ = 25 \pm 10$
- Number of  $B^+ \rightarrow D^{*0} \pi^+ = 25 \pm 10$

The raw fit results for  $B \rightarrow D_{CP+}^0 \pi$  with  $D_{CP+}^0 \rightarrow \pi^+ \pi^-$  are summarized in the table 4.4 both for  $B^-$  and  $B^+$ .

Parameter	$B^-$	$B^+$
background fraction	$0.69 \pm 0.04$	$0.76 \pm 0.04$
$f(B \rightarrow D_{CP+}^0 \pi)$	$0.89 \pm 0.06$	$0.92 \pm 0.07$
$f(B \rightarrow D^{*0} \pi)$	$0.10 \pm 0.04$	$0.0 \pm 0.02$
pion fraction in the combinatorial background	$0.69 \pm 0.06$	$0.68 \pm 0.06$

Table 4.4: Raw results from the maximum likelihood fit on the DCP sample ( $D_{CP+} \rightarrow \pi \pi$ ).

From these values we can extract other interesting information for  $B^-$ :

- $f(B^- \rightarrow D_{CP+}^0 K^-) = 1 - f(B^- \rightarrow D_{CP+}^0 \pi^-) = 0.11 \pm 0.06$
- Combinatorial background fraction =  $0.90 \pm 0.04$
- Number of  $B^- \rightarrow D_{CP+}^0 \pi^- = 72 \pm 9$
- Number of  $B^- \rightarrow D_{CP+}^0 K^- = 9 \pm 5$
- Number of  $B^- \rightarrow D^{*0} \pi^- = 18 \pm 6$

and for  $B^+$

- $f(B^+ \rightarrow D_{CP+}^0 K^+) = 1 - f(B^+ \rightarrow D_{CP+}^0 \pi^+) = 0.08 \pm 0.07$
- Combinatorial background fraction =  $1.0 \pm 0.02$
- Number of  $B^+ \rightarrow D_{CP+}^0 \pi^+ = 61 \pm 10$
- Number of  $B^+ \rightarrow D_{CP+}^0 K^+ = 5 \pm 5$
- Number of  $B^+ \rightarrow D^{*0} \pi^+ = 1 \pm 5$

In order to visualize the agreement between the fit and the data we reported the plots of fit projections. In Fig. 4.44 and 4.45 the fit projections on mass (top-left),  $\alpha$  (top-right),  $P_{tot}$  (bottom-left) and ID (bottom-right), for  $D_{CP+}^0 \pi$  with  $D_{CP+}^0 \rightarrow K^+ K^-$  modes, respectively for  $B^-$  and  $B^+$  are shown. In Fig. 4.46 and 4.47 the fit projections for  $D_{CP+}^0 \pi$  with  $D_{CP+}^0 \rightarrow \pi^+ \pi^-$  modes, respectively for  $B^-$  and  $B^+$  are shown. The point are data and the solid line are the fit projections. In particular in red we have the total projection, in green the projection relative to the  $B \rightarrow D_{CP+}^0 \pi$ , in blue the one relative to the  $B \rightarrow D_{CP+}^0 K$ , in magenta the one relative to the  $B \rightarrow D^{*0} \pi$  and finally in black the one relative to the combinatorial background.

The available statistics is too low to obtain a measurement of  $A_{CP+}$  (equation (1.36)) and  $R_{CP+}$  (equation (1.38)). We describe an evaluation of the obtainable resolution with larger samples in the following section.

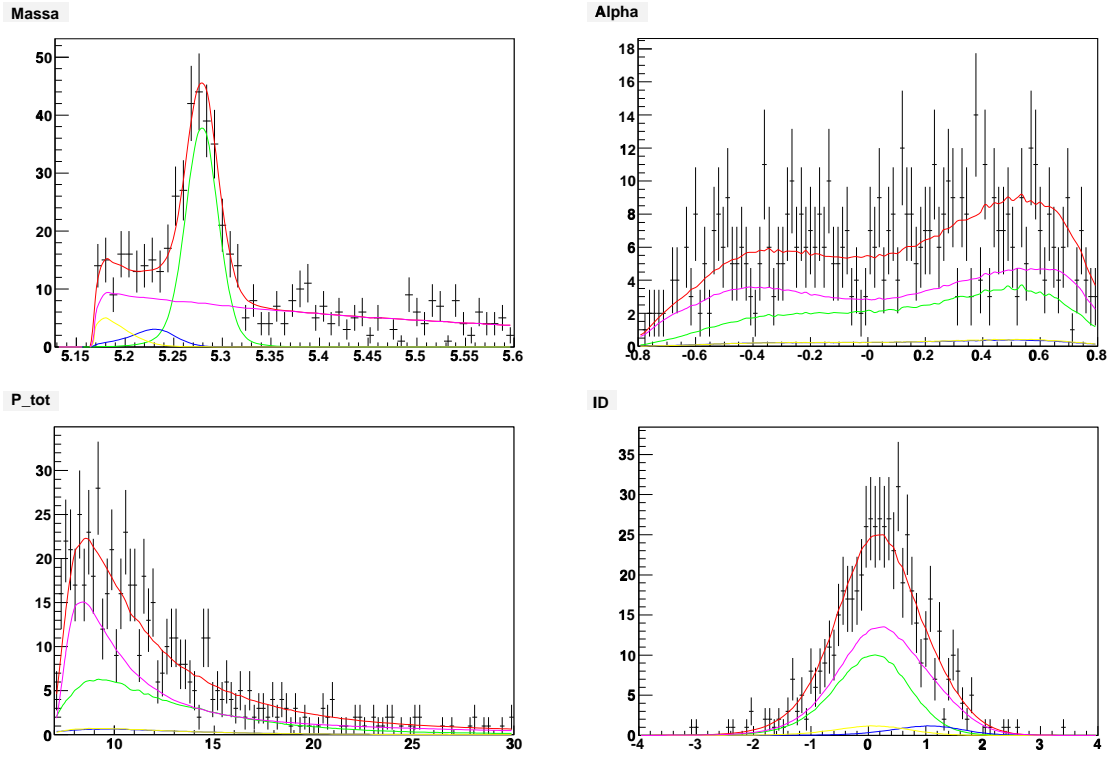


Figure 4.44: Fit projections for  $B^- \rightarrow D_{CP+}^0 \pi^- \rightarrow [K^+ K^-] \pi^-$ . Top left: projection on mass. Top right: projection on  $\alpha$ . Bottom left: projection on  $P_{tot}$ . Bottom right: projection on ID.

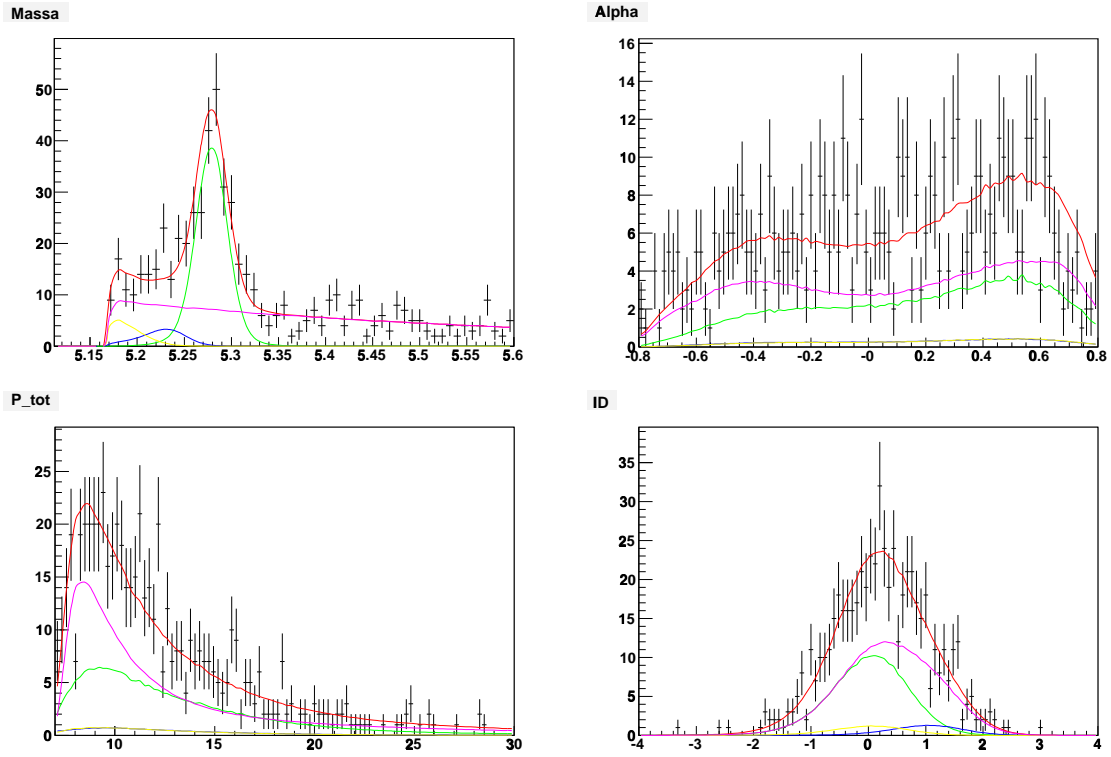


Figure 4.45: Fit projections for  $B^+ \rightarrow D_{CP+}^0 \pi^+ \rightarrow [K^+ K^-] \pi^+$ . Top left: projection on mass. Top right: projection on  $\alpha$ . Bottom left: projection on  $P_{tot}$ . Bottom right: projection on ID.

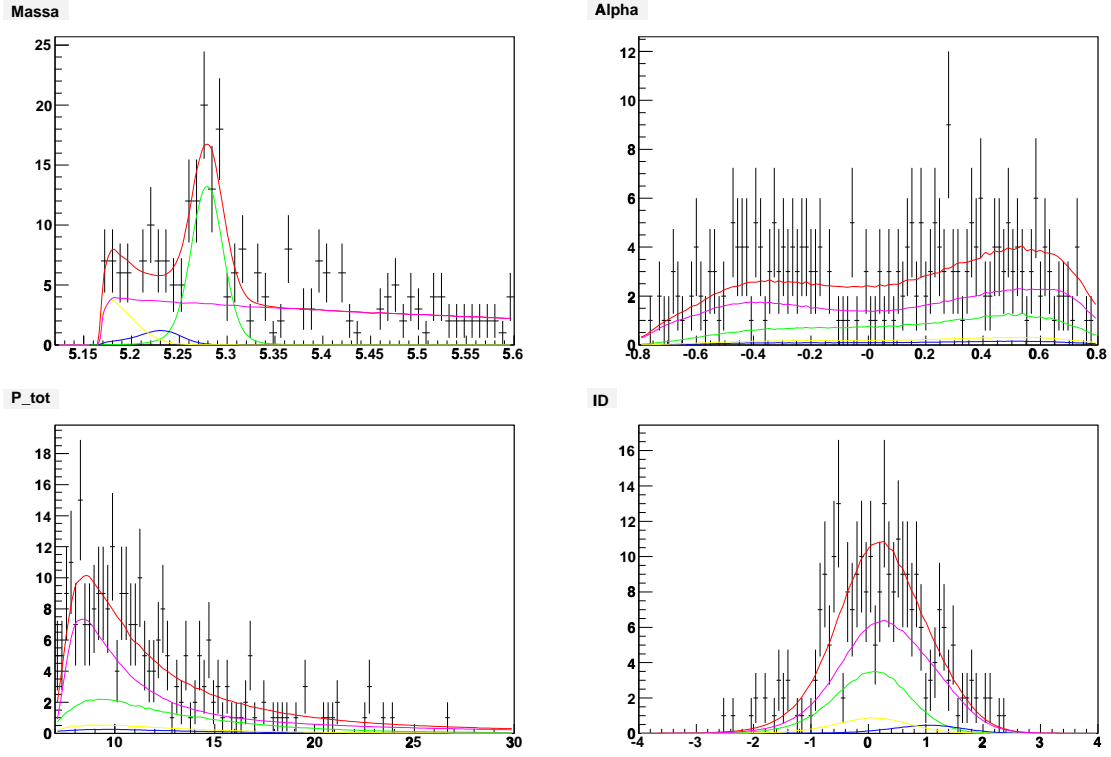


Figure 4.46: Fit projections for  $B^- \rightarrow D_{CP+}^0 \pi^- \rightarrow [\pi^+ \pi^-] \pi^-$ . Top left: projection on mass. Top right: projection on  $\alpha$ . Bottom left: projection on  $P_{tot}$ . Bottom right: projection on ID.

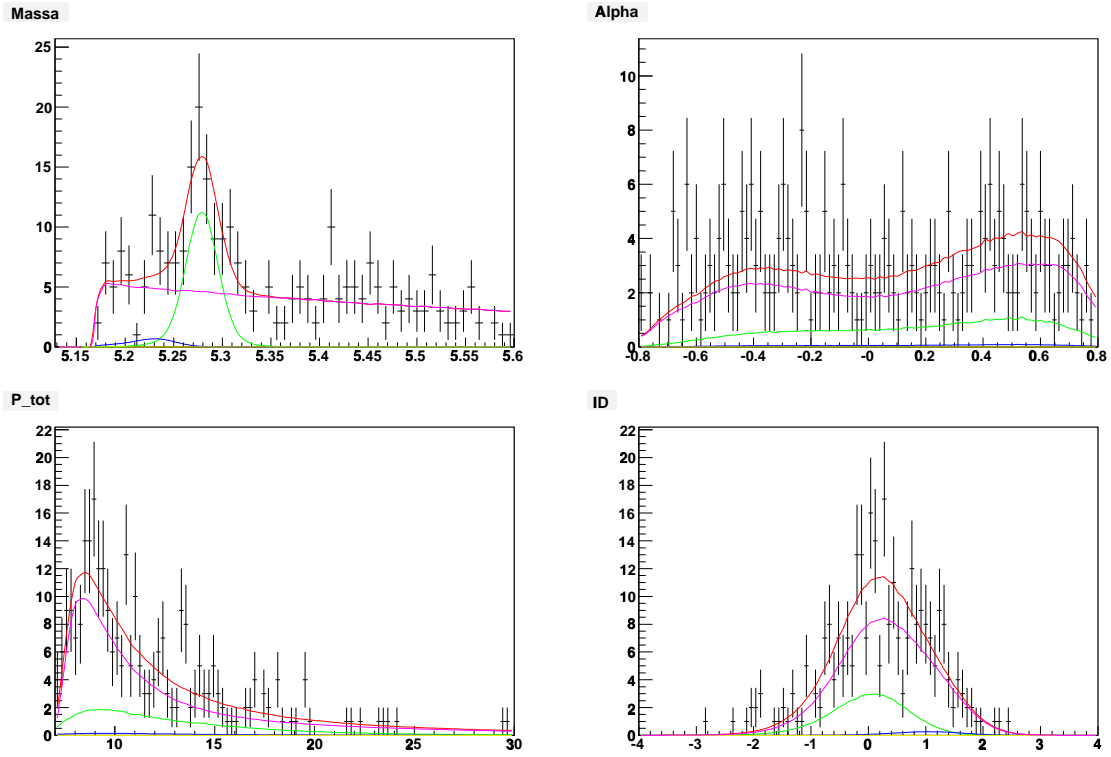


Figure 4.47: Fit projections for  $B^+ \rightarrow D_{CP+}^0 \pi^+ \rightarrow [\pi^+ \pi^-] \pi^+$ . Top left: projection on mass. Top right: projection on  $\alpha$ . Bottom left: projection on  $P_{tot}$ . Bottom right: projection on ID.

#### 4.12.1 Uncertainties achievable on $A_{CP+}$ , $R_{CP+}$

We have performed an initial evaluation of resolution by performing a em blind fit with the full sample of  $1fb^{-1}$ . While the actual parameters need much more work to be determined, a good indication of the achievable resolution can be obtained in this way.

In this fit I performed a simultaneous determination of the flavor mode  $\overline{D}^0 \pi^+ \rightarrow [K^+ \pi^-] \pi^+$  and the DCP modes  $D_{CP+}^0 \pi^+ \rightarrow [K^+ K^-, \pi^+ \pi^-] \pi^+$ . In this way we can use all the statistic to fit the parameters that are the same for all the three decays.

Recalling the expression of the fit Likelihood:

$$L = \prod_k^{N_{events}} ((1-b) \cdot (f_\pi \cdot F_\pi(\alpha, P_{tot}, M_{D^0\pi}, ID) + (1-f_\pi) \cdot F_K(\alpha, P_{tot}, M_{D^0\pi}, ID)) + b \cdot (f_D \cdot BG_D(\alpha, P_{tot}, M_{D^0\pi}, ID) + (1-f_D) \cdot BG_{comb}(\alpha, P_{tot}, M_{D^0\pi}, ID)).$$

the parameters of the maximum Likelihood fit are:

- the background fraction (b);
- the fraction of  $B^+ \rightarrow \overline{D}^0 \pi^+$  ( $f_\pi$ );
- the fraction of physical background  $B^+ \rightarrow \overline{D}^{*0} \pi^+$  ( $f_D$ );
- the fraction of pions in the combinatorial background;
- the parameter “scale”, that multiply the width of gaussians that describe the mass resolution, to take in account the differences between data and MC;
- the slope of the exponential that describe the combinatorial background.

In the simultaneously fit the parameter of scale is common to the three decays. The fraction of  $B^+ \rightarrow D_{CP+}^0 \pi^+$  is common to both the DCP modes ( $B^+ \rightarrow [K^+ K^-] \pi^+$  and  $B^+ \rightarrow [\pi^+ \pi^-] \pi^+$ ).

Performing the fit on  $1fb^{-1}$  of integrated luminosity we obtained  $\sim 10,000$   $B^+ \rightarrow \overline{D}^0 \pi^+ \rightarrow [K^+ \pi^-] \pi^+$ , so we have tripled the statistics with respect to the  $360pb^{-1}$  of data. The resolutions on  $A_{CP+}$  and  $R_{CP+}$  obtained from the fit on  $1fb^{-1}$  of data are 0.12 and 0.28 respectively.



# Conclusions and Prospects

In this thesis I have described the first measurement performed at an hadron collider of the branching fraction of the Cabibbo-suppressed mode  $B^+ \rightarrow \bar{D}^0 K^+$ .

The analysis has been performed with  $360 \text{ pb}^{-1}$  of data collected by the CDF II detector. We measured the ratio

$$R = \frac{BR(B^+ \rightarrow \bar{D}^0 K^+ \rightarrow [K^+ \pi^-] K^+)}{BR(B^+ \rightarrow \bar{D}^0 \pi^+ \rightarrow [K^+ \pi^-] \pi^+)} = 0.065 \pm 0.007(stat) \pm 0.004(sys).$$

in agreement with the world-average value of  $0.083 \pm 0.0035$ .

This measurement was approved by the CDF Collaboration ("blessed") in April 2006.

The methodology developed for this analysis is applicable to the measurement of CKM angle  $\gamma$  with the GLW and ADS methods. The GLW analysis on  $1 \text{ fb}^{-1}$  of data is underway, measuring

$$A_{CP\pm} = \frac{BR(B^- \rightarrow D_{CP\pm}^0 K^-) - BR(B^+ \rightarrow D_{CP\pm}^0 K^+)}{BR(B^- \rightarrow D_{CP\pm}^0 K^-) + BR(B^+ \rightarrow D_{CP\pm}^0 K^+)}$$

and

$$R_{CP\pm} = \frac{BR(B^- \rightarrow D_{CP\pm}^0 K^-) + BR(B^+ \rightarrow D_{CP\pm}^0 K^+)}{BR(B^- \rightarrow D^0 K^-) + BR(B^+ \rightarrow \bar{D}^0 K^+)}$$

A first test on data shows that the resolutions can be achieved with  $1 \text{ fb}^{-1}$  are:  $\sigma_{A_{CP+}} = 0.12$  and  $\sigma_{R_{CP+}} = 0.28$ .

We can compare these resolutions with the ones reached by Belle and Babar (see Tables 1.1 and 1.2) that are 0.14 (Belle) and 0.13 (Babar) for  $A_{CP+}$  and 0.16 (Belle) and 0.12 (Babar) for  $R_{CP+}$ .

So the resolutions obtained on  $1 \text{ fb}^{-1}$  are similar to the ones obtained from the B-factories, and we can look forward to obtain good results from the large run II data sample.



# Bibliography

- [1] A.Cerri, G.Punzi, G.Signorelli, “Measurement of the CKM angle  $\gamma$  with  $B^\pm \rightarrow D^0 K^\pm$ , CDF note 4881 (2000).
- [2] A. Annovi, ”Hadron collider physics with real time trajectory reconstruction”, PhD thesis, University of Pisa, 2004.
- [3] I. Furic et al., ”The Silicon Vertex Trigger Upgrade at CDF” Proceedings 10th Pisa Meeting on advanced detectors, frontier detectors for frontier physics, La Biodola, Elba, Italy May 21-27, 2006
- [4] Abulencia et al., ”The CDF II eXtremely Fast Tracker Upgrade” Proceedings 10th Pisa Meeting on advanced detectors, frontier detectors for frontier physics, La Biodola, Elba, Italy May 21-27, 2006
- [5] CDF Collaboration, “Measurement of the  $B_s$ - $B_s^*$  Oscillation Frequency”, *Phys. Rev. Lett* 97, 062003 (2006).
- [6] CDF Collaboration, “Observation of  $B_s \rightarrow K^+ K^-$  and Measurement of Branching Fraction of Charmless Two-body Decays of  $B^0$  and  $B_s$  Mesons in  $p - \bar{p}$  collisions at  $\sqrt{s} = 1.96$  TeV” hep-ex/0607021.
- [7] M.Morello et al. [CDF Collaboration], ”Measurement of the direct CP asymmetry in the  $B \rightarrow K^+ \pi^-$  decays”, CDF public note 8202 (2006).
- [8] S.L.Glashow *Nucl.Phys.* 22, 579 (1961);  
S.Weimberg *Phys. Rev. Lett.* 19, 1264 (1967);  
A.Salom in Elementary Particle Theory, ed. N.Svartholm. (Almqvist and Wisksell, Stockolm, 1968).
- [9] M. Acciari et al. [L3 Collaboration], *Phys. Lett. B* 431, 199 (1998).  
P.Abreu et al. [DELPHI Collaboration], *Z. Phys.* C74, 577 (1997).  
R.Akers et al. [OPAL Collaboration], *Z. Phys.* C65, 47 (1995).  
D. Buskulic et al. [ALEPH Collaboration], *Phys Lett B* 313, 520 (1993).
- [10] M. Kobayashi and T. Maskawa. “CP-Violation in the Renormalizable Theory of Weak Interaction”. *Prog. Theor. Phys.*, 49(2):652–657, 1973.

- [11] N. Cabibbo. “Unitary Symmetry and Leptonic Decays”. *Phys. Rev. Lett.*, 10:531–533, 1963.
- [12] Ling-Lie Chau and Wai-Yee Keung, “Comments on the parameterization of the Kobayashi-Maskawa matrix”. *Phys. Rev. Lett.* 53:1802, 1984.
- [13] W.M.Yao et al., *Journal of Physics*, **G33**(1), PDG 2006.
- [14] L. Wolfenstein. “Parametrization of the Kobayashi-Maskawa matrix”. *Phys. Rev. Lett.*, 51:1945–1947, 1983.
- [15] CKMfitter Group (J.Charles et al.) “CP Violation and the CKM Matrix: Assessing the Impact of the Asymmetric B factories”, *Eur.Phys.Jour.*, C41:1–131, 2005 [hep-ph/0406184], updated results and plots available at: <http://ckmfitter.in2p3.fr>
- [16] R.Alekson, B.Kayser and D.Landau, *Phys. Rev. Lett.* 73, 18 (1994).
- [17] M. Okamoto, ”Full determination of the CKM matrix using recent result from lattice QCD”, hep-lat/0510113.  
CDF Collaboration, ”Observation of Bd-Bsbar Oscillations” FERMILAB-PUB-06-344E, hep-ex/0609040 (2006)
- [18] J.S.Schwinger, “Spin, Statistics and the TCP theorem”, *Proc.Nat.Acad.Sci.*, 44:223-228,1958.
- [19] J.H.Christenson et al., “Evidence for the  $2\pi$  decay of the  $K_2^0$  meson”, *Phys. Rev. Lett.* 13:138-140, 1964.
- [20] B.Aubert et al. [Babar Collaboration], *Phys. Rev. Lett.* 87, 091801 (2001)
- [21] K.Abe et al. [Belle Collaboration], *Phys. Rev. Lett.* 87, 091802 (2001)
- [22] H.Burkhardt et al. [NA31 Collaboration], *Phys. Lett.* B206, 169 (1988).  
V.Fanti et al. [NA48 Collaboration], *Phys. Lett.* B465, 335 (1999).  
A.Alavi-Harati et al. [KTeV Collaboration], *Phys. Rev. Lett.* 83, 22 (1999).
- [23] B.Aubert et al. [Babar Collaboration] *Phys. Rev. Lett.* 93, 131801 (2004).  
K. Abe et al. [Belle Collaboration], hep-ex/0507045.  
C.C. Wang et al. [Belle Collaboration]. *Phys. Rev. Lett.* 94, 191802 (2005).  
B. Aubert et al. [Babar Collaboration] hep-ex/0408099.
- [24] The Heavy Flavor Averaging Group. <http://www.slac.stanford.edu/xorg/hfag/index.html>
- [25] M.Gronau and D.Wyler. “On determining a weak phase from charged B decay asymmetries” *Phys. Lett.* B 265, 172 (1991).
- [26] M.Gronau and D.London. *Phys. Lett.* B 253, 483 (1991).

- [27] D.Atwood, I.Dunietz and A.Soni. “Improved methods for observing CP violation in  $B^\pm \rightarrow KD$  and measuring the CKM phase  $\gamma$ ” *Phys. Rev. D* 63, 036005 (2001).
- [28] D.Atwood, I.Dunietz and A.Soni. “Enhanced CP violation with  $B \rightarrow KD^0(\overline{D}^0)$  Modes and Extraction of the CKM Angle  $\gamma$ ” *Phys. Rev. Lett.* 78, 3257 (1997).
- [29] A.Giri, Y.Grossman, A.Soffer and J.Zupan. “Determining  $\gamma$  using  $B^\pm \rightarrow DK^\pm$  with multibody D decays” *Phys. Rev. D* 68, 054018 (2003).
- [30] R.Fleischer, ”Flavor Physics and CP violation” hep-ph/0608010 (2006)
- [31] S.Bailey and P.Maksimovic. ”Prospects for Measuring  $\gamma$  with  $B_s \rightarrow D_s^\mp K^\pm$ ”. CDF note 4863 (2000).
- [32] M.Gronau. “Weak phase  $\gamma$  from color-allowed  $B \rightarrow DK$  rates” *Phys. Rev. D* 58, 037301 (1998).
- [33] BABAR Collaboration, B. Aubert et al. ”Measurement of  $\gamma$  in  $B^\mp \rightarrow D^{(*)}K^\mp$  decays with Dalitz analysis of  $D \rightarrow K_s\pi^-\pi^+$ ” hep-ex/0504039, submitted to *Phys. Rev. Lett.*
- [34] BELLE Collaboration, K.Abe et al., ”Measurement of  $\Phi_3$  with Dalitz Plot Analysis of  $B^\pm \rightarrow D^{(*)}K^\pm$  decay at Belle” hep-ex/0411049, contributed to FPCP2004 (2004).
- [35] Babar Collaboration “Measurement of the branching fractions and CP-asymmetry of  $B^- \rightarrow D_{(CP)}^0 K^-$  Decays”, *Phys. Rev. D* 73, 051105 (2006)
- [36] Belle Collaboration “Study of  $B^\pm \rightarrow D_{CP}K^\pm$  and  $D_{CP}^*K^\pm$  decays.” *Phys. Rev. D* 73, 051106 (2006).
- [37] BABAR Collaboration, B. Aubert et al. ”Search for  $b \rightarrow u$  transitions in  $B^- \rightarrow D^0 K^-$  and  $B^- \rightarrow D^{*0} K^-$ ” hep-ex/0504047 (2005).
- [38] BELLE Collaboration, K.Abe et al., ”Study of the Suppressed Decays  $B^\pm \rightarrow [K^\mp\pi_D^\pm]K^\pm$  and  $B^\pm \rightarrow [K^\mp\pi^\pm]_D\pi^\pm$  at Belle” hep-ex/0508048 (2005).
- [39] Belle Collaboration, hep-ex/0411049; hep-ex/0504013.
- [40] Babar Collaboration hep-ex/0507101
- [41] Alexander Shemyakin et al. [Electron Cooling Collaboration], ”Electron cooling in the recycler ring”, FERMILAB-CONF-06-147-AD (2006)
- [42] G. Aubrecht et al. ”A teachers Guide to the Nuclear Science Wall Chart”, Contemporary Physics Education Project, 2003, <http://www.lbl.gov/abc/wallchart/teachersguide/pdf/Chap11.pdf>.
- [43] C. W. Schmidt, ”The Fermilab 400-MeV Linac upgrade”, FERMILAB-CONF-93-111(1993).

- [44] Fermilab Beams Division, "Run II Handbook", <http://www-bd.fnal.gov/runII/index.html>
- [45] D. Acosta et al., *Nucl. Instrum. Methods A* 494, 57 (2002).
- [46] F. Abe et al., *Nucl. Inst. and Meth. Phys. Res.*, 271 A, 387 (1988), FERMILAB-PUB-94/024-E (1994).
- [47] R. Blair et al., "The CDF-II detector: Technical Design Report", FERMILAB-PUB-96/390-E (1996).
- [48] T. K. Nelson et al., FERMILAB-CONF-01/357-E
- [49] A. Sill et al., *Nucl. Instrum. Methods*, A447, 1-8 (2000).
- [50] T. Affolder et al., *Nucl. Instrum. Methods*, A485, 6-9 (2002).
- [51] K. T. Pitts et al., FERMILAB-CONF-96-443-E.
- [52] C.S.Hill et al., "Operational experience and performance of the CDF II silicon detector", *Nucl. Instrum. Methods*, A530, 1-6 (2004).
- [53] <http://penn01.fnal.gov/cot/>
- [54] D.Tonelli et al., "Track based calibration of the COT specific ionization". CDF Internal note 6932, INFN sez. of Roma and Pisa, Siena and Geneva University (2004).
- [55] Shin-Shanyo et al., "COT dE/dx measurement and corrections", CDF Internal note 6361, University of Pennsylvania (2003).
- [56] D.Acosta et al., "A time-of-flight detector in cdf-ii" *Nucl. Instrum. Meth.*, A518:605-608, 2004.
- [57] C. Chen, M.Jones et al., "Front end electronics for the cdf-ii time-of-flight system." *IEEE Trans. Nucl. Sci.*, 50(6),2003.
- [58] <http://huhepl.harvard.edu/cmx/cdfnotes/>
- [59] K.Anikeev et al. Event Builder abd Level-3 for aces, 2001. CDF note 5793.
- [60] P.T. Lukens (CDF IIb) FERMILAB-TM-2198
- [61] W. Ashmanskas et al., FERMILAB-CONF-02/035-E.
- [62] A.Bardi et al., *Nucl. Instrum. Methods Phys Rev. A* 485, 6 (2002).
- [63] S.R.Amendolia et al., "The AMchip: a Full-custom CMOS VLSI Associative Memory for Pattern Recognition", *IEEE Trans.Nucl.Sci.*, vol. 39, pp. 795-797, 1992.
- [64] W. Ashmanskas et al., "Performance of the CDF Online Silicon Vertex Tracker", to be published in *IEEE Trans.Nucl.Sci.*(2001).

- [65] [http://www-cdf.fnal.gov/internal/physics/bottom/bpak/pid/CombPID\\_page.html](http://www-cdf.fnal.gov/internal/physics/bottom/bpak/pid/CombPID_page.html)  
P.Squillacioti et al. "Particle Identification by combining TOF and dE/dx information" CDF note 7488 (2005).  
P.Squillacioti et al. "Update of combined PID in 5.3.4" CDF note 7866 (2005).  
P.Squillacioti et al. "Update of combined PID in 6.1.4" CDF note 8478 (2006).
- [66] S.Giagu et al. "BR ratios and direct CP violation in Cabibbo suppressed decays of D0". CDF note 6391 (2004)
- [67] P.Squillacioti et al. "TOF performance studies using  $\Lambda$  and  $K_s^0$  decays". CDF note 6757 (2004).
- [68] [http://www-cdf.fnal.gov/internal/physics/bottom/COTDEDX/COT\\_dedx\\_cali.html](http://www-cdf.fnal.gov/internal/physics/bottom/COTDEDX/COT_dedx_cali.html)
- [69] Weisstein, Eric W., "Linear congruence method". From MathWorld—A Wolfram Web Resource. <http://mathworld.wolfram.com/LinearCongruenceMethod.html>
- [70] W.T.Eadie, D.Drijard, F.E.James, M.Roos, B.Sadoulet, *Statistical Methods in Experimental Physics* (North-Holland, Amsterdam, 1971)
- [71] G.Punzi, <http://www-cdf.fnal.gov/physics/statistics/notes/punzi-separation.ps>
- [72] M.Casarsa et al. "Measurement of  $\frac{BR(B_u \rightarrow \phi K)}{BR(B_u \rightarrow J/\psi K)}$  at CDF" CDF note 6584.
- [73] J.Marriner, "Secondary Vertex Fit with Mass and Pointing Constraints (CTVMFT)", Tech. Rep. CDF/DOC/SEC\_VTX/PUBLIC/1996 (1993)
- [74] G. Bauer et al., "Measurement of  $B^0$  oscillations using Same Side Kaon Tagging in fully reconstructed decays" CDF note 7145
- [75] M.Morello et al., "Measurement of Isolation efficiency in low pt B mesons", CDF note 7049 (2004)
- [76] K.Anikeev, C.Paus, P.Murat, "Description of Bgenerator II", CDF note 5092 (1999).
- [77] P.Nason, S.Dawson, R.K.Allis, "The total cross-section for the production of heavy quarks in hadronic collisions" *Nucl. Phys.* B303:607 (1988)
- [78] W.Bell, J.Pablo Fernandez, "User guide for EvtGen at CDF" CDF note 5618 (2003)
- [79] R.Brum, R.Hgelberg, M.Hansroul and J.C Lasalle, "Geant:Simulation Program for particle physics experiments: user guide and reference manual", CERN DD-78-2 REV.
- [80] M.Abramowitz and I.A.Stegun *Handbook of Mathematical Functions: with Formulas, Graphs, and Mathematical Tables*

- [81] J. Heinrich, "A guide to the Pearson Type IV Distribution". CDF note 6820 (2004)
- [82] Belle Collaboration "Measurement of branching fraction ratios and CP asymmetries in  $B^\pm \rightarrow D_{CP} K^\pm$ " *Phys. Rev. D* 68, 051101 (2003).
- [83] CDF Collaboration "Measurement of B hadron masses in exclusive  $J/\psi$  decays with the CDF detector" *Phys.Rev.Lett.* 96 (2006) 202001
- [84] Babar Collaboration "Measurement of Branching Ratios and CP Asymmetries in  $B^- \rightarrow D_{(CP)}^0 K^-$  Decays", hep-ex/0207087 (2002)
- [85] A.Barnheim et al. "Measurements of charmless hadronic two-body B meson decays and the ratio  $B(B \rightarrow DK)/B(B \rightarrow D\pi)$ " *Phys. Rev. D* 68, 052002 (2003).